Flower-like azimuthal instability of a divergent flow at the water-air interface

Goce Koleski

THÈSE PRÉSENTÉE

POUR OBTENIR LE GRADE DE

DOCTEUR DE L'UNIVERSITÉ DE BORDEAUX

ÉCOLE DOCTORALE DES SCIENCES PHYSIQUES ET DE L'INGÉNIEUR

SPÉCIALITÉ : LASERS, MATIÈRE ET NANOSCIENCES

Flower - like azimuthal instability of a divergent flow at the water/air interface

---

Goce KOLESKI

Sous la direction de M. Thomas BICKEL

Soutenue publiquement le 25 novembre 2019 en présence du jury composé de :

Mme Laurence TALINI – Directeur de recherche, CNRS	Rapporteur
M. Christophe YBERT – Directeur de recherche, CNRS	Rapporteur
M. Christophe RAUFASTE – Maître de conférences, Nice	Examinateur
M. Jean – Pierre DELVILLE – Directeur de recherche, CNRS	Président du jury
M. Thomas BICKEL – Maître de conférences, Bordeaux	Directeur de thèse
M. Bernard POULIGNY – Directeur de Recherche, CNRS	Membre invité

In loving memory of
my grandmother
Pandora

Remerciements

"Patience et longueur de temps / Font plus que force ni que rage" écrivait Jean de La Fontaine dans *Le Lion et le Rat*, l'une de ses fables les plus célèbres. Je crois n'avoir jamais ressenti, avec plus d'acuité qu'au cours de ces années de thèse, ce que cette morale comporte de vérités. La grande aventure du doctorat s'achève, et ma persévérance a fini par payer. Nul doute désormais, ami lecteur, que le manuscrit que tu as entre les mains est le fruit d'un dur labeur ! Cela dit, n'eût été le concours de nombreuses personnes, rien de tout ceci n'aurait vu le jour. Aussi le temps est-il venu pour moi de remercier du fond du coeur celles et ceux d'entre vous qui m'ont épaulé.

Merci à mon directeur de thèse, Thomas Bickel, de m'avoir enseigné à quel point faire de la recherche est une tâche exigeante. Merci à Bernard Pouligny d'avoir toujours su nous faire atterrir en douceur, y compris par vent de travers, sur des pistes aussi exiguës que la surface d'un verre d'eau. Merci à lui de m'avoir appris à survivre à de nombreux crash tests, chaque fois que je précipitais mon frêle esprit contre le géant Marangoni. Merci à Jean-Christophe Loudet pour ses nombreuses simulations numériques qui nous ont permis de mieux appréhender les phénomènes à l'étude, en plus de les illustrer à merveille. Tous mes voeux de bonheur et de réussite t'accompagnent à Vancouver. Merci à François Nadal, Sébastien Michelin et Alois Würger pour nos discussions fructueuses.

Merci aux membres de mon jury, Mme Laurence Talini (rapporteur), M. Christophe Ybert (rapporteur), M. Christophe Raufaste (examinateur) ainsi que M. Jean-Pierre Delville (examinateur), de m'avoir fait l'honneur d'évaluer mon travail.

Merci à celles et ceux qui nous ont apporté une aide matérielle indispensable. Je pense notamment à Hamid Kellay et Christophe Pradère qui ont eu l'amabilité de nous prêter leurs caméras infrarouges afin que nous puissions réaliser des études thermographiques. Merci à Romain Houques de m'avoir accordé plusieurs après-midis de travail, à découper au diamant de nouvelles cellules expérimentales pour le maladroit que je suis. Merci à Philippe Barboteau et à Emmanuel Texier, de l'atelier mécanique du Centre de Recherche Paul Pascal, sans qui la conception des expériences n'aurait jamais franchi le cap du dessin industriel. Merci à Lionel Buisson, Pascal Merzeau, Sandrine Maillet, Julien Désenfant, Jean-Luc Laborde, Philippe Hortolland, Alain Blück, David Rivière et Eric Basier pour leurs coups de pouce réguliers en informatique. Je remercie aussi Joanna Giermanska et Frédéric Louerat de m'avoir fourni les produits chimiques dont j'avais besoin. Merci à Eric Laurichesse qui a réalisé pour nous des expériences de tensiométrie.

Merci à Alexandre Vilquin pour sa profonde implication dans ce projet. Je lui dois mon initiation à la technique de vélocimétrie par image de particules. Alexandre est en outre à l'origine du code MATLAB que j'ai exploité à maintes reprises et grâce auquel j'ai pu apporter une réelle plus – value quantitative à mon travail. Merci à Benjamin Gorin et à Amaël Mombereau d'avoir été de formidables stagiaires de Master, étudiants talentueux et chouettes camarades ayant notamment réalisé les splendides clichés thermographiques exposés dans ce manuscrit. Merci à Antoine Girot et à Noémie Danné, anciens stagiaires au CRPP à l'époque où le projet MicroMar faisait ses premiers pas, d'avoir posé les solides fondations d'un édifice intellectuel en perpétuelle construction. Merci à Elodie Millan et à Frédéric Dutin d'avoir choisi de s'immerger pour quelques temps dans le riche univers de nos recherches, afin d'en élucider certains mystères. Puissiez-vous de longues années encore tirer de vos recherches de merveilleux trésors !

Merci à tous les compagnons de route du Laboratoire Ondes et Matière d'Aquitaine (LOMA) ou du Centre de Recherche Paul Pascal (CRPP) qui ont su lever mes doutes lorsque je m'étais égaré. Il se pourrait fort que, trop modestes, vous sous – estimiez le rôle que vous avez eu dans cette histoire. Sachez pourtant qu'en me gratifiant d'un sourire ou d'un mot doux vous m'avez encouragé jusqu'au bout à me battre malgré tout. Alors, entre autres, mille mercis au LOMA à Quentin, à Julie, à Marion, à Alizée, à Paul, Matthieu, Houssem, aux Alexandre, à Léo, à Raphaël, Hugo, Laura, Stefano et Lorenzo; sans oublier Nina, Marcela, Mikaël, les Benjamin et Hernando; puis Bishal, Louis, Maxime, Jérémy, Nicolas, Valerian, Arthur, Mahdi, Aymen, Hassan, Amine, Gabriel et Gopal. Une mention spéciale pour Clément Dutreix qui m'a soutenu comme seul aurait su le faire ce frère que je n'ai jamais eu. Quant au CRPP, je tiens à remercier Sophie, Romain, Raj, Andrii, Marco, Franco et Fernando, Oksana et Hanna, Vincent, Antoine, Rafael, Marie – Charlotte et Armand, Mayte, Maeva, Rajam, Sarah, Theo, Laura, Carlotta, Simone, Katerina, Julien et Penny, Pierre – Etienne, Elodie, Maxime, Emmanuel, Morgane, Thamires et Etienne.

Les noms qui vont suivre sont ceux de personnes formidables, chercheurs ou non, qui m'ont témoigné de la bienveillance au quotidien et que je voudrais ici remercier chaleureusement : Bernadette Bergeret, Sophie Grandet, Suzanne Bessus, Josiane Parzych, Isabelle Guillaume, Annie Commarmond, Sandra Bosio, Jean – Pierre Delville, Rémi Avriller, Fabio Pistolesi, Joseph Leandri, Alois Würger, Simon Villain – Guillot, Hamid Kellay, Ulysse Delabre, Julien Burgin, Christine et Stéphane Grauby, Jérôme Cayssol, Sébastien Burdin, Thomas Salez, Thomas Guérin, Ludovic Jaubert, Denise Mondieig, Bernard Trégon, Françoise Argoul et Alain Arneodo, Etienne Harte, Fabien Moroté, Marc Tondusson, William Benharbone, Sébastien Cassagnere au LOMA; Frédéric Nallet,

Virginie Ponsinet, Cécile Zakri, Corinne Amengual, Philippe Barois, Philippe Richetti, Olivier Mondain – Monval, Alexandre Baron, Lionel Buisson, Pascal Merzeau, Emmanuel Texier, Philippe Barboteau, Jean – Paul Chapel, Jean – Christophe Baret, Wilfrid Néri, Frédéric Louerat, Joanna Giermanska, Eric Laurichesse, Alain Pénicaud, Eric Grelet, Carlos Drummond, Ahmed Bentaleb, Hassan Saadaoui, Alain Derré, Annie Colin, Rénal Backov, Emmanuelle Hamon, Nathalie Touzé, Nadine Laffargue, Béatrice Dupin, Brigitte Delord, Béatrice Huynh – Tan au CRPP. Un grand merci aux agents d'entretien, le plus souvent des femmes discrètes officiant dans l'ombre et grâce à qui la lumière fait irruption dans notre quotidien, par un sourire, des mots tendres et justes. Vous me faites à vrai dire l'impression d'anges gardiens. Merci du mal que vous vous donnez dès les premières lueurs de l'aube pour que nous puissions travailler dans un cadre digne, agréable et frais.

Je voudrais remonter dans mes souvenirs et rendre hommage aux enseignements de M. Hervé Dewez, M. Michel Labelle, Mme Jeanne Stoliaroff, M. Willie Robert ainsi que M. Jean – Marc Simon, tous professeurs exceptionnels à la passion dévorante pour la physique ou les mathématiques, et à qui je dois beaucoup du goût que j'en ai conservé jusqu'à aujourd'hui. Permettez – moi également de saluer amicalement trois chercheurs qui ont été de véritables mentors pour moi : Jean – Baptiste Fournier, Thierry Hocquet et Patrick Petitjean. Vous tous m'avez transmis une part de votre savoir en héritage et je veux vous faire honneur en m'engageant sur vos traces...

Merci à mes amis d'enfance avec qui j'ai vieilli en cours de récréation et qui sauront se reconnaître je pense malgré le passage des saisons. Merci également à tous ces amis de Paris qui, rencontrés plus tard dans ma vie, n'en sont pas moi restés présents dans mon coeur et qu'ici je remercie. Merci aussi à Kitty, Chloé et Hortense de m'avoir offert le privilège immense d'être de leurs amis.

Je souhaiterais enfin remercier ceux qui, sans même être physiciens de formation, m'ont permis de me hisser au niveau d'une thèse... je pense bien évidemment à mes proches. Vous êtes les artisans de ce que je suis et j'ai pour vous un amour infini. De mon premier souffle à mes premiers pas, de l'époque du cartable à celle du doctorat, me pensant souvent seul dans un monde qui s'est tu, dans l'ombre m'attendaient dix mains toutes tendues ! Je voudrais pour finir rendre hommage à l'abnégation de mes grands – parents paternels qui, partis de Macédoine avec leur courage comme unique bagage, suant souvent jusqu'à l'oubli nous ont bâti un nid et qui, faisant il y a cinquante ans un saut dans l'inconnu, y plantèrent une échelle afin que ma soeur et moi – même puissions contempler les nues.

Bonne lecture !

Résumé / Abstract

Un écoulement axisymétrique à une interface eau-air s'avère instable azimutalement. Durant cette thèse, nous avons mené deux expériences afin d'étudier ce point : (1) une petite fontaine subaquatique propulse un jet contre l'interface eau-air créant ainsi en surface un écoulement radial centrifuge; (2) une microbille chauffée par laser, en mouillage partiel à la surface de l'eau, engendre un écoulement thermocapillaire divergent. Lorsque la vitesse du jet ou la puissance du laser est suffisamment forte, il se produit une brisure de symétrie de l'écoulement torique initial en paires de vortex contrarotatifs entourant la source. Nous précisons les caractères morphologiques du tore ainsi que du dipôle par le biais d'expériences de tomographie laser et d'injection de colorant. Dans l'expérience du jet d'eau, nous montrons que la taille du tore est essentiellement déterminée par la distance séparant l'injecteur de la surface. Dans les deux expériences, un état "bloqué" de l'interface en régime toroïdal mais "débloqué" en régime dipolaire est mis en évidence par suivi de traceurs. Ce type de phénomène est piloté par l'élasticité de surface. Une preuve convaincante est la réponse élastique, à l'extinction du laser, de la couche de surfactants adsorbés à l'interface. Le principal intérêt de ce travail est de mettre en avant le rôle−clé que joue l'élasticité interfaciale dans le scénario de l'instabilité. D'un point de vue théorique, nous étudions la convection thermocapillaire induite par une source fixe ponctuelle à l'interface eau-air. Nous résolvons l'équation de Stokes incompressible au sein du demi−espace contenant le liquide et déterminons la solution exacte du problème advectif, non-linéaire, dans le régime axisymétrique en limite de champ lointain. Enfin, nous posons les bases sur lesquelles élaborer une théorie de l'instabilité. Ce travail de thèse devrait permettre de comprendre comment une petite sphère chaude à la surface de l'eau déclenche le type d'instabilité étudié ici, devenant de ce fait une "particule active" capable de s'autopropulser à grande vitesse.

Axisymmetric flows on a water-air interface prove to be azimuthally unstable. In this thesis work, we design two setups to explore this fact : (1) a small subaquatic fountain propelling a jet against the water-air interface where it creates a centrifugal radial flow, (2) a laser−heated microbead in partial wetting at the surface of water that induces a divergent thermocapillary flow. At sufficiently high jet speeds or laser powers appears a symmetry−breaking of the toroidal base flow in the form of counter−rotating vortex pairs surrounding the source. Morphological traits of the torus and the dipole are uncovered through a wealth of laser tomography and dye injection experiments. In the water jet experiment, we show that the torus size is primarily fixed by the distance between the injector and the surface. In both experiments, the tracking of tracer particles evidences a 'locked' interface in the toroidal regime, whereas it 'unlocks' when a dipole sets in. Such a phenomenon is conditioned by surface elasticity. Cogent evidence is brought by the elastic response to laser shutdown of a surfactant layer adsorbed at the water surface. Unveiling the key role of surface elasticity in the scenario of the instability is the main achievement of this work. On a theoretical level, we focus on thermocapillary convection induced by a fixed point source of heat sitting across the water-air interface. We solve the incompressible Stokes equation within the water−filled half−space and derive an exact solution to the advective nonlinear regime in the far−field axisymmetric limit. We then lay the groundwork on which to build a model of the instability. This thesis work paves the way for understanding how a hot microsphere found on the water surface triggers such an instability, thereby becoming an 'active particle' able to achieve self−propulsion at large speeds.

Keywords/Mots clés : divergent flows/écoulements divergents; azimuthal instability/instabilité azimutale; surfactant−laden elastic interface/interface élastique chargée en tensioactifs; Marangoni effect/effet.

'Panta rhei'

Heraclitus of Ephesus
(*c.* 535 BC – *c.* 475 BC)

Table of contents

Introduction

In this thesis, we probe the azimuthal stability of axisymmetric flows developing at a water/air interface. Two systems serve as 'radial sources': (1) a slender tube lying at a short distance under water propels against the surface a jet that creates a centrifugal radial flow, (2) a hot microsphere sitting in partial wetting across the water/air interface that induces a divergent thermocapillary flow. In the latter case, the local temperature rise gives birth to surface stresses that put the liquid into motion, a phenomenon called the Marangoni effect. In both experimental situations, surface active impurities adsorbed at the water/air interface are repelled by the outward forced flow. When the jet (1) or heating (2) is strong enough, a flower−like azimuthal instability of the divergent flow arises in the form of counter−rotating vortex pairs periodically distributed all around the source. It is this instability which motivates the present work, with potential applications for the propulsion of artificial microswimmers within self−induced Marangoni flows.

Historically, this project started with the manipulation of microparticles using an optical levitator [1] (Fig. 1): a small sphere made of a light−absorbing material, initially lying on the floor of a glass cuvette (a), is captured by a focused vertical laser beam that exerts on the latter a radiation pressure strong enough to push it against the water/air interface where it locks in partial wetting (b). Contrary to a hot sphere found in the bulk that would self−centre on the laser beam axis, a hot sphere located at the surface gets out of the trap and describes quasi−circular orbits around the laser beam axis past a threshold heating power $\mathcal{P}$ depending on the beam waist radius ω_0 [2] (Fig. 2). While these quasi−circular trajectories proved stable for any given couple ($\mathcal{P}$, ω_0) in the explored range, with a fairly well reproducible radius r_{orb} as the laser was repeatedly switched off/on, the orbital velocity v_{orb} was absolutely not: its magnitude varied significantly from one experiment to another, and it was not rare to see the laser−heated particle reverse its direction of rotation many times in the course of a single experiment. A major interest of

this device lies in its ability to efficiently trap microspheres behaving as thermally – driven Marangoni surfers [3] that self – propel very fast, at typical velocities up to 1 mm/s, with just a few milliwatts of laser power.

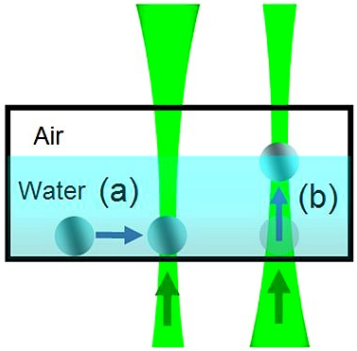

Figure 1: Optical levitator. Radiation pressure forces, typically in the order of a few piconewtons, are sufficiently strong to levitate a microsphere. *Image taken from [2].*

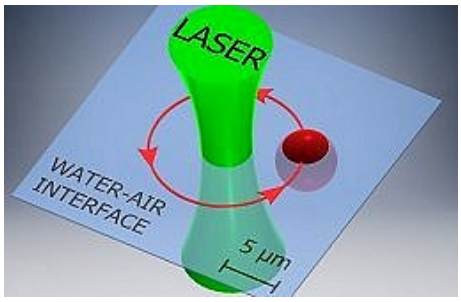

Figure 2: Closed orbital track of a light – absorbing microsphere around the centre of an optical trap. We use tiny particles about 5 μm in diameter. *Ibid.*

The thermocapillary flow induced by the laser – heated sphere was revealed using tracer particles. It was the first time we observed the multipolar instability we are interested in, as counter – rotating vortex pairs 'escorting' the microsphere in its orbital motion (Fig. 3).

Since characterising the multipolar flow patterns generated by a hot free particle seems too challenging, primarily because of the difficulty in describing the dynamic coupling between the temperature field and the particle trajectory, we opted for a simpler approach. We decided to study the convective flow developing in the vicinity of a fixed hot spot submitted to increasing heating. The first tests we conducted in this direction would use the tip of a soldering iron or that of an acupuncture needle as rudimentary heat sources of spherical geometry (Fig. 4). We observed once again the same multipolar instability, with a growing number of convection cells with increasing temperature.

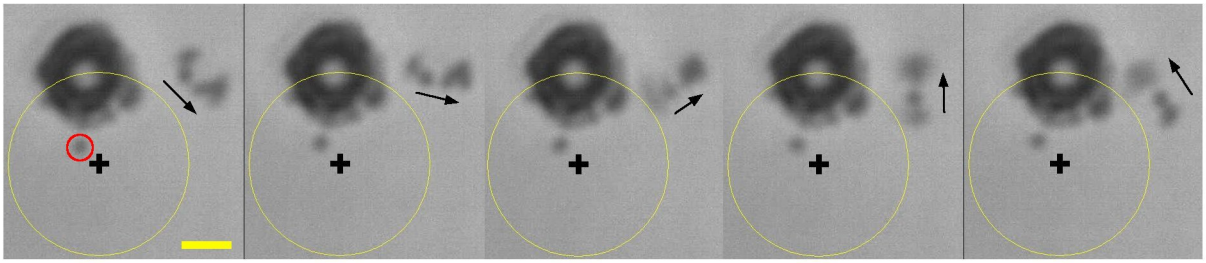

Figure 3: Vortex pair escorting the light – absorbing microsphere along its circular trajectory. Tracer particles gathered into a rotating cluster reveal the presence of a vortex ahead of the orbiting microsphere. A close inspection of the video unveils the existence of a second vortex lagging behind the particle, slightly inside the orbit (red circle). Note the corona of tracer particles coating the surface of the microsphere. Time increases from left to right, with an interval $\delta t = 24\,\mathrm{ms}$ between two successive frames. Laser beam axis marked by a black cross. The orbital motion of the heated microsphere (yellow circle) is clockwise, whereas the big vortex motion (black arrows) is anticlockwise. Experimental parameters : laser beam waist radius $\omega_0 = 6.3\,\mu\mathrm{m}$, heating power $\mathcal{P} = 28\,\mathrm{mW}$. Scale bar : $5\,\mu\mathrm{m}$. *Ibid.*

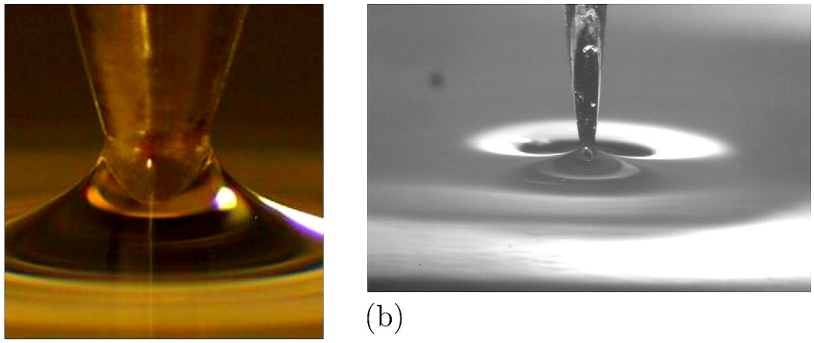

(a) (b)

Figure 4: Hot tip of a soldering iron (a) and of an acupuncture needle (b) touching the water surface. Both tips are regarded as fixed spherical heat sources in partial wetting at the water/air interface. The point of the soldering iron used in our experiments has a radius $a_{si} = 100\,\mu\mathrm{m}$ while the end of the acupuncture needle is a half – sphere of radius $a_{an} = 6.5\,\mu\mathrm{m}$. *Images from A. Girot's and A. Mombereau's internship reports.*

Recently, during A. Mombereau's internship, we designed a more sophisticated setup consisting of a carbon microbead stuck onto the end of an optic fibre. The 'hot bead experiments' that we will present later in this work were all achieved using this setup.

In fact, the azimuthal instability investigated in this project manifests in a wider range of physical situations, as it is observed in the presence of solutocapillary flows as well, *i.e.* Marangoni flows induced by a surfactant concentration gradient along the interface. Almost half a century ago, Pshenichnikov and Yatsenko yet reported the existence of such

an instability, though at the macroscopic scale [4]. The principle of their experiment is simple : a cylindrical pan of 280 mm in diameter and 40 mm in height is filled with distilled water. A 10% hydroalcoholic solution is supplied to the system through a slender tube at an extremely low mass rate, from 3×10^{-4} to 0.1 g/s (Fig. 5). Aluminium powder is spread onto the surface and time – lapse photographs are taken to visualise the streamlines.

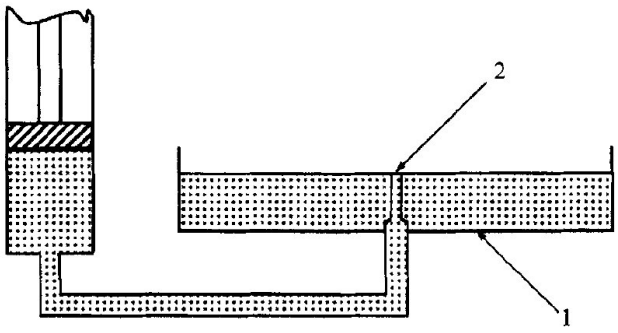

Figure 5: Setup of Pshenichnikov & Yatsenko's experiment. A 10% alcohol – water solution flows in the cylindrical pan (1) filled with distilled water through the capillary tube (2). *Image from [4].*

Remarkably, Pshenichnikov and Yatsenko observed a multipolar instability which is at least qualitatively similar to the one destabilising the axisymmetric flow visible under low heating conditions in our experiments. On Fig. 6 is displayed a photograph of a dipole captured by the authors at low flow rates. They also noted that gradually increasing the flow rate results in a larger number of vortices, as illustrated by the octupole in Fig. 6.

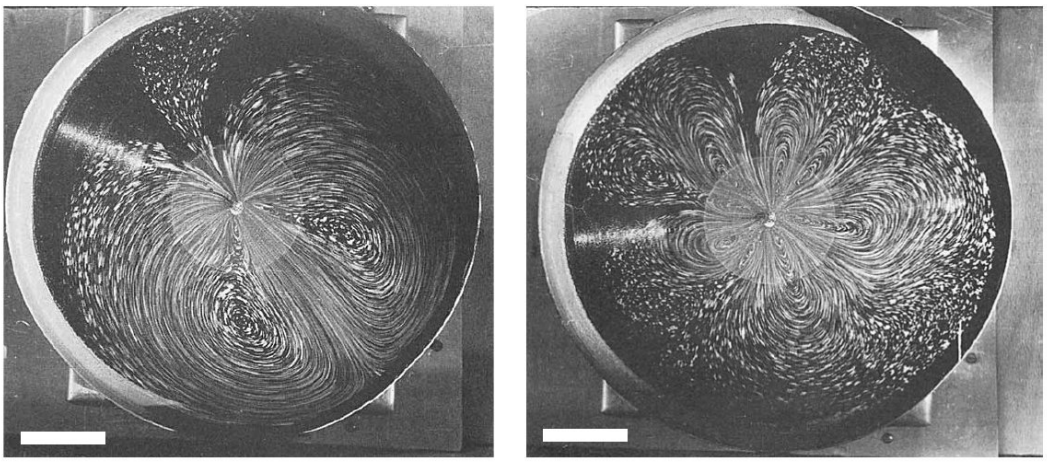

Figure 6: Example of dipolar (*left*) and octupolar (*right*) flow patterns (*top views*). Scale bar : 5 cm. *Image taken from [4].*

Mizev *et al.* [5] reproduced Pshenichnikov and Yatsenko's experiment and recovered the instability. They went further into the description of this phenomenon considering the effect of an adsorbed layer of insoluble surfactants on the concentration – driven Marangoni flow. Two experimental parameters were introduced to study the structure and stability of the interfacial convective flow : the surface density of surfactants and the Marangoni flow intensity. A dimensionless ratio, called the (solutal) Marangoni number, was used to compare the magnitude of capillary forces to viscous dissipation

$$\mathrm{Ma}_S \doteq \frac{q}{D\eta^2}\,\frac{\mathrm{d}\gamma}{\mathrm{d}\mathcal{C}}\ , \tag{1}$$

with q the mass flow rate of the ethanol solution, D the diffusivity of ethanol in water, η the dynamic viscosity of water and $\mathrm{d}\gamma/\mathrm{d}\mathcal{C}$ the surface tension γ dependence upon the surface concentration of ethanol $\mathcal{C}$. The Marangoni number, being proportional to the injection rate q, quantifies the 'strength' of the point source of surface – active material.

While varying these parameters Mizev and his coworkers noted, as Pshenichnikov and Yatsenko before them, a growing number of convection cells as the Marangoni number increased. They also observed a decreasing number of vortices as the surface density of surfactants increased. Fig. 7 retraces the evolution of the 'multivortex annulus' as the surface density of the impurity (oleic acid) increases and/or the Marangoni flow intensity decreases. As long as the impurity concentration remains moderate and the source flow is pretty intense, there exists a wide central region where the primary axisymmetric flow persists, surrounded by a secondary structure which consists of numerous vortices located at the cuvette periphery (a). The more surface contamination worsens and/or the flow weakens, the more this central region shrinks and even vanishes above some critical values of the governing parameters (b-d). Meanwhile, the vortices grow in size but their total number declines. With further increase in the surfactant concentration, one is left with a dipolar flow which disappears in its turn (e-f). Ultimately, a concentration threshold depending on the Marangoni number is reached beyond which surface motion is totally inhibited (the water/air interface is then in a 'concrete – like state').

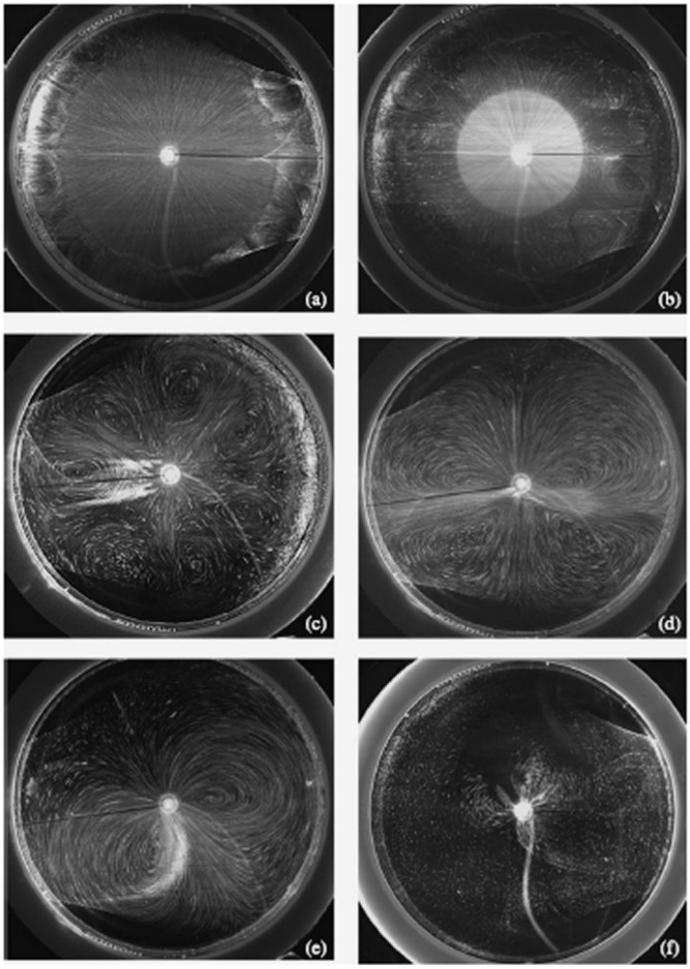

Figure 7: Evolution of the multivortex patterns with an increase in the surface density of impurities (oleic acid) and/or a decreasing flow intensity. *Image taken from [5].*

Recently, S. Le Roux *et al.* [6, 7] studied axisymmetric Marangoni flows induced at the water/air interface by the local and continuous deposition of hydrosoluble surfactants. They observed a complex interfacial flow self−organised into concentric regions (Fig. 8):

- Immediately surrounding the injection point is an area of intense light scattering (oil droplets served as tracer particles) of radius r_{s} referred to as the source.
- A little further from the injection locus comes a transparent zone of radius r_{t}, exhibiting faintly scattered light. Divergent Marangoni flows are concentrated in that region submitted to strong surface tension gradients.
- Beyond the distance r_{t} develops a 'belt' of vortex pairs.
- Still further, there is a region where tracer particles barely move, implying that surface tension is spatially homogenous in this outer area.

The authors' goal was to study how surfactant solubility (amphiphilic molecules were used) influences the surfactant – driven flow. Remarkably, they proved the universality of the interfacial velocity field within the transparent zone and derived scaling laws based upon hydrodynamics and surfactant physicochemistry that capture the flow properties very accurately. Unfortunately, the authors did not study the ring of vortices arising beyond the transparent zone that interests us so much. However, their work is of great interest for the many processes in which surfactant – induced transport phenomena play an essential role, such as emulsification and foaming, surface coating, or Marangoni drying.

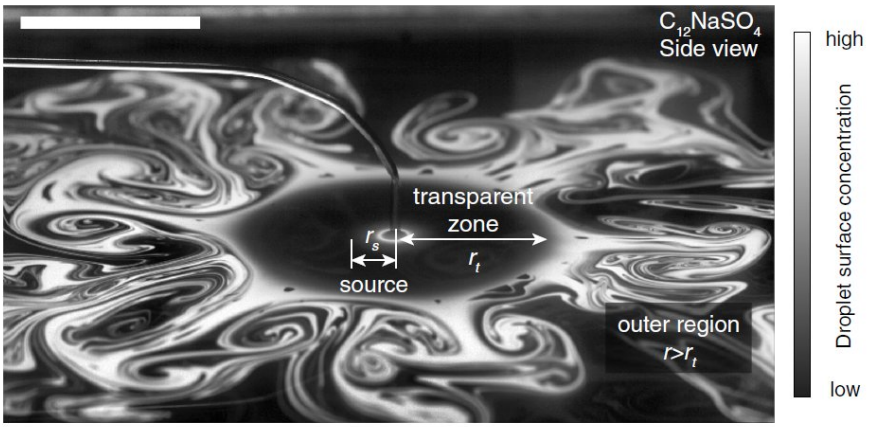

Figure 8: A side view from above the water – air interface of the Marangoni flow sustained by the local and continuous injection of an aqueous solution of surfactant on the surface of ultra – pure water. Milky – white regions are highly concentrated in oil droplets that intensely scatter light, contrary to dark regions. The stagnant zone beyond the ring of vortices is not shown. Surfactant molar flow rate $Q_a = 0.52\,\mu\text{mol.s}^{-1}$. Scale bar: 3 cm. *Image taken from [6].*

The need for taking into account contamination from adsorbed molecules of surface – active agents has become increasingly evident over the past few decades, and it is now well – known that minute quantities of a surfactant material suffice to drastically alter the interfacial hydrodynamics of a system. This is especially true for water which, owing to its high surface tension comparatively with many common liquids, acts as a receptacle for most surface – active impurities inevitably present in the environment, making the contamination of the water/air interface a recurrent issue in interfacial science [8, 9]. For instance, the central role of surfactants in retarding the motion of a bubble rising in a liquid has been evidenced in [10, 11]. Surface contamination is also suspected to affect the shape of 'coffee rings' in numerous experiments where evaporating droplets are present [12] – [14]. It has long been known that traces of surfactants can have a stabilising effect on convective instabilities [15].

Obviously, interfacial contributions become increasingly significant as the system gets smaller and smaller. As an example, microfluidic experiments have brought to light that a tiny amount of surfactants is able to severely undermine the drag reduction potential of superhydrophobic surfaces [16]. Impurities can also affect the viscoelastic response of a water/air interface, as evidenced by AFM measurements [17, 18]. Other experiments suggest that surface – active contaminants can promote the rupture of μm-thick free liquid films [19]. Interestingly, the influence of surfactants manifests even down to nanoscales : the stability of surface nanobubbles is attributed to impurities [20, 21] and nanomolar concentrations of charged contaminants are invoked to explain anomalous surface tension variations (Jones – Ray effect) in electrolyte solutions [22].

This non – exhaustive list of examples puts the accent on the ubiquity of contaminants and the utmost need to take them into consideration while studying free surface flows. It explains why great importance is attached throughout this thesis to surfactants adsorbed at the water/air interface and to their role in modifying the dynamics of surface flows by providing the water/air interface with elasticity. Our work is structured as follows :

- *In chapter 1, we briefly recall the fundamentals of surface tension, surfactants and Marangoni flows that are central to understanding this study.*

- *In chapter 2, we present an experiment based on a tiny subaquatic fountain propelling a liquid jet towards the water surface. This is the simplest way we have imagined to create a divergent flow at the water/air interface with as little physical ingredients as possible. We shall see that this 'mechanical generator' of centrifugal radial flows is a handy tool to study the azimuthal instability we are interested in and identify some of its features. Special focus will be put on the evolution of the toroidal base flow with both the injection speed and the injector – to – interface distance (the 'gap') taken as tunable parameters.*

- *In chapter 3, we present our 'hot bead experiment' as an alternative way of producing a divergent flow through heating an absorbing microbead in partial wetting at the surface of water. Although this system may seem more involved at first sight, due to the thermocapillary nature of the forced flow instead of a pressure – driven one as previously, we shall discover that it leads to basically the same interfacial dynamics, yielding multivortex flow patterns as the bead is increasingly heated similar to those observed while strengthening the injection rate in the 'water jet experiment'. Again, particular attention will be paid to the fate of the primary torus as the carbon sphere is heated to varying degrees.*

- ☞ *Finally, the problem of the thermocapillary convection induced by a fixed point source sitting across the water/air interface is addressed in chapter 4. Here, we essentially solve the incompressible Stokes equation within a half−space and derive an analytical solution to the nonlinear regime in the presence of thermal advection, before laying the groundwork on which to develop an overall approach of the multipolar instability.*

Chapter 1

The physics of interfacial flows

In this opening chapter, we remind the reader of some basic notions regarding surface tension, surfactants and Marangoni flows. We first define surface tension from both the energy and the mechanical standpoint. We then recall surfactants' main properties and review everyday life situations wherein such chemical species are commonly encountered. To finish, we introduce the Marangoni effect, a ubiquitous phenomenon in interfacial hydrodynamics. The after presentation is inspired from the introduction of S. Le Roux's thesis [23] with a few elements borrowed from the reference book [24].

1.1 Surface tension

1.1.1 Energy approach

Consider a liquid/gas interface. Van der Waals intermolecular forces ensure the cohesion of the liquid. A molecule in the bulk undergoes attractive electrostatic interactions from neighbouring molecules located all around, so that this isotropic molecular distribution exerts no net force on it. By contrast, molecules right beneath the free surface experience about half as much attractive forces as molecules found deeper. This disbalance results in an excess energy at the interface that is called surface tension (Fig. 1.1).

Let us evaluate the typical order of magnitude of surface tension. Assume a cohesion energy U per molecule in the bulk. A molecule in the vicinity of the interface has an energy $\sim U/2$. With a the size of a molecule and a^2 the surface exposed to the gas, the surplus energy per unit area scales as $\sim U/2a^2$. For oils, whose cohesion forces are Van der Waals', $U \sim k_B T \approx 1/40\,\mathrm{eV}$ at room temperature $T_{room} = 25°\mathrm{C}$. One finds a surface tension $\sim 20\,\mathrm{mJ.m^{-2}}$ for most common liquids, with the notable exception of water whose

surface tension is higher than this estimate due to strong hydrogen bonds significantly increasing the cohesion energy. Still larger surface tension values exist for liquid metals, *e.g.* mercure whose surface tension approaches $500\,\mathrm{mJ.m^{-2}}$ (table 1.2). Surface tension decreases with increasing temperature : indeed, the stronger thermal agitation, the weaker intermolecular cohesion forces and thus the smaller surface tension.

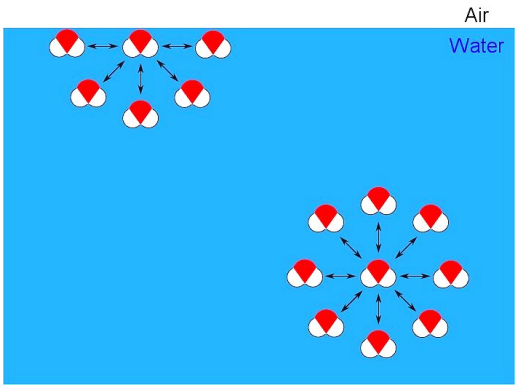

Figure 1.1: Molecular origin of surface tension. The electrostatic interactions of molecules found in the vicinity of the interface are less screened than those of molecules situated in the bulk, resulting in excess interfacial energy called surface tension. *Image taken from [23].*

Substance	Surface tension (mN/m)
Water (10°C)	74.2
Water (25°C)	72.0
Water (50°C)	67.9
Mercury (25°C)	485.5
Acetone (25°C)	23.5
Ethanol (25°C)	23.2
Formamide (25°C)	57.0
Nitrogen (77°K)	8.85

Figure 1.2: Surface tension values of some usual liquids. Note the significant decrease of the surface tension of pure water with increasing temperature. *Data from [25].*

As a response to the unfavourable extra energy of the interface, a fluid tends to minimise its energy by minimising its free surface (Fig. 1.3). In the field of interfacial thermodynamics, a theory pioneered by American physical chemist J.W. Gibbs [26] (see also [27]), surface tension is defined as the free energy F increase following an increase of interfacial area by $\mathrm{d}\mathcal{A}$, under fixed temperature T, volume V and amount of substance n

$$\gamma \doteq \left.\frac{\partial F}{\partial \mathcal{A}}\right|_{T,V,n} . \tag{1.1}$$

As a complement to the above energy approach at the molecular level, let us now move to a description of surface tension in terms of forces.

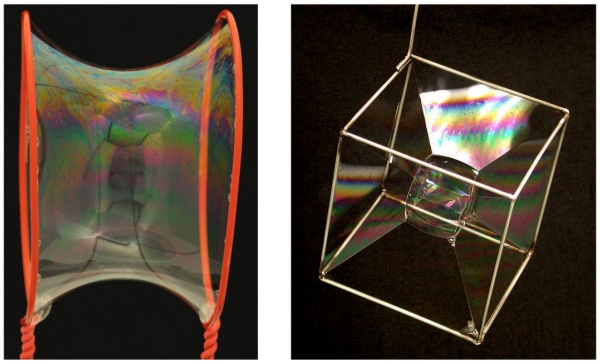

Figure 1.3: Minimum liquid surfaces. Liquids tend to minimise their energy through minimising their surface exposed to air. (*Left*) Soap film attached to twin circular rings taking the shape of a catenoid. (*Right*) Polyhedral bubble on a cubic frame. *Sources : www.soapbubble.dk/en/articles/former (catenoid soap film) & www.maths.tcd.ie/∼foams/gallery (cube soap bubble).*

1.1.2 Mechanical approach

Definition (1.1) tells us that surface tension has the dimensions of an energy per unit area which is equivalent to a force per unit length. Let us mention a classic experiment wherein surface tension – driven forces clearly manifest themselves. Consider a glass rod bent in such a way that it forms a rectangular frame open on one side. A second glass rod (length l) which is mobile and can roll on the two parallel 'rails' closes the frame on its fourth side (Fig. 1.4). The latter is then dipped into soap solution so as to form a liquid film perfectly fitting its contour. Once the device taken out of the liquid, the rod starts moving spontaneously in the direction indicated by the big arrow. Spectacularly, if we tilt the frame, the rod can even climb back up the slope against gravity but would suddenly fall down if the soap film is punctured. As a matter of fact, the liquid lamella naturally tends to minimise its energy through minimising its surface exposed to air. To balance the tensile force this liquid membrane exerts on the moving rod, the experimenter must perform a mechanical work which, given a small displacement $\mathrm{d}x$ of the rod, writes

$$\delta W \doteq \mathrm{F}\mathrm{d}x = 2\gamma l \mathrm{d}x \,(\equiv \gamma \mathrm{d}\mathcal{A})\,, \tag{1.2}$$

with a factor 2 coming from the fact that we have a total of two liquid/air interfaces, one at the top of the soap film and the other at its bottom. This expression shows us that $\vec{\gamma}$ can be interpreted as a force applying per unit length of the rod. Bear in mind that the latter is an in – plane force perpendicular to the rod and directed towards the liquid.

Surface tension – driven forces are ubiquitous in nature. They explain for example the ability of certain insects to float on the water, such as species of genus *Gerris* commonly

called 'water striders'. Likewise, it explains why it is possible to make a paperclip float on the surface of water albeit it is made from steel denser than water (Fig. 1.5). But if washing – up liquid is added to the water, both the insects and the paperclip immediately sink ! Explaining such a phenomenon is the purpose of the upcoming part.

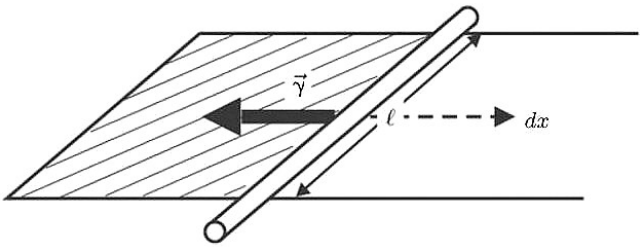

Figure 1.4: Schematic layout of a simple experiment showing the existence of surface tension forces. *Image taken from [24].*

Figure 1.5: Examples of flotation enabled by surface tension. (*Left*) An insect of genus *Gerris* floating on the surface of water. (*Right*) A paperclip floating on the surface of water. *Sources : www.thoughtco.com, Gerhard Schulz photographer (Gerris) & www.pixels.com (paperclip).*

1.2 Surfactants

Surfactants (contraction of 'Surface Active Agents') are often amphiphilic compounds, *i.e.* they possess a double affinity owing to their specific molecular structure. Generally speaking, a surfactant molecule is composed of a hydrophylic polar head group, either ionic or not, combined with a long hydrophobic (and hence often lipophilic) carbon chain. This ambivalency is what gives surfactants their surface active properties. Sodium Dodecyl Sulfate (SDS) is a perfect example of an amphiphilic molecule having a 12 – carbon chain bound to an anionic sulphate head group. Its full chemical formula is $CH_3(CH_2)_{11}SO_4Na$ (Fig. 1.6). SDS is today one of the most widely used surfactants in the industry and even this work is no exception to the rule as we use it in our own experiments.

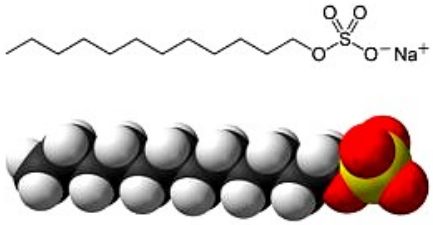

Figure 1.6: A widespread surfactant molecule : Sodium Dodecyl Sulfate (SDS). SDS is an amphiphilic compound, thus consisting of a long hydrophobic carbon chain (black and white balls) and a hydrophilic polar head group (yellow and red balls). CMC = 8.2 mM in water at 25°C. Molar mass $M_{SDS} = 288\,g/mol$. *Source : Wikimedia Commons.*

Consequently, a surfactant molecule adsorbed at the water/air interface puts its head under water whereas it keeps its tail in the air (Fig. 1.7). It follows a local drop in the surface tension at the adsorption sites. Indeed, while adsorbing at the water/air interface, surfactant molecules take up space that was initially occupied by water molecules. Since the former have a surface free energy weaker than the latter, the excess of interfacial energy is decreased, therefore resulting in a lower surface tension.

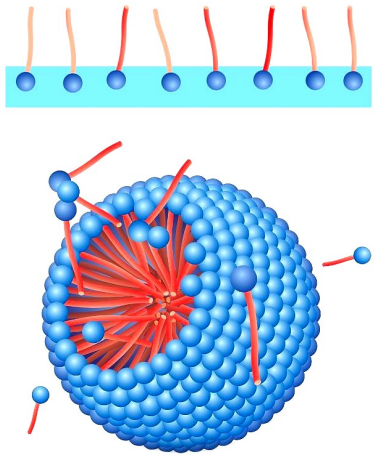

Figure 1.7: Interface/bulk equilibrium in the presence of soluble surfactants. (*Top*) Surfactant molecules adsorbed at the interface with their hydrophilic heads put under water and their hydrophobic tails in the air. (*Bottom*) Structure of a micelle. *Source : www.dataphysics-instruments.com.*

In the case of soluble surfactants, molecules are shared between the interface and the bulk such that the system is at equilibrium. A key feature of surfactants in solution is their critical micelle concentration (CMC), *i.e.* the threshold concentration in surfactants beyond which self−organising aggregates called micelles nucleate in the bulk and any additional surface active molecule joins them (Fig. 1.7). A steep decline of the surface tension with surfactant concentration is usually noted slightly before reaching the CMC,

followed by a saturating surface tension above the CMC. The CMC of a given surfactant strongly depends on the temperature as micelle formation is only possible above the Krafft temperature. It can also depend on pressure, on pH, on the presence of electrolytes in the solution ... Obviously, the CMC depends upon the surfactant's affinity for the solvent.

As we have just seen, a fluid interface is a place submitted to many stresses. This can be readily understood while compressing a monolayer of insoluble surfactants with the movable barrier of a Langmuir – Blodgett trough. The surfactant – laden interface is then conveniently described using the surface pressure defined as

$$\Pi(\Gamma) \doteq \gamma_{\text{water}} - \gamma(\Gamma)\,, \tag{1.3}$$

where γ_{water} is the surface tension of pure water ($\gamma_{\text{water}} = 72.8\,\text{mN/m}$ at $T_{\text{room}} = 20°\text{C}$) and $\gamma(\Gamma)$ the surface tension of water while a concentration Γ of insoluble surfactants covers the interface. Sizeable variations of this quantity are measured as the surfactant monolayer is gradually compressed. What occurs during compression is that surfactant molecules constantly self – organise in a way that minimises their energy, going through phases reminiscent of the states of matter as the area available to each molecule shrinks (Fig. 1.8): first a non – cohesive and disordered gaseous phase under low compression, followed by a weakly cohesive though still disordered liquid phase, and finally a highly cohesive and ordered solid phase under high compression. The surfactant monolayer even ruptures if surface pressure exceeds a critical value Π_c .

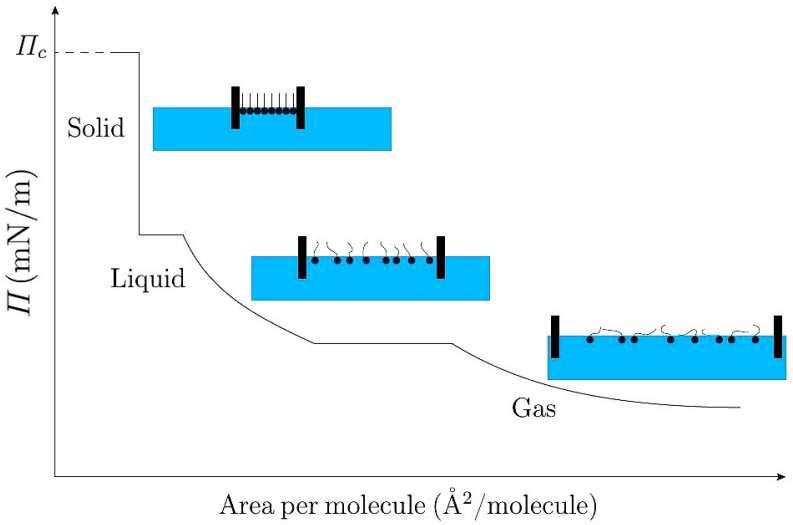

Figure 1.8: Evolution of an insoluble surfactant monolayer under compression. The surfactant monolayer gets more and more compact as the Langmuir barrier is further displaced, from a gaseous state under low compression to a solid state under high compression. *Image taken from [23].*

To finish, note that surfactants support a wealth of industrial applications spanning from detergents (surfactant molecules attach to fatty compounds, thus removing stains when rinsing) to emulsions and foams (surface active agents usually serve as stabilisers in such multi−interface systems). Surfactants can be encountered in biology as well. One example is the Infantile Respiratory Distress Syndrome (IRDS) which is a disease in premature infants due to developmental deficiency of pulmonary surfactant production (Fig. 1.9). As a matter of fact, patients suffering from IRDS sorely lack surfactants to 'unglue' their pulmonary alveoli and thereby breathe normally. A common treatment consists in ventilating neonates artificially along with injecting through the intubation cannula a dose of pulmonary surfactant extracted from bovine lungs (*e.g.* Beractant®).

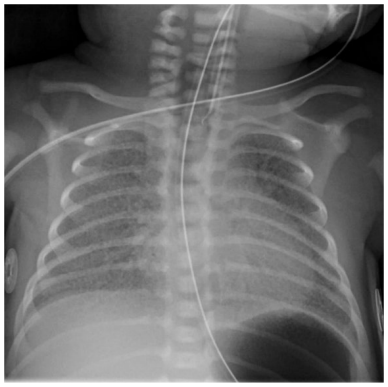

Figure 1.9: Infantile Respiratory Distress Syndrome. Opacification of the lungs visible on this radiograph. *Source : www.soinped.ch/wiki/maladie-des-membranes-hyalines-mmh.*

1.3 The Marangoni effect

In the above section, we described surfactants from a 'static' viewpoint introducing their adsorption properties and the concept of CMC. Yet, as we shall see, surface active agents also play a role in interfacial hydrodynamics through the Marangoni effect [27]−[32]. The Marangoni effect denotes the driving of a flow at a fluid interface under the action of a surface tension gradient (Fig. 1.10). The latter is caused by temperature or surfactant concentration inhomogeneities. Temperature−driven Marangoni flows are referred to as thermocapillary flows and surfactant−induced ones as solutocapillary flows.

Regarding solutocapillary flows, we make a distinction between an intrinsic and an extrinsic origin of the flow. In the intrinsic case, the total amount of surfactant molecules remains fixed. An internal inhomogeneity of the surfactant concentration spontaneously

arises and the Marangoni effect then tends to rehomogenise the system. One such example is what occurs in a soap film. Capillary suction is responsible for fluid migration towards the menisci which leads to film thinning. As a result, the flat central region of the film is depleted of surfactants and a Marangoni effect then opposes capillary suction and 'heals' the soap film, a phenomenon known as 'self−cicatrisation' (Fig. 1.11).

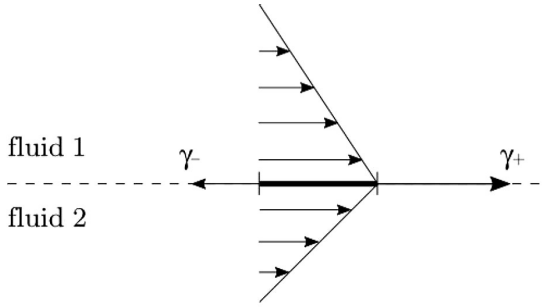

Figure 1.10: Schematic layout explaining the Marangoni effect. The interface between fluid 1 and fluid 2 exhibits surface tension inhomogeneities. A small portion of the surface (black segment) is out of equilibrium due to unequal surface tension forces γ_-/γ_+ on the left and on the right. In response to this disbalance, the fluids start flowing and the viscous forces resulting from this relative motion eventually bring this portion of the interface back to equilibrium. *Image taken from [23].*

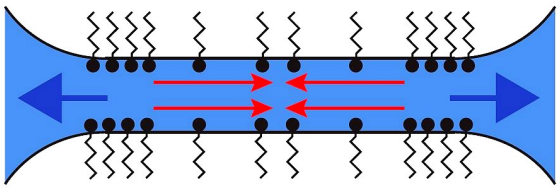

Figure 1.11: Self−cicatrising soap film. A Marangoni counterflow (red arrows) resists capillary suction (blue arrows) that tends to make the film thinner and thence weaken it. *Image taken from [23].*

A daily life example is that of tears of wine [31, 33]. The latter manifests as a liquid film lining the inner wall of a wine glass from which regularly spaced droplets detach and drop back into the wine (Fig. 1.12). This phenomenon is explained as follows. When wine is poured into a glass, a meniscus forms on its wettable walls by capillary adhesion. Wine is basically a water−ethanol mixture. Ethanol, which acts as a surfactant, is continuously evaporating from the surface at a rate higher than water owing to a higher equilibrium vapour pressure in relation to water. The concentration of ethanol decreases faster in the meniscus than in the bulk of the wine because of the former comparatively larger surface−to−volume ratio. This nonhomogeneous evaporation of alcohol is what causes a surface driving force to push up the meniscus along the glass sides, from central regions of high alcohol concentration/low surface tension towards peripheral regions of low alcohol

concentration/high surface tension. As the meniscus starts forming a thin film on the surface of the walls, it gets even more depleted of alcohol, which in turn worsens the surface tension disbalance. More wine is driven up the walls until the growing film gets too heavy, collapses under its own weight and teardrops finally run down.

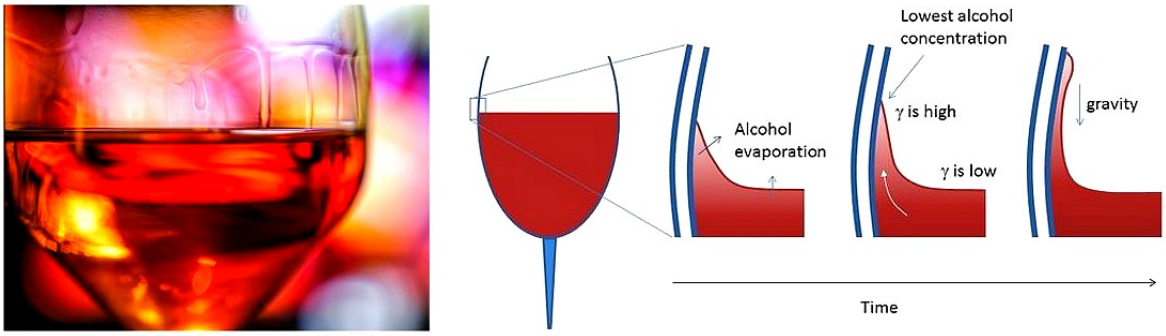

Figure 1.12: Tears of wine. (*Left*) Photograph of the phenomenon. (*Right*) The Marangoni−driven destabilising mechanism. *Source : gigazine.net/gsc_news/en/20190307-physical-phenomena-make-wine-crying (photograph) & www.comsol.com/blogs/tears-of-wine-and-the-marangoni-effect (schematic).*

Another manifestation of the Marangoni effect can be observed at home. Fill a metal pie pan with water and sprinkle pepper evenly across the surface. Then soak the tip of a toothpick with washing−up liquid. Gently touch the surface of the water right in the middle with the soapy toothpick and see the pepper flakes suddenly chased away ! What happens is that surfactant molecules contained in the dish soap lower the surface tension at the deposition site. The surface tension is now higher at the periphery of the pan than at the centre. In reaction to this surface tension gradient, a centrifugal solutocapillary flow arises which drives the outward motion of the pepper flakes (Fig. 1.13). By the way, this explains why insects floating on the water suddenly sink if soap is added to the pond, as the surface literally falls down under their feet due to the local drop of surface tension.

Figure 1.13: Pepper and soap experiment showing the solutal Marangoni effect. Surfactant molecules contained in the drop of washing−up liquid drive an outward solutocapillary flow repelling the pepper flakes towards the edges of the dish. *Source : sciencearoundus1.blogspot.com.*

Note that the Marangoni effect is involved in many industrial processes. For instance, this effect is used for the drying of silicon wafers during the manufacturing of integrated circuits. Droplets shall be thoroughly removed from the surface of the wafer to prevent oxidisation of its components. To do this, alcohol vapour is spread on the wet wafer. The resulting solutocapillary flow helps gravity eliminating water to get a perfectly dry surface. The Marangoni effect is also encountered in fields as varied as fine arts or life sciences. *Suminagashi* (literally 'floating ink'), the 12th century ancestor of European paper marbling, relies on the Marangoni – driven spreading of coloured inks (ox – gall soap is deposited on water) to draw concentric circle patterns on the surface (Fig. 1.14). *Stenus Comma* (Fig. 1.15), nicknamed the 'water skater rove beetle', leverages the Marangoni effect to achieve motion : its abdomen releases into water a surface active material called *stenusin* that locally lowers the surface tension and thus allows the rove beetle to quickly glide away from predators, a survival technique known as skimming.

Figure 1.14: Paper marbling through the countries and the ages. (*Left*) Suminagashi (Japan, 12th century). (*Middle*) Ebru (Turkey, 16th century). (*Right*) European marbling (detail of the binding of a 1880 book). *Sources : www.japansociety.org/event/suminagashi-japanese-marbling, Linh Truong photographer (suminagashi), aregem.ktb.gov.tr (ebru) & Wikipedia's article on paper marbling.*

Figure 1.15: The water skater rove beetle. (*Left*) Photograph of a *Stenus Comma*. (*Right*) The molecular structure of stenusin. *Source : Wikimedia Commons.*

Chapter 2

The water jet experiment

In this chapter, we characterise the divergent surface flow generated by a submerged jet perpendicularly impinging the water/air interface (Fig. 2.1). First of all, we present the materials and methods implemented in the course of our experiments. We then provide detailed observations of the axisymmetric ground flow state and the dipolar mode of the instability, paying particular attention to their morphological traits in function of two control parameters, the injection speed V_{inj} and the gap H between the injector and the interface. Surface velocity measurements are given next. Finally, a few complementary studies are presented before discussing the main experimental findings.

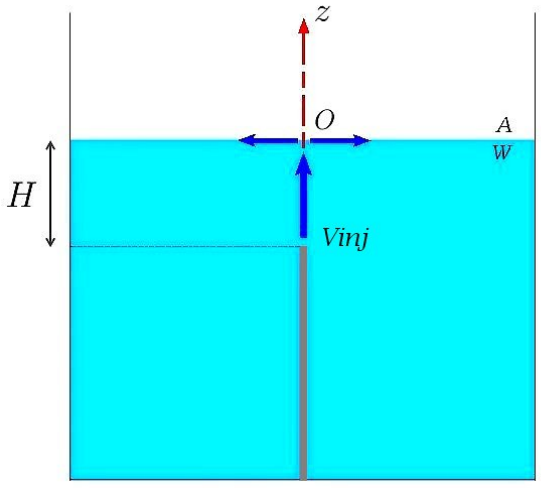

Figure 2.1: Schematic layout of the water jet experiment.

Despite the apparent simplicity of this system, we shall see that the flow becomes more and more complex as the injection speed increases or the gap decreases.

2.1 Materials and methods

2.1.1 The injection unit

Unless otherwise specified, we always use the same experimental vessel of radius $R = 17.5\,\text{mm}$. The inner (resp. outer) radius of the injection tube is $r_- = 0.275\,\text{mm}$ (resp. $r_+ = 0.4\,\text{mm}$) in all experiments. The injection speed V_{inj} ranges between a few mm.s^{-1} and a few cm.s^{-1}, while the gap H ranges from a few tenths of a mm up to 1 cm.

2.1.2 The injection setups

The 'gravity flow' injection setup

A tank filled with the working liquid is placed above the experimental cell in which it empties under the sole action of gravity. The injection rate Q_{inj} is controlled by varying the height difference Δ between the tank and the cell. The hydraulic circuit is closed by a peristaltic pump (model Minipuls 2 from GILSON) that sends liquid back to the reservoir at an adjustable pumping rate Q_{pump} (Fig. 2.2). This instrumentation results in a 'feedback loop' that allows the experimenter keeping about constant the gap H by tuning the device such that $|Q_{\text{inj}}| \approx |Q_{\text{pump}}|$.

The 'head – to – tail syringes' injection setup

Two syringes are mounted on a syringe pump (model BIOSEB 8000) in a head – to – tail layout. Once the apparatus activated, the plungers of the syringes move on block in their barrels : one syringe acts as an injector, the other one as an aspirator. This setup ensures almost perfect constancy of the gap, which is more difficult to achieve with the first setup.

More technical aspects about both setups are provided in Appendix A.

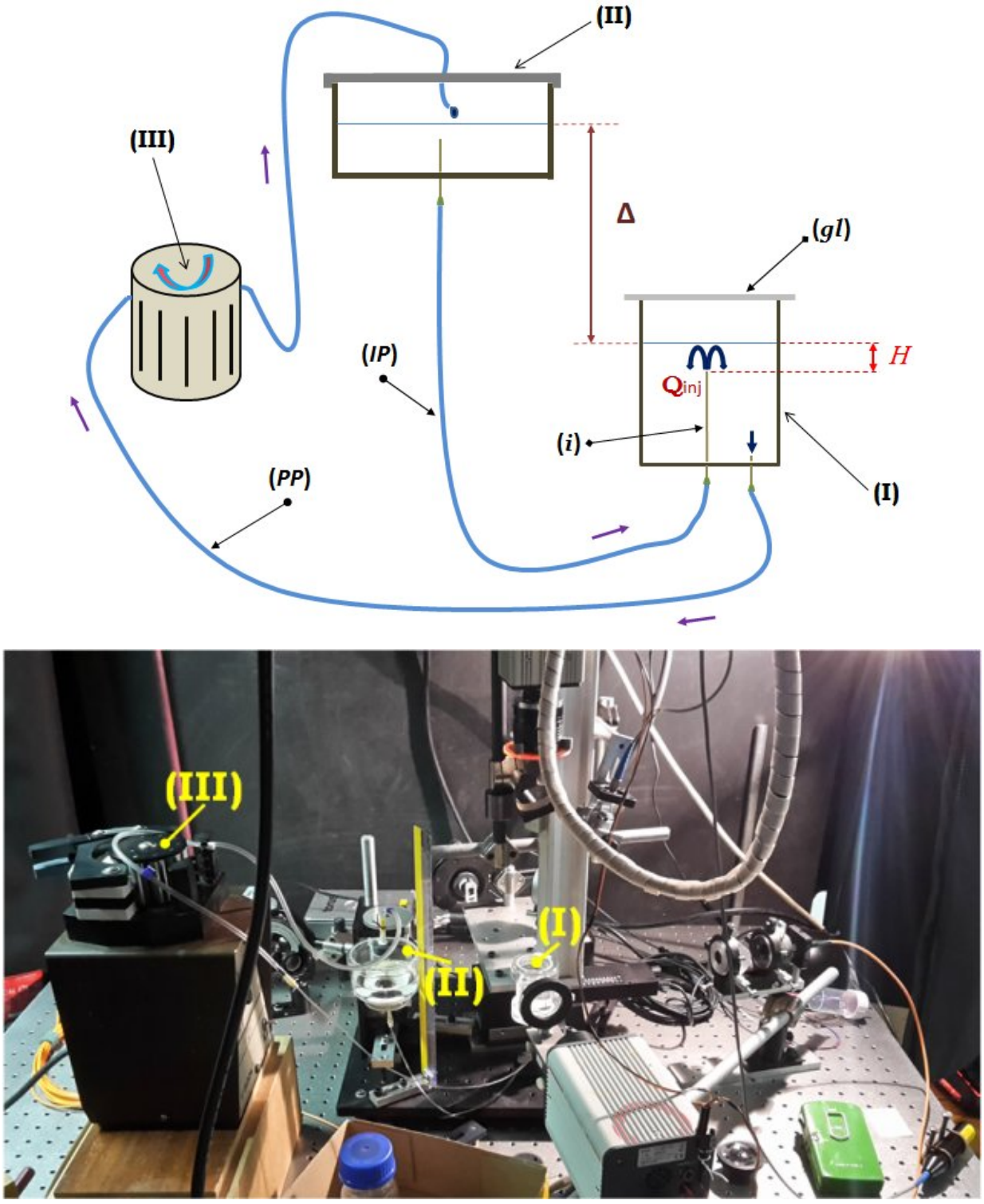

Figure 2.2: The 'gravity flow' injection setup of the water jet experiment. (*Top figure*) Diagram of the closed−loop hydraulic circuit (not to scale). (*Bottom figure*) Photograph of the setup under actual operating conditions. (I) cell; (II) tank; (III) pump (same numbering on both figures). (*IP*) and (*PP*) are the injection and pumping pipes, respectively. (*i*) injection tube. (*gl*) glass lid to limit the contamination of the sample.

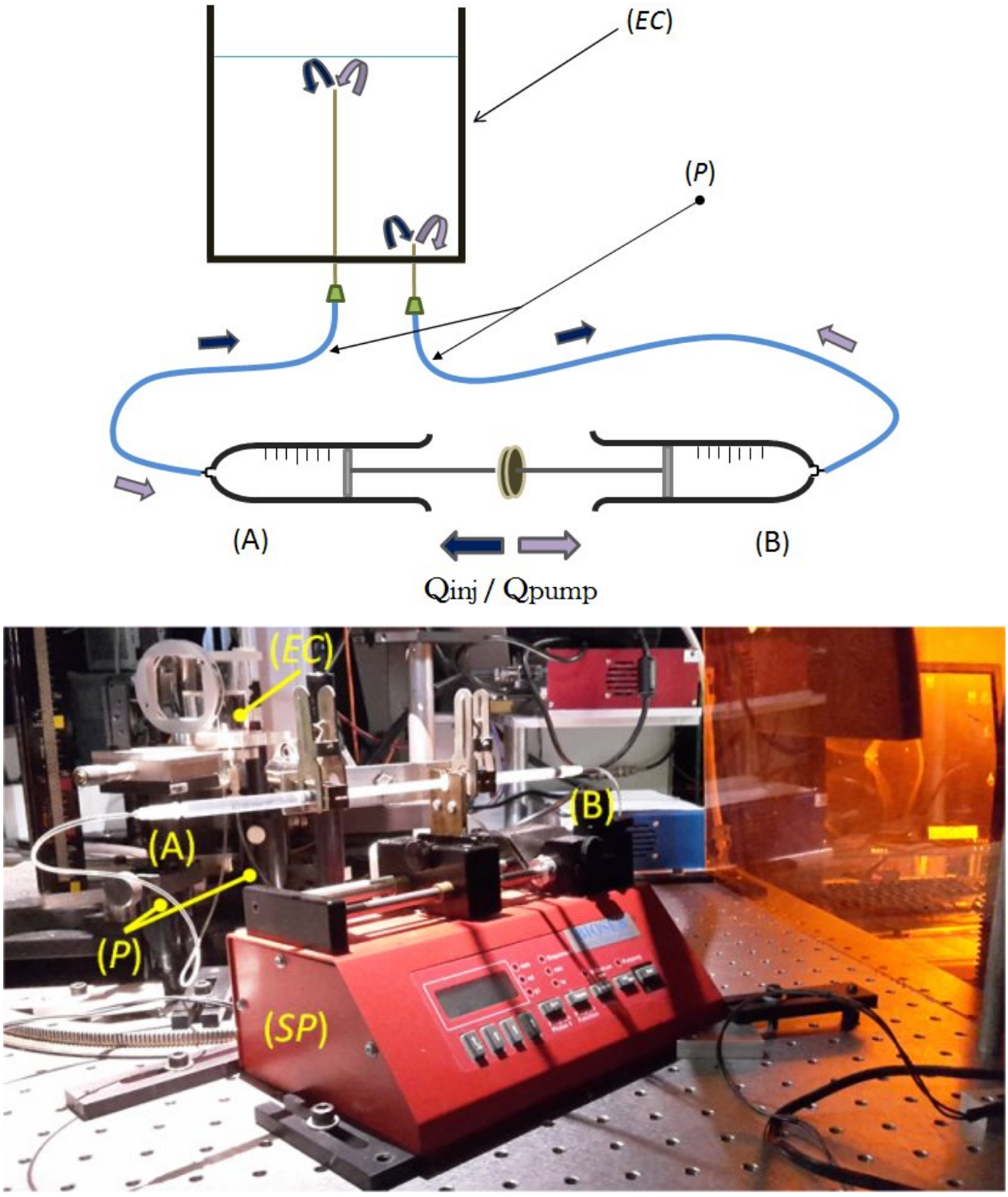

Figure 2.3: The 'head – to – tail syringes' injection setup of the water jet experiment. (*Top figure*) Schematic of the device (not to scale). (*Bottom figure*) Photograph of the setup under actual operating conditions. (*EC*) experimental cell; (*P*) thin flexible pipes; (A) and (B) are the two syringes assembled in a 'head – to – tail' configuration. (*SP*) syringe pump, not drawn on the schematic for clarity but shown on the photograph below. Injection rate Q_{inj} directly tuned on the syringe pump control box.

2.1.3 Preparation of the surfactant solutions

As will become clear in the following, the state of cleanliness of the free surface is crucial. To control the surface state, a given amount of a surfactant, Sodium Dodecyl Sulfate (Fig. 1.6) purchased from Sigma – Aldrich, is mixed with water at a bulk concentration $\mathcal{C}_{\mathrm{SDS}} = 1.03\,\mathrm{mM}$ or $8.2 \times 10^{-2}\,\mathrm{mM}$ corresponding to CMC/8 and CMC/100, respectively.

The experimental cell is filled with the same SDS solution as in the reservoir ('gravity flow' setup) or the syringes ('head – to – tail syringes' setup). Unless otherwise specified, our SDS solutions are concentrated at $\mathcal{C}_{\mathrm{SDS}} = \mathrm{CMC}/100$. The latter are prepared with ultrapure water (resistivity 18.2 MΩ.cm at 25°C, TOC : 3 ppb) withdrawn from a Millipore Milli-Q A10 Gradient purification system. Before running any experiment, the glassware is carefully rinsed with pure water supplied by a Millipore Elix 10 purification system.

2.1.4 Surface tension measurements

The surface tension γ is measured with the pendant drop method, in which γ is computed fitting a numerical solution of the Young – Laplace equation to the profile of the drop [34].

We carry out pendant drop experiments using a single drop automatic tensiometer purchased from Teclis (measurement error $\pm 1\,\mathrm{mN/m}$). The drops are enclosed into a small container partially filled with pure water to minimise their evaporation.

For comparison purposes, we measure experimentally the surface tension of pure water at room temperature $T_{room} = 20°\mathrm{C}$ and we find $\gamma_{\mathrm{water}} = (72.8 \pm 1)\,\mathrm{mN/m}$. Surface tension measurements of our SDS solutions yield $\gamma_{\mathrm{CMC}/100} = (72.5 \pm 1)\,\mathrm{mN/m}$ for the lower SDS bulk concentration $\mathcal{C}_{\mathrm{SDS}} = 8.2 \times 10^{-2}\,\mathrm{mM}$, and a surface tension $\gamma_{\mathrm{CMC}/8} = (67 \pm 1)\,\mathrm{mN/m}$ for the higher bulk concentration $\mathcal{C}_{\mathrm{SDS}} = 1.03\,\mathrm{mM}$. The latter values are in line with those of the specialist literature (see for example Fig. 3 in ref. [35]).

2.1.5 Flow visualisation and measurement techniques

Our visualisation setup is based on laser sheet illumination that goes together with the seeding of tracer particles in the system. Dye injection experiments are also performed as an alternative to the use of tracer particles. *Particle Image Velocimetry* (PIV) is achieved to obtain velocity field measurements and the 'hydraulic bump' generated by the upward water jet pushing the interface is characterised by shadowgraphy experiments.

Laser sheet illumination

We built up an optical setup to generate laser sheets that cut the sample along selected planes. Laser sheets are produced when laser light fans out through a cylindrical lens (focal length $f20$). A spherical lens ($f200$) is added to collimate and focus the laser sheet. The latter is a few tens of μm thick in the observation area. A first horizontal laser sheet, that can be translated vertically, is positioned right beneath the water/air interface ($z \approx -0.1\,\mathrm{mm}$) when we aim to visualise the surface flow. Note that, strictly speaking, we do not observe the flow at the water/air interface but rather the flow in a subsurface layer that extends down to a few tenths of a millimeter below the surface. Indeed, the deformation of the meniscus strongly impairs any proper observation of the interface with a laser sheet. A second vertical laser sheet provides cross – sectional views of the bulk flow. An 'azimuthal scan' can be performed rotating it around the injector. In practice, the vertical laser sheet is kept tangent to the injector because, in case of direct illumination, the latter cast shadow would prevent any observation in the half – plane located behind it. We use a green laser light source (model Torus 532 from Laser Quantum, $\lambda_g = 532\,\mathrm{nm}$). Laser light is sent into a single mode optical fibre. A fibre optic coupler (Thorlabs) ensures laser light transmission with moderate losses. The output power is $\mathcal{P}_{\mathrm{out}} \sim 10\,\mathrm{mW}$.

Red fluorescent polystyrene microbeads ($\varnothing\, 5.1\,\mu\mathrm{m}$), extracted from a 5 mL colloidal suspension purchased from Magsphere (mass concentration 2.5% w/v), serve here as tracer particles. Tracer particles seeded in the sample emit a fluorescent light when crossing the laser sheet. Only two droplets of the suspension in $V \approx 100\,\mathrm{mL}$ of distilled water (volume fraction of tracer particles, $\phi_v \sim 10^{-5}$) are sufficient to ensure proper flow visualisation.

Two cameras are used : one for the top views, the other one for the corresponding side views (Fig. 2.4). The setup is modular as the cameras are interchangeable and both the laser sources and the cameras are assembled on a rigid mounting, forming a block that can rotate around the axis of the cell. A full series of cross – sections, preferentially captured along the symmetry axes of the multipolar flow patterns, can be thus obtained during a single experiment. A 2.8 megapixel digital camera, the ORCA-flash2.8 model, and the C5985 B/W chilled CCD camera (both from Hamamatsu) are utilised. For a qualitative exploration of the flows arising with varying gap or injection speed, a low rate of a few frames per second (FPS) is sufficient (flows recorded at 4 FPS). Either the ORCA-flash2.8 camera or the C5985 camera are suited for this purpose. Still, only the former camera enables a PIV quantitative treatment which requires recording the flows at higher frame rates (we set 45.4 FPS, ORCA-flash2.8 maximum frame rate in full resolution).

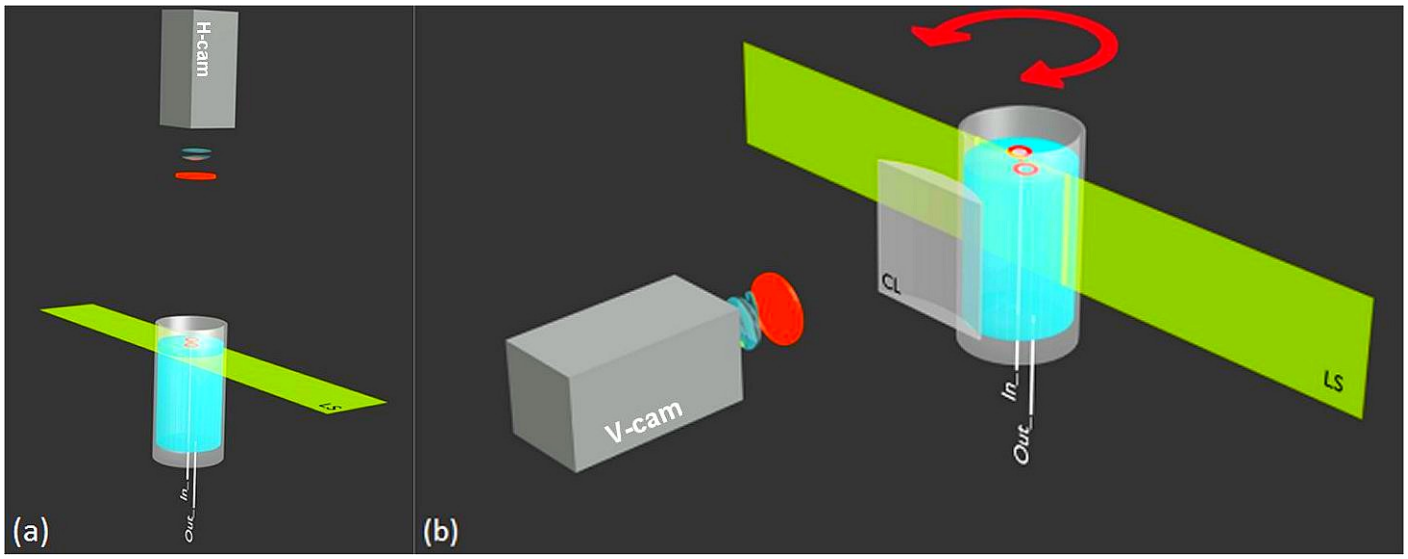

Figure 2.4: Flow visualisation based on laser sheet illumination. (a) A horizontal laser sheet (LS) is positioned just beneath the water/air interface to visualise surface flows. (b) A second vertical laser sheet is rotated (red double arrow) to get cross−sectional views of the bulk flows. Top and side cameras, respectively denoted H-cam and V-cam, record the signals emitted by tracer particles (not drawn). Filters (red−orange disks) prevent the cameras' sensors from being damaged by direct exposure to intense laser light while allowing fluorescent light to pass.

Image acquisition is achieved with 'HCImage', Hamamatsu's software for the ORCA-flash2.8 camera, and 'VideoHamamatsu.vi', a homemade software for the C5985 camera. Image processing is performed with ImageJ (open source software from the American National Institutes of Health). An average frame is generated out of a series of pictures called a stack. The average light intensity (encoded on a greyscale) of pixels located at the same position in each slice of the stack is computed. The resulting image shows streaks of light corresponding to the trajectories of the tracer particles averaged over time. More technical details are given in Appendix C.

Dye injection

In an auxiliary experiment, a fluorescent dye (fluorescein $C_{20}H_{12}O_5$, molar mass $M_{Fluo} = 332\,g/mol$, density $\rho_{Fluo} = 1.602\,g/mL$) is injected in the sample to visualise the flow streamlines. A volume $\mathcal{V}_{Fluo} \approx 200\,\mu L$ of dye is injected with a micropipette in the tank and dilutes rapidly in the carrier liquid. This mixture flows through the supply pipe for a few seconds before spilling out in the experimental cell. Precisions about the way dye injection experiments are performed are provided in Appendix D.1. The correlation of the 'coloured cloud' with the underlying hydrodynamic structure is discussed in Appendix D.2.

Particle Image Velocimetry (PIV)

Particle Image Velocimetry (PIV) is a technique which combines laser sheet illumination with image processing to derive velocity field measurements as well as related dynamic properties of flows such as their vorticity, divergence and so on. In what follows, I briefly recall the basic principles of PIV before introducing our own PIV studies.

The basic principles of PIV

PIV is based on the motion of seeding particles that must be chosen carefully as flow characterisation relies on their ability to closely follow the streamlines. One thus selects particles that are small compared with the flow length scales. The velocity of each tracer particle is then a reliable indicator of the local flow velocity.

Once flow visualisation done using laser sheet illumination, particle images captured by high – resolution cameras are computer treated. Image pairs are cross – correlated, which amounts to 'superimposing' them until the best matching is found in terms of average particle displacement. Data post – processing is finally achieved to eliminate and replace spurious vectors, a key step to ensure reliable computations of local derivatives [36] – [38].

Our PIV studies

Our objective is to figure out the orders of magnitude of the velocity field associated with the dipolar surface flow. The MATLAB code we use, which is inspired from PIVlab, follows the processing steps mentioned above. PIVlab is a time – resolved PIV software not limited to the computation of the velocity distribution based on particle image pairs, but equally used to derive, display and export many features of the flow pattern. A user – friendly graphical interface (GUI) makes PIV analysis very fast and efficient. Developed by W. Thielicke and E. J. Stamhuis [39], this program benefits from regular updates. Running our code, we derive several flow properties such as the velocity magnitude, the spatial evolution of each velocity component, and the flow vorticity. Particular attention is given to the latter which is a key quantity in characterising the vortex pair of the dipole. Our PIV results are presented in sec. 2.3.2.

Shadowgraphy

Shadowgraphy is used to measure the dimensions of the interface deformation provoked by the upward water jet. A collimated light beam uniformly illuminates the surface over an area of about 1 cm in width centred on the injector's axis. The height h and extent

ξ of the bulge are inferred from the features of the shadowgram ('shadowgraphy stain') it produces on a screen positioned above the interface. A comprehensive presentation of shadowgraphy applied to the present case can be found in Appendix E.

Shadowgraphy also tells us whether or not the multipolar instability is correlated with the interface deformation. Indeed, any symmetry breaking of the flow that accompanies the azimuthal instability must be reflected in some symmetry breaking of the shadowgram. If not, this would be a cogent evidence of the lack of correlation between the interface deformation and the onset of the instability. This question is answered in sec. 2.5.2.

2.2 The axisymmetric base state

2.2.1 Description of the axisymmetric state

We describe the axisymmetric state observed at low injection speeds and/or big gaps. Given the cylindrical symmetry of our jet produced by a cylindrical injector in the middle of a cylindrical vessel, we naturally expect an axisymmetric surface flow. The streamlines displayed on Figs 2.5 and 2.6 support the existence of a toroidal base flow (Fig. 2.8). The radial streamlines on Fig. 2.5 diverge up to a certain distance from the source before sinking into the bulk and wrapping around a torus that sits upon the injector (hereafter referred to as the 'injection torus'), a cross−section of which clearly exhibits a pair of counter−rotating vortices (Fig. 2.6). Interestingly, the injection torus is observed in the absence of SDS as well (Fig. 2.7). What is more, we remark that the centrifugal jet flow is surrounded by a centripetal flow. Beneath the injection torus usually arise multivortex flow patterns due to finite size effects (flow confinement in the small experimental cell, plus the presence of the drain tube at its bottom), but the study of the whole 3D structure of the flow including these bulk components lies beyond the scope of this work. Here we focus on the hydrodynamic fate of the injection torus as the control parameters are varied.

Figs 2.5 and 2.6 give the orders of magnitude of the velocity in various regions of the surface and the bulk flows, respectively. A neat decrease of the velocity as we move away from the source can be noted on Fig. 2.5 : the surface velocity reduces by 100 within a radius of about 1 cm, from $V_{\text{surf}} \sim 1\,\text{mm/s}$ close to the source down to $V_{\text{surf}} \sim 10\,\mu\text{m/s}$ at the frontier between the centrifugal and the centripetal flows. This observation holds true for the bulk flow, as shown on Fig. 2.6. Two regions appear : the 'sphere of influence' of the jet flow delimited by the injection torus, where the typical velocity is $V_{\text{bulk}} \sim 1\,\text{mm/s}$ (even up to $V_{\text{inj}} \sim 1\,\text{cm/s}$ at the tube outlet) and the far region near the sidewalls with

a centripetal velocity as small as $V_{\text{bulk}} \sim 10\,\mu\text{m/s}$. The magnitudes are here obtained by manually tracking the tracer particles. So the concentric circles drawn on the figure roughly delineate the flow regions of interest. Yet the relative positions of these borderlines slightly vary with the gap or the injection speed. Remarkably, the velocity magnitudes remain unchanged over the whole variation range of the control parameters.

A closer inspection of these pictures reveals that the axial symmetry of the 'base flow' is not perfect : the diverging streamlines are never strictly radial but slightly curved along some preferential direction. Such a polarisation of the flow yet occurs at very low injection speeds $V_{\text{inj}} \leqslant 7\,\text{mm/s}$. This phenomenon is described in further detail in sec. 2.2.3 and plausible explanations of its origin are discussed in sec. 2.6.

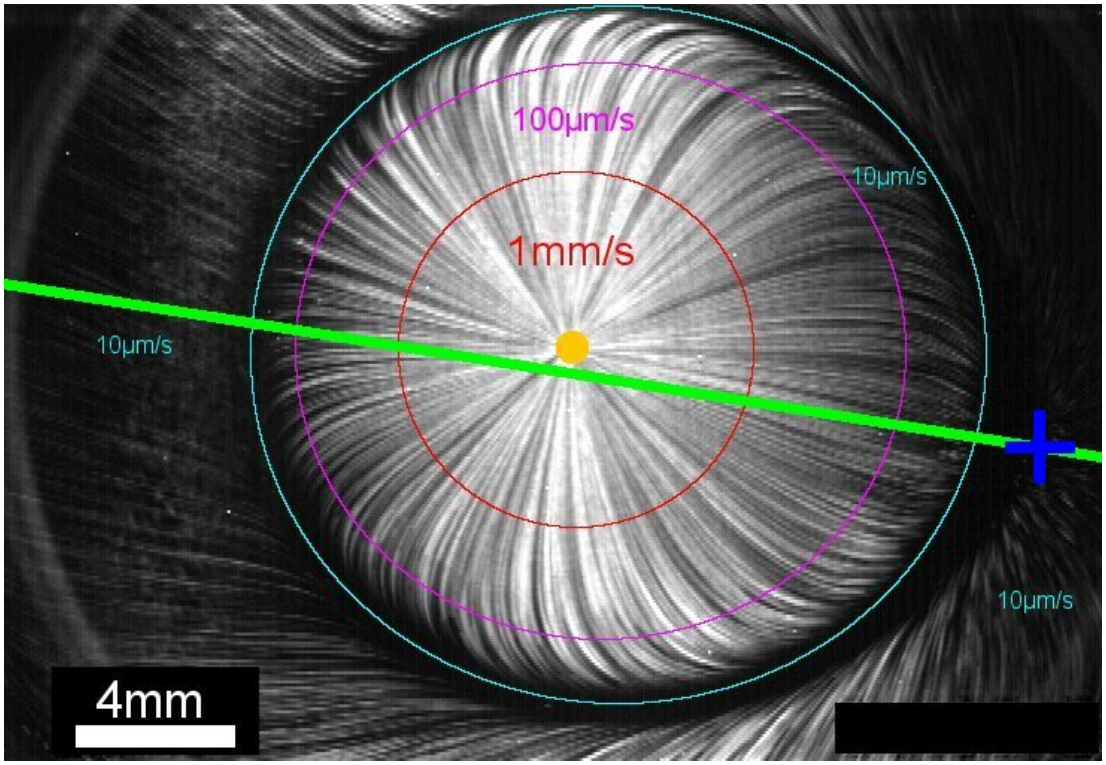

Figure 2.5: Axisymmetric flow caused by a submerged jet perpendicularly impinging the water surface (*top view*). The green line marks the vertical laser sheet passing near the injection point (orange disk). Image selected from an experiment conducted with the 'gravity flow' setup (Fig. 2.2). Experimental parameters : injection speed $V_{\text{inj}} \approx 5.8\,\text{cm/s}$, gap $H \approx 10.5\,\text{mm}$ ($\mathcal{C}_{\text{SDS}} = \text{CMC}/8$).

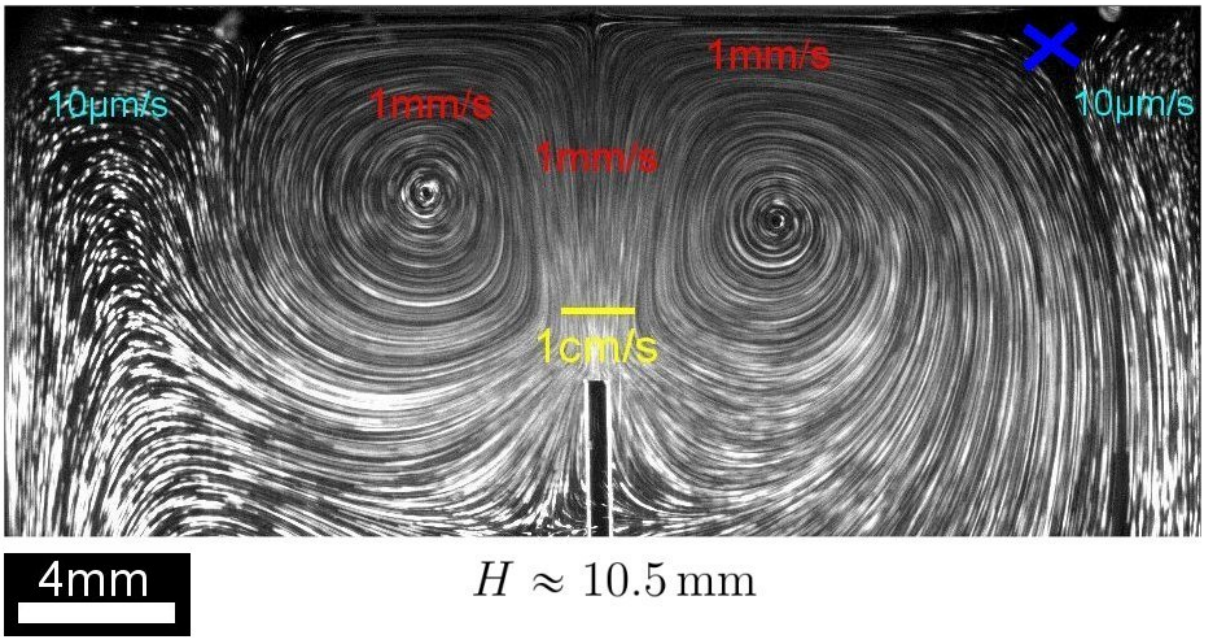

Figure 2.6: Axisymmetric flow caused by a submerged jet perpendicularly impinging the water surface (*side view*). Cross−sectional view along the vertical laser plane spotted by the green solid line on Fig. 2.5. Same experiment as before.

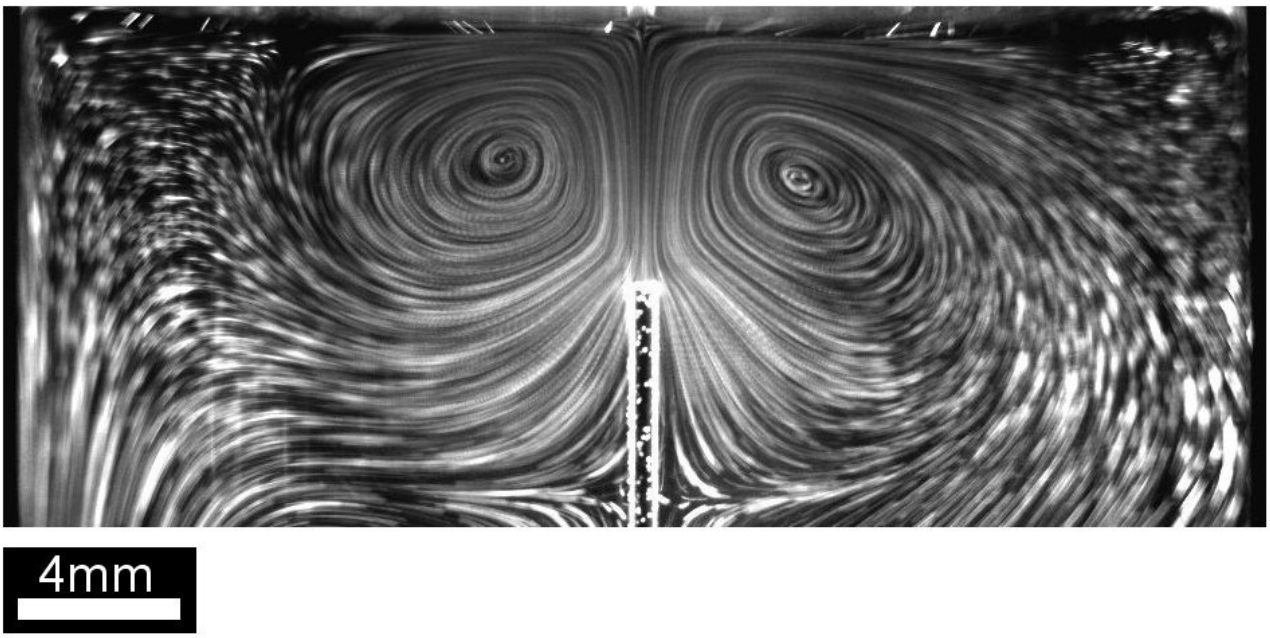

Figure 2.7: Example of an injection torus observed in the absence of SDS (*side view*). Image from an experiment carried out with the 'gravity flow' setup (Fig. 2.2). Experimental parameters: injection speed $V_{\mathrm{inj}} \approx 2.9\,\mathrm{cm/s}$, gap $H \approx 7.38\,\mathrm{mm}$.

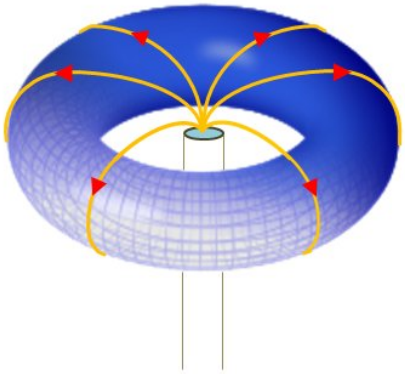

Figure 2.8: Schematic view of the axisymmetric base state. Our tiny subaquatic fountain generates a toroidal flow in its vicinity.

2.2.2 Evolution of the torus size with the control parameters

Let d_t denote the torus diameter defined as the centre – to – centre distance between the two vortices visible on a cross – section of the injection torus. Figs 2.9 and 2.10 display the evolution of d_t with increasing gap H and at various injection speeds V_{inj} , for a solution without SDS and a solution with a concentration $\mathcal{C}_{\text{SDS}} = \text{CMC}/8$, respectively.

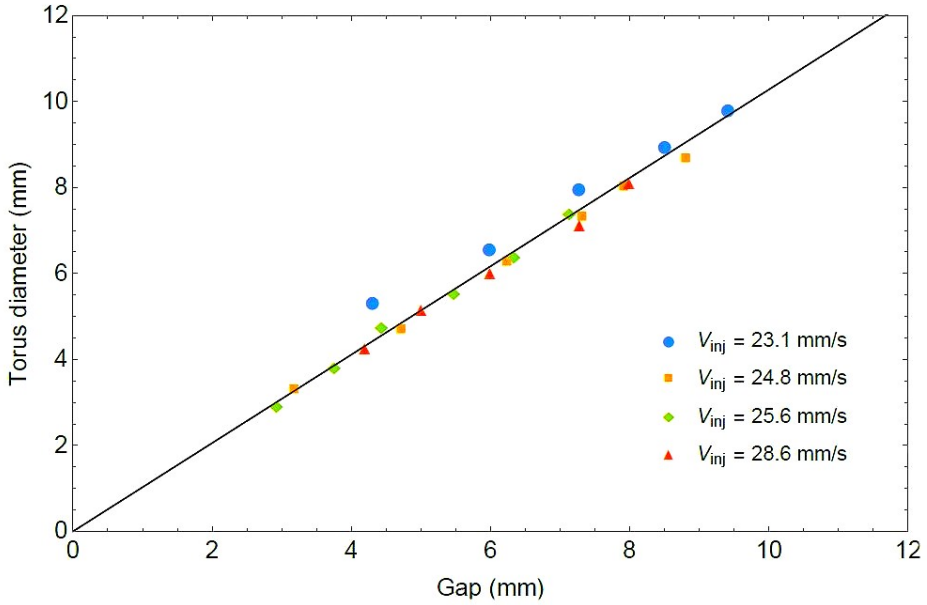

Figure 2.9: Evolution of the torus diameter with the gap, for various injection speeds, in the absence of SDS.

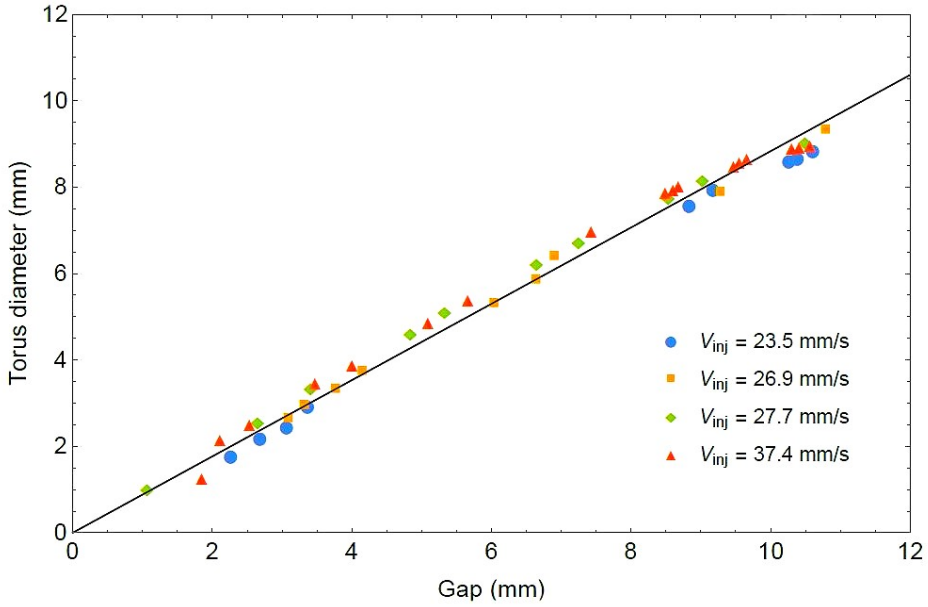

Figure 2.10: Evolution of the torus diameter with the gap, for various injection speeds, in the presence of SDS ($\mathcal{C}_{\mathrm{SDS}} = \mathrm{CMC}/8$).

We see that the torus diameter grows linearly with the gap and independently of the injection speed in the absence of SDS. Strikingly, the torus diameter exhibits the same behaviour in the presence of SDS, the only difference with the previous case lying in the different slope : the radius of the torus increases as $r_t \approx 0.51H$ without SDS while $r_t \approx 0.44H$ with SDS. These experimental facts will be discussed in detail in sec. 2.6.

2.2.3 Flow polarisation

I return to Figs 2.5 and 2.6 pointing out the lack of axisymmetry of the flow. Fig. 2.5 reveals a 'binary flow' : a centripetal flow girdles the centrifugal source flow, the two being separated by a ring−shaped dark area from which tracer particles are massively depleted. More precisely, the centrifugal flow is swept from left to right by the centripetal flow that drives it along a preferential direction. The 'focal spot', the point of convergence of all the surface streamlines, is marked by a cross on both figures. The effect of flow polarisation on the bulk flow is visible on Fig. 2.6. The torus is not perfectly axisymmetric : the centres of its vortices are not at the same altitude, the centre of the clockwise rotating vortex on the right being shifted downwards compared with the counterclockwise vortex on the left. We view this quasi−axisymmetric flow, usually observed at big gaps $H \geqslant 6\,\mathrm{mm}$, as a precursor state on the route towards the multipolar instability.

2.3 Symmetry – breaking of the axisymmetric base state

I present some observations regarding the instability of the axisymmetric flow, *i.e.* the symmetry – breaking of the base torus resulting in multipolar patterns, especially a dipole.

2.3.1 Transition to a multipolar flow

Now that we have characterised the quasi – axisymmetric base state, we aim at identifying the conditions leading to its destabilisation. We look for the transition to a multipolar flow by conducting experiments in which the gap H varies significantly. After presenting the way we perform such experiments, a series of typical observations is displayed.

Experimental protocol

Either increasing or decreasing gap experiments are achieved. Injection is primed moving up the tank until the upper stop position is reached at an altitude $\Delta \approx 55\,\mathrm{mm}$ (Fig. 2.2), imposing this way the maximum injection speed attainable in our configuration. It then only remains to tune the pumping rate so that the liquid level in the cell either rises ($Q_{\mathrm{inj}} > Q_{\mathrm{pump}}$) or lowers ($Q_{\mathrm{pump}} > Q_{\mathrm{inj}}$) at a rate $|\mathrm{d}H/\mathrm{dt}| \sim 0.1\,\mathrm{mm/min}$, thus resulting in a typical variation of the gap $|\Delta H| \sim$ a few mms over an experiment time $\Delta t_{\mathrm{exp}} \sim 1\,\mathrm{h}$.

Such a slowly varying gap ensures the generation of quasi – steady flows. Let τ be the characteristic response time of a flow structure, either the time τ_{receding} it needs to fade out after injection is switched off or τ_{onset} the time it takes to regenerate after injection is turned on again. Let ΔH be the typical variation of the gap that separates two flow states, *e.g.* the quasi – axisymmetric and the dipolar flows of Fig. 2.11. From Fig. 2.11, we learn that $\Delta H \sim$ a few mms. With Δt the time for the liquid level to change by ΔH, a necessary condition to go through a sequence of quasi – stationary states as the gap is varied writes $\Delta t \gg \tau$. This is the case here, as 'injection outage' experiments (a surgical clamp compresses the flexible pipe strongly enough to block injection) conducted on a dipolar surface flow reveal that $\tau_{\mathrm{receding}} \sim 1\,\mathrm{min}$ and $\tau_{\mathrm{onset}} \sim$ a few s, whereas it takes $\Delta t \sim 10\,\mathrm{min} \gg \tau$ for the gap to change by 1 mm.

To compare the flows observed at different gaps, running increasing and decreasing gap experiments under similar conditions is crucial. So the tank is placed at its upper stop position in both cases, ensuring comparable injection speeds : increasing gap experiments are conducted at an average injection speed $V_{\mathrm{inj}} \approx 5.5\,\mathrm{cm/s}$, while a bit stronger injection speed $V_{\mathrm{inj}} \approx 5.88\,\mathrm{cm/s}$ is set in decreasing gap experiments (see Appendix B.2 for details).

Transition from the quasi – axisymmetric polarised state to a dipole

Fig. 2.11 shows the step – by – step evolution from the quasi – axisymmetric to a dipolar flow state. From $H \approx 10.5\,\mathrm{mm}$, the gap is gradually decreased to very small positive values $H \sim$ a few tenths of a mm. At big gaps $H \geqslant 6\,\mathrm{mm}$ [(a) – (b)], the flow is quasi – axisymmetric, while a dipolar flow develops at sufficiently small gaps $H \leqslant 3\,\mathrm{mm}$ [(f) – (h)]. For intermediate gap values $3\,\mathrm{mm} \leqslant H \leqslant 6\,\mathrm{mm}$ [(c) – (e)], a hybrid state is observed in the sense that the base flow seems to coexist with a dipole at the embryonic stage. The three vortex bulk flow that exists at big gaps $H \geqslant 6\,\mathrm{mm}$ [(a') – (b')] in the presence of a quasi – axisymmetric flow persists at smaller gaps $H \leqslant 3\,\mathrm{mm}$ [(f') – (h')] after the onset of a dipole (Fig. 2.12). The vortex pair of the torus becomes more symmetric as the torus gets smaller with decreasing gap : the centres of the vortex ring, vertically shifted relative to each other at big gaps (white lines), are located on the same line at smaller gaps $H \leqslant 4.5\,\mathrm{mm}$ (d'). Note that the 'robustness' of the flow patterns has been tested through series of increasing/decreasing gap experiments. On this occasion, similar flow structures have been observed in both cases for comparable gaps.

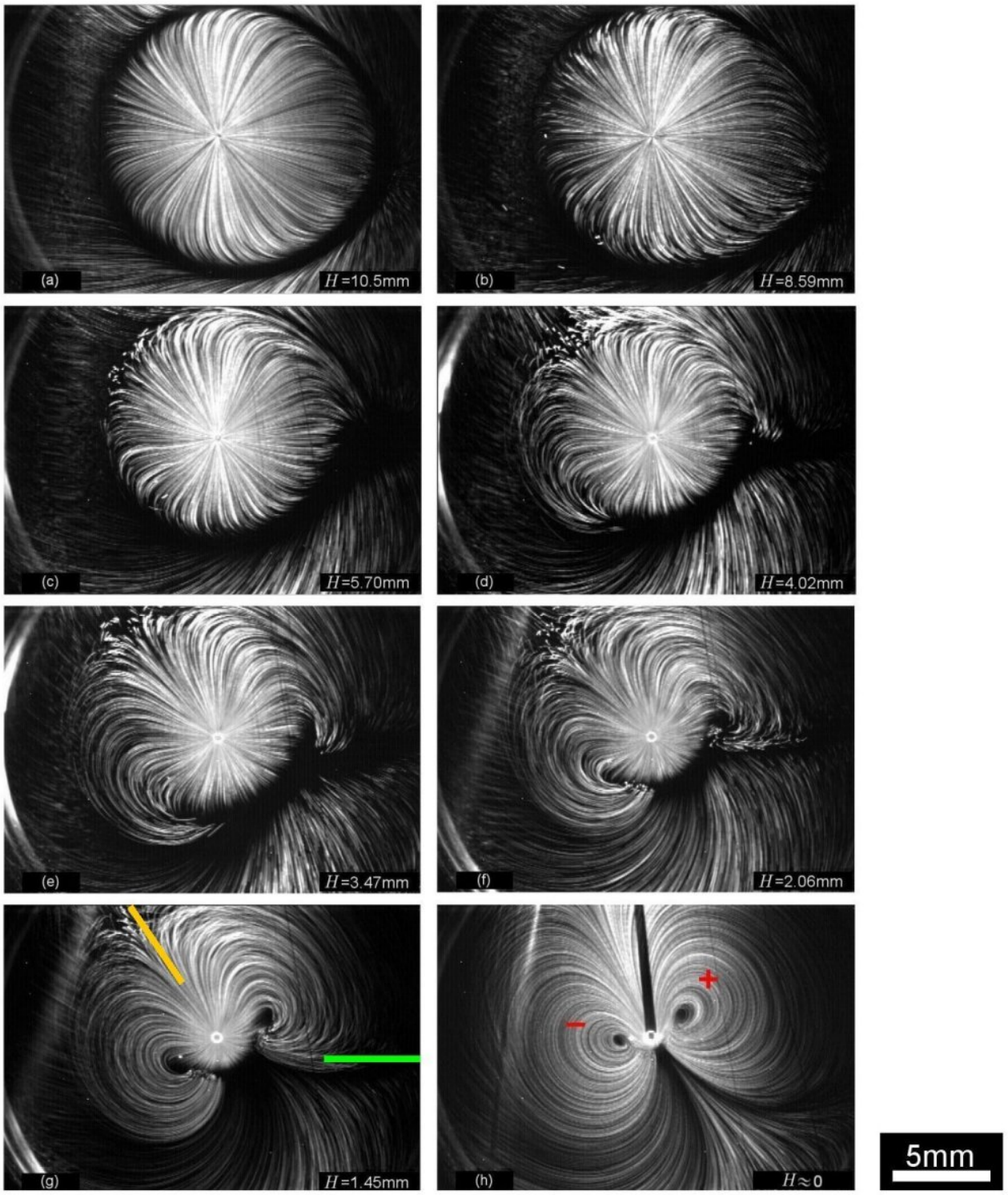

Figure 2.11: Transition from the quasi − axisymmetric to a dipolar flow state with decreasing gap (*top views*). Clockwise (resp. counterclockwise) vortex rotation symbolised by a red + (resp. −) sign. Strikingly, the orientation of the dipole (orange stick) makes a wide angle with the polarisation axis of the base flow (green stick) initially observed at big gaps. Gap H indicated in the bottom right corner of each picture. The dark strip visible on fig. (h) is the drop shadow of the injector's tip intercepted by the horizontal laser sheet. Injection speed $V_{\text{inj}} \approx 5.88\,\text{cm/s}$ ($\mathcal{C}_{\text{SDS}} = \text{CMC}/8$).

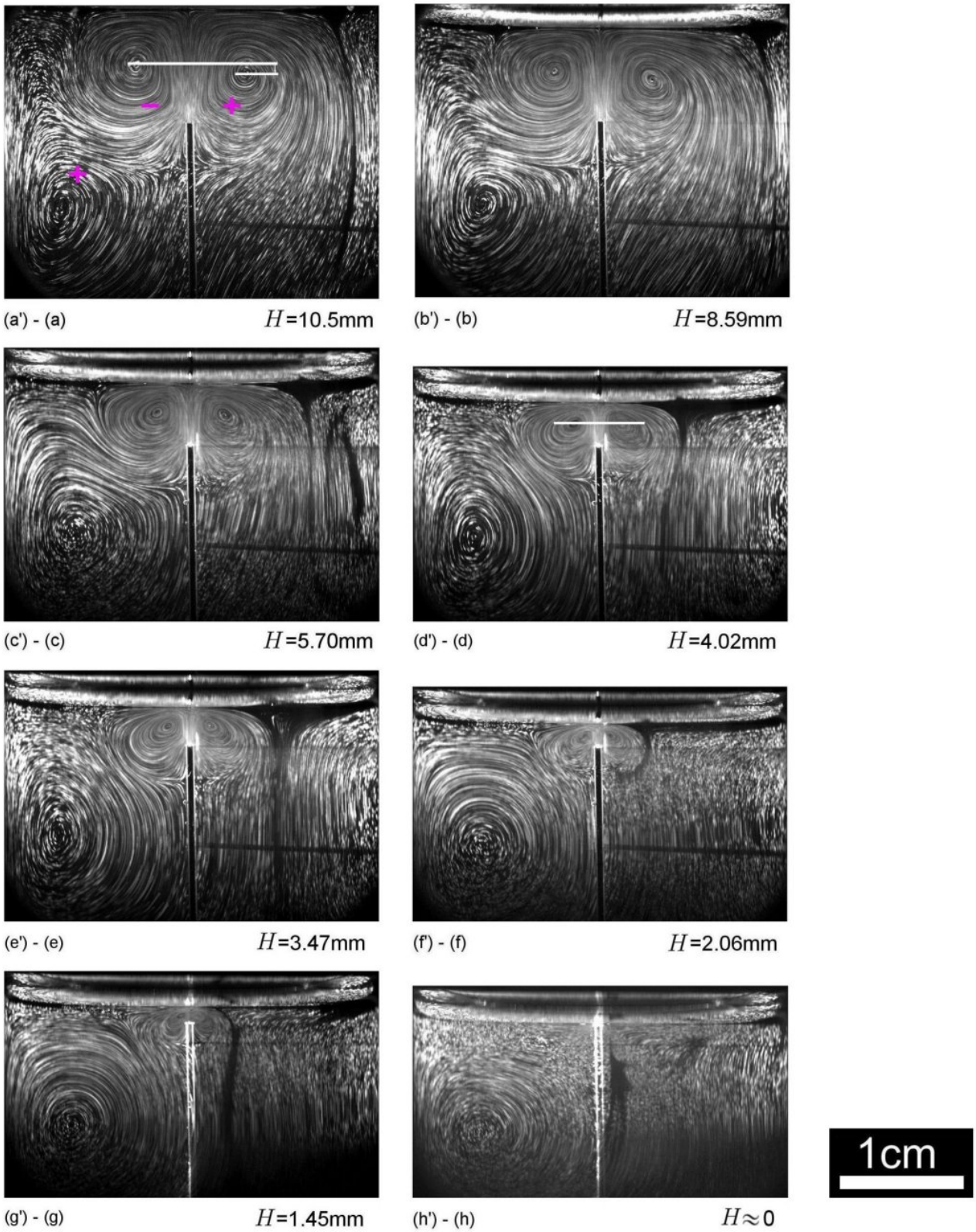

Figure 2.12: Transition from the quasi – axisymmetric to a dipolar flow state with decreasing gap (*side views*). Vertical laser sheet oriented along the polarisation axis of the quasi – axisymmetric flow (green solid line on Fig. 2.5). (a') is the side view associated with the top view (a) displayed on Fig. 2.11, (b') with (b) etc. Clockwise (resp. counterclockwise) vortex rotation indicated by a magenta + (resp. −) sign. Same experimental parameters as before.

2.3.2 Thorough characterisation of the dipolar state

This part provides a qualitative as well as quantitative (PIV) description of the dipole. Let me precise that, even though high multipolar order flows are not forbidden in principle, we observe almost exclusively dipolar flows. Quadrupolar, hexapolar... flow patterns are expected at stronger injection rates, with gap−dependent threshold values separating the different regimes. Actually, quadrupolar and even hexapolar flows are observed on rare occasions but they are uncontrolled short−lifetime flows.

Description of the dipolar state

Method M1 − Collecting streamlines maps

The vertical laser sheet is aligned with the 'dipole mirror symmetry plane' (DMSP) and along a perpendicular plane (PP) (see sec. 2.1.5 for technical details). Fig. 2.13 shows characteristic views of the bulk flow in these two planes.

- On the top view (TV), we see a dipole with a peculiar arc−shaped pattern joining one vortex centre to the other (rounded yellow rectangle).
- The side view captured in the DMSP (SV − DMSP) reveals a strong distortion of the streamlines on the right. The side position of the arc−shaped surface pattern is marked by the rounded yellow rectangle. Locally, the streamlines 'crash against' the rear part of the original torus before passing under it.
- The bulk flow looks more symmetric when seen from the front (SV − PP). Clusters of points instead of bright lines are found on the torus sides (rounded blue rectangles), since the streamlines are there perpendicular to the observation plane.

More information is acquired thanks to an azimuthal scanning : the 'imaging block' (horizontal and vertical laser sheets plus the cameras) captures intermediate views while rotated around the injector. The dipole mirror symmetry plane (DMSP chosen as the reference plane O°), the plane perpendicular to it (90°), and intermediate planes at 45° and 60° from the DMSP are selected (Fig. 2.14). Starting from the DMSP, recognisable at first glance with its strongly asymmetric flow pattern, the 'laminar' streamlines seem to shorten (cyan stick) as we turn around the injector, suggesting the existence of a stretched structure in the direction of the flow. The toroidal symmetric structure appearing in a limited area of the back view reinforces this vision. We shall also pay attention to the whirlpools situated on both sides of the vortex ring (rounded blue rectangles).

It is instructive to cut the flow structure into slices by lifting down the horizontal laser sheet (Fig. 2.15). Let us examine the series of top views captured deeper and deeper in the bulk, focusing our attention on the orientation of the streamlines near the injector.

- As long as the laser sheet is located a few tenths of a mm beneath the surface, the flow close to the injection point appears centrifugal (TV1).
- If we now put our light blade deeper, at about half the gap, we see like a point cloud emerging in the middle (cyan circle on TV2). The bright spots forming this cloud glitter on the real – time recordings. Here again, the streamlines flow perpendicularly through the recording plane and are hence seen from the top as a set of points.
- As we bring the cut plane even closer to the tip of the injector, the streamlines suddenly reverse, becoming centripetal (red arrows on (TV3) – (TV5)).

These three flow configurations, along with the side views, confirm the existence of a torus sitting upon the injection tube. Let us add a few words concerning the fate of the dipole vortex pair as the laser sheet is lifted down. The following trends can be reported : (1) the distance between the vortex centres grows, (2) these centres drift downstream and (3) the whirlpools become fainter and fainter. Given the information collected so far, we assume the existence of some elongated structure parallel to the dipole symmetry axis and flanked by a whirlpool on each side.

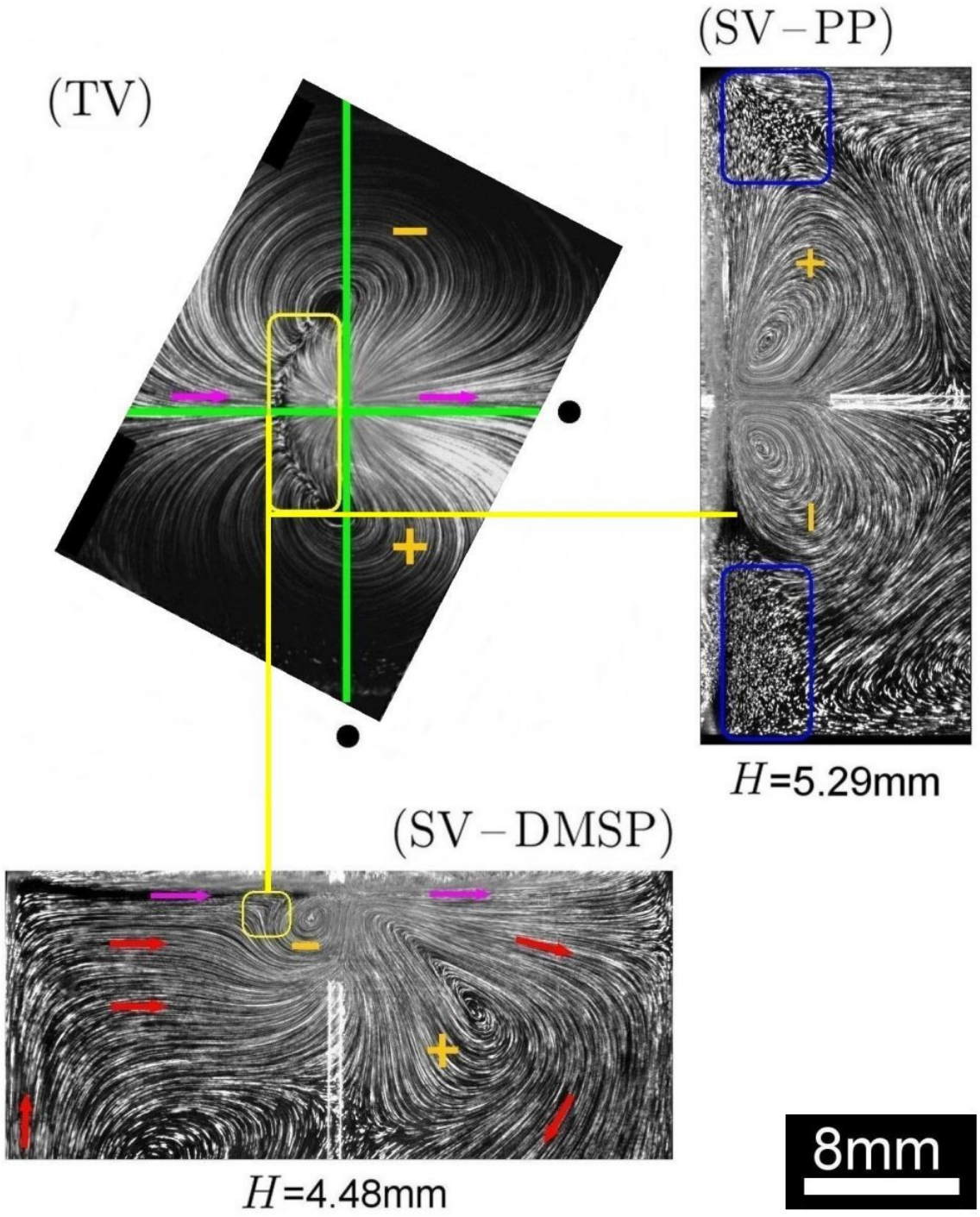

Figure 2.13: Typical views of the bulk flow associated with a dipolar surface flow. The orientations of the vertical laser sheet are spotted by the perpendicular green solid lines. The black disks mark the positions of the observer. The gap is reported below each side view. Even though both values are not the same, they are close enough to each other for the views to be comparable, at least qualitatively. The yellow lines point out structural links between the views. The magenta (resp. red) arrows (arbitrary lengths) indicate the direction of the surface (resp. bulk) flow. The orange sign + (resp. −) denotes clockwise (resp. anticlockwise) vortex rotation. $V_{\text{inj}} \approx 5.5\,\text{cm/s}$ ($\mathcal{C}_{\text{SDS}} = \text{CMC}/100$).

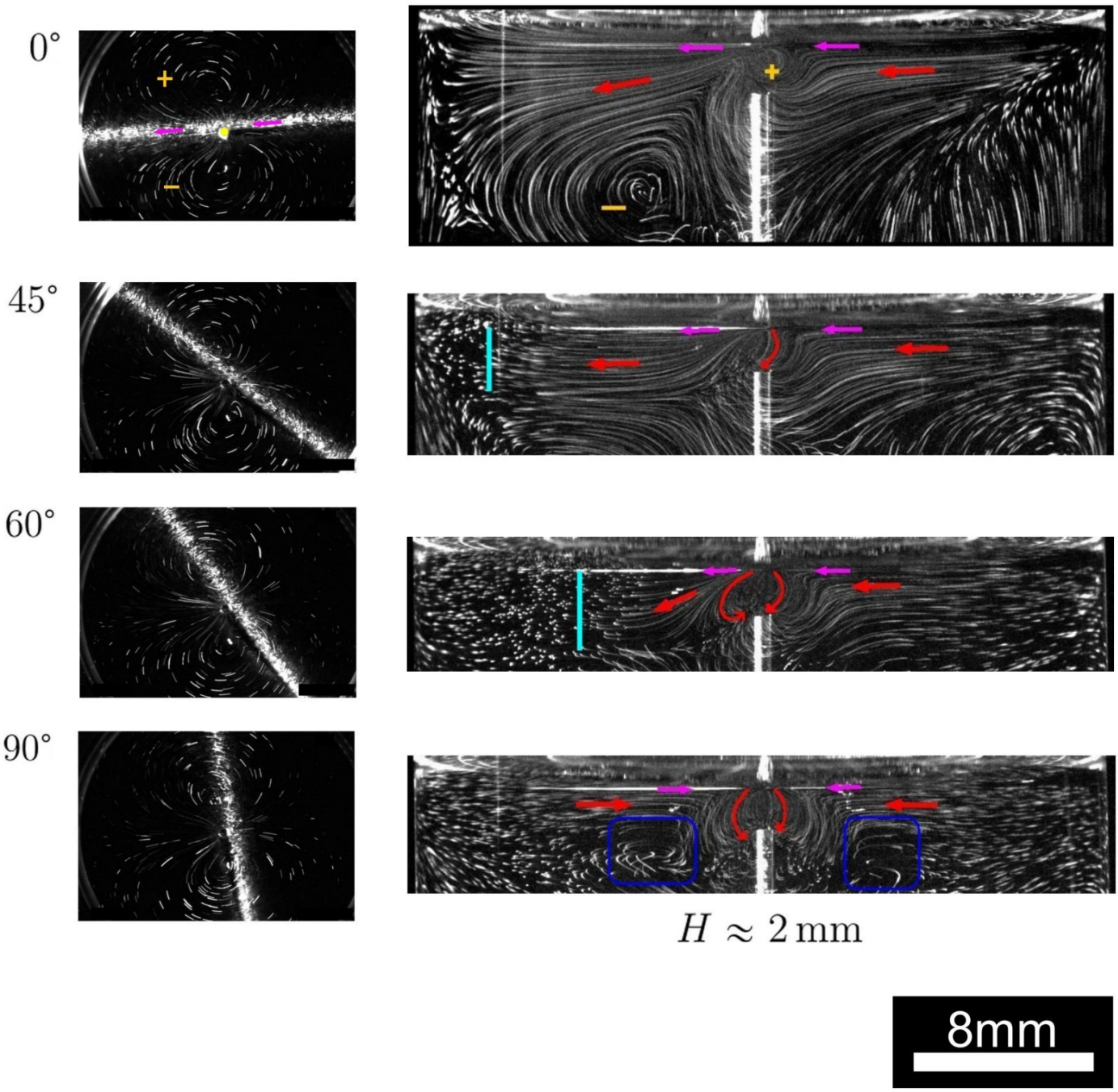

Figure 2.14: Azimuthal scan of the bulk structure associated with a dipolar surface flow. The top views on the left show the orientation (45°, 60°, 90°) of the laser sheet (bright strip) with respect to the axis of the dipole (0°). The corresponding side views are displayed on the right with their scale bar. The yellow disk marks the injection site. Other graphic elements are the same as in Fig. 2.13. The gap is about $H \approx 2\,\mathrm{mm}$ over $\Delta t_{\mathrm{exp}} = 10\,\mathrm{min}$. $V_{\mathrm{inj}} \approx 5.5\,\mathrm{cm/s}$ ($\mathcal{C}_{\mathrm{SDS}} = \mathrm{CMC}/100$).

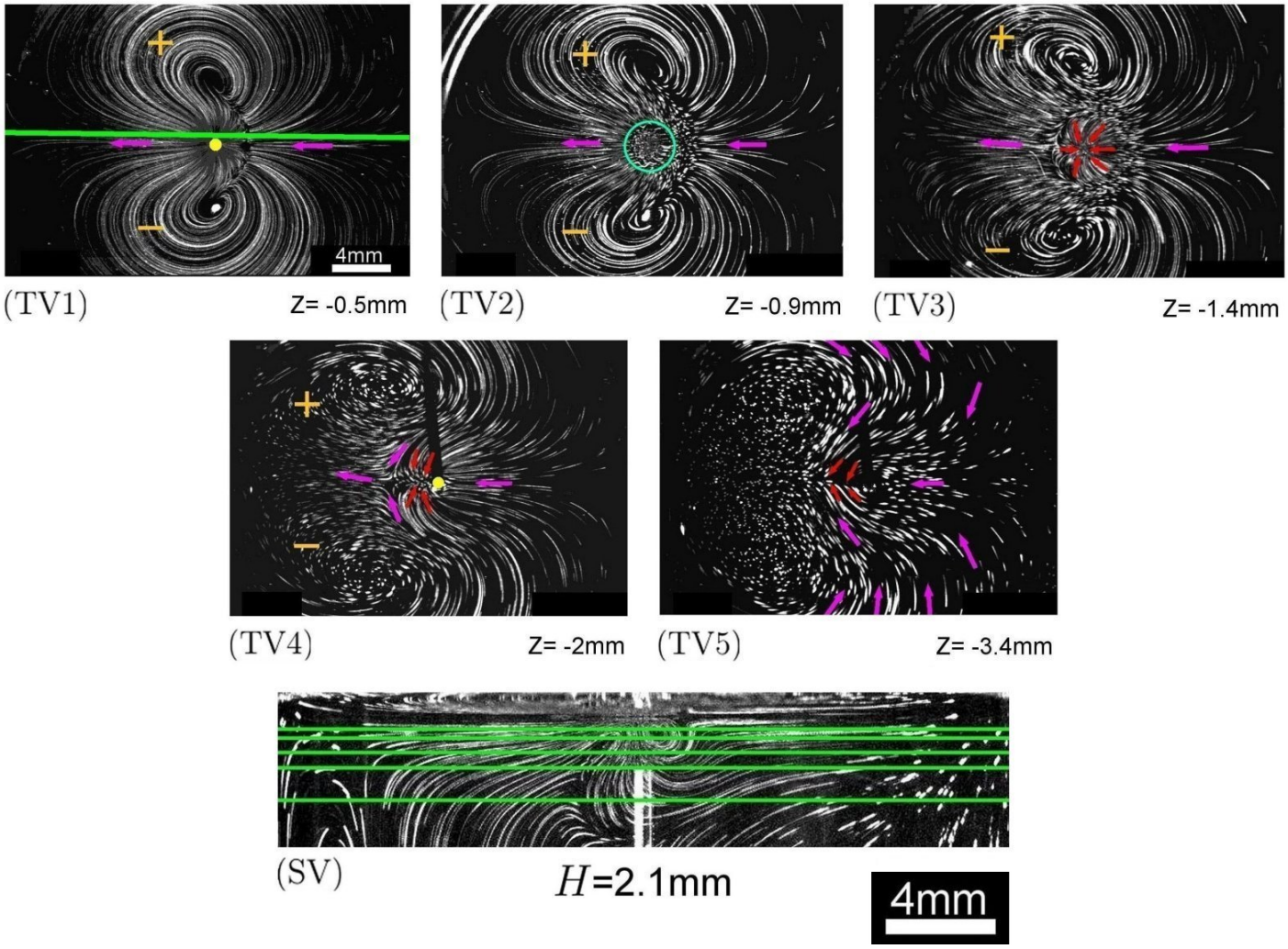

Figure 2.15: Scanning in depth the structure of a dipolar flow. The successive positions of the laser sheet deeper and deeper in the bulk are indicated on the side view (SV). The latter is captured in the symmetry plane of the dipole spotted by the green solid line on the top view (TV1). The corresponding depths are indicated below each top view and the gap H is reported below the side view. For a better readability the scale of the top views is not harmonised with that of the side view. Other graphic elements are the same as previously, except that here red arrows indicate the flow direction in the vicinity of the injector. $V_{\text{inj}} \approx 5.5\,\text{cm/s}$ ($\mathcal{C}_{\text{SDS}} = \text{CMC}/100$).

Method M2 – Unveiling the 3D dipolar structure with fluorescent dye

Fig. 2.16 is an overview of the coloured cloud correlated to a dipolar surface flow. The colour pictures displayed on this plate are high – resolution photographs offering an accurate view of the cloud shape. Although these images are only projections of the cloud volume, their transparent appearance sheds light on some morphological traits :

- On the top view (TV), we see part of a 'double air chamber' at the rear of the injector : the 'inner air chamber' stretches forward in the form of two 'coloured ribbons' symmetrically located on either side of the dipole axis, while the 'outer air chamber' extends in the form of an envelope folded on itself that gives birth to a pair of counter – rotating whirlpools whose ends come back to the injector.
- On the side view (SV) captured in the symmetry plane of the dipole, we recover a ribbon with a multi – layered inner structure. What is new and not evidenced by the top view (TV) is the large angle at which this 'arm' sinks, separating from a thin dye layer confined to the surface that spreads forward as the colouring is ejected. Whirlpools passing under the 'air chamber' are visible on the back view (BV).

Comparing streamlines views with dye distribution maps

We conclude this presentation by comparing streamlines views with dye distribution maps (Fig. 2.17). These diptych – like views point out the structural matching that exists between the repartition of the streamlines and that, closely correlated, of the coloured cloud. Of particular interest is the overlay displayed on the side view, clearly showing that the width of the 'dye ribbon' perfectly fits the locally sharp – angled streamlines. Intriguingly, whilst the streamlines densely cover the entire viewing field, the coloured cloud is rather localised within a subregion.

Computer reconstruction of the coloured cloud volume

A 3D reconstruction of the coloured cloud volume is achieved (for technical details, see Appendix D.1). Figs 2.18 –2.19 provide a detailed view of the multi – layered internal structure of the cloud. Following the cross – sections of the 'arms' throughout the back (or front) 'peeling' (matter behind the cut plane is removed while the part of the structure located ahead is preserved) of the volume is instructive : one remarks that the 'arms' gradually sink and spread apart as we move downstream.

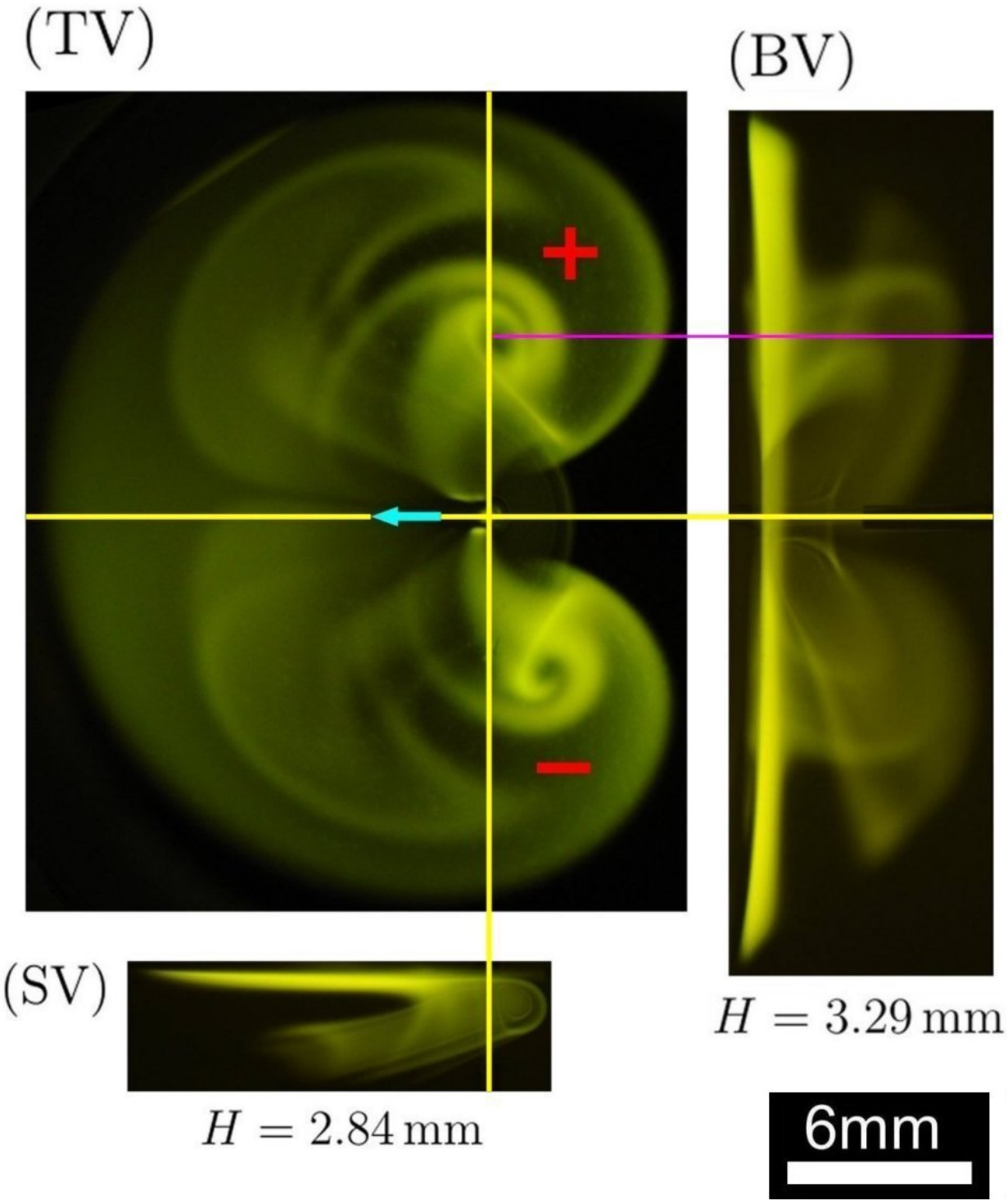

Figure 2.16: Photographs showing the 3D structure correlated to a dipolar surface flow, as revealed by dye injection. The arrow shows the flow direction along the symmetry axis of the dipole. The + (resp. −) red sign denotes clockwise (resp. anticlockwise) rotation of the whirlpools. The gap is reported below each side view. Although both values are not the same, they are close enough to each other for the views to be at least qualitatively comparable. The magenta line points out structural links between the views. $V_{\text{inj}} \approx 5.5\,\text{cm/s}$ ($\mathcal{C}_{\text{SDS}} = \text{CMC}/100$).

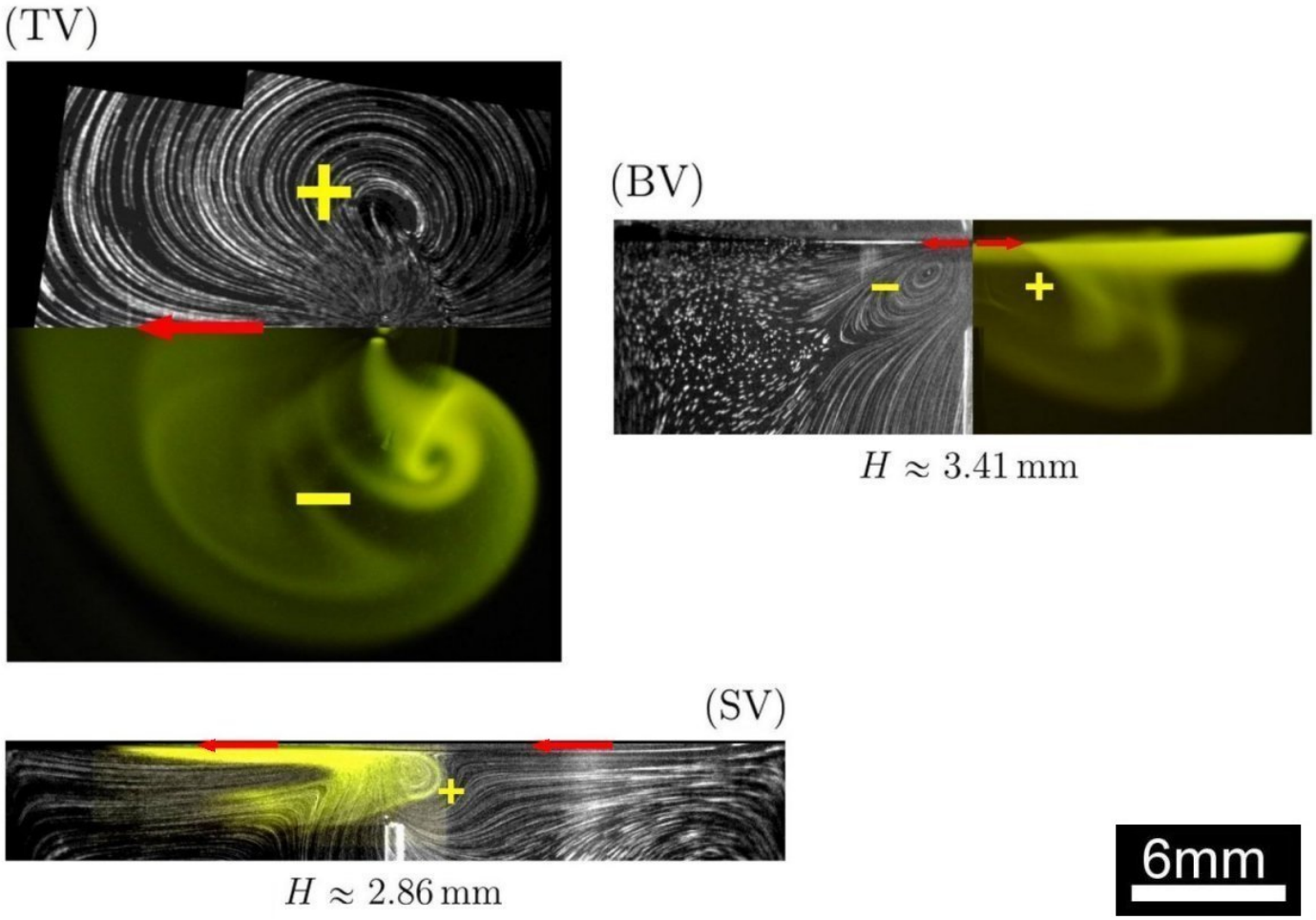

Figure 2.17: Comparison streamlines/dye distribution. The yellow + (resp. −) sign denotes clockwise (resp. anticlockwise) vortex rotation. Arrows show the surface flow direction. Though the gaps are not the same on the streamlines and the coloured cloud views, they are close enough to each other for a proper structural comparison. Because of readability issues, both kind of maps are superimposed on the side view (SV) but simply juxtaposed on the top (TV) and back (BV) views. Harmonised top and side scales setting 25 μm/pix as the unique scale. $V_{\mathrm{inj}} \approx 5.5\,\mathrm{cm/s}$ ($\mathcal{C}_{\mathrm{SDS}} = \mathrm{CMC}/100$).

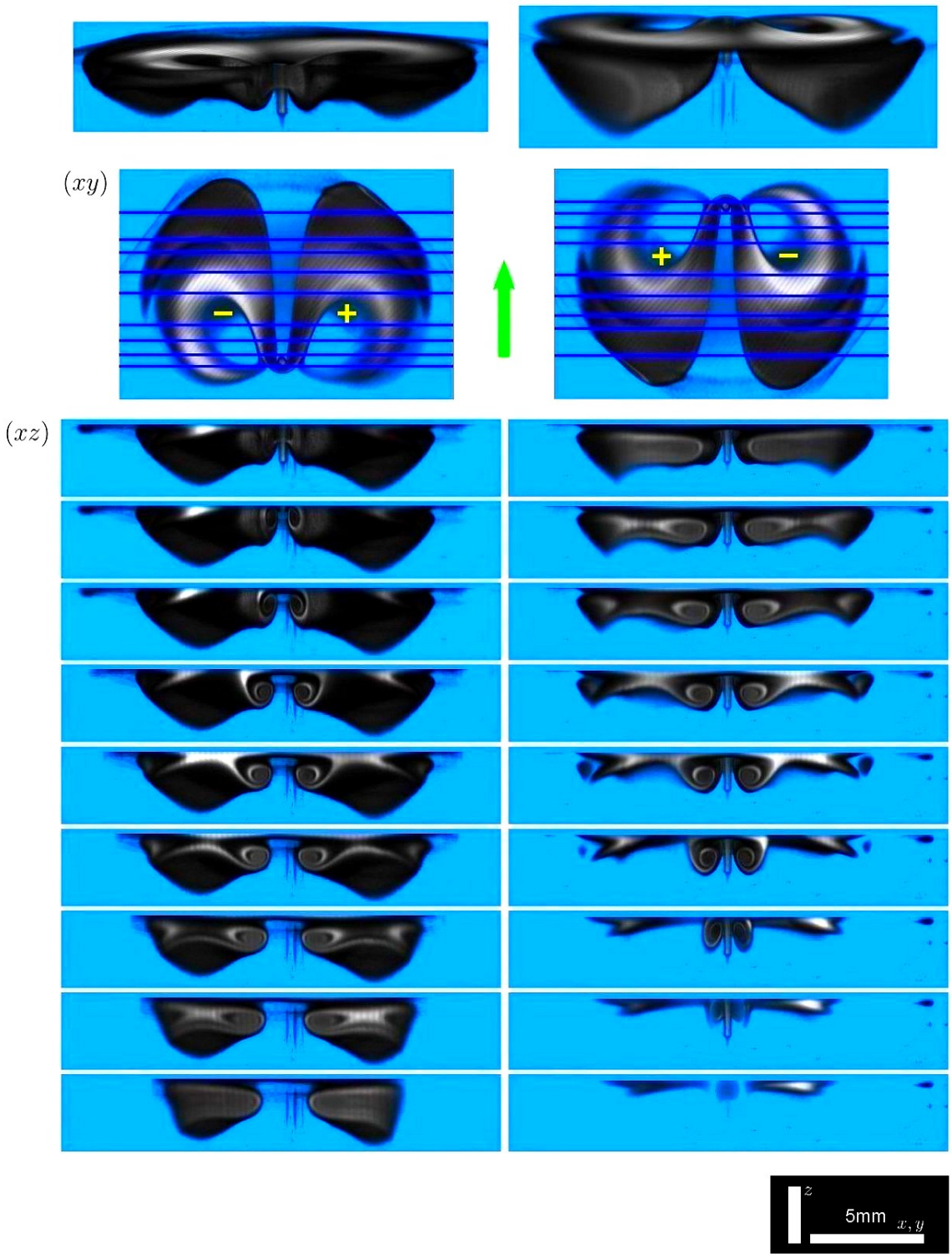

Figure 2.18: Peeling the coloured cloud. Series of back (resp. front) 'cut views' shown in column on the left (resp. right). (xy) denotes the horizontal plane of the top views and (xz) the vertical plane of the back/front views. Successive positions of the cut plane marked by blue lines. Volume 'peeled' in the direction of the arrow. The perspective views in the header of the plate give a global insight of the cloud shape. To ensure good visibility, each voxel is rescaled to a size $\delta x\,\delta y\,\delta z = (34.26 \times 34.26 \times 68.52)\,\mu\text{m}^3$ by imposing an aspect ratio $\delta z/\delta x = 2$ instead of the initial 1.3 value and performing a zoom that multiplies all lengths by 1.52. The yellow + (resp. −) sign denotes clockwise (resp. anticlockwise) vortex rotation.

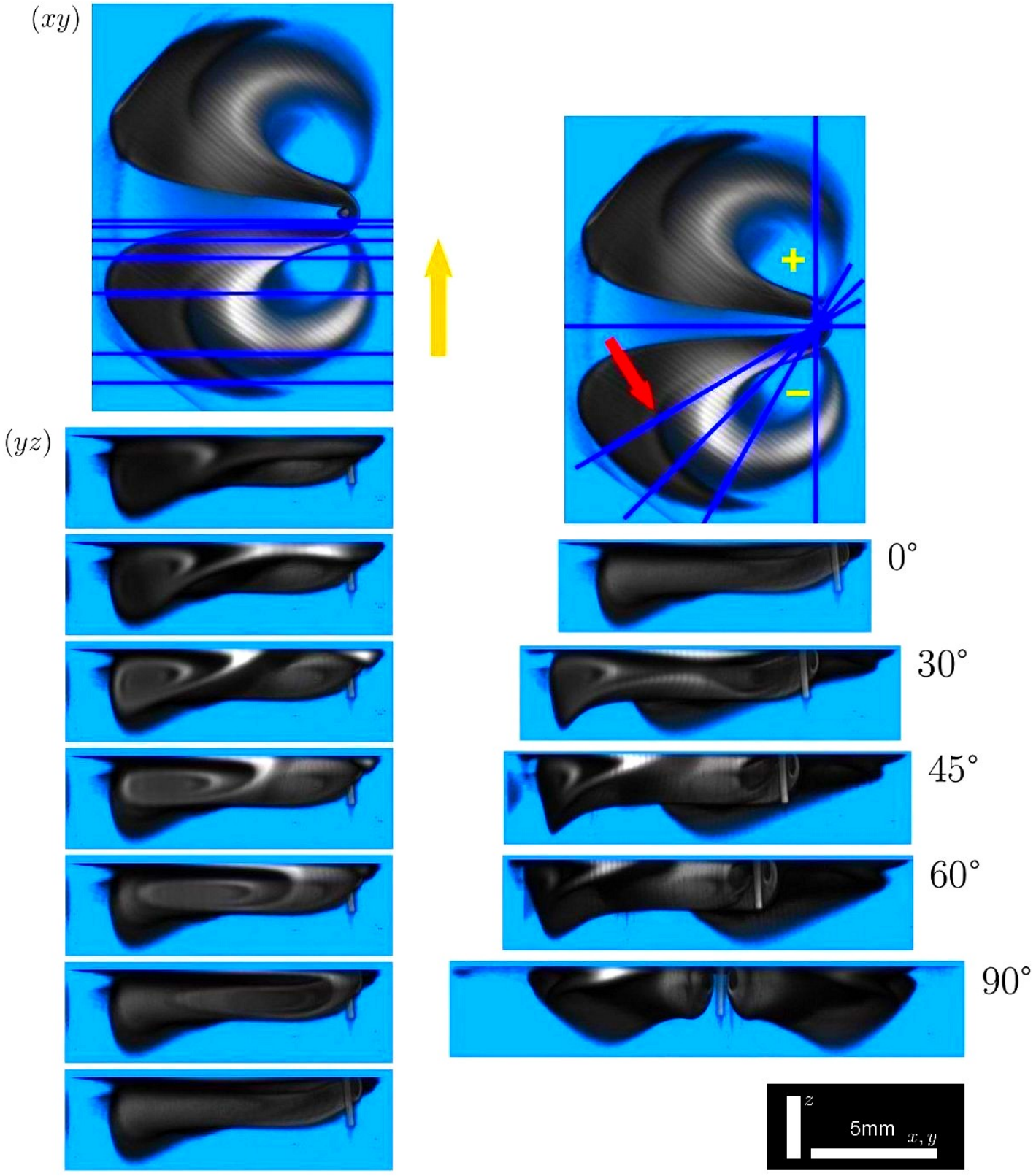

Figure 2.19: Peeling the coloured cloud. Series of parallel (resp. angular) side views shown in column on the left (resp. right). (xy) denotes the horizontal plane of the top views and (yz) the vertical plane of the side views. Same graphic codes as in Fig. 2.18.

PIV – based characterisation of the dipolar state

Now that the dipolar flow has been qualitatively described, we supplement our analysis with quantitative PIV data. A standard PIV procedure is implemented whose key steps are briefly reminded in sec. 2.1.5. We aim at figuring out the order of magnitude of the velocity in the different regions of the dipolar flow, together with the evolution of both velocity components $v_{\parallel}$ and $v_{\perp}$ along the dipole 'eigenaxes'. Particular attention is also paid to vorticity which is essential in characterising the vortex pair of the dipole. More advanced aspects are next addressed, seeking an order parameter that would capture the 'torus – to – dipole' symmetry breaking.

Unless otherwise specified, PIV results are derived from experiments performed in the 'head – to – tail syringes' configuration (Fig. 2.3). We recall that the syringe pump we use sustains injection speeds V_{inj} in the range $0.7 - 14\,\text{cm/s}$. Small $H \approx 0.25\,\text{mm}$, moderate $H \approx 1.25\,\text{mm}$ as well as big $H \approx 2.5\,\text{mm}$ gaps are considered. The ORCA-flash2.8 camera being the only one suited for PIV, which requires high frame rates (45 images/s), it serves as the top camera. The calibration is $52.08\,\mu\text{m/pix}$ in this new layout of the cameras.

Characteristic maps of the dipolar flow

Let us start with a few maps typical of the dipolar flow observed for $H = 1.25\,\text{mm}$ and $V_{\text{inj}} = 3.5\,\text{cm/s}$. For guidance, we provide an average frame showing the streamlines of the dipole (Fig. 2.20). Figs 2.21 – 2.23 give the associated velocity and vorticity maps.

Fig. 2.21 reveals a strong velocity gradient extending over about 1 cm along the dipole symmetry axis (rainbow – like region near the injection site). Note the velocity decline in the core of the vortices (deep blue) well captured by our PIV processing. Fig. 2.22 shows typical fields of the velocity components $v_{\parallel}$ (a) and $v_{\perp}$ (b), the counterparts of v_x and v_y defined in the dipole reference frame. Their variation (a') along the symmetry axis of the dipole (black dashed line on fig. (a)) and (b') the line perpendicular to it (blue dashed line on fig. (b)) is displayed. One remarks that the profile (a') is double – peaked : the most intense of the two peaks arises from the highest (positive) contributions to $v_{\parallel}$ in the dark red region located in front of the injection site, while the secondary peak is likely attributable to local acceleration, some streamlines winding around the rear part of the injection torus. Fig. 2.23 reveals that the vorticity takes significant values only close to the injection site and vanishes everywhere else. Similar series of maps are derived in Appendix F for many other values of the control parameters.

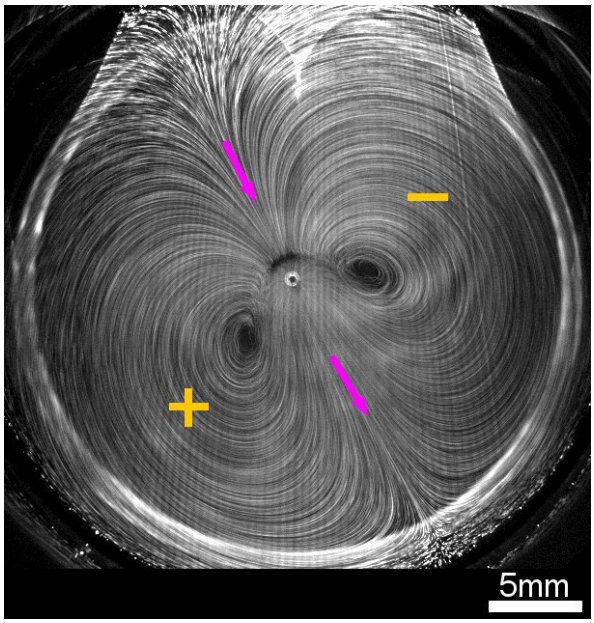

Figure 2.20: Dipolar flow (top view). Average frame from a stack of 1000 images (45 FPS $\rightarrow \Delta t \approx 22\,\mathrm{s}$). Moderate gap $H = 1.25\,\mathrm{mm}$ and injection speed $V_{\mathrm{inj}} = 3.5\,\mathrm{cm/s}$. The + (resp. −) sign denotes clockwise (resp. anticlockwise) vortex rotation. The magenta arrows indicate the flow direction along the symmetry axis. Injection outlet visible in the middle. $\mathcal{C}_{\mathrm{SDS}} = \mathrm{CMC}/100$.

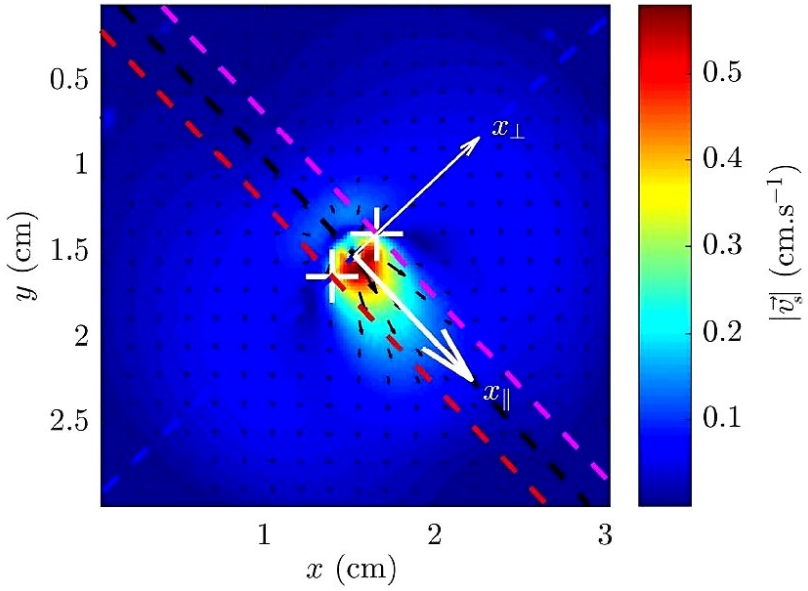

Figure 2.21: Typical surface velocity field. Black (resp. blue) dashed line aligned with (resp. perpendicular to) the dipole symmetry axis (Fig. 2.20). White arrows show the orientation of the dipole 'eigenaxes' $x_\parallel$ and $x_\perp$. The crosses mark the positions of the maxima of vorticity (see Fig. 2.23 hereafter).

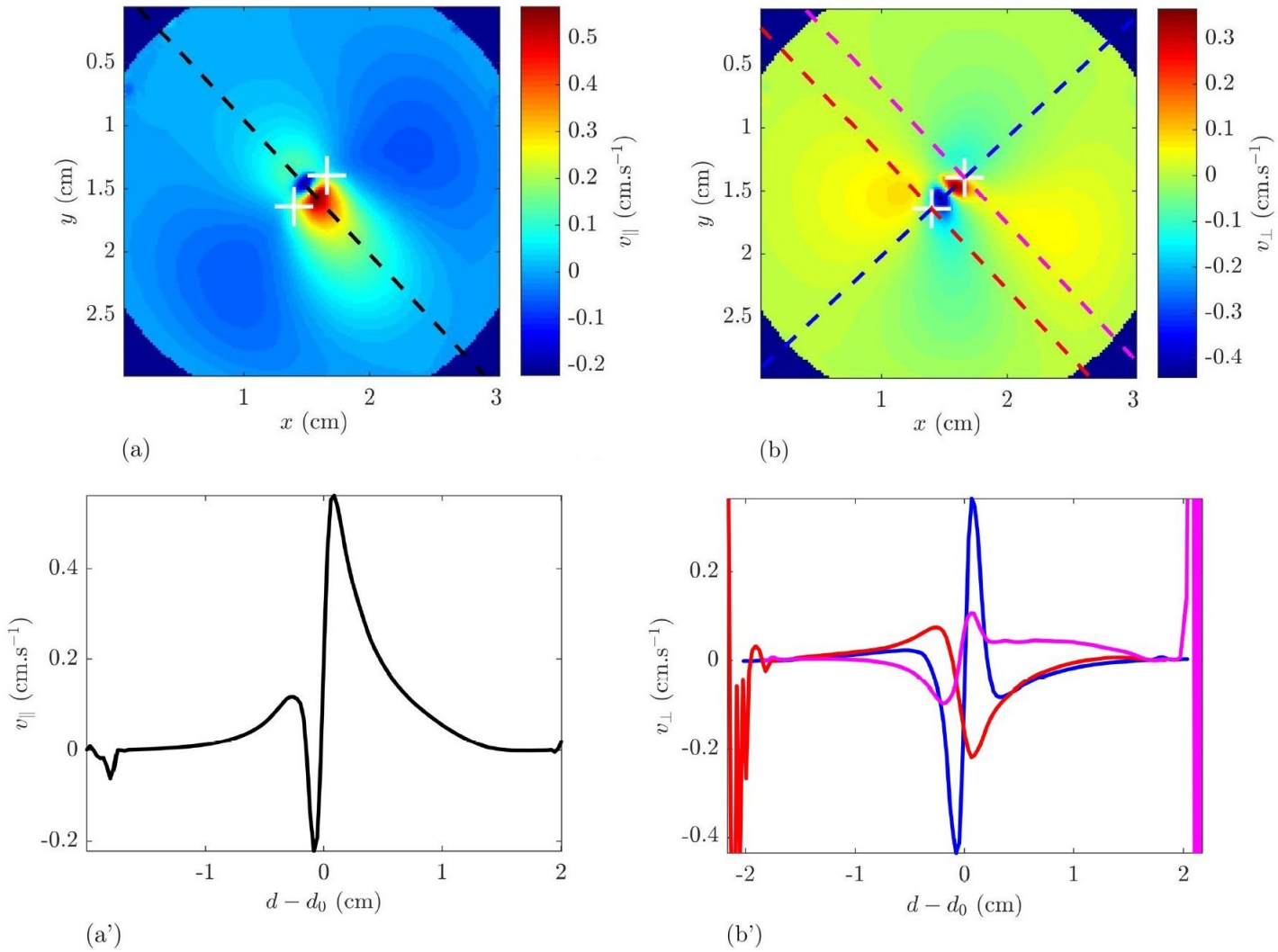

Figure 2.22: Characteristic fields of the velocity components $v_{\parallel}$ (a) and $v_{\perp}$ (b), together with their evolution along the dipole axes (a') – (b'). '$d - d_0$' denotes the distance to the point of maximum vorticity (white cross) measured along the selected colour line.

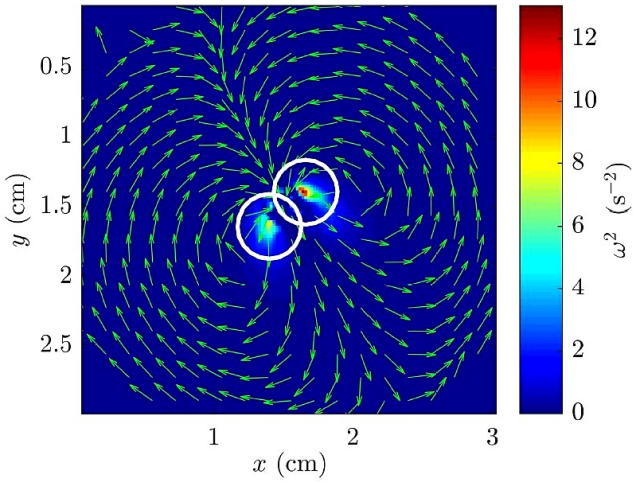

Figure 2.23: Typical interfacial vorticity field. For convenience, the square of the vorticity ω^2 is plotted rather than vorticity itself. This way we handle only positive values, whereas vorticity is an algebraic quantity. The vector field is the one of the velocity map shown above, save that here all vectors have the same length normalised to unity so as to make the dipolar pattern more visible. The centres of the white circles coincide with the maxima of vorticity.

Order parameter of the 'torus – to – dipole' transition

We are seeking an order parameter, *i.e.* some quantity switching from zero to a finite value above a critical threshold of the control parameters. Such a sharp change, which recalls the physics of phase transitions, would be here interpreted as the signature of symmetry breaking from the axisymmetric to the dipolar state.

A hydrodynamic counterpart to electrostatic dipolar moments, here below denoted $\mathcal{D}$, is examined as a possible order parameter. Prior to computing $\mathcal{D}$ for a whole series of experiments run at various H and V_{inj}, we define a 'total hydrodynamic charge' $\mathcal{Q}$ as

$$\mathcal{Q} \doteq \frac{1}{\mathcal{S}} \iint_{(\text{I})} \mathrm{d}x\,\mathrm{d}y\ \omega(x,y)\,, \tag{2.1}$$

with $\mathcal{S} = \iint_{(\text{I})} \mathrm{d}x\,\mathrm{d}y$ the surface of the viewing area (I) the vorticity field $\omega(x,y)$ of the dipole is integrated over ((I) is the illuminated region of the interface). The vorticity being defined as the curl of the flow velocity vector $\boldsymbol{\omega} \doteq \boldsymbol{\nabla} \wedge \boldsymbol{v}$, $\mathcal{Q}$ has the dimension of the inverse of a time. In principle, one expects $\mathcal{Q}$ to be zero : the positive definite vorticity of the clockwise rotating vortex shall exactly balance the negative vorticity of the anticlockwise rotating vortex, in a way analogous to the charges of an electrostatic dipole having the same absolute values but opposite signs. In practice, however, $\mathcal{Q}$ is not

exactly zero but very small $6.70 \times 10^{-5}\,\mathrm{s}^{-1} \leqslant |\mathcal{Q}| \leqslant 1.68 \times 10^{-2}\,\mathrm{s}^{-1}$, as only a portion of the dipole is located inside the viewing area (I) and the dipole is not perfectly symmetric.

The total dipolar moment $\mathcal{D}$ is then computed using the relation $\mathcal{D}^2 = \mathcal{D}_x^2 + \mathcal{D}_y^2$ where

$$\mathcal{D}_x \doteq \frac{1}{\mathcal{S}} \iint_{(\mathrm{I})} \mathrm{d}x\,\mathrm{d}y\ (x - x_0)\ \omega(x,y)\,, \quad \mathcal{D}_y \doteq \frac{1}{\mathcal{S}} \iint_{(\mathrm{I})} \mathrm{d}x\,\mathrm{d}y\ (y - y_0)\ \omega(x,y)\,. \tag{2.2}$$

$\mathcal{D}_x$ and $\mathcal{D}_y$ have the dimension of a velocity. The couple (x_0, y_0) denotes the coordinates of $\mathcal{C}$, the midpoint of the segment of length L joining the centres O_1 and O_2 of the vortex pair. Note that $\mathcal{D}_x = \widehat{\mathcal{D}_x} - x_0\mathcal{Q}$ and $\mathcal{D}_y = \widehat{\mathcal{D}_y} - y_0\mathcal{Q}$. We check numerically that the quantities $\{x_0\mathcal{Q}, y_0\mathcal{Q}\}$ are negligible, being one to two orders of magnitude smaller than the 'uncentered' dipolar moments $\{\widehat{\mathcal{D}_x}, \widehat{\mathcal{D}_y}\}$ in the explored range of the control parameters (H,V_{inj}). Therefore, all PIV computations are indifferently achieved in the natural frame $(X\mathcal{C}Y)$ that complies with the orientation of the dipole (Fig. 2.24). The computations of L and $\mathcal{D}$ necessitate a vortex locating tool implemented via a dedicated piece of code working out the coordinates (x_1, y_1) (resp. (x_2, y_2)) of O_1 (resp. O_2) and deducing those of point $\mathcal{C}$. To locate the centre of a vortex, an option is to evaluate the cross product of the velocity map with a radial 'test field' everywhere in (I).

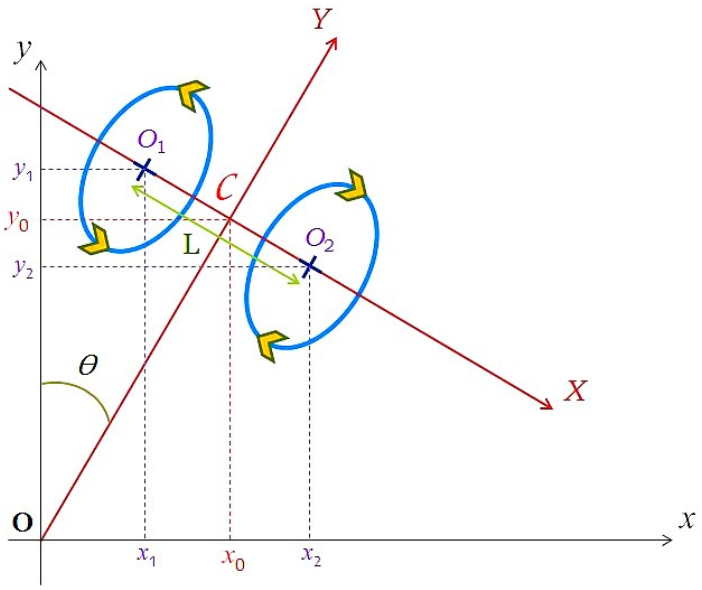

Figure 2.24: Parametrisation of the dipole.

Plotting the maximum velocity $V_{\max}$ in function of V_{inj} evidences a threshold speed $V_{\mathrm{inj}}^{\star} = 1.5684/0.1218 \approx 1.29\,\mathrm{cm/s}$ (Fig. 2.25 – (a)) below which we are in the axisymmetric base flow state characterised by a zero surface velocity (experimental proof in sec. 2.4).

Curiously, the linear evolution of $V_{\max} = f(V_{\text{inj}})$ does not depend much upon the gap H, at least over the investigated range. The graph of the dipole maximum vorticity $\omega_{\max}$ in function of V_{inj} exhibits the same (up to some numerical error in computing derivatives) threshold speed $V_{\text{inj}}^{\star}$ (Fig. 2.25 – (b)). Let me precise that to get $V_{\max}$ and $\omega_{\max}$ for each couple of control parameters (H,V_{inj}), I just read the maximum values on the colour scales associated with the PIV maps of the velocity norm and the vorticity.

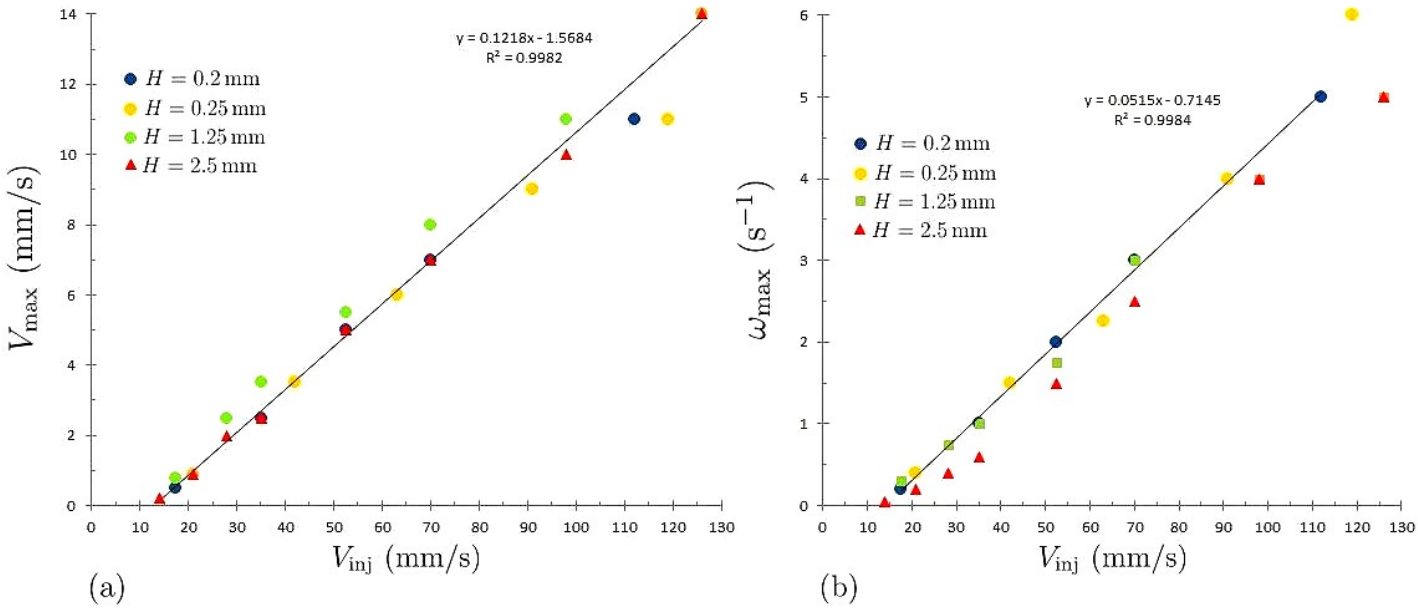

Figure 2.25: Maximum velocity $V_{\max}$ and vorticity $\omega_{\max}$ of the dipole in function of the injection speed V_{inj}, for various gaps H. On both figures, a threshold speed $V_{\text{inj}}^{\star} \approx 1.29\,\text{cm/s}$ appears below which we are in the axisymmetric state that has a zero surface velocity (sec. 2.4). Triangles and squares are used instead of dots to distinguish between superposed points. $\mathcal{C}_{\text{SDS}} = \text{CMC}/100$.

Let us trace the dipolar order parameter $\mathcal{D}$ in function of the injection speed V_{inj}, for various gaps H (Fig. 2.26). Contrary to Fig. 2.25, no threshold speed is identifiable on this last plot and the dispersion of the points is important. Actually, the closest point to the origin P_{axi} ($H = 1.25\,\text{mm}, V_{\text{inj}} = 0.7\,\text{cm/s}$) (magenta circle) is the only one corresponding to the axisymmetric flow, any other point corresponding to the dipole. We shall see in sec. 2.4 that a threshold separating the axisymmetric flow regime from the dipolar state exists in the interval between the first two points of the graph. Moreover, the point P_{axi} should lie on the x – axis, the axisymmetric state having a zero surface velocity (sec. 2.4 again). The reason why the interfacial velocity of the axisymmetric flow appears here very small but finite is probably due to the fact that our PIV measurements are based on a horizontal laser sheet. Indeed, the latter is never exactly at the interface but intercepts a thin subsurface layer wherein tracer particles move at an extremely low but finite speed.

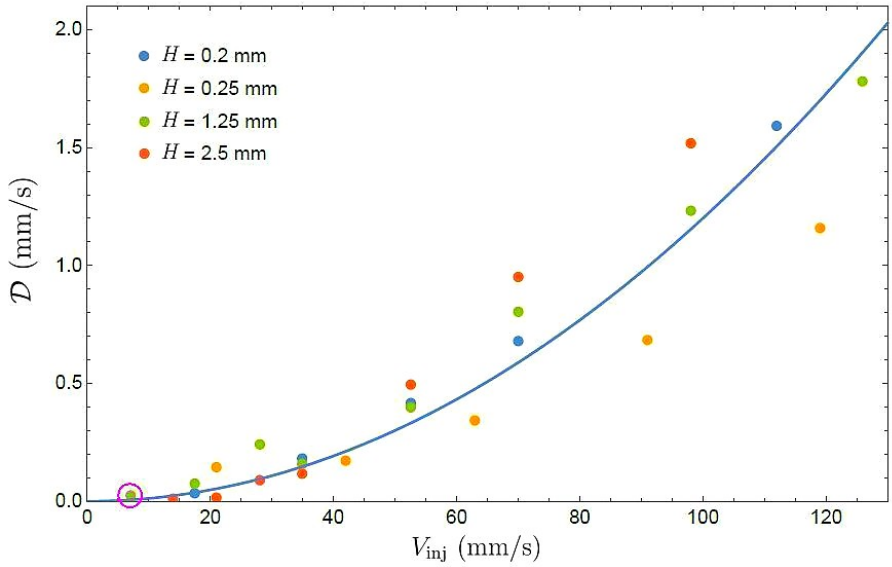

Figure 2.26: Evolution of the dipolar order parameter $\mathcal{D}$ with the injection speed V_{inj}, for different gaps H. Point P_{axi} ($H = 1.25\,\text{mm}, V_{\text{inj}} = 0.7\,\text{cm/s}$) associated with the axisymmetric flow surrounded by a magenta circle. The colour code is the same as in Fig. 2.25 since the dataset is the same. The blue curve is a guide to the eye. $\mathcal{C}_{\text{SDS}} = \text{CMC}/100$.

To conclude, both the maximum velocity V_{max} and vorticity ω_{max} seem to evidence that the dipolar instability arises at an injection speed threshold $V_{\text{inj}}^{\star} \approx 1.3\,\text{cm/s}$. Still, none of the points shown in Fig. 2.25 corresponds to the axisymmetric base state. To be completely rigorous, this analysis would ask for many points like P_{axi} (Fig. 2.26). Unfortunately, even the smallest rate available on the syringe pump control unit, $Q_{\text{inj}} = 100\,\mu\text{L/min}$, is too strong to unfailingly generate an axisymmetric flow, a dipole appearing most often yet at such a low injection rate (in the explored range of gap values).

2.4 Interface unlocking

We present an experiment which uncovers some correlation between the interfacial flow morphology and the dynamics of surface/subsurface tracer particles. We will see that the interface is in a 'locked' or in a 'passing' state depending on the nature of the surface flow.

Experiments are realised with the 'head – to – tail syringes' setup (sec. 2.1.2). We first select a strong injection rate $Q_{\text{inj}} = 800\,\mu\text{L/min}$. The experiment is then repeated at lower injection rates $Q_{\text{inj}} = 700, 600... \,\mu\text{L/min}$ until a minimum value $Q_{\text{inj}} = 100\,\mu\text{L/min}$. A horizontal cut view is recorded each time to visualise the surface flow structure, along with a vertical (quasi – diametrical) cross – section on which surface and subsurface tracer

particles are tracked with the aim of estimating their velocity. Tracking is achieved using ImageJ's 'Manual Tracking' tool. Trajectories of interfacial tracer particles ($z = 0$) are reconstructed, as well as those of subsurface particles situated a few tenths of a mm below the surface. The depth of a subsurface tracer particle is evaluated based on its mirror image through the interface. In particular, tracer particles found exactly at the interface, in $z = 0$, do not produce mirror images. Despite a possible measurement error in the order of $\mathrm{d}z \approx 30\,\mu$m (the size of a pixel), this method proves efficient as it is in fact easy to see if a tracer particle is at rest or driven by the flow together with other tracer particles located deeper. The bulk flow is captured by the ORCA-flash camera at a rate of 10 frames/s. The typical duration of 'horizontal' and 'vertical' recordings is $\Delta t \approx 30\,$s.

Fig. 2.27 displays some surface flows observed at various injection rates Q_{inj}. From the slightly polarised toroidal flow routinely observed at low injection rates ($Q_{\mathrm{a}} = 200\,\mu$L/min), the surface flow becomes fully dipolar at stronger injection rates ($Q_{\mathrm{inj}} \geqslant Q_{\mathrm{c}} = 400\,\mu$L/min). On Fig. 2.28 are reported measurements of the velocity of surface and subsurface tracer particles driven by these interfacial flows. The following observations can be made :

a. $Q_{\mathrm{a}} = 200\,\mu$L/min : at low injection rate, surface tracer particles are motionless whereas subsurface tracer particles are entrained by the toroidal base flow, with equal strength to the right and to the left of the injector (on Fig. 2.28 – (a), the blue squares are distributed in such a way that $|V_{200}^{\mathrm{min}}| \approx |V_{200}^{\mathrm{max}}|$).

b. $Q_{\mathrm{b}} = 300\,\mu$L/min : surface tracer particles start moving a bit, as evidenced by the red balls 'jumping' out of the $x-$axis. Here the red balls are all associated with positive velocities, contrary to the blue squares which alternate between negative velocities in the region $x < x_{\mathrm{inj}}$ to the left of the injector and positive ones in the region $x > x_{\mathrm{inj}}$ on the right. Surface tracer particles thus move collectively from the left to the right, whereas subsurface tracer particles are still entrained by the toroidal flow. In the region $x < x_{\mathrm{inj}}$, the surface tracer particles move against the centrifugal flow imposed by the torus, which probably results in important shear stresses at a short distance beneath the surface.

c. $Q_{\mathrm{c}} = 400\,\mu$L/min : the interfacial flow is fully dipolar. The polarisation stream, directed along the symmetry axis of the dipole from the left to the right, drives all the surface as well as the subsurface tracer particles. Both groups move at the same speed as suggested by the nearly coinciding red balls and blue squares. Positive velocities of subsurface tracer particles are measured now in the region $x < x_{\mathrm{inj}}$, meaning that the influence of the toroidal flow has completely faded out.

By the way, the fact that the velocities at the interface and those measured right below are very similar is good news for the PIV study of sec. 2.3.2 based on horizontal cut views, since in this case possible mistakes in segregating surface tracer particles from subsurface ones turn out to have little impact on velocity computations.

In conclusion, the interface switches from a 'locked' state at low rates to a 'passing' state at stronger injection rates. The transition, which takes place at $Q_{\rm tr} \approx 300\,\mu$L/min $\rightarrow$ $V_{\rm tr} \approx 2\,$cm/s, is accompanied by the emergence of a surface dipole out of a toroidal flow. This phenomenon, which is of utmost importance, will be further discussed in sec. 2.6.

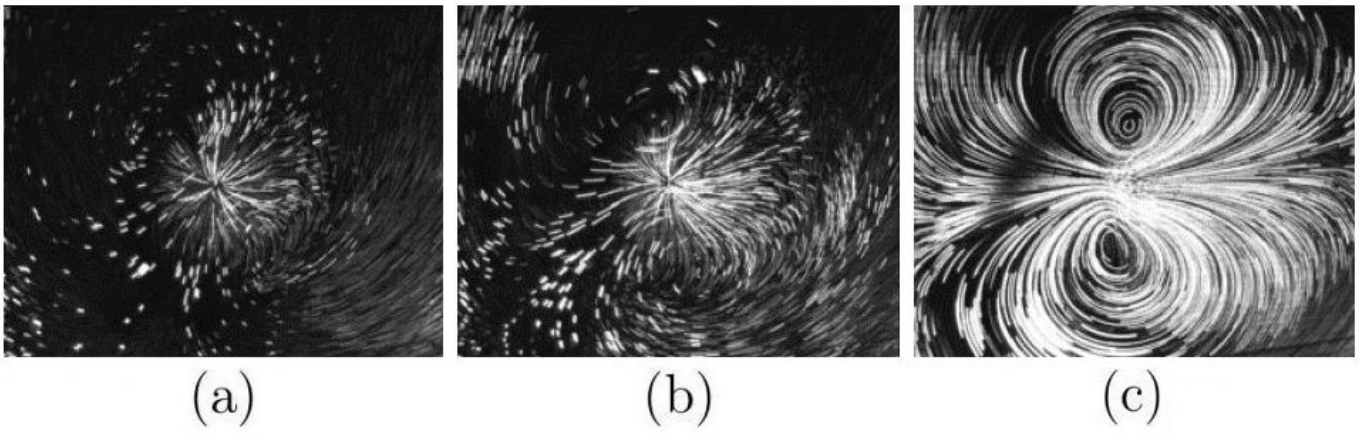

Figure 2.27: Surface flows arising at various injection rates (*top views*). (a) Slightly polarised toroidal flow observed for an injection rate $Q_{\rm a} = 200\,\mu$L/min corresponding to an injection speed $V_{\rm a} = 1.4\,$cm/s. (b) Intermediate state. $Q_{\rm b} = 300\,\mu$L/min, that is $V_{\rm b} = 2.1\,$cm/s. (c) Dipolar surface flow. $Q_{\rm c} = 400\,\mu$L/min $\rightarrow$ $V_{\rm c} = 2.8\,$cm/s. The vertical laser sheet (not represented) is aligned with the dipole symmetry axis. $H \approx 2.1\,$mm ($\mathcal{C}_{\rm SDS} = $ CMC/100).

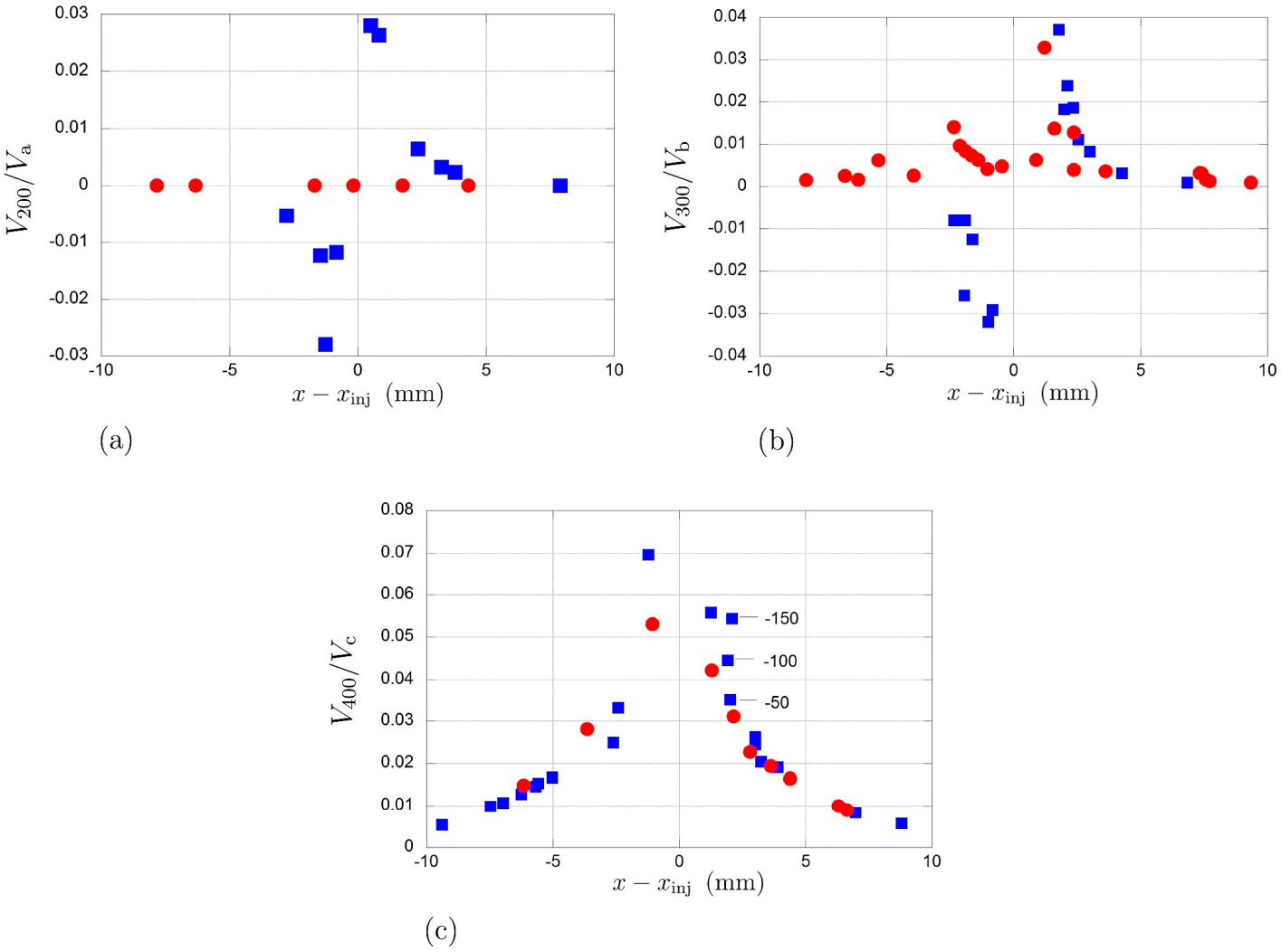

Figure 2.28: Velocity of surface and subsurface tracer particles measured for various interfacial flows. The flows are those of Fig. 2.27. Injection rates/speeds: (a) $Q_a = 200\,\mu$L/min $\rightarrow$ $V_a = 1.4$ cm/s; (b) $Q_b = 300\,\mu$L/min $\rightarrow$ $V_b = 2.1$ cm/s; (c) $Q_c = 400\,\mu$L/min $\rightarrow$ $V_c = 2.8$ cm/s. Each red ball depicts a tracer particle at the interface while blue squares symbolise tracer particles found within a 0.2 mm thick subsurface layer. The numerical values reported next to three squares of fig. (c) indicate the depths dz (in μm) at which the corresponding tracer particles are found. Measurements made in a cross−section aligned with the dipole symmetry plane (Fig. 2.27−(c)). $H \approx 2.1$ mm ($\mathcal{C}_{SDS} = $ CMC/100).

2.5 Complementary studies

2.5.1 The influence of confinement over the instability

Two cell sizes are selected to probe the effects of confinement on the instability : a small cell of inner diameter $\varnothing_s$ 35 mm and a large one $\varnothing_l$ 154 mm. Hitherto, we have focused on experiments achieved with the small cell. Let us now present the observations made with the large cell and compare them to the foregoing results.

Remarkably, dipolar flows of modest size compared with the radius of the wide cell spring up at injection speeds and gaps akin to those set in small cell experiments. Fig. 2.29 shows an example of a dipole arising in the large cell whose vortices are separated by a distance L $\approx 1\,\mathrm{cm} \ll \varnothing_l$. This observation suggests that flow confinement is not the cause of the instability. Said differently, the instability would develop even in an infinite system, which is by the way a valuable information to simplify theoretical models. This, however, does not mean that containment exerts no influence on the flow patterns. Clearly, the peripheral streamlines of the dipole are pressed against the cell wall beyond a certain injection speed, resulting in reshaped vortices. Fig. 2.30 illustrates this phenomenon : the aspect of the growing vortices changes as the jet flow strengthens, from a rounded shape at moderate injection speeds (a) to a more oblong shape at higher speeds (b).

Fig. 2.31 compares the evolution of the intervortex separation L with the two control parameters (V_{inj}, H) in the large (a) and in the small (b) cells. Clearly, in the large cell L increases with the gap whatever the injection speed. For a given gap, L tends to grow with the injection speed. In the small cell, L also increases with the gap H (though this becomes less obvious at small gaps $H \sim 0.1\,\mathrm{mm}$). For a fixed gap, however, the way L evolves now depends upon how large is the gap : L increases at small gaps $H \sim 0.1\,\mathrm{mm}$, decreases at big gaps $H \sim$ a few mms (save what is likely an outlier) and, at intermediate gaps $H \sim 1\,\mathrm{mm}$, reaches a maximum before declining past a high enough injection speed.

The first behaviour may seem counterintuitive. For a given injection speed, we expect the 'effective pressure' exerted by the jet on the interface to be less and less experienced by the latter as the gap increases, resulting in weaker interfacial constraints and hence in a smaller dipolar pattern... Anyhow, this observation stresses the leading role the gap plays in setting the typical size of the flow patterns. The non – monotonic behaviour at $H \sim 1\,\mathrm{mm}$, as well as the decline of L at still bigger gaps, manifesting themselves in the small cell but not in the large one, are probably due to flow confinement : the dipole would

expand as the dilatational source flow is intensified but is prevented by the sidewalls from doing it, and at a certain point the 'interaction' of the dipole with the walls becomes so strong that it shrinks if the injection speed or the gap is further increased.

Comparing the intervortex separations in the large and small cells for similar values of the control parameters, we find that L ranges between 3 and 10 mm in both cases. For instance, with a gap $H \approx 0.25\,\text{mm}$ and an injection speed $V_{\text{inj}} \approx 9.1\,\text{cm/s}$, one measures $\text{L} \approx 5.38\,\text{mm}$ in the small cell while in the large cell $\text{L} \approx 5.47\,\text{mm}$ for $H \approx 0.35\,\text{mm}$ and $V_{\text{inj}} \approx 8.8\,\text{cm/s}$. This similarity seems to indicate that flow confinement does not considerably affect the size of the dipole.

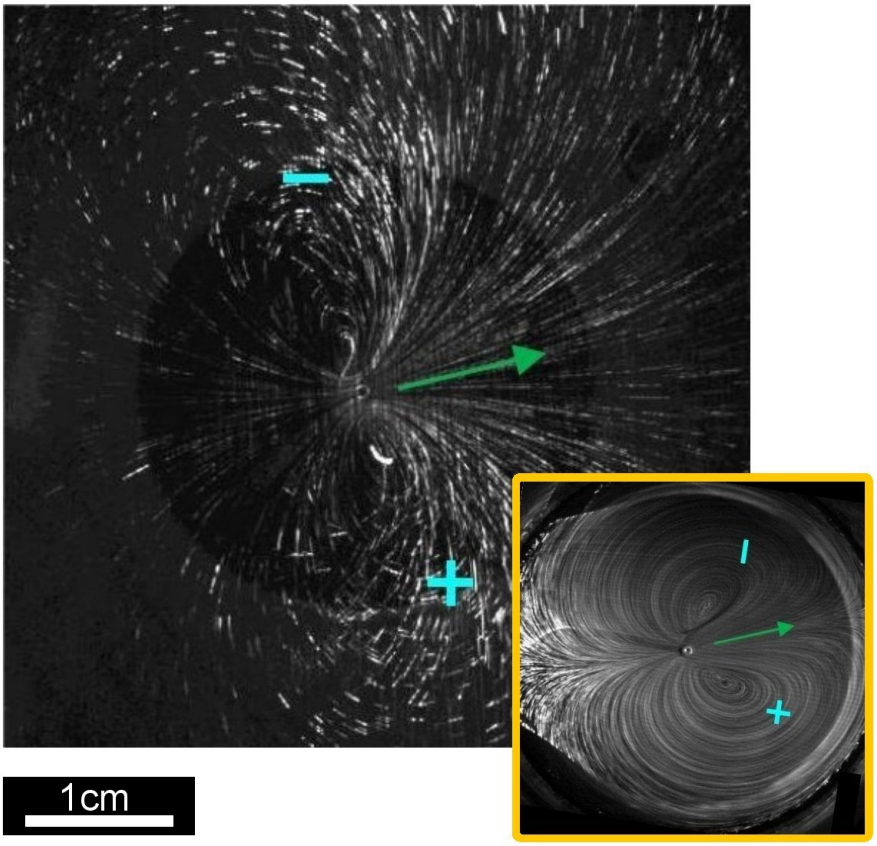

Figure 2.29: Dipolar flow in the large and the small cell. For comparison sake, the gap is set to $H \approx 1\,\text{mm}$ and the injection speed is $V_{\text{inj}} \approx 5.5\,\text{cm/s}$ in both cases. Green arrows show the flow direction along the dipole symmetry axis. Cyan + (resp. −) signs denote clockwise (resp. anticlockwise) vortex rotation. The sidewalls are out of the field of view on the picture captured in the large cell but are visible on the picture taken in the small vessel (insert). *Image from B. Gorin's internship report.*

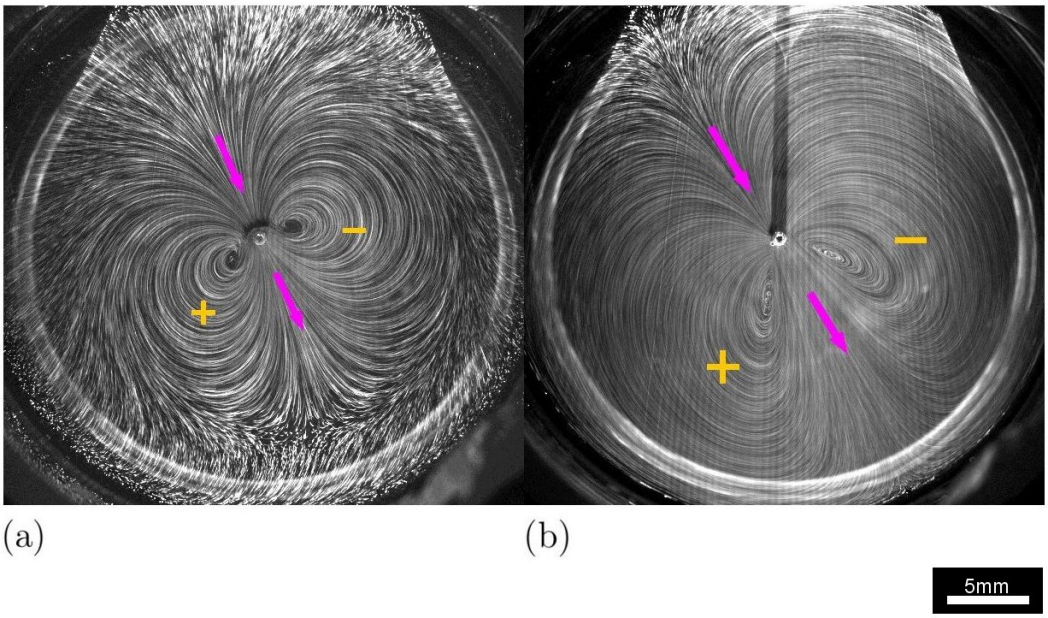

Figure 2.30: Confinement – induced reshaping of a vortex pair. (a) Dipolar surface flow observed at a gap $H \approx 0.25\,\mathrm{mm}$ and an injection speed $V_{\mathrm{inj}} \approx 1.75\,\mathrm{cm/s}$. (b) Same dipole for a much stronger jet flow at $V_{\mathrm{inj}} \approx 9.8\,\mathrm{cm/s}$. Arrows show the flow direction. Orange + (resp. −) signs denoting clockwise (resp. anticlockwise) vortex rotation. Small cell ($\varnothing_s$ 35 mm). $\mathcal{C}_{\mathrm{SDS}} = \mathrm{CMC}/100$.

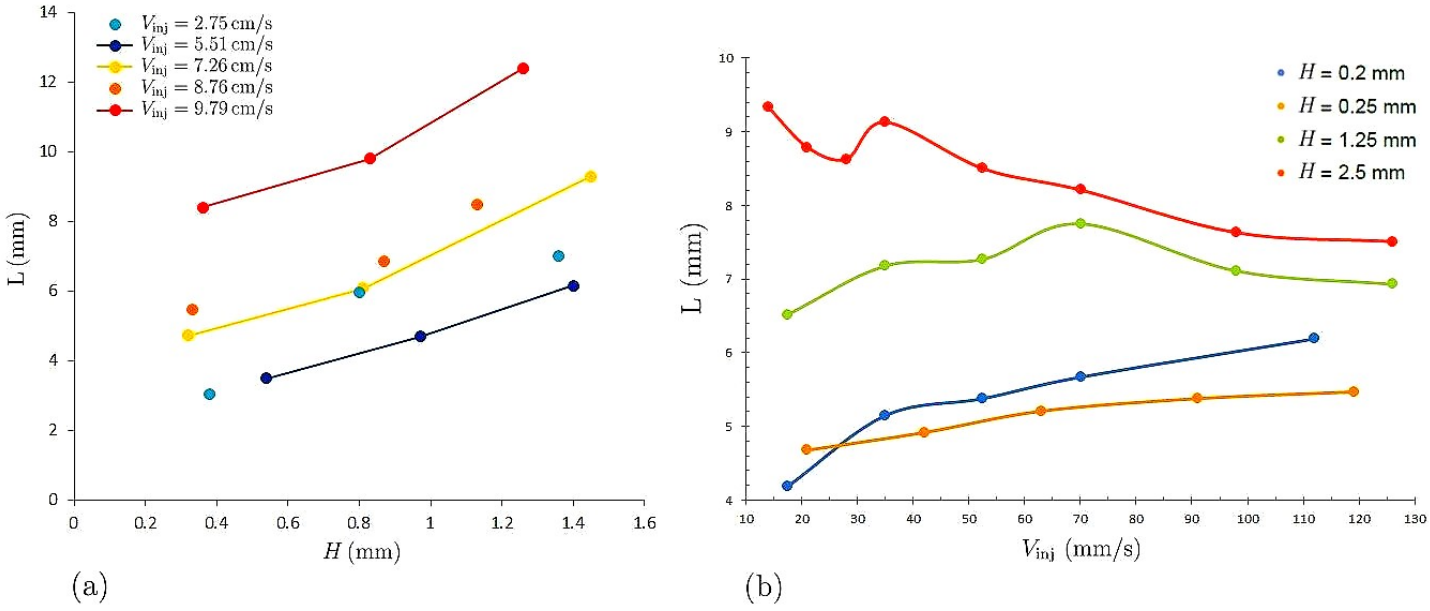

Figure 2.31: Evolution of the intervortex separation L with the control parameters (V_{inj}, H) in the large (a) and in the small (b) cells. Curves are a guide to the eye. *Large cell data from B. Gorin.*

2.5.2 The influence of interface deformation over the instability

Our shadowgraphy results are presented below. We remind the reader that shadowgraphy serves us to measure the size of the 'hydraulic bump' generated at the interface by the vertical water jet. This technique is also a tool for investigating the influence of surface deformation over the instability : does it induce it or not ? This section is structured around these two axes. A comprehensive presentation of shadowgraphy applied to the present case is provided in Appendix E. Note that the experiments presented in this part are all conducted at a SDS concentration $\mathcal{C}_{\mathrm{SDS}} = \mathrm{CMC}/8$.

Measuring the size of the bump−like interface distortion

Experiments aimed at measuring either small or large surface deformations are run, wherein the screen is placed at a critical distance $\mathcal{D}^\star = 40\,\mathrm{cm}$ or $\mathcal{D}^\star = 2.5\,\mathrm{cm}$ depending on the case (Fig. E.3). The height h and extent ξ of the bulge are inferred from the dimensions of its shadowgram and the value of $D^\star$ using the formulas (E.1). A concrete example of how to apply these formulas is detailed in Appendix E.4. Fig. 2.32 summarises our shadowgraphy results on the dimensions of the jet−induced interface deformation.

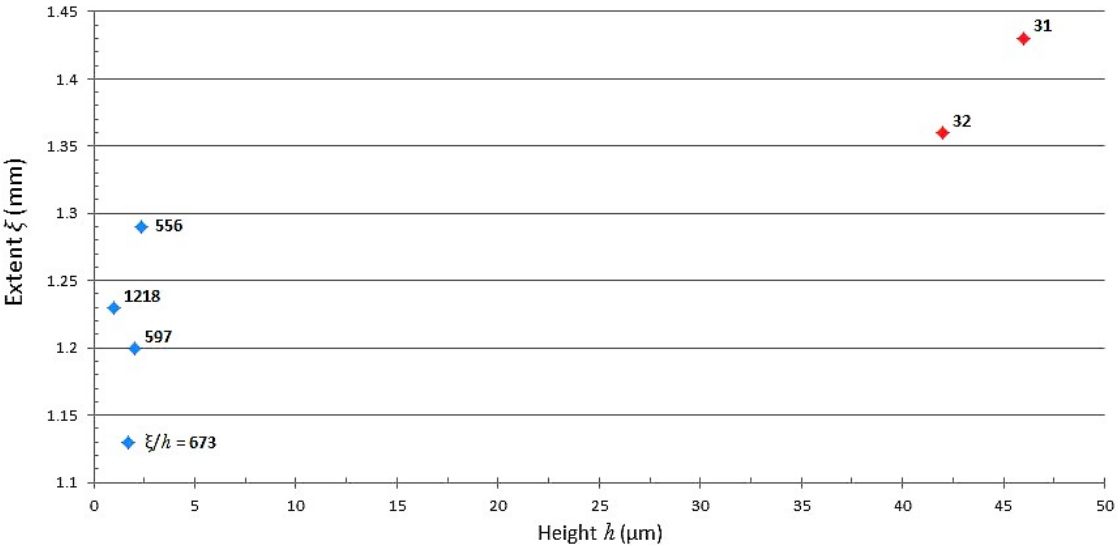

Figure 2.32: Extent ξ of the jet−induced interface deformation in function of its height h. The graph is divided into two point clouds. The blue one corresponding to low deformations ($\mathcal{D}^\star = 40\,\mathrm{cm}$), made up of measuring points obtained for gaps $H \geqslant 0.3\,\mathrm{mm}$. The red one corresponding to large deformations ($\mathcal{D}^\star = 2.5\,\mathrm{cm}$), composed of measuring points derived at vanishing gap $H \approx 0$. Aspect ratio ξ/h of the hydraulic bump indicated next to each point. $V_{\mathrm{inj}} \approx 3.3\,\mathrm{cm/s}$ ($\mathcal{C}_{\mathrm{SDS}} = \mathrm{CMC}/8$).

Thus we see that the 'bump' is extremely flat, being tens to hundreds times more elongated than elevated : its typical height does not exceed a few tens of microns and its extent is comparable to (half) the capillary length $l_c = \sqrt{\gamma/\rho g} \approx 2.7\,\mathrm{mm}$ of pure water at room temperature, the characteristic length that sets the scope of capillary forces shaping the interface at small scales. The fact that $\xi \gg h$ validates *a posteriori* our assumption of a flat interface $|f'(a)| \ll 1\,,\ \forall\, a \in [-A, +A]$ (see Appendix E.3). Although we cannot fathom that so tiny a deformation could influence the multipolar flows, no cogent evidence has been brought so far to corroborate this point. We remedy this issue now.

Probing a possible correlation between the surface deformation and the instability

To probe a possible correlation between the interfacial bump and the instability, the recording plane is placed at a critical distance $\mathcal{D}^\star = 2.5\,\mathrm{cm}$ above the surface, covering half the cell and letting the other half clear for direct flow visualisation. This way, both the streamlines and the shadowgram are simultaneously captured. The uncovered part of the cell allows a glimpse of a dipolar flow pattern and the associated shadowgram is imaged on the screen covering the right half of the cell (Fig. 2.33). One remarks that the symmetry breaking of the flow leaves the shadowgram axisymmetric, which suggests that the surface deformation induced by the jet and the multipolar instability of the toroidal base flow are uncorrelated, the former not being at the origin of the latter.

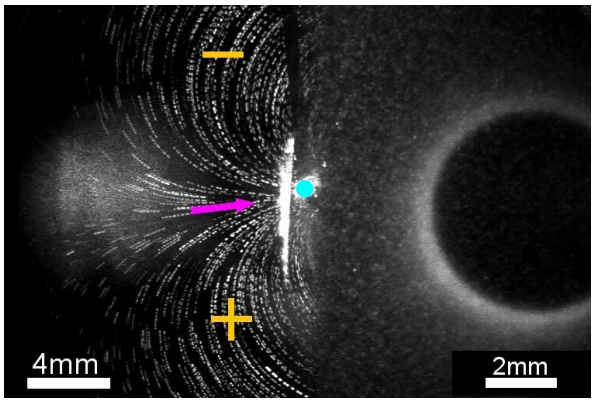

Figure 2.33: Comparing the symmetry of the dipolar surface flow with that of its shadowgram. (*Left half*) The + (resp. −) sign marks clockwise (resp. anticlockwise) vortex rotation. The arrow shows the flow direction along the dipole symmetry axis. Injection site depicted by a cyan disk. (*Right half*) Shadowgram. Since the recording plane sits on top of the cell ($\mathcal{D}^\star = 2.5\,\mathrm{cm}$) the calibration of the shadowgram ($21.74\,\mu\mathrm{m/pix}$) differs from that of the streamlines views ($37.81\,\mu\mathrm{m/pix}$). Average frame from a stack of 10 images (4 FPS $\rightarrow \Delta t = 2.5\,\mathrm{s}$). 'Glowing strip' in the middle probably due to stray light diffused by the edge of the screen. Patch of light on the left due to the incident laser beam passing through the paper screen. $V_{\mathrm{inj}} \approx 2.7\,\mathrm{cm/s}$, $H \approx 0$ ($\mathcal{C}_{\mathrm{SDS}} = \mathrm{CMC}/8$).

2.5.3 Flow reversibility

Another question that is worth raising concerns the reversibility of the flows. Although the littleness of our water jet device brings us closer to the field of microfluidics, inertial effects cannot be automatically discarded. Are we really working at low Reynolds numbers $\mathrm{Re} \ll 1$ (definition given in sec. 2.6 below) ? Two ways of investigating this point are considered experimentally :

- *With the 'gravity flow' setup* (Fig. 2.2) — A minute volume of dye ($\mathcal{V}_{\mathrm{fluo}} \approx 200\,\mu\mathrm{L}$) is incorporated into the working liquid. At the very moment the colouring spurts out in the cell the reservoir is quickly lifted down from a height $+\Delta$, typically set at $\Delta = 55\,\mathrm{mm}$ for which $V_{\mathrm{inj}} \approx 5.5\,\mathrm{cm/s}$, to its symmetric position $-\Delta$ relative to the reference level of the liquid in the cell. The injector hence turns into an aspirator (the cell empties into the reservoir), the velocity switching from $V_{\mathrm{inj}} = +V$ to $V_{\mathrm{asp}} = -V$ near the tube outlet. Does the tube swallow back the colouring ?

- *With the syringe pump* (Fig. 2.3) — One readily reverses the translational motion of the paired syringes on the syringe pump control unit, therefore turning the injector into a drain tube whereas the drain tube at the bottom of the cell becomes an injector. Are aspiration flows the 'time – reversed version' of injection flows ?

  Response elements about these questions are given in what follows.

Swallowing back the cloud

Several experiments of the first type are run. On Fig. 2.34, the series of images (A) – (G) displays side views of the perturbed coloured cloud in a vertical plane tangent to the injection tube. The side views (A') – (F') focus on the jet evolution, the laser cut plane intercepting this time the injector. As the tank is driven down, there comes a moment when the structure gets destabilised by wavelets (B) – (D) (rounded magenta rectangle) and breaks apart soon after (E) – (G) : the front of the dye surface layer is 'thrown against' the walls and, with some delay, part of the thin jet of dye is propelled forward (yellow ellipse), likely entrained by the inertia of the preexisting dipolar flow.

It might be that this disruptive wave train consists of 'varicose waves' responsible for the breakup of the jet (see the rippling of the jet on picture (C')). Yet, we cannot exclude that the latter phenomenon is simply caused by parasitic mechanical vibrations, despite all the care taken in eliminating them while the reservoir moves on its rack and pinion.

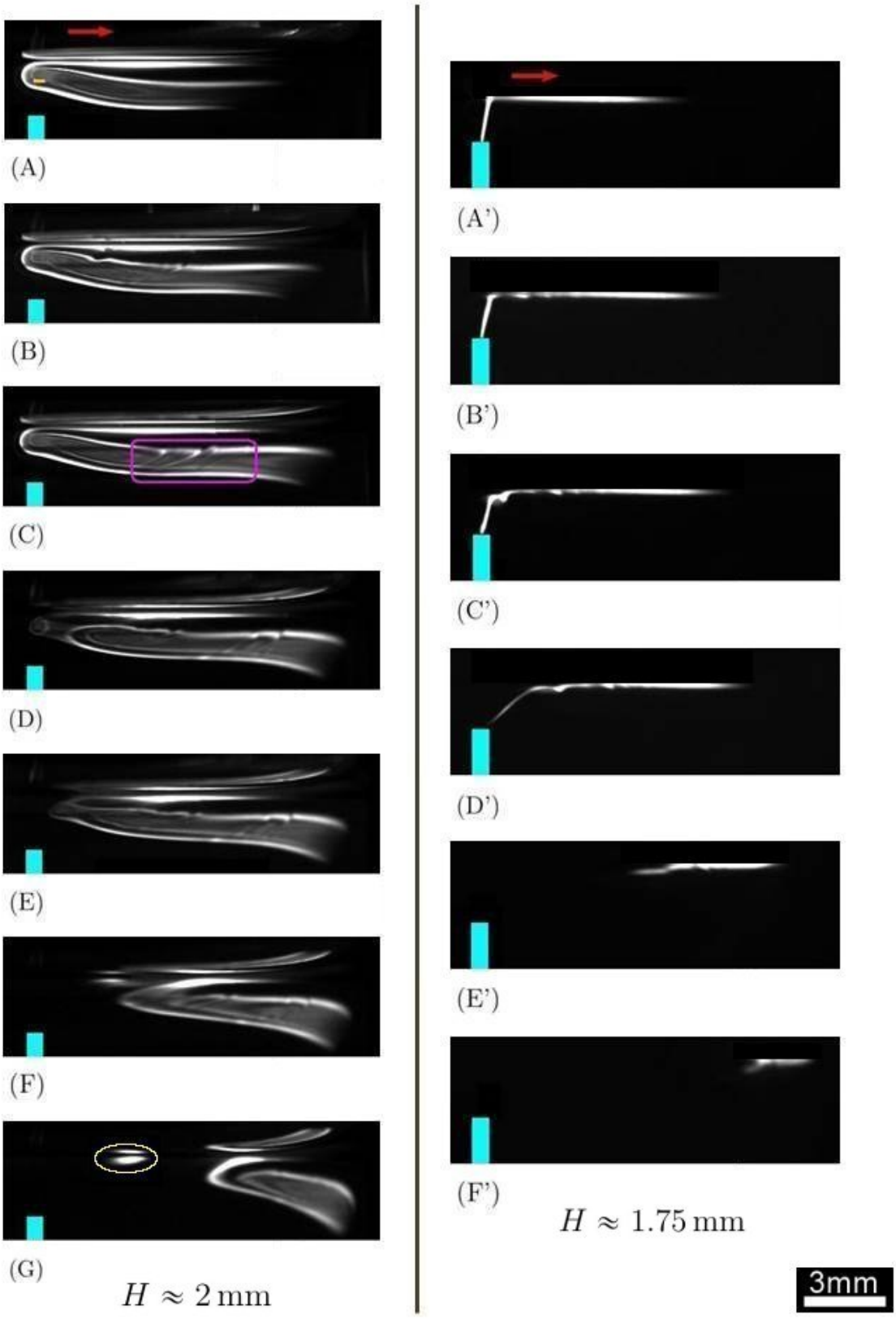

Figure 2.34: Fate of the coloured cloud in the reversed flow experiments (side views). The − sign denotes an anticlockwise rotation of the vortex above the injector (cyan tube). Arrows showing the flow direction. Gap H reported below each series of frames. $V_{\mathrm{inj}} \approx 5.5\,\mathrm{cm/s}$ ($\mathcal{C}_{\mathrm{SDS}} = \mathrm{CMC}/100$).

Aspiration experiments

Aspiration experiments are achieved in the small cell ($\varnothing\,35\,\mathrm{mm}$) at various gaps $H \approx 0.25, 1.25, 2.5...\,\mathrm{mm}$ and injection speeds $V_{\mathrm{inj}} \approx 1.75, 3.5, 5.25, 7...\,\mathrm{cm/s}$. Note that above a certain injection speed, *e.g.* $V_{\mathrm{inj}} = 7\,\mathrm{cm/s}$ at a gap $H = 2.5\,\mathrm{mm}$ (even less at smaller gaps), the drain tube turned into an injector expulses so intense a jet towards the surface that the aspiration flow is strongly perturbed, preventing us from studying it.

Contrary to injection experiments, aspiration flows exhibit no multipolar instability, whatever the values of the control parameters. No counter – rotating vortices are visible but a quasi – axisymmetric flow with slightly curved centripetal streamlines (Fig. 2.35).

The inertial drive of the dislocating coloured structure and the disparity between aspiration and injection flows suggest that the Reynolds numbers at play are not so small : Re $\sim$ 1 (resp. 10) for injection speeds of a few cm/s and the injector's radius $r_{\mathrm{inj}} = 0.275\,\mathrm{mm}$ as the length scale (resp. the gap $H \sim 1\,\mathrm{mm}$). In other words, inertial effects from the non – linear term $\mathbf{V}.\boldsymbol{\nabla}\mathbf{V}$ of the Navier – Stokes equation are not completely negligible. They are involved in the irreversibility of the flows. Still, we shall see in the next chapter that substantial grounds exist to believe that this instability is not inertial (in a model, inertial effects would be then set as 'higher – order corrective terms').

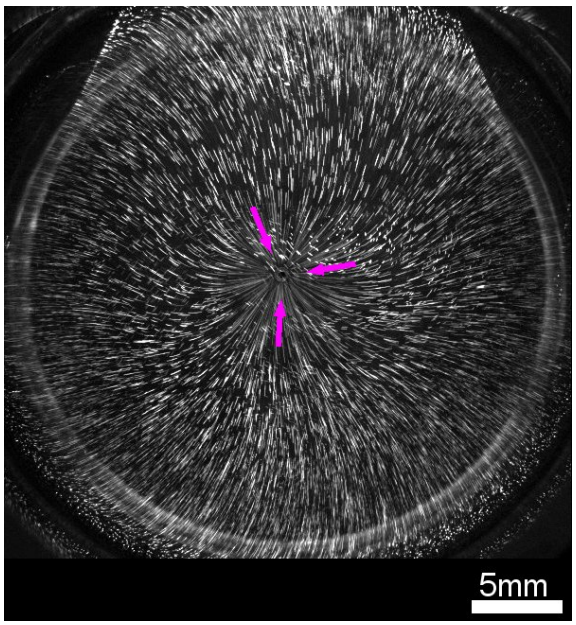

Figure 2.35: Aspiration flow (top view). Arrows showing the flow direction. Average frame from a stack of 1500 images (45 FPS $\rightarrow \Delta t \approx 33\,\mathrm{s}$). $H \approx 1.25\,\mathrm{mm}$, $V_{\mathrm{inj}} \approx 3.5\,\mathrm{cm/s}$ ($\mathcal{C}_{\mathrm{SDS}} = \mathrm{CMC}/100$).

2.6 Discussion

In this chapter, we presented a simple experiment that consists in a small subaquatic fountain generating a centrifugal radial flow at the water surface (Fig. 2.1).

The 3D morphology of the base flow observed at low injection speeds (and/or big gaps) is that of a polarised torus, namely a toroidal flow whose streamlines are oriented along a preferential direction (Figs 2.5 – 2.6). Factors that can induce this 'polarisation' (= departure from pure axisymmetry) of the base flow are at least of two types : (1) a parasitic temperature gradient between the cell boundaries; (2) geometric flaws.

(1) We call 'residual convection' the low thermocapillary flow, caused by a temperature gap ΔT between the cell sidewalls, that persists when injection is off. The Marangoni boundary condition, see Eq. (2.7), provides the after relation between orders of magnitude

$$\Delta T = \epsilon \frac{\eta}{\gamma_{\mathrm{T}}} U \,, \tag{2.3}$$

with U the velocity scale of the flow. The constant $\gamma_{\mathrm{T}} \doteq |\mathrm{d}\gamma/\mathrm{d}\Theta| \sim 10^{-4}\,\mathrm{N.\,m^{-1}.\,K^{-1}}$ [40] quantifies the variation of surface tension with the temperature. $\epsilon = \mathrm{d/h} \sim 1$ represents the ratio of the cell diameter $\mathrm{d} = 3.5\,\mathrm{cm}$ to the height $\mathrm{h} \approx 3\,\mathrm{cm}$ of liquid it contains. The dynamic viscosity of water is $\eta \sim 10^{-3}\,\mathrm{Pa.s}$. Given the velocities measured in the toroidal base flow (Figs 2.5 and 2.6), ranging from $U_{\mathrm{axi}} \sim 10\,\mu\mathrm{m/s}$ in the outer area of the vessel up to $U_{\mathrm{axi}} \sim 1\,\mathrm{mm/s}$ within the torus, Eq. (2.3) yields a temperature gap $\Delta T \sim 10^{-4} - 10^{-2}\,\mathrm{K}$. Such modest temperature gradients are commonplace in a room where no special care is taken to control the temperature. Parasitic convection is thus systematically present in our experiments and may influence the base flow as both are of comparable strength.

(2) Geometric flaws may also impact the polarisation of the base flow. For instance, a careful inspection of the injector outlet reveals a rough surface (Fig. 2.36). This may alter surface flows, especially at very small gaps $H \sim 0.1\,\mathrm{mm}$ for which the size of the injection nozzle (outer diameter $\varnothing 0.8\,\mathrm{mm}$) is strongly 'sensed' by the flow. At larger scales comparable to the cell size (inner diameter $\varnothing 35\,\mathrm{mm}$), the lack of verticality $\delta\theta$ of the injector biases the flow direction : turning the injector to reorient its tilt, we observe that the dipole symmetry axis is driven by the enforced rotation in most cases, albeit with some angular delay. At intermediate scales, the flow undergoes the combined effect of all these factors without the possibility of saying that one dominates the others.

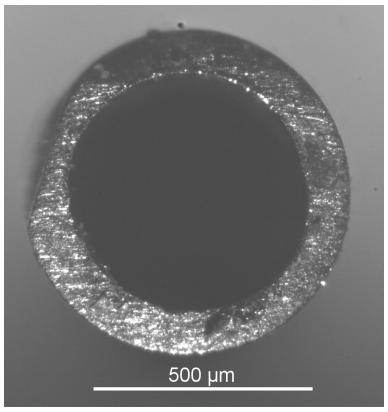

Figure 2.36: Microscopy image of the injection nozzle. The bevel on the left side of the injector's edges is caused by abrasion on a grinding wheel used to cut straight the point of a needle.

We have evidenced a linear growth of the torus diameter d_t with the gap H at different injection speeds V_{inj}, both in the absence of SDS and for a SDS solution at $\mathcal{C}_{\text{SDS}} = \text{CMC}/8$ (Figs 2.9 –2.10). Note that this linear behaviour has been observed over a large interval of gap values $1 < H < 11\,\text{mm}$. However, to be fully confirmed, this finding would deserve further experiments over a wider range of injection speeds (here $2.31 \leqslant V_{\text{inj}} \leqslant 3.74\,\text{cm/s}$).

The fact that the torus diameter increases linearly with the gap in the absence of SDS can be understood assuming an infinitely thin injection tube in an infinitely wide vessel. The gap H is then the only relevant length scale and the size of the injection torus is thus directly proportional to it. Yet a deviation from this linear behaviour is expected at very small gaps $H \sim 0.1\,\text{mm}$ comparable with the injector's radius $r_{\text{inj}} = 0.275\,\text{mm}$, but also at very big gaps $H \approx R$ (R is the radius of the vessel, $R = 17.5\,\text{mm}$), a scale at which the liquid enclosed in the cell experiences the presence of the boundaries (flow confinement). Therefore, the size of the flow patterns is properly measured in terms of the sole gap H provided the latter is neither too small nor too large. Unfortunately, for gaps $H \sim 0.1\,\text{mm}$, the torus is so small that it is not clearly recognisable on the pictures and hence its diameter cannot be correctly measured. Regarding very big gaps $H \approx R$, we simply did not examine such gap values.

It is instructive to introduce the Reynolds number Re. The latter, which compares the magnitudes of inertial and viscous forces, is defined as the following dimensionless ratio

$$\text{Re} \doteq \frac{Ua}{\nu}\,, \tag{2.4}$$

with a some characteristic length scale of the system, U a typical velocity scale, and $\nu \doteq \eta/\rho$ the water kinematic viscosity ($\nu \sim 10^{-6}\,\text{m}^2/\text{s}$ under standard temperature and

pressure, $T_{room} \approx 20°C$ and $P_{atm} \approx 1bar$). In the limit $r_{inj} \ll r \ll R$, the jet is regarded as spurting from a point source in a semi–infinite liquid. As mentioned above, the gap H is then the only relevant length scale and the velocity can be expressed under the simple form $v(r,z) = V_{inj}\,\Phi(r/H, z/H)$. Since $v = 0$ at a vortex centre, it ensues that $\Phi = 0$ regardless of V_{inj} , and this explains why the slopes of Figs 2.9–2.10 are independent of the injection speed (at least in the explored range). Still, this factorisation makes sense only in the purely viscous regime $Re = 0$. Indeed, if inertial effects were to influence the torus size, additional length scales would appear in the system. Taking U as the injection speed V_{inj}, and thus identifying a with the radius r_{inj} of the injector ($r_{inj} = 0.275\,mm$), the Reynolds numbers associated with the experiments of Figs 2.9–2.10 lie between $Re_{min} \approx 6.4$ and $Re_{max} \approx 10.3$. These non–negligible Reynolds numbers suggest taking inertial effects into account, however, the linear scaling of Figs 2.9–2.10 informs us that this is irrelevant as far as the torus size is concerned. Besides, it is not obvious why the torus diameter keeps behaving the same way with the control parameters in the presence of SDS, as the latter uneven distribution at the interface should introduce supplementary length scales.

Most interestingly, surface velocity measurements revealed a 'locked' interface in the quasi–axisymmetric flow regime (Fig. 2.28 – (a)).

The divergent flow at the interface proved very sensitive to azimuthal perturbations : when the jet is strong enough, the base torus turns into multipolar flows taking the form of counter–rotating vortex pairs periodically distributed all around the source [4, 5]. Note that a dipole emerges at the surface in our practical conditions (Fig. 2.13). The onset of the instability seems to be marked by a threshold $V_{inj}^{\star} \approx 1.3\,cm/s$, as suggested by the abrupt behaviour of 'order parameters' such as the maximum surface velocity (Fig. 2.25). Amazingly, the value of $V_{inj}^{\star}$ does not seem to depend on the gap (at least in the explored range $0.2\,mm \leqslant H \leqslant 2.5\,mm$). Velocity measurements on the dipole beyond $V_{inj}^{\star}$ have shown that the interface is now in a 'passing state' characterised by surface and subsurface tracer particles moving at the same speed (Fig. 2.28 – (c)).

The transition of the interface, from a 'locked state' in the quasi–axisymmetric base flow to a 'passing state' in the presence of a dipolar flow, can be considered the main finding of our water jet experiments. Such a phenomenon can be readily understood if we assume a surfactant–laden interface. This assumption is all the more natural as it is well known that water, having a high surface tension compared with most common liquids ($\gamma_{water} = 72.8\,mN/m$ at 20°C), gets easily contaminated by surfactant molecules from the ambient air, and presumably from an imperfect cleaning of the glassware [41].

But are the unfreezing of the interface and the onset of the multipolar instability two sides of the same coin characterised by a unique threshold speed ? This remains an open question. Finding a way to visualise in real time the distribution of surfactant molecules adsorbed at the water/air interface may be convenient to address this point.

The concentration Γ of insoluble surfactants obeys the advection – diffusion equation

$$\partial_t \Gamma + \boldsymbol{\nabla}_\parallel \cdot \left(\mathbf{V}_\parallel \Gamma \right) = D \nabla_\parallel^2 \Gamma, \tag{2.5}$$

where the projection of a vector $\mathbf{a}$ onto the plane of the interface ($z = 0$) is defined as $\mathbf{a}_\parallel \doteq (\mathbb{1} - \mathbf{e}_z \mathbf{e}_z) \,.\, \mathbf{a}$. D is the mass diffusion constant. The equilibrium concentration (*i.e.* in the absence of flow) is denoted Γ_0. While putting Eq. (2.5) in dimensionless form, a parameter quantifying the relative contribution of surfactant advection and diffusion naturally appears. The latter, called the (solutal) Péclet number Pe, is defined as

$$\mathrm{Pe} \doteq \frac{U a}{D} \,. \tag{2.6}$$

a and U are the same length and velocity scales as those appearing in the definition (2.4) of the Reynolds number. Experimentally, the latter are identified with the radius r_{inj} of the injector and the injection speed V_{inj}. The diffusion constant ranging from $D \sim 10^{-9}\,\mathrm{m}^2.\,\mathrm{s}^{-1}$ for smaller surfactant molecules, down to $D \sim 10^{-12}\,\mathrm{m}^2.\,\mathrm{s}^{-1}$ for bigger ones, very high experimental Péclet numbers $\mathrm{Pe} \sim 10^3 - 10^6$ ($r_{\mathrm{inj}} = 0.275\,\mathrm{mm}$ and $V_{\mathrm{inj}} \sim 1\,\mathrm{cm/s}$) are expected. Surfactant transport along the interface is thus advection – dominated.

While adsorbing at the water surface, surfactant molecules transform it into an 'elastic membrane' undergoing Marangoni stresses. In general, the surface tension γ decreases with a local increase in the surfactant concentration. The interfacial flow velocity and the surfactant concentration fields are coupled through the Marangoni boundary condition

$$\eta \frac{\partial v_r}{\partial z}\bigg|_{z=0} = \frac{\partial \gamma}{\partial r} \,, \tag{2.7}$$

where $z = 0$ marks the position of the interface assumed perfectly flat (sec. 2.5.2). This relation states that an inhomogeneity of surface tension induces a shear stress along the interface and hence a flow in the aqueous phase [32]. Interfacial stresses are conveniently discussed defining the surface pressure $\Pi(\Gamma) \doteq \gamma_0 - \gamma(\Gamma)$, with $\gamma_0 = \gamma(\Gamma = 0)$ the surface tension of the pristine interface. At low surface density, $\gamma(\Gamma) = k_B T \Gamma$ (k_B : Boltzmann constant, T : absolute temperature) according to the 2D ideal gas equation of state.

The accumulation of surfactants near the edges of the vessel causes the interface to stiffen. The challenge is then to quantify the competition between the enforced shear stress and the resisting elastic interface. Following [42], we define the surface compressibility β as the dimensionless ratio of viscous over surface tension gradient forces

$$\underline{\underline{\beta \doteq \frac{\eta V_{\text{inj}}}{E_0}}}\,, \tag{2.8}$$

where E_0 denotes the reference Gibbs elasticity at equilibrium.

Restricting the analysis to the stationary regime, and since surfactant transport is here advection – dominated $\text{Pe} \gg 1$, Eq. (2.5) integrated once yields

$$\boxed{v_r(r,0)\Gamma(r) = 0\,.} \tag{2.9}$$

This equation is reminiscent of the stagnant cap condition first considered by Levich [10] in the context of the buoyant motion of a bubble rising in a liquid [43, 44] : due to the external flow on the rising bubble's sides, surfactants are driven down to its trailing pole where they accumulate and rigidify the bottom part of the bubble's surface, resulting in a 'stagnant cap' that drastically slows down the ascending motion of the bubble.

Two distinct flow regimes ensue from the solving of Eq. (2.9) : (a) the compressibility β is small enough so that the surfactant concentration remains finite everywhere; (b) either the velocity or the concentration vanishes in some region of the interface (see [45]).

In situation (a), Eq. (2.9) comes down to

$$v_r(r,0) = 0\,, \quad \forall r\,, \tag{2.10}$$

meaning that, at low β, the interface appears as stiff as a wall so that it remains perfectly still despite the ongoing bulk flow.

In case (b), we are naturally led to assume the existence of a critical radius r_d which marks the border between a surfactant – depleted inner region ($r < r_d$) and a rigid outer region ($r > r_d$), *i.e.*

$$\Gamma(r) = 0\,, \quad 0 \leqslant r < r_d\,, \tag{2.11a}$$

$$v_r(r,0) = 0\,, \quad r > r_d\,. \tag{2.11b}$$

This theoretical prediction of two interfacial regimes well separated by a crossover value $\beta_{\text{cross}} = 1$ echoes our observations. At low injection speeds $V_{\text{inj}} < V_{\text{inj}}^{\bigstar}$, the interface

behaves as a rigid wall imposing a no–slip boundary condition (= 'locked' state). But as soon as $V_{\text{inj}} > V_{\text{inj}}^{\star}$, the shear stresses induced by the centrifugal forced flow overcome the elastic resistance of the contaminated interface. The no–slip constraint is suddenly released, resulting in a jump of the surface velocity from zero to a finite value (= 'passing' interface). It is this 'unlocked' axisymmetric flow state that we believe is unstable. We think that the edge of the surfactant–free region does not remain circular while subject to azimuthal disturbances. The unjamming of the interface probably takes place along a preferential direction, which results in the formation of a pair of counter–rotating vortices (keep in mind that the mirror symmetry axis of the dipole does not necessarily coincide with the polarisation axis of the toroidal primary flow, see for example Fig. 2.11–(g)).

Assuming that the surfactant elastic layer behaves as a 2D ideal gas in the dilute regime $\Gamma \ll \Gamma_\infty$ (Γ_∞ is the concentration at saturation defined through the finite area occupied by individual surfactant molecules), for which $E_0 = k_B T \Gamma_0$, the condition $\beta_{\text{cross}} = 1$ leads to the following expression of the crossover surfactant concentration Γ_{cross}

$$\Gamma_{\text{cross}} = \frac{\eta V_{\text{inj}}}{k_B T} \ . \tag{2.12}$$

Considering an injection speed $V_{\text{inj}} \sim 1\,\text{cm/s}$ yields $\Gamma_{\text{cross}} \approx 2400\,\text{molecules}/\mu\text{m}^2$, a minute quantity comparable with that invoked by Hu and Larson to account for the suppression of Marangoni flows in evaporating droplets [46]. Note that such a small surface coverage induces a drop in the surface tension that lies far below the measurement accuracy of standard tensiometers ($\pm 1\,\text{mN/m}$ in our case). Given a maximum packing concentration in the order of 10^6 molecules/μm^2 [47], we are in the limit $\Gamma_{\text{cross}} \ll \Gamma_\infty$ which justifies why emphasis is put on the dilute regime. Even traces of surfactants are therefore sufficient for a transition from no–slip to slip conditions to occur at the interface [16, 18, 44, 48].

A prospect for upcoming works is to figure out theoretically the relationship between the occupancy rate of the interface by surface active molecules, the size of the injection torus, and the instability threshold which directly depends upon the surface elasticity. In this manner, the concentration of surfactant molecules adsorbed at the interface can be indirectly deduced from the torus dimensions, making our water jet setup an ultra–sensitive hydrodynamic probe of traces of surfactants at a water/air interface [45, 48].

There exist in the literature systems falling within the same class as ours, namely systems involving pressure–driven divergent flows that repel some elastic layer formed by surfactant molecules. For instance, Couder *et al.* [49] observed a quadrupolar flow on the surface of a soap film blown by a vertical air jet. The resemblance with our own water jet

experiment is obvious. The authors do not develop any theory of this phenomenon but make valuable comments on the competition between the jet – induced centrifugal flow and the Marangoni counterflow arising from the accumulation of surfactant molecules in the outer region of the film. We think that this competition between conflicting flows exists in our system and that it leads to the multipolar instability we observe. Another example is the work by Liger – Belair *et al.* [50, 51] on ascending bubble driven flow patterns in champagne glasses. Strikingly, self – organising 2D convective cells were evidenced at the surface of champagne as an ascending column of bubbly liquid was impinging the surface. The liquid column is created by a laser – etched ring at the bottom of the champagne flute which acts as a bubble generator thanks to its many nucleation sites.

To finish, we should mention a slightly different class of 'divergent flow generators' that enforce Marangoni flows. One can cite for example the works by M. Roché *et al.* [6, 7]. The authors would continuously deposit a small amount of a hydrosoluble surfactant at the water/air interface through a thin needle in contact with the surface, unlike us who inject 'pure water' with a tube lying at a short distance underwater. They would observe many vortices forming a corona far from the injection site (Mizev *et al.* [5] reported similar observations while reproducing Pshenichnikov and Yatsenko's experiment [4]). We may wonder to what extent such vortical patterns are connected with the multipolar flows we observe, as in our case a 'pure water jet' sweeps away some preexisting surfactant layer, whereas the surfactant – enriched jet is itself the source of a Marangoni flow.

In the next chapter, we present what we call the 'hot bead experiment' which is an alternative way of creating a divergent interfacial flow by heating an absorbing microbead in partial wetting at a liquid surface. Unlike in the case of the water jet experiment for which a centrifugal forced flow is generated pushing 'mechanically' on the liquid surface, we now consider a thermally driven Marangoni flow. We shall see that this *a priori* more complex system produces similar multivortex flow patterns as the bead is increasingly heated, much like what is observed while increasing injection in the water jet experiment.

Chapter 3

The hot bead experiment

A motionless hot bead sits in partial wetting across the water (W)/air interface (A) (Fig. 3.1). The temperature gradient arising in the vicinity of this heat source induces a local decline of the surface tension γ. The ensuing surface tension inhomogeneities are accompanied by the emergence of shear stresses along the interface that put the fluid into motion : an outward thermocapillary flow appears that tends to rub out the surface tension disbalance. In other words, this hot spot serves as a fixed source of divergent flows at the water/air interface, just as the water jet presented in chapter 2.

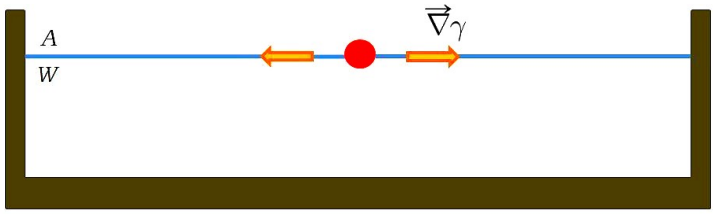

Figure 3.1: Schematic layout of the hot bead experiment.

Our main tunable parameter is the heating power $\mathcal{P}$ ranging from a few milliwatts up to a few tens of milliwatts. The heating power $\mathcal{P}$ plays here a role analogous to the one the injection speed V_{inj} plays in the water jet experiment. The size of our bead slightly varies from one experiment to another around the typical diameter $\varnothing_b \approx 295\,\mu$m.

In this chapter, I first present our fully instrumented and tunable hot bead device. Then I review some of the flow patterns arising as the bead is heated to varying degrees. Finally, I discuss the experimental observations.

3.1 Materials and methods

3.1.1 Experimental setup

Preparation of the samples

Our cell is a quartz cuvette purchased from Thuet France (Fig. 3.2). Opting for quartz is justified by its high visible light transmission along with its resistance to sulfochromic acid $H_2SO_4 - (K_2/Na_2)Cr_2O_7$, a very corrosive substance used to strip the impurities that settle on the cell walls. As we shall see, the uttermost responsiveness of the water surface to surfactant contamination strongly impacts the flow patterns. This is why great care is paid in cleaning the cuvette. After a few hours bathing in sulfochromic acid, the cuvette is thoroughly rinsed with pure water supplied by a Millipore Elix 10 purification system. The cuvette is then filled with ultrapure water (resistivity 18.2 MΩ.cm at 25°C, TOC : 3 ppb) from a Millipore Milli-Q A10 Gradient purification system. To slow down the adsorption of air contaminants on the water surface, a plate drilled with a 12 mm circular hole is placed a few millimeters above the interface (Fig. 3.6).

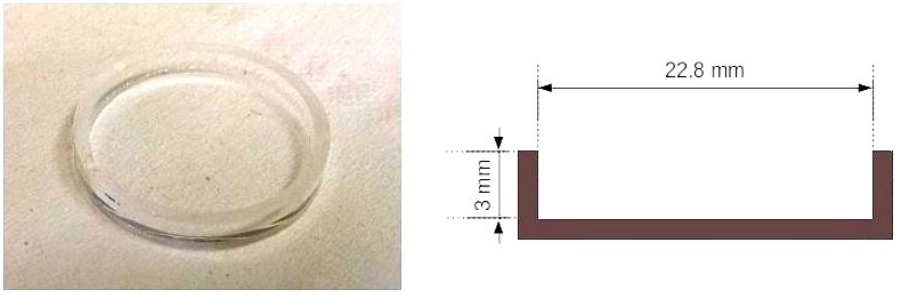

Figure 3.2: Quartz cuvette. On the left, photograph of a quartz cuvette used as the experimental cell. On the right, schematic layout of a cross−section of the cuvette with its main dimensions. *Images selected from A. Mombereau's internship report.*

Hot sphere and heating system

A carbon bead ($200 \leqslant \varnothing_b \leqslant 300\,\mu$m) is stuck onto the end of an optic fibre stripped up to the cladding (see Appendix H for a presentation of the bead collage setup). Carbon is prized for its capacity to absorb the incident laser light while resisting photodegradation. We use a single−mode fibre (F-SA-C Newport) with a 488−633 nm operating range. This fibre guides a 532 nm green laser beam generated by a Quantum Opus source towards the surface of the bead so as to heat it up. A fibre optic coupler (Thorlabs) ensures efficient

light transmission. The maximum power delivered at the fibre inlet is $\mathcal{P}_{\text{in}}^{\max} \approx 650\,\text{mW}$. Above this value, there is a risk of damaging either the fibre or the sphere. Because of transmission losses within the fibre, we roughly estimate that its output efficiency amounts to only $\epsilon \approx 20\%$ of the input power $\mathcal{P}_{\text{in}}$. The latter value is obtained through measuring with a power meter (model SP404 from Spectra–Physics equipped with an attenuator having a calibration range $[2, 50]\,\text{mW}$ and ahead of which we add a light diffuser) the power of the divergent laser beam fanning out from the optic fibre at an angle of approximately 30°. Hence, the bead absorbs at most a power $\mathcal{P}^{\max} = \epsilon\,\mathcal{P}_{\text{in}}^{\max} \approx 130\,\text{mW}$. However, we cannot infer from the sole estimation of the fibre efficiency what is the power effectively heating the bead due to parasitic reflections of the incident light.

Bead – water contact

In order to minimise the number of factors influencing the system, we endeavour to keep the interface as plane as possible: the cuvette is prefilled to the brim and liquid is then removed up to the moment squares on a grid paper seen through the liquid surface appear undistorted. The smooth pinning of the meniscus on the cuvette edges results in a flat interface at large distances from the source. Next, to orient the fibre axis perpendicularly to the interface while passing through the lid, the fibre is bent using a sewing thread tied around its coating and stretched (adjustable tension) between the latter fixture point and the fibre mounting plate (Fig. 3.3).

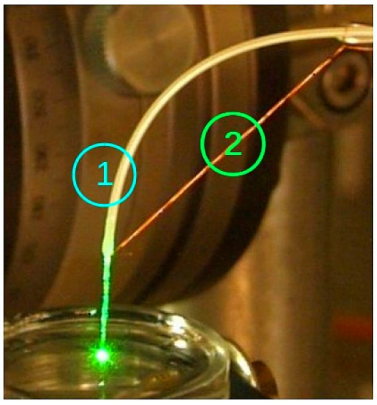

Figure 3.3: Bending the optic fibre. (1) optic fibre; (2) sewing thread of adjustable tension. *Image selected from A. Mombereau's internship report.*

The bead is displaced with a manual xyz translation stage till being partially immersed in water. Contrary to a free particle that would self–position across the surface in such a way that the interface remains flat in its vicinity, the tension the fibre exerts upon the

bead leads to the formation of a meniscus that wraps the sphere (Fig. 3.4). Here again, to restrict the number of physical parameters, we shall approach a perfectly planar interface which necessitates getting rid of such a steep meniscus.

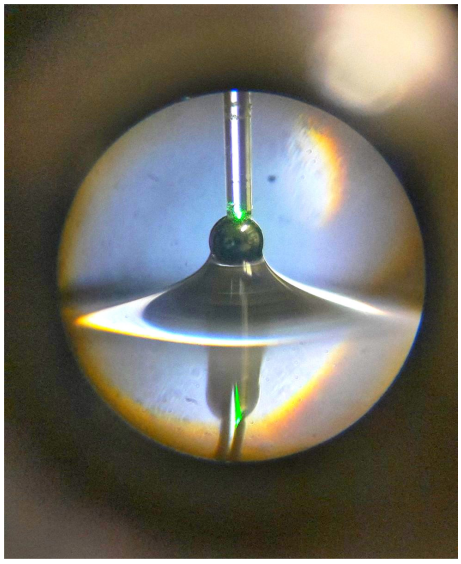

Figure 3.4: A partially wetted microbead stuck onto the end of an optic fibre.

A ring encrusted with light−emitting diodes (see Fig. 3.6 below), positioned under the cuvette, appears on the computer screen as a luminous circle whose radius is related to the deformation state of the meniscus (Fig. 3.5). In fact, due to intense evaporation at the contact line, the meniscus gets hollower and the circle hence grows as time goes by. As a practical consequence, the experimenter must repeatedly make sure that the meniscus remains as flat as possible by reducing the radius of the circle until the light spots are all brought together behind the bead. Note that any accidental detachment of the bead from the surface would be signaled by the complete absence of this luminous circle.

Aligning the aiming line of the side camera with the flow symmetry axes is essential to construe the bulk flow structure properly. Therefore, a spinning mechanism must be implemented. However, only due to lack of space, the solution adopted was not as simple as grouping together in a single block the ensemble {vertical laser sheet + side camera} like in the water jet experiment. Finally, the idea was to rotate the optic fibre with the bead stuck onto it, this unit resting on a circular guide rail (angular excursion $\Delta\theta_{\mathrm{exc}} \approx 90°$), while keeping fixed the position of the side camera (see Fig. 3.6 below).

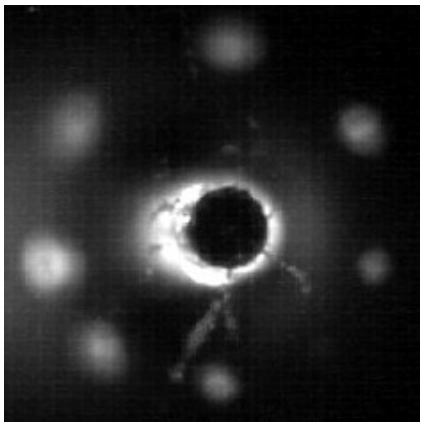

Figure 3.5: Image of the LEDs on the computer screen. Here we can see the 'light mark' the ring of LEDs leaves on the screen while reflecting on the water surface acting as a mirror. The bead is the dark disk well visible in the middle.

Flow visualisation

The small volume $V \approx 1.2\,\mathrm{mL}$ of solution filling the cuvette is seeded with exactly the same tracer particles as in the water jet experiment (fluorescent polystyrene microbeads, $\varnothing 5.1\,\mu\mathrm{m}$). A couple of laser sheets powered by a 514 nm green laser source (Genesis CX 514 – 2000 STM from Coherent, maximum output power : 2W) ensures flow visualisation. A beamsplitter (Melles Griot) divides the incident laser beam into two secondary beams passing through combinations of cylindrical lenses. Our setup is thus made of two 'optical channels' generating a horizontal and a vertical laser sheet (thickness $e \approx 50\,\mu\mathrm{m}$), exactly as in the water jet experiment (Fig. 3.7).

The lighting power is directly tuned on the supply system and the relative intensity of each laser beam is adjusted with a half – wave plate put right before the beamsplitter. To ensure an optimal operating efficiency of the ensemble $\{\lambda/2$ retarder + beamsplitter$\}$, a quarter – wave plate is added so as to restore a linear polarisation of the incident light, the latter being in general elliptically polarised at the fibre outlet (Photonetics Finnova single – mode optic fibre). A plane – parallel plate ensures an up – and – down translation of the horizontal laser sheet while a circular plane mirror redirects the vertical laser sheet towards the sample. Adjusting the tilt of the mirror relative to the cuvette, one achieves an approximate translation of the vertical laser sheet. In order to incrementally displace the laser sheets, both the plane – parallel plate and the mirror are mounted on Thorlabs CR1/M motorised continuous rotation stages actuated by TDC001 T – Cube DC servo motor controllers (software 'APT User'). Note that for the horizontal laser sheet to travel a vertical distance $\Delta z = 3.5\,\mathrm{mm}$ within one minute, the rotation stage should rotate at a

constant angular speed $v_{\mathrm{rot}} \approx 0.4^\circ/\mathrm{s}$ ($\Delta\theta/\Delta z = 7^\circ/\mathrm{mm}$). In the same spirit, the mirror should rotate at $v_{\mathrm{rot}} \approx 0.062^\circ/\mathrm{s}$ as a rotation by an angle of $\Delta\theta \approx 3.5^\circ$ is needed to travel in one minute the $\Delta x = 12\,\mathrm{mm}$ circular aperture of the lid ($\Delta\theta/\Delta x = 0.29^\circ/\mathrm{mm}$).

The horizontal laser sheet allows the experimenter to acquire cut views of the flow structure at various depths while the vertical laser sheet provides cross–sectional views. Actually, this second laser sheet which travels from one end of the cuvette to the other is never rigorously vertical but slightly inclined, the whole setup being tuned in such a way that the laser sheet approaches perfect verticality as it gets closer to the bead. Indeed, the obstruction by the optic fibre located in central position prevents us from performing diametral sections of the flows. Horizontal and vertical views of the flows are alternately captured thanks to a couple of remotely–activated homemade beam stops, each beam stop assuming only two positions 0/1. We take advantage of this attribute to block either one or the other optical channel. The quality of the side views, impaired by astigmatism issues stemming from the curvature of the cuvette, is enhanced using a correction lens (focal length $f240$), a trick that has already proven effective in the water jet experiment. The quality of the images, even it is moderate, suffices to uncover the flow morphology. A technical description of the cameras used to record the flows can be found in Appendix G.

Figs 3.6 and 3.7 both provide schematic layouts and photographs of the ‘hot bead setup’ described above.

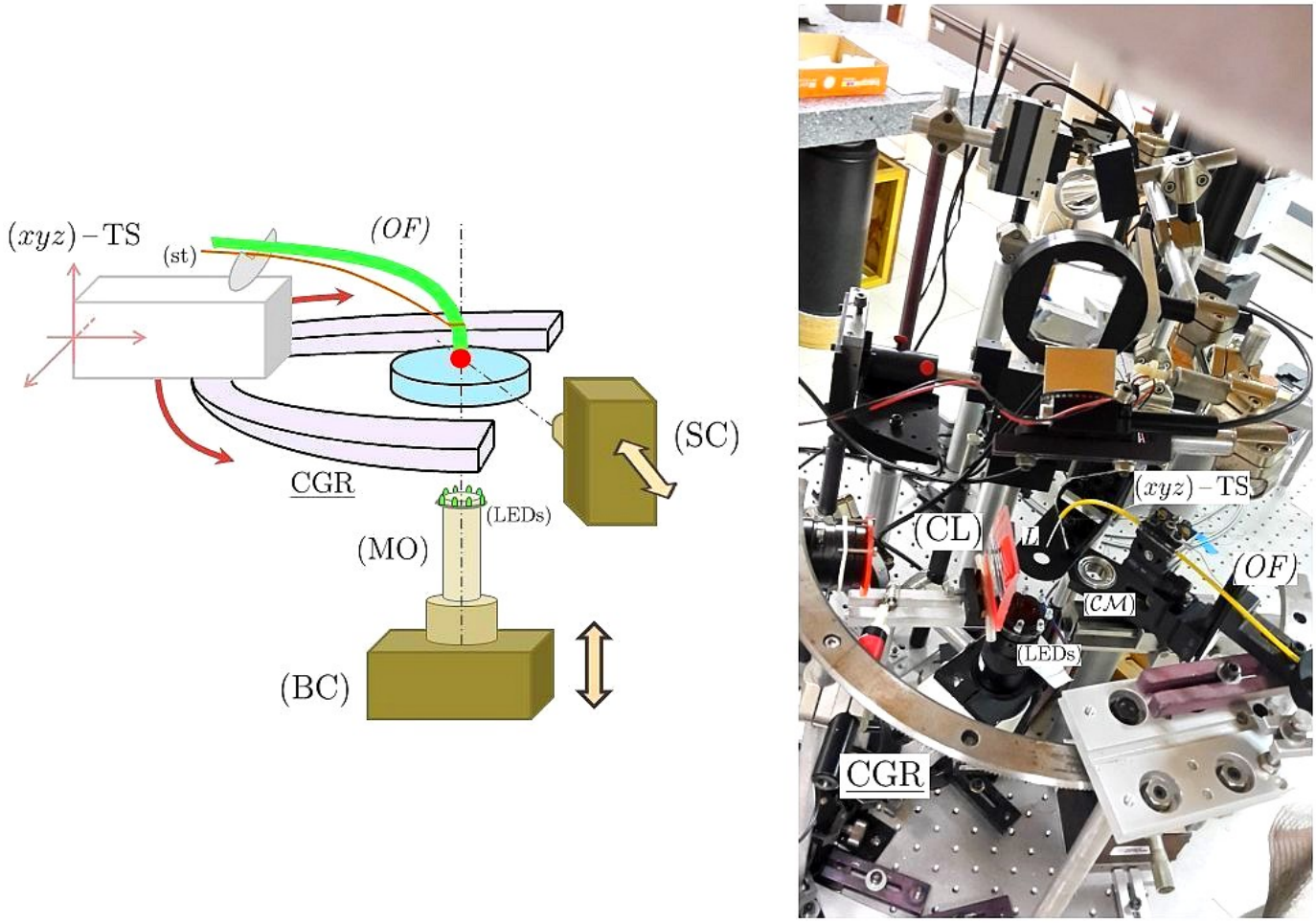

Figure 3.6: The core of the 'hot bead setup'. (*Left figure*) Schematic of the central part of the device (not to scale). {*(OF)* + (st)}, optic fibre + sewing thread (adjustable tension); CGR circular guide rail; $(xyz)-$TS, xyz translation stage; {(BC) + (MO)}/(SC) bottom camera + microscope objective/side camera; (LEDs) ring encrusted with light−emitting diodes. (*Right figure*) Photograph under actual operating conditions. Same abbreviations plus $(\mathcal{CM})$ cuvette mounting; L lid; (CL) correction lens.

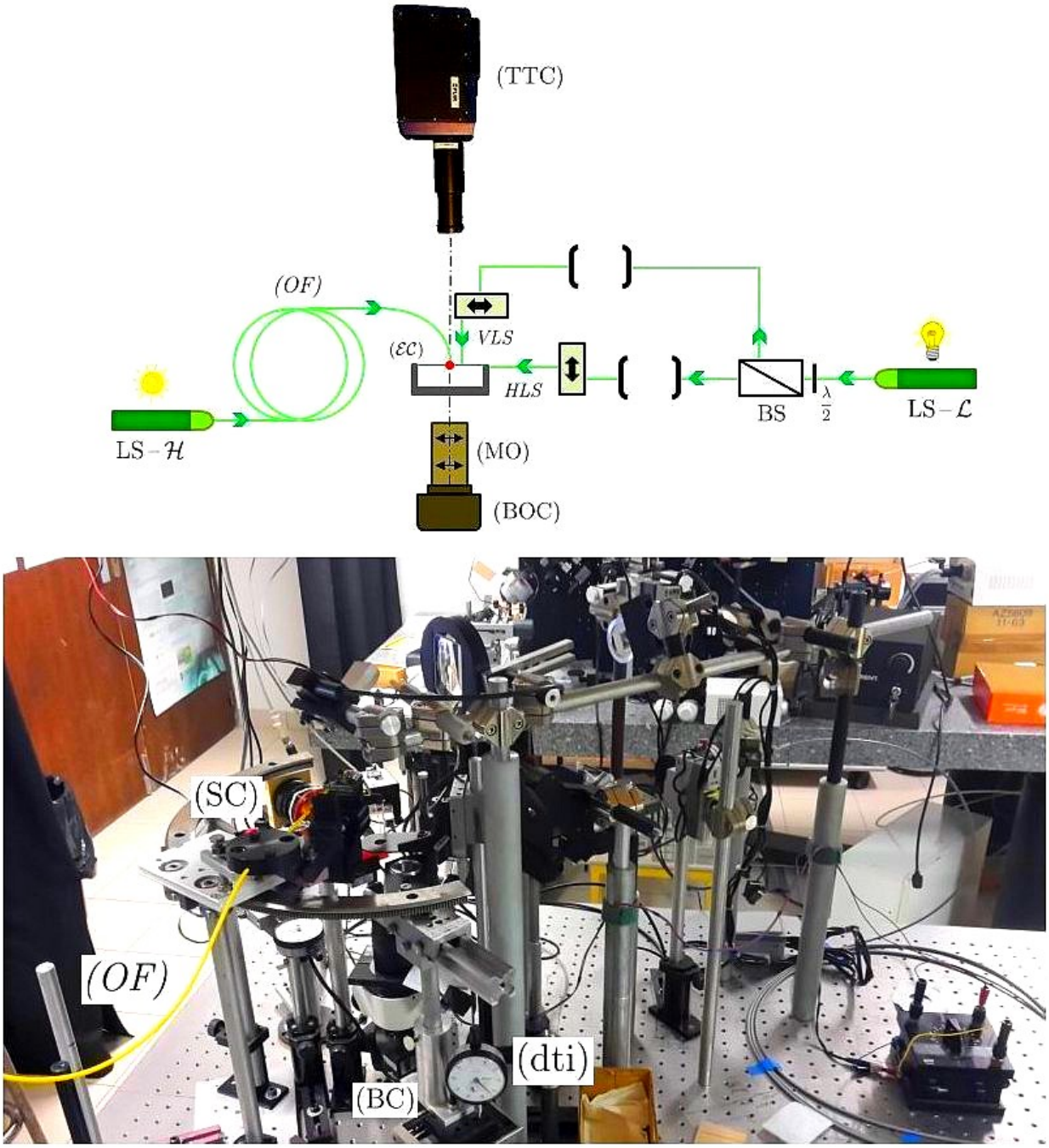

Figure 3.7: Global view of the 'hot bead setup'. (*Top figure*) Schematic of the device (not to scale). ($\mathcal{EC}$) experimental cell; *(OF)* optic fibre; LS$-\mathcal{H}$ and LS$-\mathcal{L}$, laser sources for heating ($\mathcal{H}$) and lighting ($\mathcal{L}$); *HLS*/*VLS*, horizontal/vertical laser sheet; $\{\lambda/2 + \text{BS}\}$, half$-$wave plate + beamsplitter; {(BOC) + (MO)}, bottom optical camera + microscope objective; (TTC) top thermography camera. (*Bottom figure*) Photograph of the setup under actual operating conditions. (BC)/(SC) bottom/side camera; (dti) dial test indicator. For clarity, the after components are not sketched : the automation system of the laser sheets, the position indicators, the filters, the control microscope, the quarter$-$wave plate. Optical channels schematised as brackets. The 'horizontal' optical channel consists of the series of components {(beam stop) + 2 cylindrical lenses + plane$-$parallel plate} and the 'vertical' channel of {(beam stop) + fixed mirror + 2 cylindrical lenses + automatised swivelling mirror}.

3.1.2 Thermography

Here I introduce our thermography experiment presenting first its goal and then the device we use. The interested reader is referred to the reference book [52] for an excellent course on the basic principles of infrared thermography and its wealth of applications.

Goal of the experiment

Given the small–scale thermocapillary flows investigated in the present work, we suspect thermal advection rather than inertia to be at the origin of the multipolar instability. The basic idea is that the flow influences the temperature field which in turn modifies the flow etc ... this mechanism self–amplifying until the onset of the instability. We thereby use thermography with the aim of probing 'hydrothermal' coupling effects. Temperature maps will be superimposed on streamlines views characteristic of different flow states. Information about how strong thermal advection is in each hydrodynamic environment will be inferred from the relative orientation between the streamlines and the isotherms. We are also searching for some symmetry–breaking in the thermal signal that would be closely correlated to the flow symmetry–breaking and therefore to the instability.

Note that our aim is not to measure absolute temperatures at any point of the surface, which calls for a blackbody–based calibration. We focus on temperature gradients, so even if the temperature values are somewhat erroneous it does not matter for our purposes. What is more, errors on the actual temperature values are 'systematic' (not random).

Thermographic device

The layout {optic fibre + bead} offers the opportunity to capture both the temperature and the flow fields in the course of a single experiment, contrary to earlier configurations. Indeed, the bottom of the cuvette as well as the liquid layer being highly IR absorbing media, any recording of the interfacial temperature field from below is doomed to failure. From above, however, we are facing another issue : while using fine metal tips as heat sources, the thermography camera is 'blinded' by the parasitic IR signal emitted by the imperfectly insulated heating resistor attached to the needle. This is not the case of our new configuration {optic fibre + bead} that confines heating solely to the source.

We borrowed from H. Kellay (*Laboratoire Ondes et Matière d'Aquitaine, UMR5798*) a highly sensitive and versatile IR camera, the FLIR SC7600 model (pixel resolution 640×512, dynamic range 14 bit ; spectral band $1.5 - 5.1\,\mu$m ; NETD : Noise Equivalent

Temperature Difference $< 20\,\mathrm{mK}$, with a temperature measurement accuracy $\pm 1°\mathrm{C}$) (see Fig. 3.7 above). We equipped this camera with a medium – wave infrared (MWIR) macro lens having a long working distance $d \approx 250\,\mathrm{mm}$ and a 1/3 lens magnification that allows for imaging a $3.3 \times 2.8\,\mathrm{mm}$ object on the sensor (scale : $11.20\,\mu\mathrm{m/pix}$). The acquired data are processed using the software 'FLIR tools'.

In sum, our full setup comprises the EO/PCO camera to capture views of the surface streamlines placed in bottom position, plus the FLIR camera to image the interfacial temperature field placed in top position. Because the IR camera is located on the vertical laser sheet's path to the sample, we cannot capture simultaneously cross – sectional views of the streamlines and surface temperature maps in our experimental configuration.

3.2 An overview of the multiple flow patterns

3.2.1 From a torus to a family of multipolar patterns

We now describe the different flow patterns arising as the bead is increasingly heated. Unsurprisingly, the base flow (bf) which emerges under slight heating conditions, namely for heating powers $\mathcal{P}_{\mathrm{bf}} \sim 1\,\mathrm{mW}$, takes the form of a torus extending over the whole width of the cell (Fig. 3.8). Seen from the surface, the latter appears as a centrifugal radial flow with a myriad of divergent streamlines (magenta arrows) surrounding the source up to a finite distance. In the bulk, these streamlines self – organise into a pair of counter – rotating convection rolls centred on the axis of the source, with an ascending column of accelerated liquid between them (yellow arrow). Thus the hot bead generates a base flow whose 3D structure is similar to that induced by the water jet presented in chapter 2.

Departing from the ideal case of the theory (see next chapter), the real interfacial streamlines are not strictly radial but slightly curved yet at very low heating powers. This 'polarisation effect', analogous to the one reported in the water jet experiment, tends to get more pronounced for stronger heating. Just like what happens as the jet strengthens, the quasi – axisymmetric flow destabilises into multipolar patterns (Fig. 3.9) as soon as heating is sufficiently intense, typically for powers $\mathcal{P}_{\mathrm{mf}} \sim 10\,\mathrm{mW}$ (mf : multipolar flows). We expect the total number of azimuthal cells to increase monotonically with increasing temperature of the source, but the practical reality turns out to be more intricate than this simple vision (see sec. 3.2.2). Interestingly, two types of quadrupolar patterns are visible on Fig. 3.9, the second being less symmetrical than the first 'square – shaped' one. Also note that the size of each vortex pair may frequently change over time.

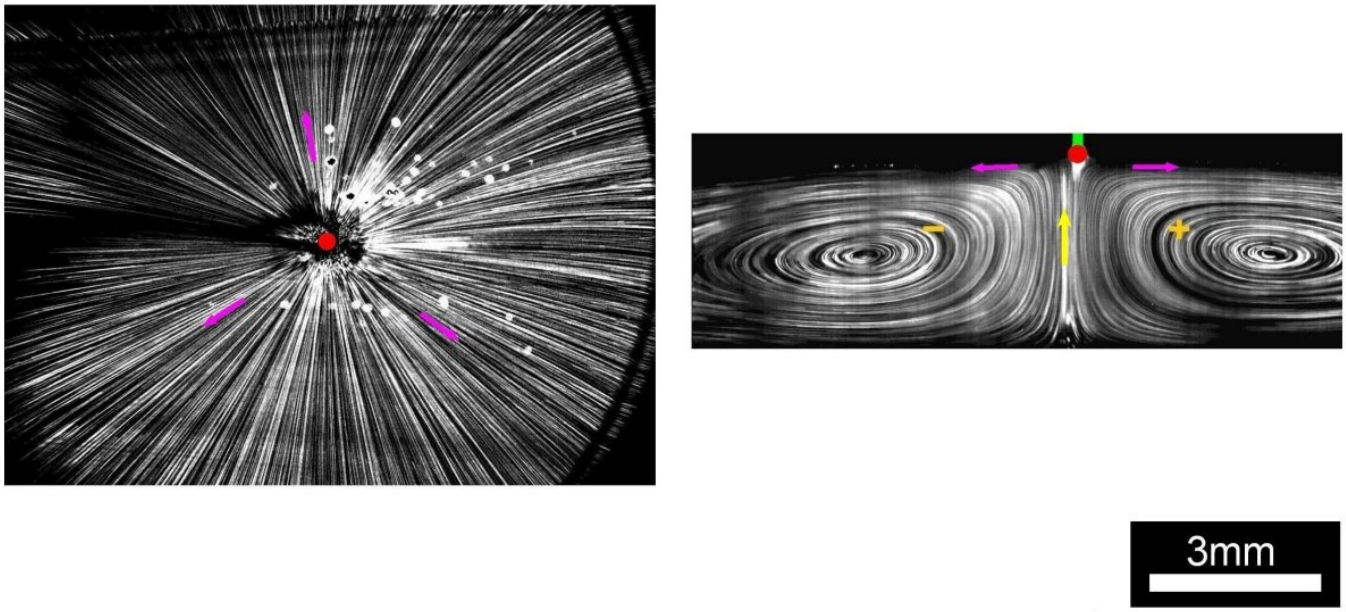

Figure 3.8: The toroidal base flow. (*Left image*) View of the centrifugal surface flow. (*Right image*) Cross−section of the torus showing a pair of counter−rotating convection rolls. Clockwise (resp. anticlockwise) vortex rotation marked by an orange + (resp. −) sign. Hot bead spotted as a red disk (approximate position). Heating power: $\mathcal{P} \sim 1\,\mathrm{mW}$. Scale common to both views: $10\,\mu$m/pix.

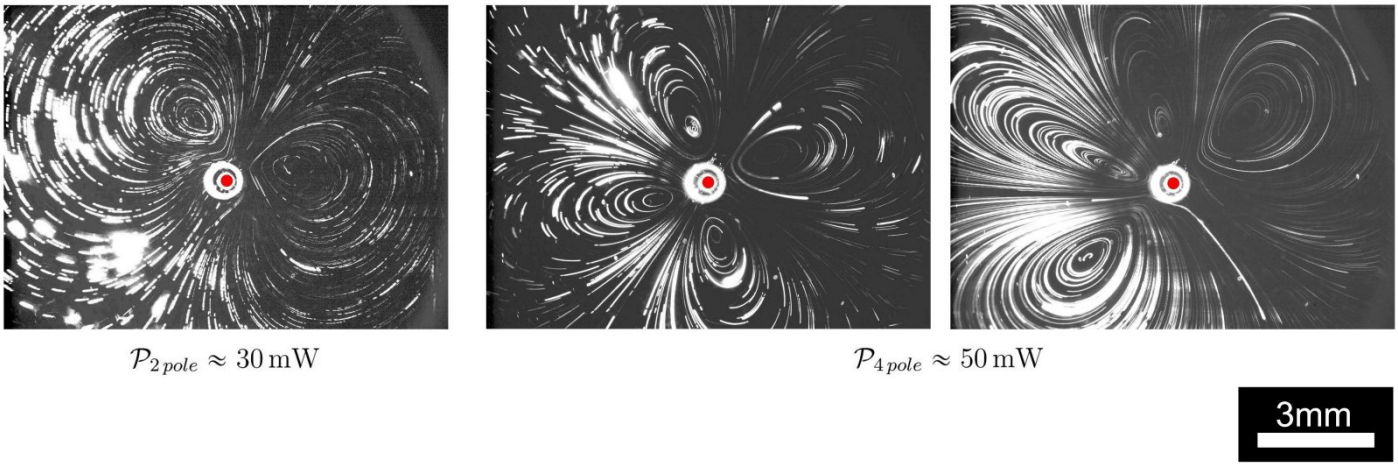

Figure 3.9: Examples of multipolar surface flows. (*From left to right*) Interfacial dipole followed by two types of quadrupoles. The approximate heating powers at which we observe these flow patterns are indicated below the pictures. Both quadrupoles arise within a few milliwatts power window centred on the value 50 mW. Hot bead ($\varnothing_b = 335 \pm 10\,\mu$m) spotted by a red disk.

3.2.2 The unpredictability of the flow state

Here we put the accent on the unpredictability of the flow state. Figs 3.10 and 3.11 display sequences of flow patterns that emerge at the interface as the heating power is increased from $\mathcal{P}_1 \approx 4\,\mathrm{mW}$ to $\mathcal{P}_2 \approx 60\,\mathrm{mW}$, and next decreased from $\mathcal{P}_2$ to $\mathcal{P}_1$, at a rate $\dot{\mathcal{P}} = \pm\,1\,\mathrm{mW/min}$. Surface flows are recorded at a rate of 2 frames per second, all the pictures shown resulting from averaging over $\Delta t = 25\,\mathrm{s}$.

Counterintuitively, the multipolarity of the flow patterns does not always burgeon with increasing heating: for instance, seeing a quadrupole followed by a dipole at a higher power is not so rare (*e.g.* transition $(c) \rightarrow (d)$ on Fig. 3.10). Furthermore, sharp power thresholds separating the different flow regimes do not seem to exist (hence the interval boundaries on the friezes are approximate). Only can we state that the quasi–axisymmetric base flow develops at typical powers $\mathcal{P}_{\mathrm{bf}} \sim 1\,\mathrm{mW}$ whereas multipolar flows arise at $\mathcal{P}_{\mathrm{mf}} \sim 10\,\mathrm{mW}$. Rather stable phases are interspersed by transient states, the number of azimuthal cells (and/or their size) fluctuating rapidly in a way that recalls mode competition (*e.g.* transitions $(e) \rightarrow (f)$, Fig. 3.10 and $(a') \rightarrow (b')$, Fig. 3.11), a core concept in the study of dynamical systems. What is more, these 'power–up' and 'power–down' sequences reveal discrepancies in the 'hydrothermal history' of the system, the sequence at decreasing power not being a 'film rewind' of the evolution at increasing power. Besides that, for a given heating power, you may observe a dipole in the morning but a quadrupole in the afternoon, and even something else the next day! This great spatiotemporal variability of the flow patterns is briefly discussed in sec. 3.6.

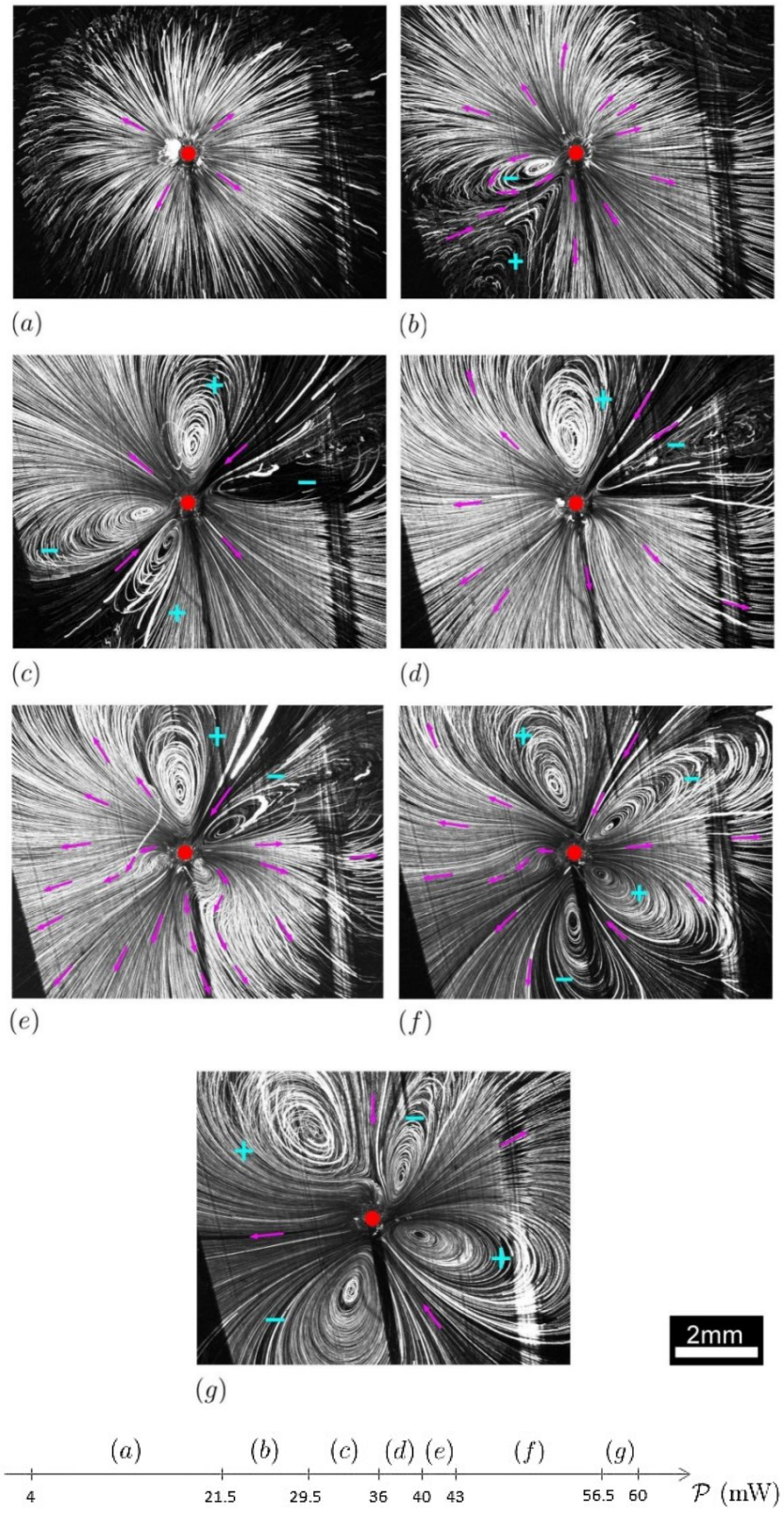

Figure 3.10: Sequence of surface flow patterns arising with increasing heating. (*Upper part*) Bottom views of surface flow states denoted $(a), (b) \ldots (g)$. Hot bead ($\varnothing_b \approx 295\,\mu$m) sketched by a red disk. Arrows of arbitrary length show the flow direction. The + (resp. −) sign denotes clockwise (resp. anticlockwise) vortex rotation. Bead's drop shadow forming a dark strip. (*Lower part*) Frieze giving the power range over which each interfacial state is observed.

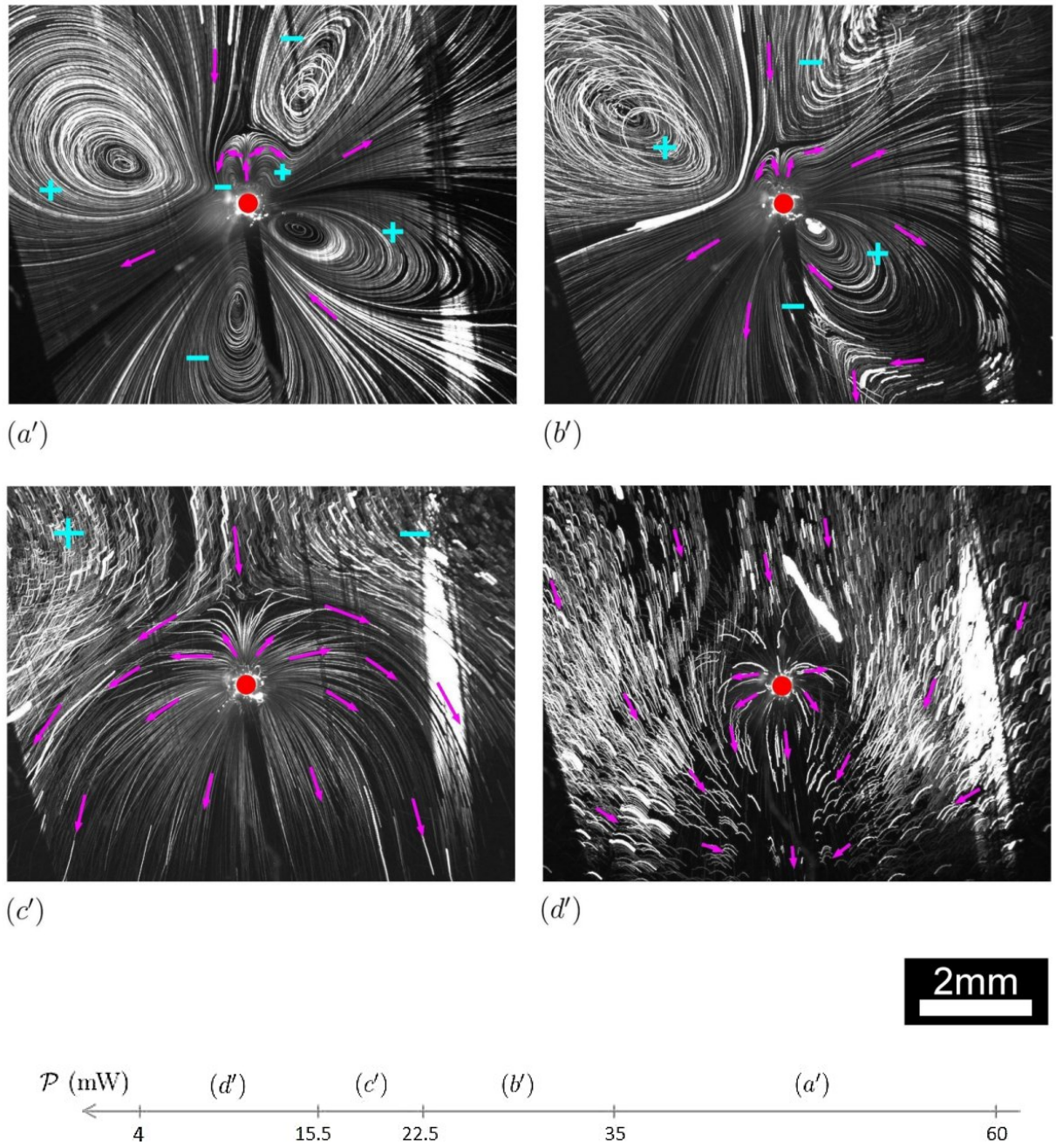

Figure 3.11: Sequence of surface flow patterns arising with decreasing heating. The corresponding bottom views are respectively denoted $(a')...(d')$. This 'power−down' sequence has been captured a few minutes after that of Fig. 3.10. Same graphic code as above.

3.2.3 Competing multipolar modes

Let me add a few words about the way competing multipolar modes manifest themselves after the onset of the instability. While several modes are competing against one another, we observe streamlines snaking between the convection cells surrounding the hot bead. These 'snake – like' streamlines mark the emergence of new vortex pairs. On Fig. 3.12, the 'yellow snake' visible in state (a) gives birth to a counter – rotating vortex pair in state (b), making the system transit from a dipole to a quadrupole. Still, the system fails to reach a hexapolar state : after a brief burst in (b), the 'orange snake' eventually dies in (c). Note the substantial growth of both vortex pairs between the evolution phases (b) and (c). Often, the vortex in the outward – looking portion of the serpentine curve would spring up at some distance from the heat source. Shortly after, this vortex would migrate to the surface of the bead whereon it would anchor.

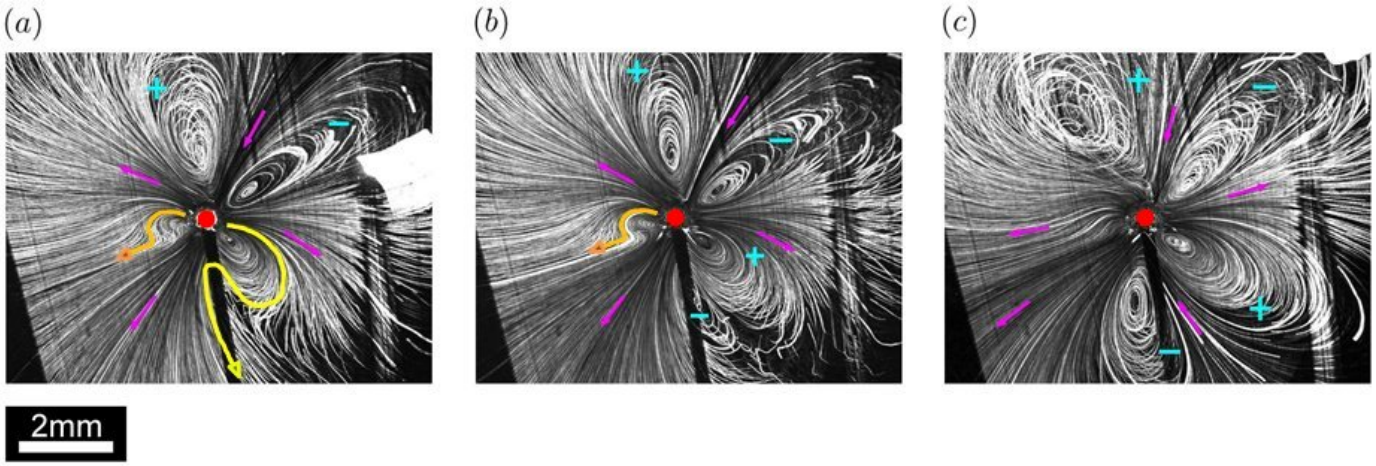

Figure 3.12: Serpentine surface streamlines (*bottom views*). $+/-$: clockwise/anticlockwise vortex rotation. Arrows of arbitrary length show the flow direction. Hot bead ($\varnothing_b \approx 295\,\mu$m) sketched by a red disk. Surface flows recorded at a rate of 2 frames per second and averaged over $\Delta t = 25$ s. State (b) immediately follows (a) while $\Delta t_{(b)\to(c)} = 100$ s separate (c) from (b). The 'shining square' on fig. (a) is an 'average' light mark left by a threadlike impurity. Bead's drop shadow forming a dark strip.

3.3 Quantitative study of the toroidal base state

This section is dedicated to a few quantitative features of the base torus. First, emphasis is placed on the velocity field in this ground flow state. We will see how sensitive to surfactant contamination the interface dynamics is. Direct evidence of this contamination is then given through manifestations of the elasticity surfactants provide the interface with.

3.3.1 Characterisation of the velocity field

This part is twofold : a 'locked' interfacial state associated with the base flow regime is first uncovered when comparing surface and subsurface velocities while, in a second step, the time evolution of the radial position of a surface tracer particle is studied. The influence of surfactant contamination over the flow velocity is pointed out in both studies.

Boundary condition on the interfacial velocity

The quasi – axisymmetric base flow is ordinarily observed under slight heating conditions. In the present case, the interface is 'locked' in the sense that surface velocities are very low and markedly smaller than subsurface velocities. However, contrary to what happens in the water jet experiment, the velocity is not strictly zero but minimum at the interface. In fact, thermal diffusion prevents here the interface from getting completely blocked.

To reach this conclusion, we compare the velocity of tracer particles moving at the interface with that of particles found in a shallow layer extending down to a few tenths of a millimetre underwater. In practice, the motion of a cluster of tracer particles (hereafter referred to as a 'molecule') is monitored at regular time intervals τ in a cross – section of the toroidal base flow (Fig. 3.13). The centrifugal motion of a molecule 2.5 mm far from the hot bead is tracked over time. The latter is composed of four 'atoms': the one on top is situated at the interface ($z = 0$) while the other three lie at a shallow depth below the surface ($z < 0$). On Fig. 3.14, the trajectories of the atoms we are tracking provide quantitative evidence of the above observation. The mean centrifugal velocity of each tracer particle is provided in table 3.15 : subsurface flow velocities are indeed noticeably higher than interfacial velocities, a visual proof being the counterclockwise rotation of the molecule well visible in the top insert of Fig. 3.14.

Let us now extract quantitative data from velocity profiles in a vertical cross – section of the toroidal base flow. These profiles are obtained through the usual PIV processing (sec. 2.1.5). Figs 3.16 – 3.18 show a collection of PIV maps reflecting the variations of the

bulk velocity $\vec{v}_b$. The longitudinal velocity v_x is especially significant in a millimetre thick subsurface layer and, to a lesser extent, near the bottom of the cell. Most importantly, as foreshadowed by the preliminary study, $|v_x|$ goes through a maximum at a finite depth and not at the water/air interface as may have been expected. The transverse velocity v_z takes important values in a region beneath the hot bead where a column of rapidly ascending liquid arises, but is negligible everywhere else. The transverse derivative of the longitudinal velocity $\partial_z v_x$ exhibits 'stratified layers'. Generally speaking, the closer we are to the heat source, the higher the velocity. One also checks that the velocity declines while approaching a vortex centre. These features are even clearer on the evolution curves of the bulk velocity components displayed in Fig. 3.19. One notices that:

- Both $|v_x|$ and $|v_z|$ diminish with increasing radial distance R to the heat source.
- The maximum longitudinal velocity $|v_x|_{\max}$, between $100\,\mu$m/s and $200\,\mu$m/s, is reached at a depth $z_{\max}$ such that $-0.8\,\text{mm} < z_{\max} < -0.4\,\text{mm}$ in the investigated range of radial positions. The highest transverse velocity $|v_z|_{\max}$ is attained for $-1.5\,\text{mm} < z_{\max} < -1\,\text{mm}$. In both cases, $z_{\max}$ increases with increasing R.
- The full v_x-curves are symmetrical with respect to the half$-$depth $z_{1/2}$. A reversal of the velocity is observed over there. In fact, v_x is negative (resp. positive) in the upper half (resp. lower half) of the left convection roll. The v_z-curves are equally symmetrical with respect to $z_{1/2}$ but the transverse velocity is negative (vectors oriented upwards) everywhere within the explored region.

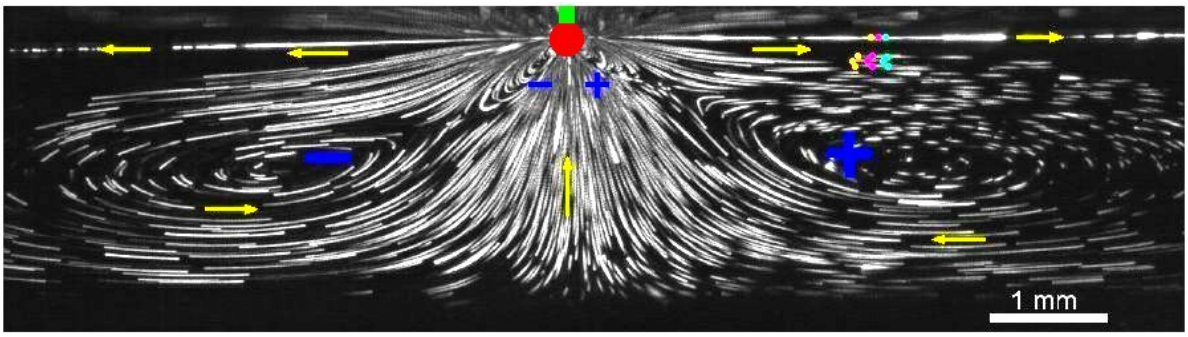

Figure 3.13: Evolution of the subsurface velocities of tracer particles in a vertical cross – section of the toroidal base flow. The arrows indicate the local bulk flow direction and the + (resp. −) sign denotes clockwise (resp. anticlockwise) vortex rotation. Hot bead ($\varnothing_b \approx 295\,\mu$m) represented as a red disk (approximate vertical position). Each molecular configuration at a given time t_i is depicted by a single colour, orange/magenta/cyan in that order. Successive observation times separated by $\tau = 1$ s. Streamlines map from a stack containing 100 frames of a video at 10 fps, corresponding thus to a recording time $\Delta t = 10$ s. Average frame captured more than 30 s after laser switching on, so that the flow probably reached a steady state. Heating power : $\mathcal{P} \approx 21$ mW.

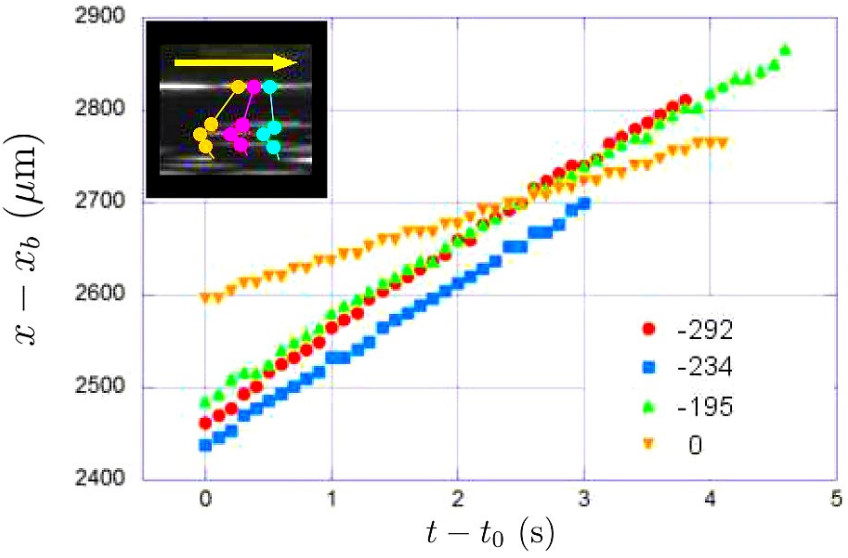

Figure 3.14: Time evolution of the distance to the hot bead $x - x_b$ of surface and subsurface tracer particles in a vertical cross – section of the toroidal base flow. t_0 denotes the instant at which we start tracking the molecule (Fig. 3.13) whose zoomed view is provided in the top insert. Note the counterclockwise rotation of the molecule as time goes by. The arrow marks the flow direction. 'Travelling depth' of each atom indicated (in μm) next to its corresponding symbol in the bottom right insert. The colour scheme used for the curves has nothing to do with that of the top insert. The former permits us to discriminate between tracer particles found at different depths whereas the latter differentiates between the conformations of the same molecule observed at different times.

Depth z (μm)	Velocity v (μm/s)
0	42
−195	81
−234	86
−292	92

Figure 3.15: Centrifugal velocities v of surface and subsurface tracer particles as a function of depth z, in a vertical cross−section of the toroidal base flow. The values reported in this table are nothing but the slopes of the curves displayed in Fig. 3.14.

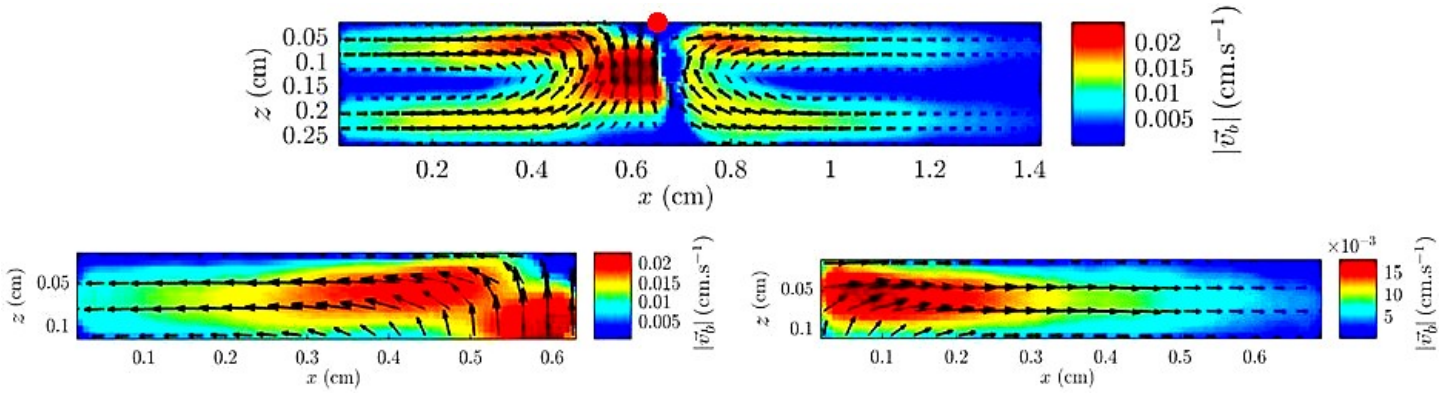

Figure 3.16: PIV map of the bulk velocity magnitude $|\vec{v}_b|$ in a vertical cut plane of the toroidal base state. (*Top part*) Velocity map over a large portion of the sample. The red disk roughly marks the position of the hot bead partially wetted at the surface. Curiously, the latter is right shifted with respect to the column of quickly ascending liquid found in the intervortex region. The blue stripe (very weak flow) mapped in this area has no physical meaning: actually, a parasitic cast shadow prevents the PIV code from computing local velocities properly. (*Bottom part*) Magnified views of the velocity map in the left and right halves of a millimetre thick subsurface layer. PIV map from a record at 17.45 fps, with original scales 7.94 μm/pix (horiz.) and 9.43 μm/pix (vert.). Heating power: $\mathcal{P} \approx 8$ mW.

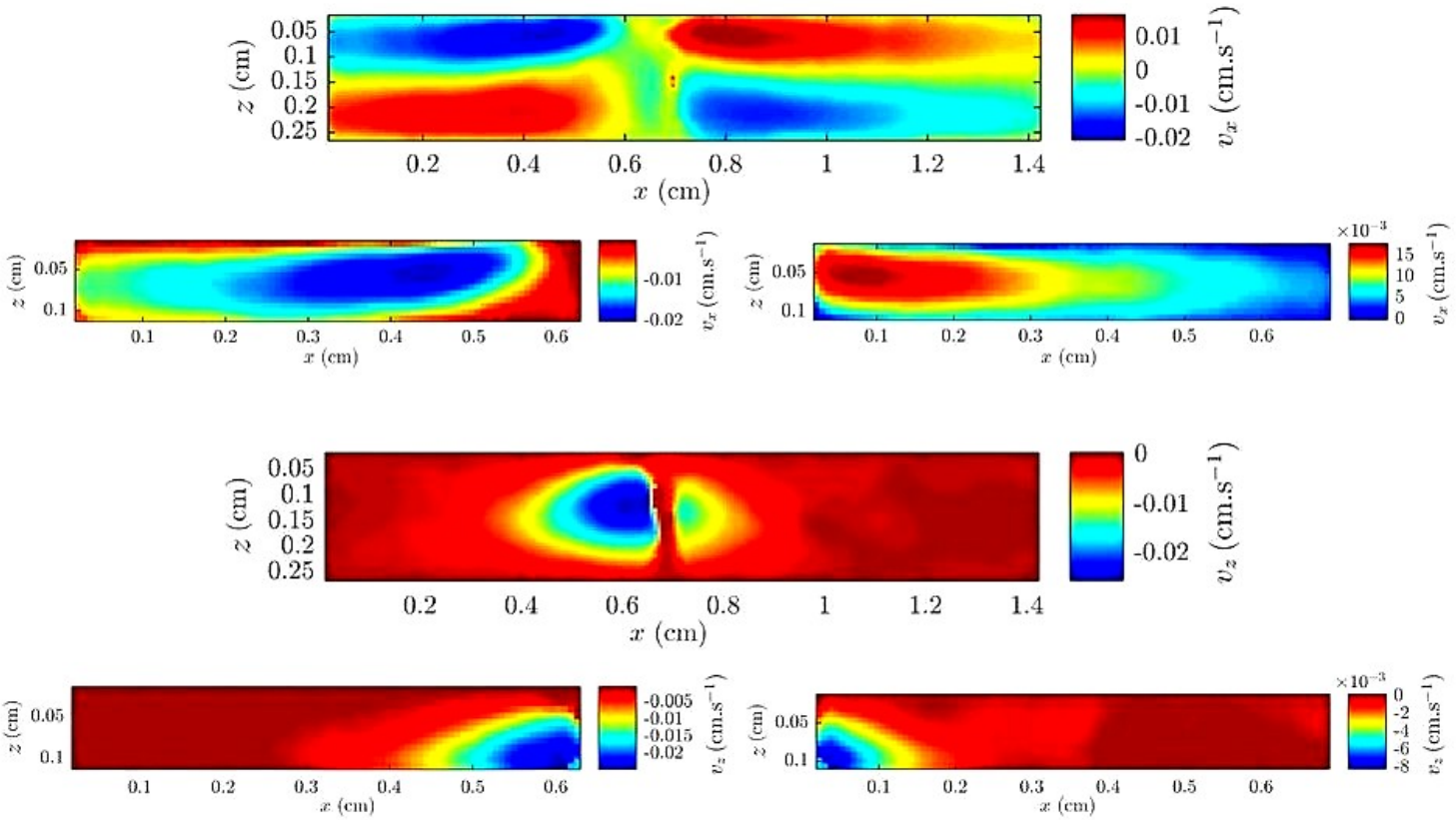

Figure 3.17: PIV maps of the longitudinal v_x and the transverse v_z bulk velocities (*vertical cross – section*). Main figures: maps over a large part of the cell. Subfigures: zoomed views in a millimetre thick subsurface layer. Raw data are those of Fig. 3.16.

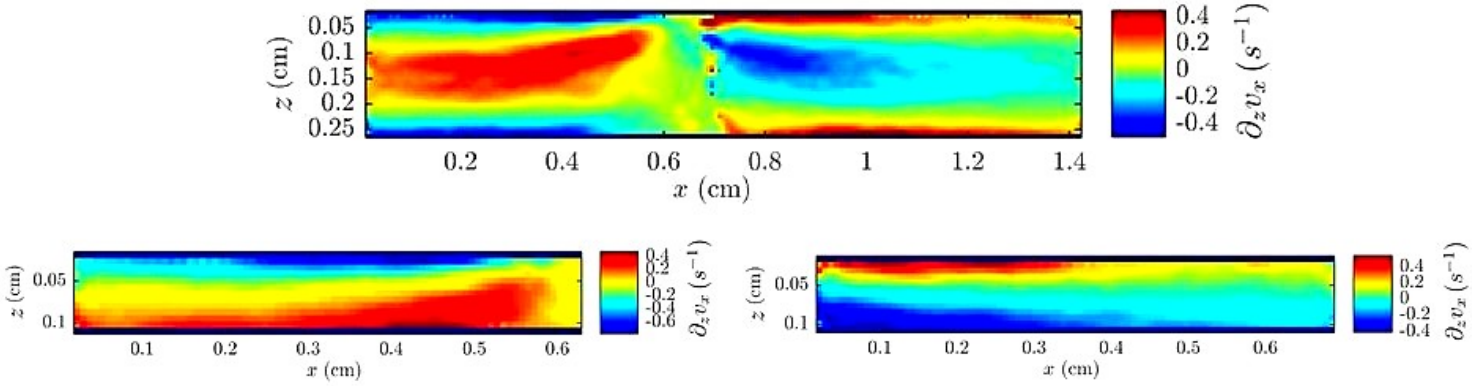

Figure 3.18: PIV map showing the transverse derivative of the longitudinal velocity component $\partial_z v_x$ (*vertical cut plane*). (*Top figure*) Map over a large part of the cell. (*Bottom figures*) Zoomed left and right views in a 1 mm thick subsurface layer. Derivatives are computed based on local linear fits inside a three – point sliding window. Same experiment as above.

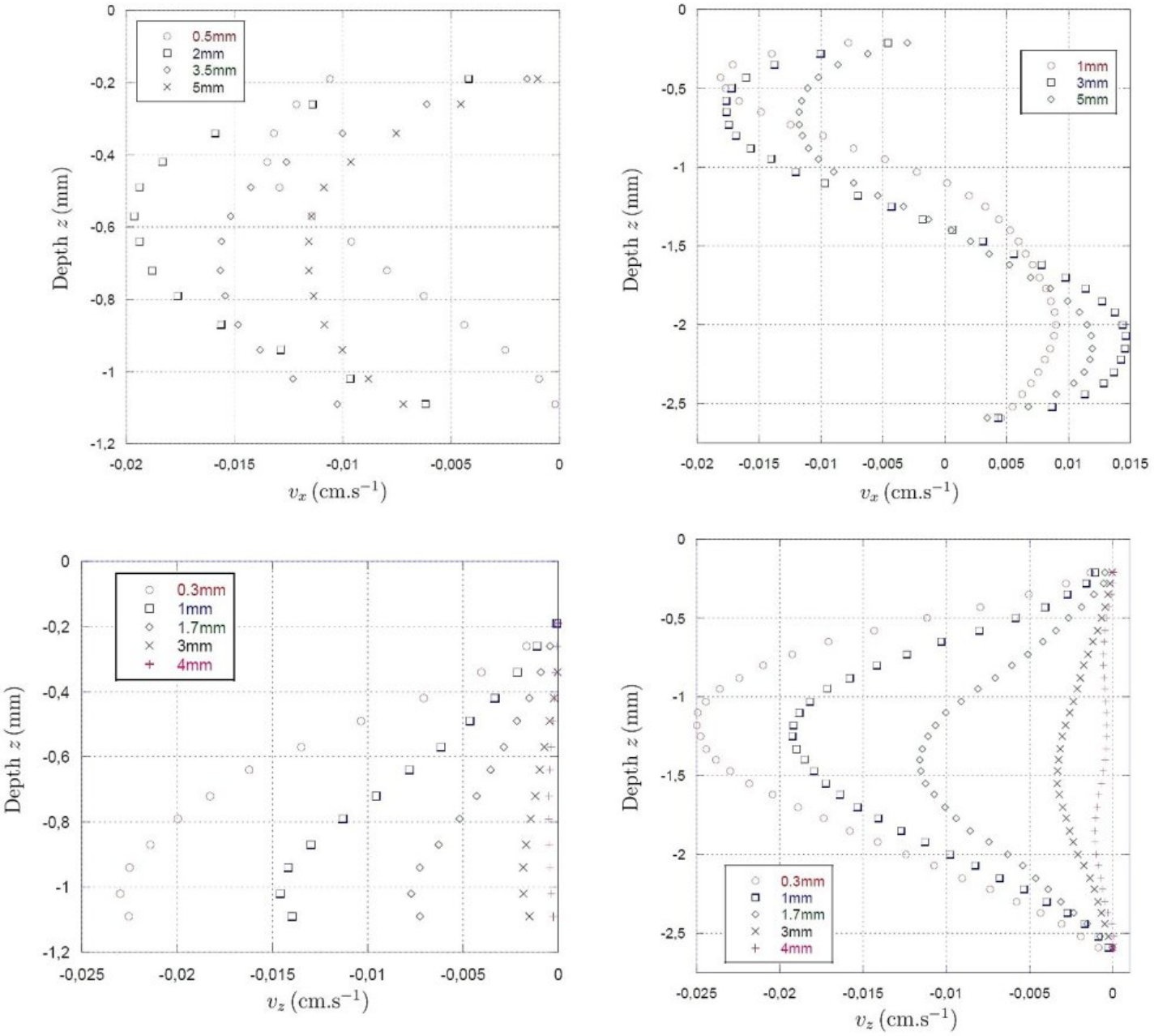

Figure 3.19: Bulk evolution of the longitudinal v_x and the transverse v_z velocities. (*Left*) Velocity profiles in a millimetre thick subsurface layer. (*Right*) Profiles over the whole height of the cell. Plots for various radial positions (see inserts) to the left of the hot bead.

Centrifugal motion of a surface tracer particle

We derive the time evolution of the centrifugal radial motion of a surface tracer particle in the toroidal flow regime. Experiments are thus achieved at low heating powers, in the range $\mathcal{P} \in [13.5, 14.4]\,\mathrm{mW}$. In practice, using vertical cut views rather than top views is by far preferable if one wants to spot surface tracer particles properly. Indeed, we notice on the side views that particles found exactly at the interface ($z = 0$) do not generate mirror images across the surface, contrary to particles located underwater ($z < 0$). The trajectories of surface tracer particles situated at varying distances from the hot bead are 'bound together' so as to reconstruct a complete radial trajectory. This 'time–shifting method' to obtain a single representative trajectory out of the trajectories of individual tracer particles assumes that the flow is stationary. Let me present the results of three experiments wherein this procedure has been applied :

1. *Experiment with a freshly prepared sample. Heating power set at* $\mathcal{P} = 13.5\,\mathrm{mW}$.

   A slightly polarised flow is observed (Fig. 3.20). In practice, we take care not to orient the laser sheet along the flow preferential direction, so as to keep a left/right symmetry and thus avoid an irrelevant bias in the position measurements. Fig. 3.21 displays trajectories of surface tracer particles in the base flow state of Fig. 3.20. These graphs demonstrate that the distance of the interfacial tracer particles to the hot bead varies as $t^{1/3}$. The tracking of a tracer particle located at $z \approx -160\,\mu\mathrm{m}$ under the interface confirms that subsurface particles move faster than surface ones ('locked' interface), as evidenced by the upward deflected red curves of Fig. 3.21 departing from the time behaviour typical of the motion of surface particles.

2. *Experiment with an 'aged' sample. Heating power set at* $\mathcal{P} = 14.4\,\mathrm{mW}$.

   We let the system get more and more 'aged' for nearly one hour and a half. Once this time elapsed, we note that the flow structure has remained qualitatively the same at the interface as well as in the bulk. Nonetheless, particle tracking reveals some oscillatory surface dynamics (Fig. 3.22). Smoothening the curve, one removes velocity fluctuations and recovers approximately the above $t^{1/3}$ law. Note that the average slope value initially equal to $1.67\,\mathrm{mm}^3/\mathrm{s}$ (Fig. 3.21) has more than halved, now amounting to only $0.81\,\mathrm{mm}^3/\mathrm{s}$.

3. *Experiment with a renewed sample. Heating power set at* $\mathcal{P} = 14.4\,\mathrm{mW}$.

   We thoroughly rinse the cuvette with ultrapure water. The experiment, run without delay, yields a quasi–axisymmetric flow a bit more polarised than the one previously observed. The above results are recovered, especially the $t^{1/3}$ law of motion, the only

difference lying in a larger mean slope value now equal to $2.75\,\mathrm{mm}^3/\mathrm{s}$ (Fig. 3.23). We check once again that subsurface tracer particles move faster than surface ones. The targeted particle, located at $z \approx -65\,\mu\mathrm{m}$ underwater, seems to travel at the same speed as surface particles but actually a slight deviation appears after a while.

To conclude, surface tracer particles move along their centrifugal radial trajectories at a pace $\propto t^{1/3}$ provided a 'fresh' sample is used.

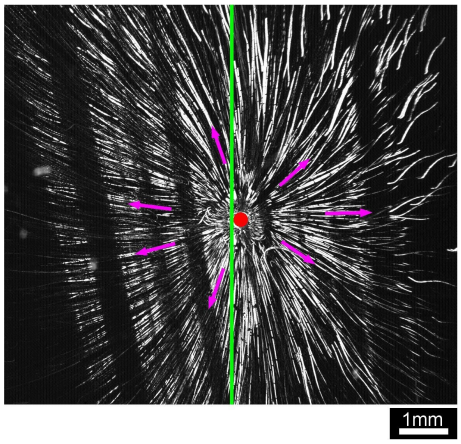

Figure 3.20: Top view of the quasi – axisymmetric base flow observed at $\mathcal{P} = 13.5\,\mathrm{mW}$. Arrows mark the flow direction. Laser sheet sketched by a green line almost perpendicular to the direction of polarisation. Hot bead ($\varnothing_b \approx 295\,\mu\mathrm{m}$) depicted by a red disk. Average frame from a record at 9 fps.

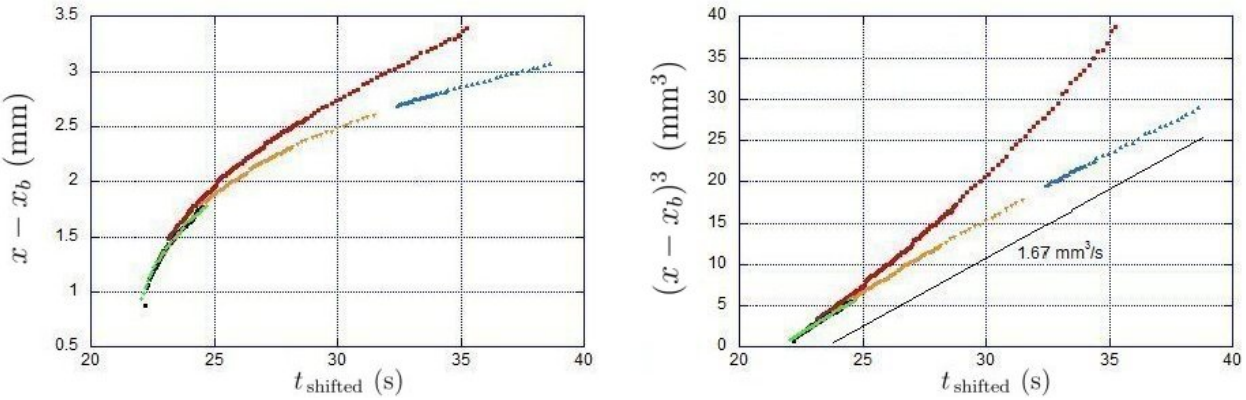

Figure 3.21: Time evolution of the distance to the hot bead $x - x_b$ of interfacial tracer particles in the quasi – axisymmetric state ('fresh' sample). (*Left*) Distance $(x - x_b)$ in function of the temporal shift t_{shifted}. (*Right*) Cube of $(x - x_b)$ in function of t_{shifted} revealing a linear relationship. Successive positions of a tracer particle found at $z \approx -160\,\mu\mathrm{m}$ below the interface reported on the red curve, whereas other curves correspond to surface tracer particles found at various distances to the left of the hot bead. Heating power : $\mathcal{P} = 13.5\,\mathrm{mW}$. Measurements from a record at 16.4 fps.

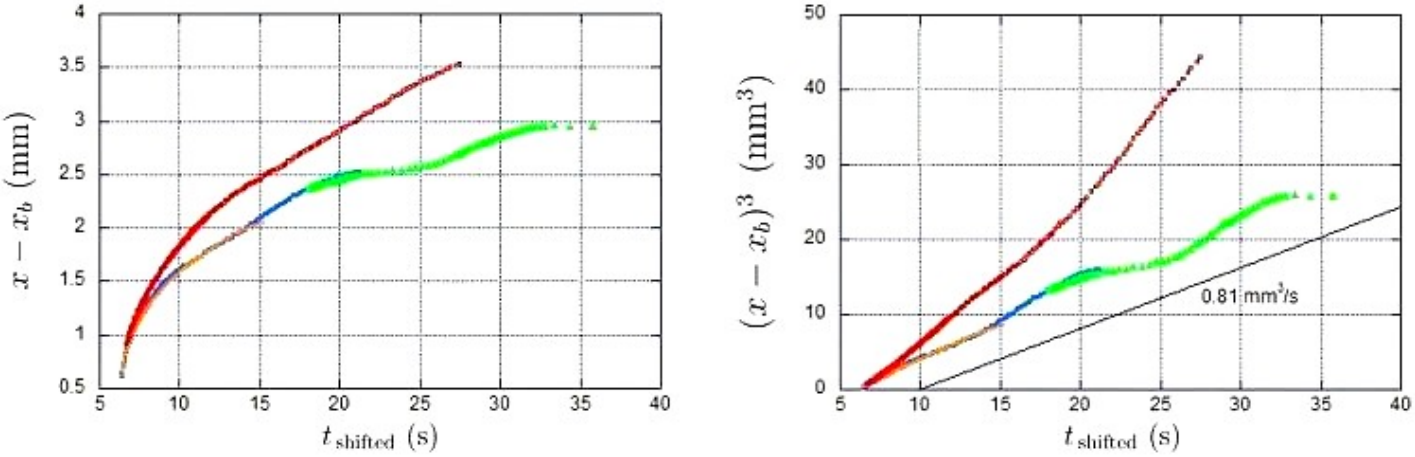

Figure 3.22: Time evolution of the distance to the hot bead $x - x_b$ of interfacial tracer particles in the quasi – axisymmetric state ('aged' sample). Same comments as for Fig. 3.21 save that the subsurface tracer particle is now at $z \approx -95\,\mu$m below the interface. Heating power : $\mathcal{P} = 14.4\,$mW. Records at 24 fps.

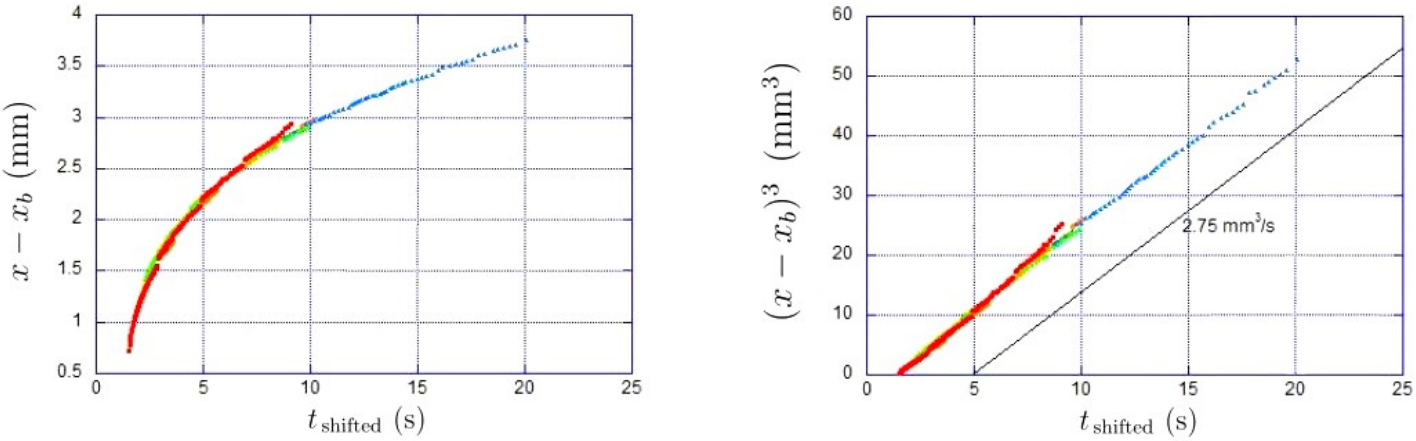

Figure 3.23: Time evolution of the distance to the hot bead $x - x_b$ of interfacial tracer particles in the quasi – axisymmetric state (new sample). Same comments as above except that the subsurface tracer particle (red curve) is closer to the interface, at $z \approx -65\,\mu$m. Heating power : $\mathcal{P} = 14.4\,$mW. Records at 9.75 fps (horizontal)/30.4 fps (vertical).

3.3.2 Direct evidence of surface elasticity

We provide direct evidence of surface elasticity through 'power shutdown experiments', namely experiments wherein the laser power supply is alternately switched off/on.

Power shutdown experiments

In the experiment whose results are reported below, the laser source is turned on at a time $t_{\rm on} = 4.50\,{\rm s}$ after we start recording the flow (at 10 fps). Approximately $\Delta t_{\,{\rm on}\to{\rm off}} \approx 44\,{\rm s}$ later, at $t_{\rm off} = 48.33\,{\rm s}$, the laser is suddenly turned off using a beam stop. The time interval $\Delta t_{\,{\rm on}\to{\rm off}}$ (resp. $\Delta t_{\,{\rm off}\to{\rm on}}$) during which the source is on (resp. off) is chosen sufficiently long for the flow to reach a steady state (resp. vanish). With a heating power set at a moderate value $\mathcal{P} \approx 21\,{\rm mW}$, for which the system is still in its polarised toroidal state, the characteristic onset $\tau_{\rm onset}$ and relaxation $\tau_{\rm relax}$ times are such that $\tau_{\rm onset} \cong \tau_{\rm relax} \approx 20\,{\rm s}$. Note that to estimate these typical times, we monitor the repartition of the streamlines over time until no apparent change is noticeable, meaning that the flow is then 'stabilised'.

Fig. 3.24 shows a typical bulk flow, frequently seen in our thermocapillary experiments, that consists of two corotating tori : a small fast rotating torus located in the vicinity of the hot bead coaxial with a larger slowly rotating torus that sits at the bottom of the cell. Past a 20 s response time (in fact, $\tau_{\rm onset} \approx 20\,{\rm s}$ is the onset time of the big torus, the small torus forming within a much shorter time not captured by our recordings at 10 fps), the flow remains in this initial (I) stationary state as long as $\mathcal{P} \approx 21\,{\rm mW}$ of heating power feed the system. Once heating is interrupted, the small torus disappears in a split second while the big torus keeps flowing outwards under the effect of its own inertia. Redrafting the Navier – Stokes equation as a vorticity transport equation, one defines a diffusion length $l = \sqrt{\nu\tau}$ where ν denotes the kinematic viscosity and τ is the vorticity diffusion time. With a kinematic viscosity of water $\nu \sim 10^{-6}\,{\rm m^2.s^{-1}}$ and writing that $\tau \equiv \tau_{\rm onset} \approx 20\,{\rm s}$, one finds $l \approx 4.5\,{\rm mm}$. This value, comparable to the size of the flow structure, leads to the conclusion that the dynamics of the big torus is essentially inertial. In addition, we observe a short – lived ($\approx 10\,{\rm s}$) centripetal motion of surface tracer particles, so that important shear stresses arise within a few tenths of a millimetre thick subsurface layer. This is a concrete proof of the elastic response of the water/air interface to laser shutdown.

Tracking interfacial tracer particles confirms the occurrence of an 'elastic retraction phenomenon' at the precise moment $t = t_{\rm off}$ the laser is switched off. Fig. 3.25 clearly evidences how the speed of the tracer particles sharply (angular point) reverses at $t = t_{\rm off}$:

after laser shutdown, the tracer particles move in the direction opposite to the one they had before, as revealed by a change in the sign of the slope being nothing but the radial velocity of the particles. The closer the tracer particle to the heat source, the sharper the peak of the curve, *i.e.* the higher its pre – and post – shutdown radial velocity.

Fig. 3.26 displays trajectories of tracer particles situated in a thin subsurface layer. Following laser shutdown, the latter are driven by the convection rolls of the big torus. Save a fleeting deceleration phase induced by the retracting elastic interface which does not last for more than a few seconds after t_{off} (look at the little jumps followed by slight drops on the (A) or (C) curves of Fig. 3.26), subsurface tracer particles keep moving outwards contrary to interfacial ones. They also sink a bit while moving away from the source, as visible in (B). Again, we check that the interface is in a 'locked state', *i.e.* that velocities are higher in the subsurface region ($\mathrm{Z} < 0$) than at the interface ($\mathrm{Z} = 0$). For instance, at $\mathrm{R} = 2.3\,\mathrm{mm}$ to the right of the fibre axis, a bulk velocity $80\,\mu\mathrm{m/s} \leqslant v_b \leqslant 100\,\mu\mathrm{m/s}$ is measured for depths in the range $-600\,\mu\mathrm{m} \leqslant \mathrm{Z} \leqslant -190\,\mu\mathrm{m}$, whereas the velocity drops to only $v_s = 43\,\mu\mathrm{m/s}$ at the interface. Bear in mind that, unlike the case of the water jet, the velocity does not fall to zero but to a minimum at the interface.

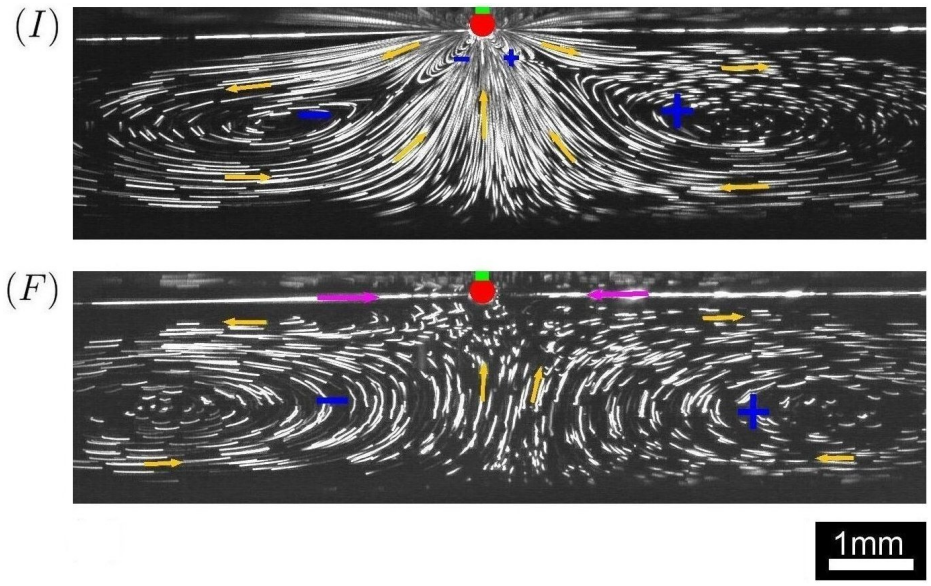

Figure 3.24: Power shutdown. (*Cross – sections*) (I) Doubly toroidal (quasi –)axisymmetric flow. Laser switched on at $t_{\text{on}} = 4.50\,\mathrm{s}$. Frame obtained by averaging over $\Delta t_{(I)} = 10\,\mathrm{s}$, from time $t_1 = t_{\text{on}} + 25.5\,\mathrm{s}$ to $t_2 = t_{\text{on}} + 35.5\,\mathrm{s}$. (F) Sheared toroidal flow immediately following power shutdown at $t_{\text{off}} = 48.33\,\mathrm{s}$. Averaging over $\Delta t_{(F)} = 15\,\mathrm{s}$ after laser switching off. $+/-$: clockwise/anticlockwise vortex rotation. Orange arrows show the bulk flow direction while magenta arrows depict the centripetal motion of tracer particles after laser interruption. Hot bead ($\varnothing_b \approx 295\,\mu\mathrm{m}$) sketched by a red disk. $\mathcal{P} \approx 21\,\mathrm{mW}$.

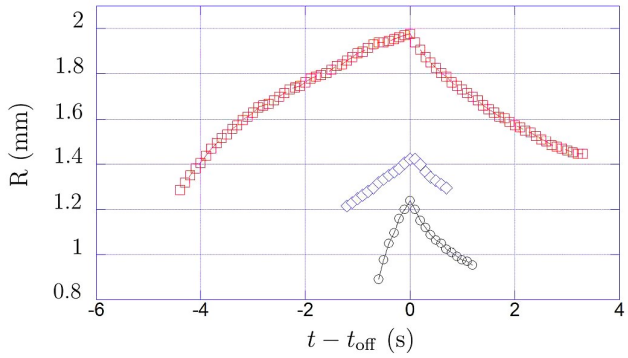

Figure 3.25: Elastic retraction of interfacial tracer particles at laser shutdown. The radial position R of tracer particles moving at the water/air interface is plotted as a function of the interval separating the generic time t from the instant $t_{\rm off}$ of laser shutdown (abrupt power decrease $\mathcal{P} \approx +21\,\mathrm{mW} \rightarrow 0\,\mathrm{mW}$). Tracer particles either left (red and black curves) or right (blue curve) from the hot bead are tracked. Clearly, the particle speed reverses at $t = t_{\rm off}$.

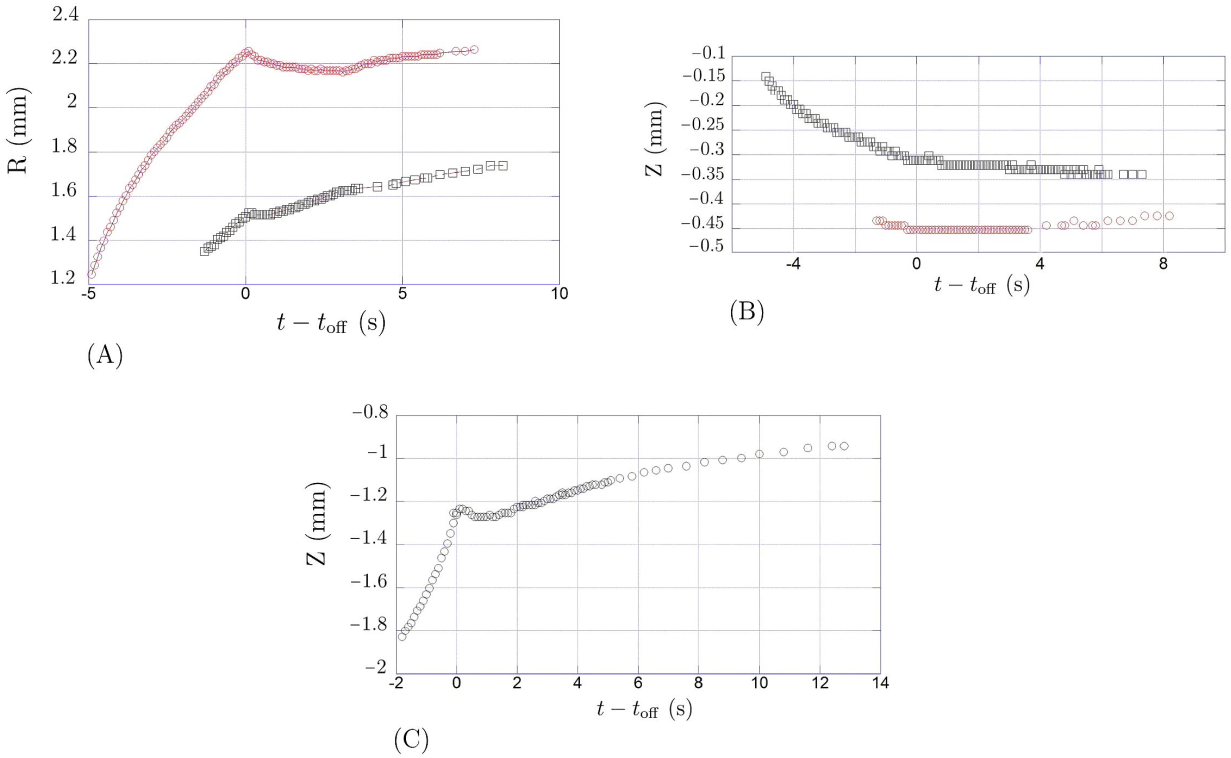

Figure 3.26: Trajectories of tracer particles in a thin subsurface layer after laser shutdown. (A) & (B) Centrifugal motion of subsurface tracer particles in the near region $(\mathcal{NR}) = \{1\,\mathrm{mm} < \mathrm{R} < 2.5\,\mathrm{mm}, -0.5\,\mathrm{mm} < \mathrm{Z} < -0.1\,\mathrm{mm}\}$, *i.e.* along streamlines belonging to the upper part of the big torus. Red circles (resp. black squares) mark the successive positions of a tracer particle originally found right (resp. left) from the hot bead. (C) Vertical motion of a tracer particle within the column of accelerated liquid rising between the big torus convection rolls, that is about the axis of the source. (R, Z) denote the radial position and the depth of a tracer particle in a cross−sectional plane, respectively.

3.4 Quantitative study of a quadrupolar flow

3.4.1 Tomographic prospection of a quadrupolar flow

This section is dedicated to the exploration, using laser tomography, of the 3D structure associated with a surface quadrupole (see technical details in sec. 2.1.5). Figs 3.27 and 3.28 provide, respectively, a series of cross−sections and horizontal cut views of the structure under investigation (in practice, we perform automatic laser scans with the two Thorlabs rotation stages in 'Sequencer' mode). One should examine the streamlines maps keeping in mind that the length of the luminous streaks left by the tracer particles is not only a gross indicator of the flow velocity in the region of interest, but also provides information on the local orientation of the streamlines relatively to the cut plane : the longer (resp. shorter) these luminous streaks, the more parallel (resp. perpendicular) to the cut plane the flow locally is. Note that streamlines simply reduce to twinkling spots in flow regions where they are rigorously perpendicular to the viewing plane.

What is presumably a couple of whirlpools develops quite symmetrically on either side of the source axis (see the two 'orange pockets' on Fig. 3.27 − 1). Interestingly, we clearly remark that streamlines end in a point as they are rising back towards the hot bead. This fact is especially apparent in a vertical cut plane brushing the bead, as marked by cyan 'chevrons' in Fig. 3.27 − 6. This remarkable morphological trait reminds us of the sharp streamlines observed previously in the water jet experiment (see again sec. 2.3.2).

Vortex centres move away from one another along one direction while getting closer in the perpendicular direction, as yet discernable on Fig. 3.28 and definitively attested while tracking them with increasing observation depth (Fig. 3.29).

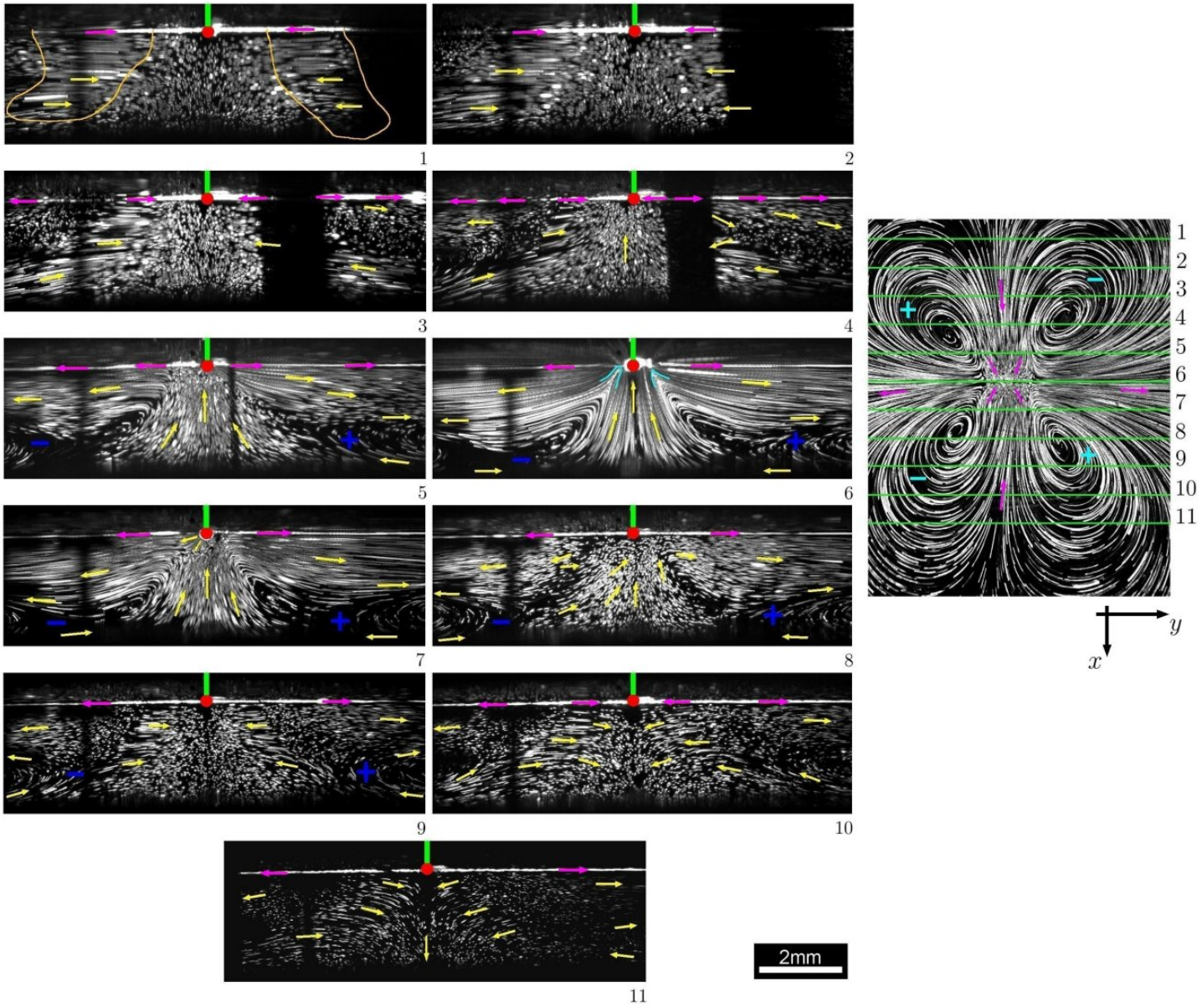

Figure 3.27: Cross−sectional views of the 3D structure of a surface quadrupole. Pictures captured in successive (following the ascending numerical order of the top view on the right) cut planes parallel to the 'centrifugal symmetry axis' of the quadrupole. Yellow (resp. magenta) arrows show the local bulk (resp. surface) flow direction, but not its magnitude. +/−: clockwise/anticlockwise vortex rotation, either in the bulk (deep blue colour) or at the surface (cyan colour). Hot bead ($\varnothing_b \approx 295\,\mu$m) depicted as a red disk (rough vertical position). Heating power: $\mathcal{P} \approx 57$ mW. Average frames generated out of stacks containing 100 images captured at 17.5 fps (recording time: $\Delta t \approx 6$ s). The dark stripe of varying width (see for instance image 3) is the drop shadow of the optic fibre end intercepted from different angles by the quasi−vertical laser sheet scanning the sample.

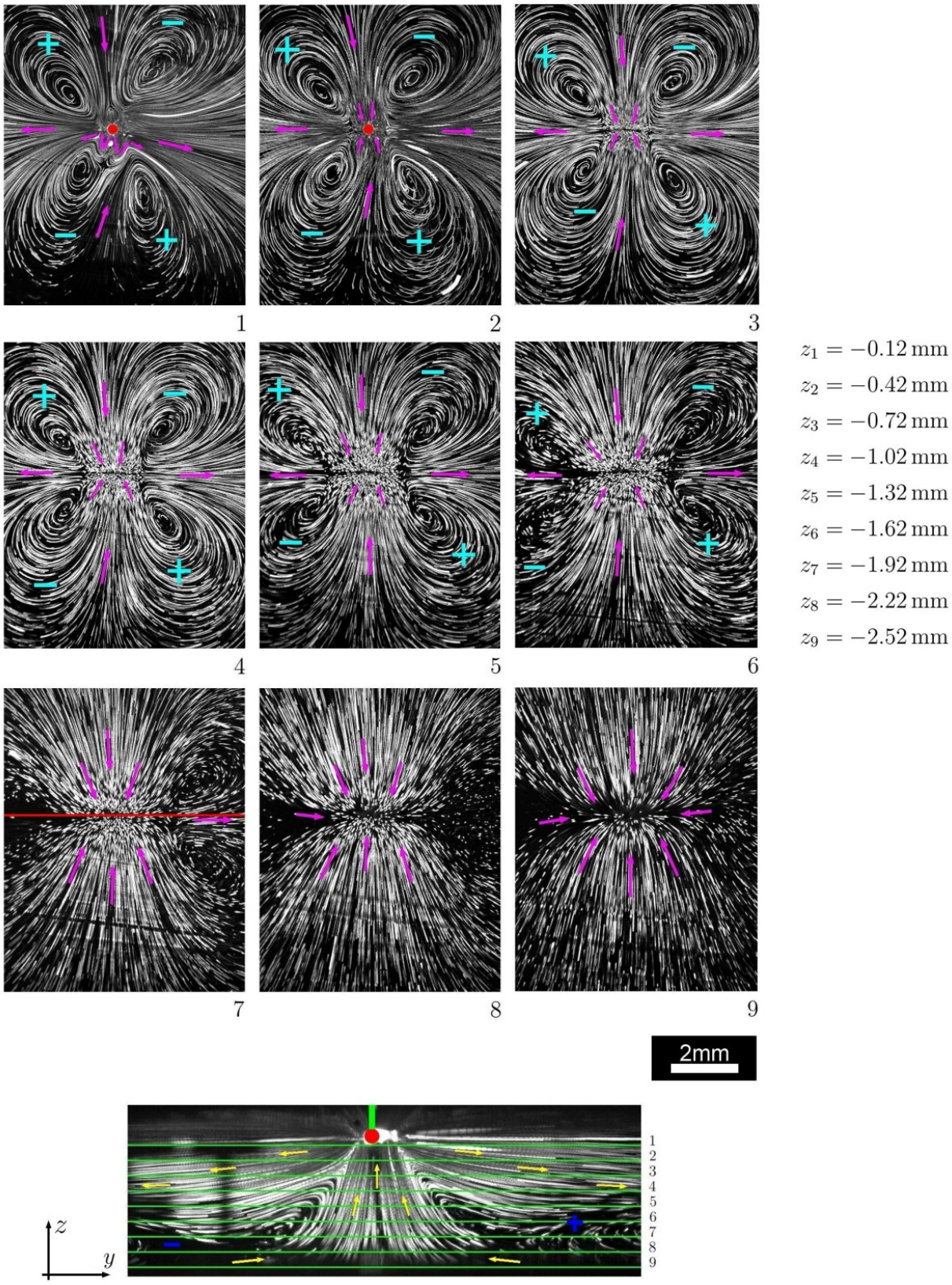

Figure 3.28: Series of horizontal cut views of the 3D structure associated with a surface quadrupole. Successive positions of the horizontal laser sheet in the bulk marked by parallel green lines on the bottom picture. On the right is a list giving the observation depths $\{z_i\}_{i \in [\![1,9]\!]}$. Same graphic codes as those of Fig. 3.27. Data from the very same experiment as in Fig. 3.27 except that stacks of 75 images captured at 17.5 fps over $\Delta t \approx 4\,\mathrm{s}$ are processed here to generate these average frames.

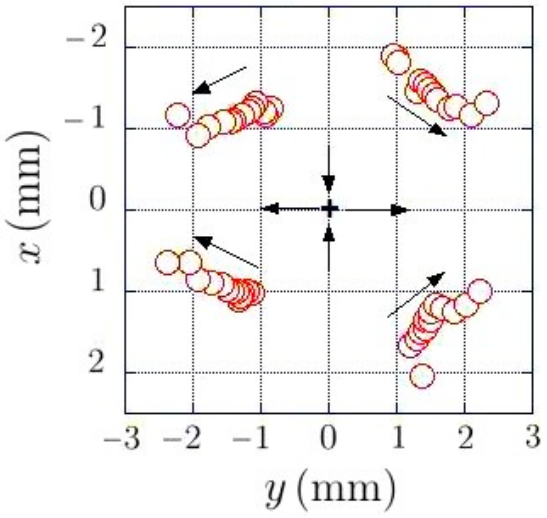

Figure 3.29: Evolution of the (xy) positions of the four vortex centres with depth. Each red circle represents a measuring point derived at a given depth. The latter is gradually increased in the direction indicated by the arrows, from $z_i = 0$ (water/air interface) down to $z_f = -1.80\,\text{mm}$. The black cross right in the middle of the figure marks the reference position of the heat source, while the black arrows immediately surrounding it depict the centrifugal and the centripetal symmetry axes of the surface quadrupole. Same experiment as above.

3.4.2 Boundary conditions on the interfacial velocity

Vertical cut views of a quadrupole are analysed in order to compare the velocities of a few tracer particles moving at the interface with those of particles located in a shallow layer extending down to a few tenths of a millimetre underwater. To enrich our study with visuals, 'molecule tracking' is here again performed in the very same spirit as in sec. 3.3.1.

All results presented below come from an experiment conducted under strong heating conditions. Much like the one of Figs 3.27 – 3.28, the quadrupolar flow considered here exhibits two counter – rotating vortex pairs with four vortices separated from one another by two 'channels', one centrifugal and the other centripetal, intersecting at right angles. An intense flow is measured along these 'hydrodynamic separators', by contrast with the vanishing flow observed in the core regions of the vortices. To come to this conclusion, the flow has been scrutinised in a couple of cross – sectional planes : a first viewing plane is located in the middle of the centrifugal channel and a second cut plane, parallel to the first one, cuts through the whirlpools. More precisely, local velocities are measured in the immediate vicinity of points A – D (Fig. 3.30). This study is supplemented by a rough estimate of the velocity near point E situated in the centripetal channel.

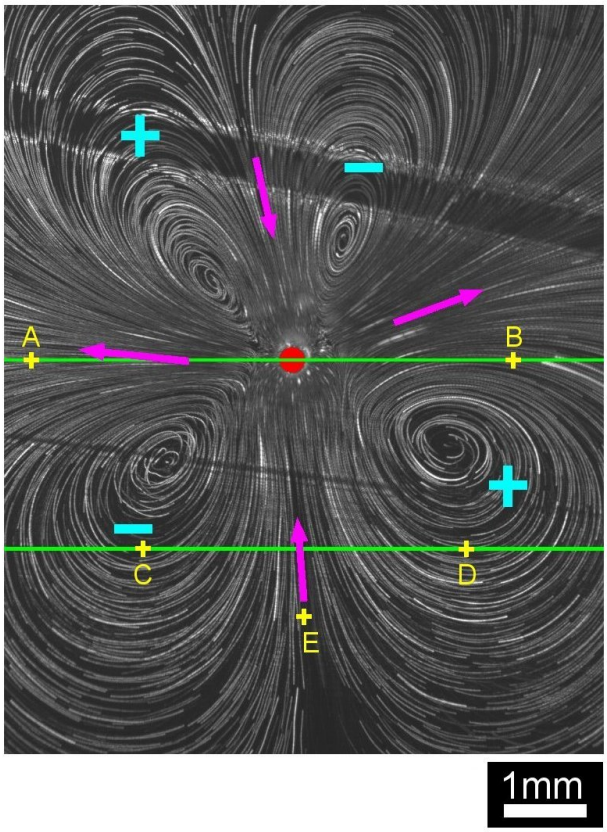

Figure 3.30: Velocity measurements in different regions of a surface quadrupole. Average top view from a stack containing 200 frames of a video at 17 fps, corresponding to a recording time $\Delta t \approx 12\,\mathrm{s}$. Local flow direction along both the centrifugal and the centripetal 'channels' indicated by magenta arrows. +/−: clockwise/anticlockwise vortex rotation. Vertical cut planes marked by green solid lines. Velocity measurement areas selected along these lines, in the immediate vicinity of points A−D. The observation site associated with point E lies within the centripetal channel. Hot bead ($\varnothing_b \approx 295\,\mu\mathrm{m}$) depicted by a red disk. Heating power: $\mathcal{P} \approx 70\,\mathrm{mW}$.

Cut plane AB (centrifugal channel)

The temporal monitoring of bunches of subsurface tracer particles in the cross−section AB reveals that 'molecules' are tilting forward during their centrifugal motion (Fig. 3.31). This is a visual evidence of the fact that in this case, contrary to what is observed for the quasi−axisymmetric base flow (sec. 3.3.1), the velocity is higher at the interface than in the subsurface region, in other words, that the interface is now in a 'passing state'. The graphs of Fig. 3.32, corresponding to the trajectories of the atoms forming the two molecules, provide quantitative evidence of this last observation.

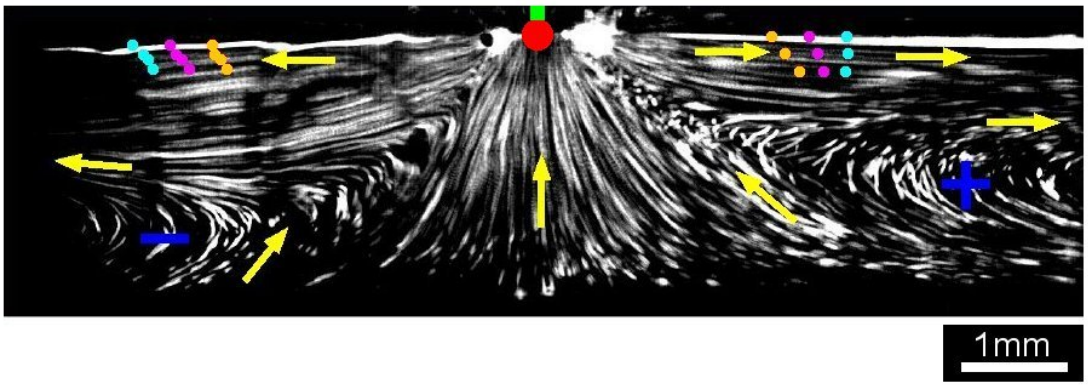

Figure 3.31: Evolution of the velocities of tracer particles in a subsurface layer of cut plane AB. The centrifugal motion of two 'molecules', found on the right and on the left of the hot bead, is tracked over time. Each molecular configuration at a given time t_i is depicted by a single colour, orange/magenta/cyan in that order. For simplicity, the same colour scheme is adopted for the right (RM) and the left (LM) molecules, despite slightly different time intervals $\tau_{\mathrm{RM}} = 0.53\,\mathrm{s}/\tau_{\mathrm{LM}} = 0.29\,\mathrm{s}$ between their successive positions. Data from the same experiment as in Fig. 3.30 except that stacks of 150 images captured at 17 fps over $\Delta t \approx 9\,\mathrm{s}$ are processed to generate this streamlines view. A slight distortion effect, probably due to a liquid droplet covering the optics, impairs a bit the image quality on the left.

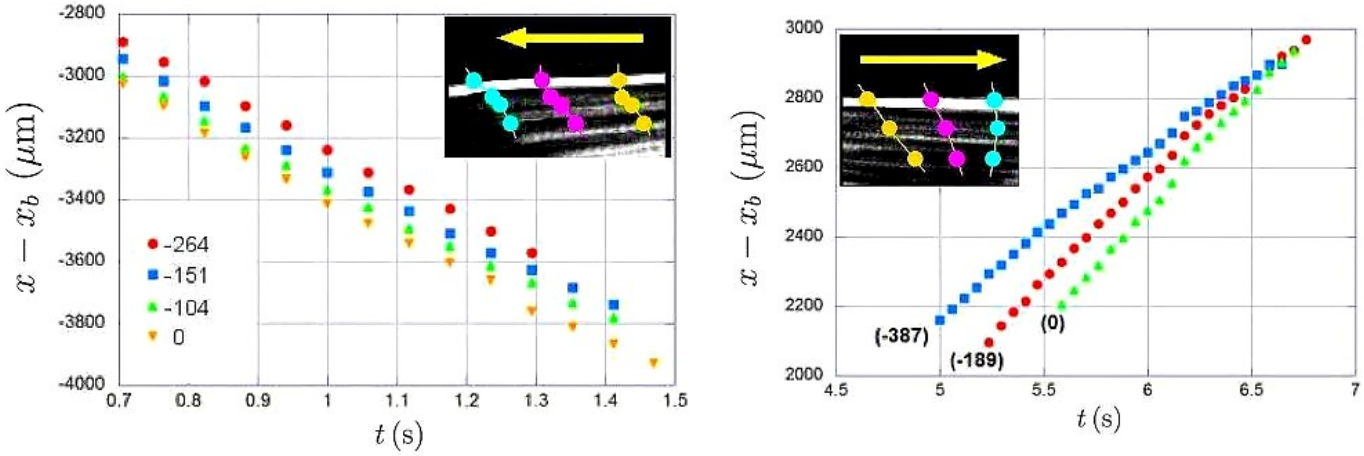

Figure 3.32: Time evolution of the distance to the hot bead $x - x_b$ of the tracer particles forming the left and the right molecules selected in the cut plane AB. Top inserts are zoomed views of the two tracked molecules (Fig. 3.31). Note the clockwise rotation of the right molecule as time goes by. Arrows showing the flow direction. 'Travelling depth' of each atom indicated (in μm) either in brackets below the trajectories of the right molecule constituents or inside an additional insert for the atoms of the left molecule. The colour scheme used for the curves has nothing to do with that of the top inserts. The former permits us to discriminate between tracer particles at different depths whereas the latter differentiates between 'molecular conformations' observed at different times.

To finish, the mean centrifugal velocity of each tracer particle considered above is given in the tables 3.33 (these values are the slopes of the curves displayed in Fig. 3.32). Clearly, the velocity of the tracer particles composing the right molecule (RM) declines with increasing depth. The situation is less obvious for the left molecule (LM) but still informative, as reflected in the sharp velocity drop $\Delta v_{\mathrm{LM}} = -70\,\mu$m/s measured between the interface in $z = 0$ and an observation depth $z = -104\,\mu$m. The uncertainty in the velocity of a tracer particle is $\delta v = \pm 40\,\mu$m/s.

Depth z_{LM} (μm)	Velocity v_{LM} (μm/s)
0	−1180
−104	−1110
−151	−1130
−264	−1165

Depth z_{RM} (μm)	Velocity v_{RM} (μm/s)
0	666
−189	601
−387	485

Figure 3.33: Centrifugal velocities v of both surface and subsurface tracer particles as a function of depth z (*cut plane AB*). The table on the right (resp. on the left) provides data obtained by tracking the right molecule (RM) (resp. the left molecule (LM)) shown in Fig. 3.31.

The centrifugal channel of a surface quadrupole is thus a region submitted to intense flows, with a typical velocity one order of magnitude higher than measured in the toroidal state. The fact that our measurements yield surface velocities larger in the left half than in the right half of the interface is seemingly due to the misalignment of the laser sheet with the centrifugal channel on the right, compared with their relative orientations in the left part of the surface (Fig. 3.30). Indeed, on the right side, the laser sheet cuts across streamlines located near a vortex centre, where the flow is slower than along the channels.

Point E (centripetal channel)

Here the vertical laser sheet is not oriented parallel to the centripetal channel and thus we cannot repeat as complete a particle tracking as previously. Yet, it is possible to estimate local flow velocities close to point E (Fig. 3.30) on the basis of top views. While surface tracer particles can be identified unambiguously on the side views, as they do not display mirror images across the interface, we do not have access to this information on the top views and hence cannot be absolutely sure that the particles we track are on the surface. However, even if the tracked particle is not exactly in $z = 0$, it may not be located deeper than a few tenths of a millimetre beneath the surface, that is within the subsurface area where the horizontal laser sheet is positioned. Fig. 3.34 shows the trajectory of a tracer particle along the portion of the centripetal channel near point E.

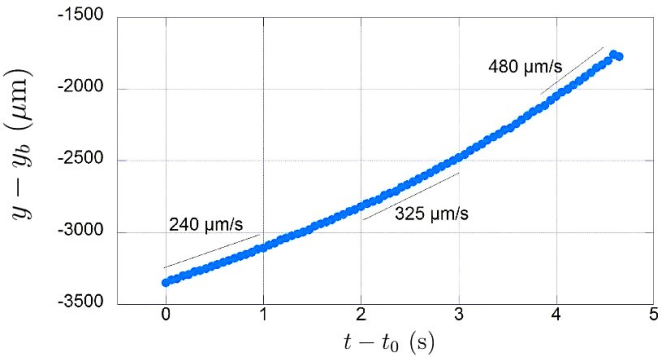

Figure 3.34: Time evolution of the distance to the hot bead $y - y_b$ of a tracer particle along the centripetal channel. t_0 denotes the instant at which particle tracking is initiated in the region next to point E (Fig. 3.30). Centripetal velocities indicated on the curve.

The centripetal velocity values reported here are about half those measured along the centrifugal channel. Most likely, the situation is qualitatively the same for the centrifugal and the centripetal channels, namely the interface is in a 'passing state' in both cases.

Cut plane CD (through the whirlpools)

To finish, let us examine the flow behaviour in the subsurface area of the cut plane CD. Both points C and D are located near vortex centres, in a region of the whirlpools where the flow is locally centripetal. Fig. 3.35 gives a first glimpse of the motion of the 'molecules' in the viewing plane CD, while Fig. 3.36 displays the trajectory of each 'atom' in detail.

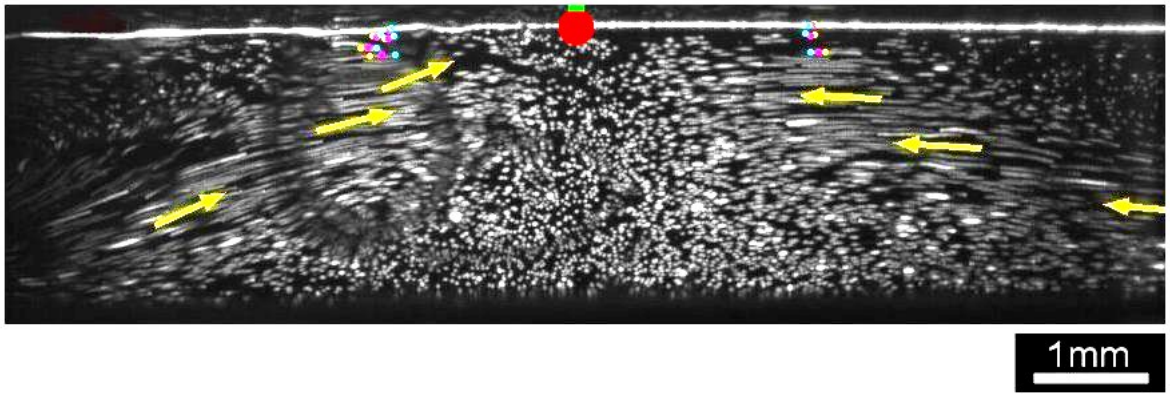

Figure 3.35: Evolution of the velocities of tracer particles in a subsurface layer of cut plane CD. The centripetal motion of two molecules, on the right and on the left of the hot bead, is tracked over time. Same colour scheme adopted for the right (RM) and the left (LM) molecules, despite slightly different time gaps $\tau_{\mathrm{RM}} = 0.7\,\mathrm{s}/\tau_{\mathrm{LM}} = 0.9\,\mathrm{s}$ between their successive positions. Data from the same experiment as in Fig. 3.30 except that stacks of 100 images captured at 17 fps over $\Delta t \approx 6\,\mathrm{s}$ are processed to generate this streamlines view. Further information is the same as in the caption of Fig. 3.31.

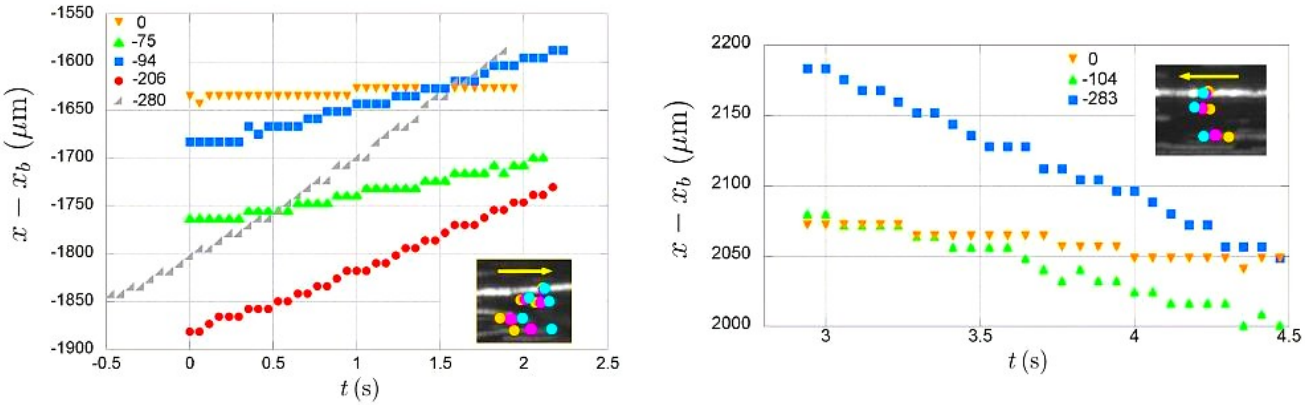

Figure 3.36: Time evolution of the distance to the hot bead $x - x_b$ of the tracer particles forming the left and the right molecules selected in the cut plane CD. Same caption as that of Fig. 3.32 above.

To finish, the mean centripetal velocity of each tracer particle is given in the tables 3.37 (these values are the slopes of the curves displayed in Fig. 3.36). In this case, velocities are clearly lower than those measured in either the centrifugal (plane AB) or the centripetal (around point E) channel. Most importantly, in the swirling flow region CD, subsurface velocities are higher than interfacial ones, contrary to what happens in the centrifugal channel where an intense surface flow is observed. The interface is here in a 'locked state', much like in the quasi−axisymmetric flow regime.

Depth z_{LM} (μm)	Velocity v_{LM} (μm/s)
0	6.6
−75	31
−94	45
−206	73
−280	122

Depth z_{RM} (μm)	Velocity v_{RM} (μm/s)
0	−20
−104	−53
−283	−90

Figure 3.37: Centripetal velocities v of both surface and subsurface tracer particles as a function of depth z (*cut plane CD*). The table on the right (resp. on the left) provides data obtained by tracking the right molecule (RM) (resp. the left molecule (LM)) shown in Fig. 3.35.

In summary, tracer particles move along the centrifugal channel AB at very large speeds in the order of $v \sim 1\,\mathrm{mm/s}$, yet in a shallow subsurface layer and even more at the interface. In comparison with the toroidal base flow state, the relative increase in the flow velocity is more pronounced at the surface (×30) than in the bulk (×14), and significantly higher than the laser powers ratio (×3).

Remarkably, the regions between the vortices of the quadrupole are subject to strong flows characterised by velocities higher at the surface than in the bulk, in conjunction with a 'passing interface'. Though the foregoing results clearly evidence this fact in the sole case of the centrifugal channel, no doubt that the same conclusion applies to the centripetal channel. By contrast, close to the centre of a whirlpool, the situation seems reminiscent of the 'locked interface' reported earlier in the quasi – axisymmetric base state.

3.5 Thermal imprint of the flow symmetry – breaking

We present the findings of our thermographic study of the interfacial flows induced by the hot bead at various heating levels. The results provided here are partly those of A. Mombereau, being thus anterior to this thesis work. Other results were obtained by B. Gorin, a Master student I had the opportunity to co – supervise during his 2018 internship.

Since we suspect 'hydrothermal' couplings, among other possible triggers, to play a key role in the activation of the instability, it is crucial to get a better grasp of how important thermal advection is in the different flow regimes. The flow acts on the temperature field and the temperature gradient moulds the flow in turn, so that any symmetry – breaking of the flow shall be reflected in a symmetry – breaking of the temperature field itself.

Fig. 3.38 compares thermography and streamlines maps of the surface flow at varying heating levels. The quasi – axisymmetric states (A) and (B) exhibit a potato – shaped distribution of their isotherms that slightly departs from the rotation invariant pattern expected for a perfectly axisymmetric base flow. The temperature map of the (unsteady) 'pseudodipolar' flow (C) at $\mathcal{P}_{(\mathrm{C})} \approx 36.8\,\mathrm{mW}$ is crescent – shaped. A dumbbell – shaped repartition of the isotherms, which appears in state (D) ($\mathcal{P}_{(\mathrm{D})} \approx 36.8\,\mathrm{mW}$) and ripens in state (E) ($\mathcal{P}_{(\mathrm{E})} \approx 53.6\,\mathrm{mW}$), accompanies the development of a surface quadrupole. Thus, Fig. 3.38 can be regarded as a pictorial evidence of the correlation that exists between the flow and the temperature field symmetry – breakings. Better still, one can infer the morphology of the surface flow on the sole basis of the temperature (IR) maps.

Let us recall the advection – diffusion heat equation which, in dimensionless form, writes as follows

$$\mathbf{V}.\boldsymbol{\nabla}\Theta = \frac{1}{\mathrm{Pe}}\,\nabla^2\Theta\,, \tag{3.1}$$

where thermal advection is expressed as the scalar product between the flow velocity field $\mathbf{V}$ and the temperature gradient $\boldsymbol{\nabla}\Theta$. The quantity Pe, named the Péclet number and

defined as $\mathrm{Pe} \doteq aU/D$ (a and U denote respectively typical length and velocity scales and D the heat diffusion constant, $D \sim 10^{-7}\,\mathrm{m}^2.\mathrm{s}^{-1}$), compares the magnitudes of thermal advection and diffusion : the larger this dimensionless parameter, the stronger thermal advection with respect to heat diffusion. One inference from Eq. (3.1) is that the strength of thermal advection depends upon the relative orientation of the streamlines and the isotherms, the $\boldsymbol{\nabla}\Theta-$vector being everywhere perpendicular to the $\Theta-$constant curves. This is precisely what we explore while superimposing the flow patterns onto the matching temperature maps (Fig. 3.39) in the base flow state (a) as well as in a multipolar state (b). Two salient features can be reported :

- The streamlines of a surface multipole (*e.g.* quadrupole) are locally tangent to their isotherms, and hence perpendicular to the temperature gradient. The configuration $\mathbf{V} \perp \boldsymbol{\nabla}\Theta$ implies that $\mathbf{V}.\boldsymbol{\nabla}\Theta = 0$, a condition satisfied in the advection$-$dominated limit $\mathrm{Pe} \gg 1$ (zero heat diffusion) as readily checked on Eq. (3.1).

- On the contrary, streamlines are perpendicular to the isotherms in the quasi$-$axisymmetric state and therefore colinear with the temperature gradient. In this diffusion$-$dominated limit ($\mathrm{Pe} \ll 1$, no advection), the flow is driven solely by the surface tension gradient itself proportional to the temperature gradient. It ensues that the velocity $\mathbf{V}$ and the temperature gradient $\boldsymbol{\nabla}\Theta$ are parallel to each other.

To finish, Fig. 3.40 shows the superposition of the streamlines and the temperature maps of a dipolar interfacial flow. Interestingly, a 'thermal plume' propagates in the flow direction, that is along the mirror$-$symmetry axis of the dipole.

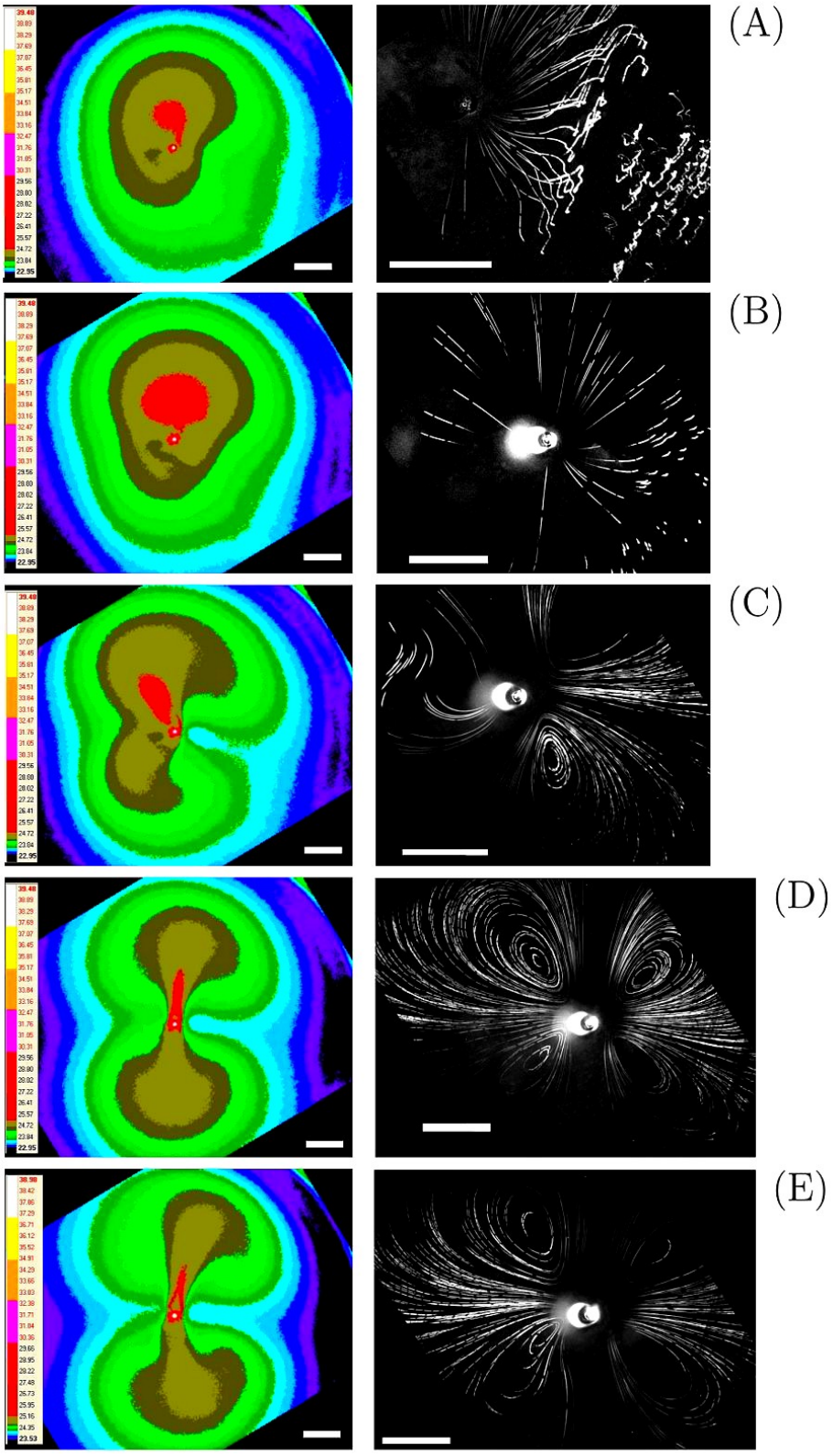

Figure 3.38: 'Hydrothermal' symmetry – breaking. Series of simultaneous temperature (*left*) and streamlines (*right*) maps at increasing power $\mathcal{P}$. (A) Quasi – axisymmetric steady state at $\mathcal{P}_{(A)} \approx 21.8\,\mathrm{mW}$. (B) – (D) Pictures captured $t_{(B)} = 1\,\mathrm{min}$, $t_{(C)} = 2\,\mathrm{min}$ and $t_{(D)} = 4\,\mathrm{min}$ after the heating power is set to $\mathcal{P}_{(B)-(D)} \approx 36.8\,\mathrm{mW}$. (E) Stationary quadrupolar flow at $\mathcal{P}_{(E)} \approx 53.6\,\mathrm{mW}$. Scale bar : 2 mm. *Plate from A. Mombereau's internship report.*

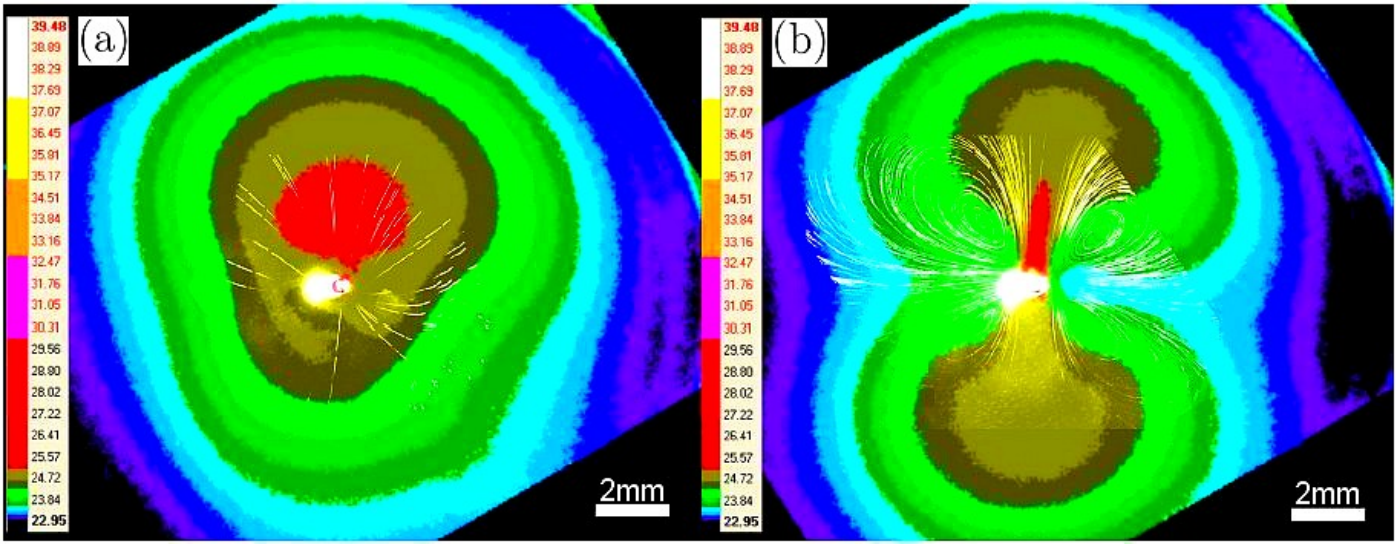

Figure 3.39: Superposed streamlines and temperature maps. (a) quasi−axisymmetric flow; (b) surface quadrupole ($\mathcal{P}_{(a)} = \mathcal{P}_{(b)} = 36.8\,\mathrm{mW}$). Maps superposed in (a) (resp. (b)) are those already shown in Fig. 3.38−(B) (resp. (D)). Very rough absolute temperature values reported next to the colour scales (in °C). *Ibid.*

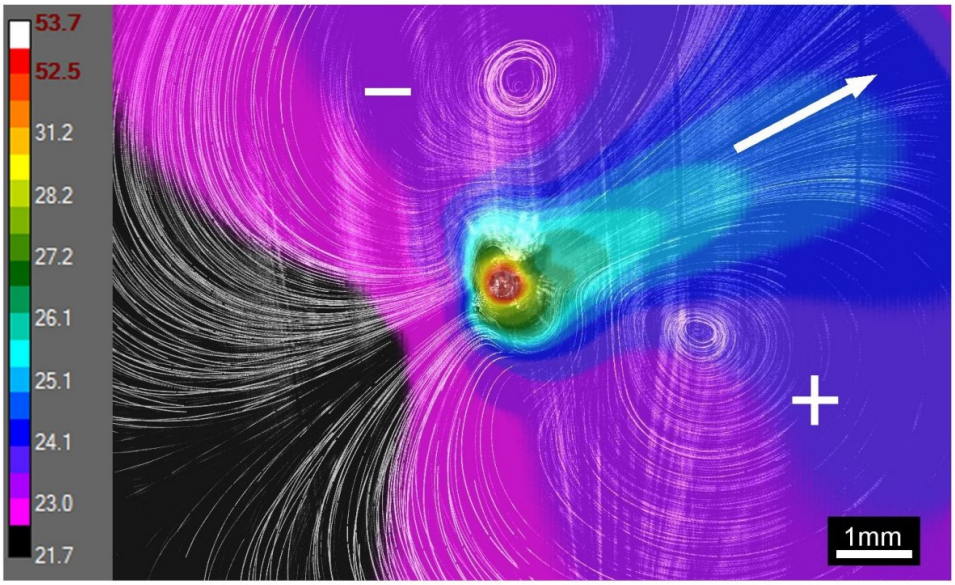

Figure 3.40: Superposed streamlines and temperature maps in the presence of a surface dipole. Heating power $\mathcal{P} \approx 15.4\,\mathrm{mW}$. +/−: clockwise/anticlockwise vortex rotation. Arrow showing the flow direction. Here again, absolute temperatures (in °C) reported on the colour scale are 'false' since temperature measurements are not calibrated. One can only trust temperature differences. Scale of the temperature map harmonised with that of the streamlines optical views (pco.pixelfly used as the bottom camera: 8.22 μm/pix, zoom ×0.75). *Image from B. Gorin's internship report.*

3.6 Discussion

In this chapter, we studied the centrifugal thermocapillary flow that a partially wetted hot bead generates at the water/air interface (Fig. 3.1). In a way similar to what we did in the water jet experiment while increasing the injection speed, the focus was put here on the evolution with increasing heating of the convective flow which develops in the vicinity of the heat source. From a simple convection torus at low temperatures (Fig. 3.8), the flow destabilises into multipolar structures at sufficiently high heating powers (Fig. 3.9), much like what we reported in the water jet experiment. This (at least qualitative) analogy between the flows induced by the hot bead and the water jet is *a priori* far from being self–evident, owing to the different nature of the flow enforced in each case, thermally driven with the hot bead but 'pressure–driven' with the water jet. Note that no SDS has been added here to the liquid. We actually learnt, from numerical simulations achieved by J-C. Loudet in the water jet configuration, that further adding a controlled amount of a surfactant material is of little avail as far as the flow structure and size are concerned.

The hot bead experiment exhibits a higher level of complexity compared with the water jet, since the temperature field Θ is here coupled to the flow velocity $\mathbf{V}$ in addition to the surfactant concentration field Γ. Therefore, one has to consider both heat and mass advection–diffusion equations

$$\partial_t \Theta + \mathbf{V}.\boldsymbol{\nabla}\Theta = D_T \nabla^2 \Theta + \Sigma\,, \tag{3.2a}$$

$$\partial_t \Gamma + \boldsymbol{\nabla}_{\parallel}.\left(\mathbf{V}_{\parallel}\Gamma\right) = D_S \nabla_{\parallel}^2 \Gamma, \tag{3.2b}$$

with D_T and D_S the heat and mass diffusion constants, respectively. The notation '$\boldsymbol{\nabla}_{\parallel}$' denotes the 2D projection of the nabla operator onto the plane of the interface. I do not dwell on the 'source–term' Σ that will be specified in the next chapter. Note that there is no term accounting for mass exchanges between the surface and the bulk in the right–hand side of Eq. (3.2b) as we consider only insoluble surfactants. When rewriting these equations in dimensionless form, two parameters quantifying the relative contribution of heat (resp. surfactant) diffusion and advection naturally appear. The latter, called the thermal (resp. solutal) Péclet number Pe_T (resp. Pe_S), are defined as

$$\mathrm{Pe}_T \doteq \frac{Ua}{D_T}\,, \quad \text{and} \quad \mathrm{Pe}_S \doteq \frac{Ua}{D_S}\,, \tag{3.3}$$

where a and U are typical length and velocity scales, respectively. Given that the mass diffusion constant $D_S = 10^{-9} - 10^{-10}\,\mathrm{m}^2.\mathrm{s}^{-1}$ is two to three orders of magnitude smaller than the heat diffusion constant $D_T = 10^{-7}\mathrm{m}^2.\mathrm{s}^{-1}$, we have $\mathrm{Pe}_S \gg \mathrm{Pe}_T$ meaning that

the physics of the system is dominated by the advective transport of surfactant molecules along the interface. We recall that the Reynolds number, defined as the ratio of inertial to viscous forces $\mathrm{Re} \doteq Ua/\nu$ (ν: water kinematic viscosity, $\nu \sim 10^{-6}\,\mathrm{m}^2/\mathrm{s}$ under standard conditions), is in the order of $\mathrm{Re} \sim 10^{-2}$ in the hot bead experiments (taking a bead radius $a \sim 100\,\mu\mathrm{m}$ and a Marangoni velocity $U \sim 100\,\mu\mathrm{m/s}$) so that inertia is negligible.

The 'hydrosolutal' ($\mathbf{V}$, Γ)–coupling has been evidenced by the direct manifestation of surface elasticity in laser shutdown experiments: interfacial tracer particles reverse their motion, from centrifugal to centripetal, at the precise moment the laser is switched off (Fig. 3.25). As for the 'hydrothermal' ($\mathbf{V}$, Θ)–coupling, thermography revealed the 'thermal signature' of the flow symmetry–breaking, with streamlines either perpendicular (in the quasi–axisymmetric base state) or tangent (in the presence of multipoles) to the isotherms (Fig. 3.39). Yet, evaluating the prominence/negligibility of thermal advection in the different flow regimes and at varying distances from the heat source, through the value of $\mathbf{V}.\boldsymbol{\nabla}\Theta$ or, equivalently, that of the Péclet number Pe_T, requires a comprehensive knowledge of the flow and the temperature fields that is currently lacking.

Again, we have shown that the base torus is in a 'locked' interfacial state characterised by subsurface velocities significantly higher than surface ones (Figs 3.14–3.15 and 3.19) which, due to thermal diffusion, are not strictly zero contrary to the case of the jet. Tracking interfacial tracer particles along their centrifugal radial trajectories, we found that their distance r to the heat source evolves in time as $t^{1/3}$ (Figs 3.21–3.23), resulting in a decrease of the surface velocity $\sim 1/r^2$. Such experimental findings go against the image of a pristine interface only subject to a thermocapillary flow, for which one naturally expects the flow velocity to be highest at the surface ($z = 0$) owing to maximum shear stresses out there. Moreover, in the viscous flow regime ($\mathrm{Re} \ll 1$) considered here, we have $\mathrm{Pe}_S \gg 1$ but $\mathrm{Pe}_T \ll 1$, so that Eq. (3.2a) simplifies to the heat diffusion equation and the steady–state radial component of the interfacial velocity is then given by [3]

$$v_r(r, z = 0) = U\left(\frac{a}{r}\right), \tag{3.4}$$

a power decay different from the experimental one. This discrepancy between theoretical predictions and experimental observations can only be explained by the existence of a surfactant elastic layer at the interface that damps the surface dynamics.

Besides that, we characterised the quadrupolar flow mode, something not achieved in the water jet experiments. Sharp surface velocity gradients have been uncovered between the 'intervortex channels', where intense inward/outward flows are visible, and the core

regions near vortex centres where the flow almost vanishes (compare the experimental data of both tables 3.33 and 3.37). Most importantly, the channels are in a 'passing' interfacial state characterised by a flow velocity higher at the surface than in the bulk, whereas a reversed 'up – down hierarchy' among velocities is noted in the central regions which is strongly reminiscent of the 'locked' interfacial state reported for the base torus.

Surfactants are repelled by the dilatational flow towards the edges of the cell – whether the source flow is thermocapillary like in the present experiment or 'mechanical' like in the water jet experiment – which induces a solutocapillary counterflow in response to the inhomogeneous distribution of impurities along the interface. We conjecture that the instability results from the periodic azimuthal deformation of the elastic depletion front under the action of high shear stresses these competing flows induce locally (Fig. 3.41). Such an instability mechanism has been already proposed by Couder *et al.* [49] to account for multipolar flow patterns developing on the surface of horizontal soap films blown by a vertical air jet, a practical situation that closely resembles our water jet experiment. The experimental verification of this conjecture requires the direct visualisation of surfactant molecules. One can use some fluorescence – labeled surfactant, a standard approach in biological sciences. Note that it is possible to probe the state of the surfactant layer using Brewster angle microscopy (see [53] for a presentation of this technique).

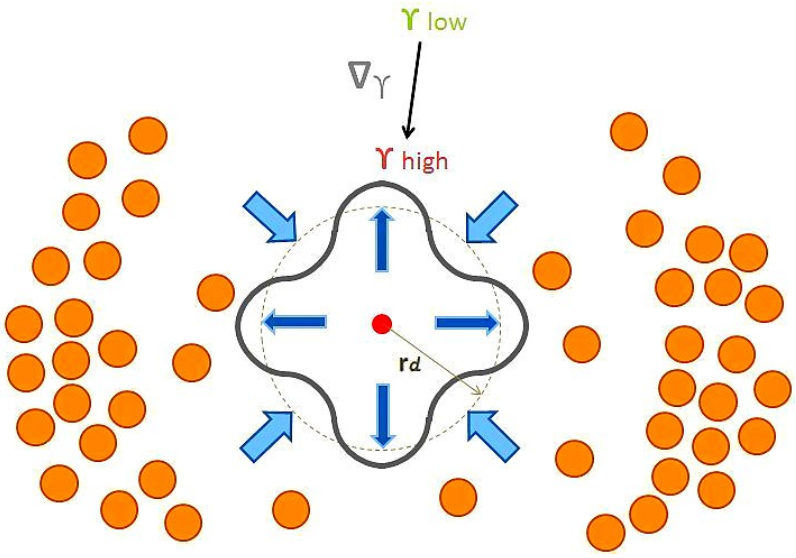

Figure 3.41: Postulated instability mechanism. Surfactant molecules (orange balls) repelled beyond a depletion radius r_d from the heat/matter source (red disk) lower the surface tension (γ_{low}) in the region close to the cell walls (not drawn). The competition between the centrifugal forced flow (deep blue arrows) and the solutocapillary counterflow (light blue arrows) periodically bends the depletion front (four – lobed grey line). The instability arises beyond a critical surface tension gradient $\boldsymbol{\nabla}\gamma$.

I also want to stress the unpredictability of the flow state marked by mode competition (Fig. 3.12). Tempting though it may be to ascribe the great spatiotemporal variability of the flow patterns to hysteresis in the 'hydrothermal history' of the system, it could equally well be attributed to unsteady effects. Anyhow, all this results in poorly reproducible hot bead experiments. Factors which may explain this situation are numerous, starting with all physical mechanisms responsible for fluctuations of the contact line, such as intense evaporation in the vicinity of the bead that affects its wetting configuration or asperities randomly distributed on its surface on which the contact line transiently gets pinned.

Let me add a few words about a serendipitous observation we made while changing the degree of immersion of the bead. A pulsatile flow would arise as the bead was fully immersed, a phenomenon that can be regarded as another manifestation of the elasticity of the surfactant–laden interface (Fig. 3.42). Interestingly, varying either the heating power or the immersion depth of the bead allows modulating the pulse frequency of the flow. Further experiments are needed to underpin these observations.

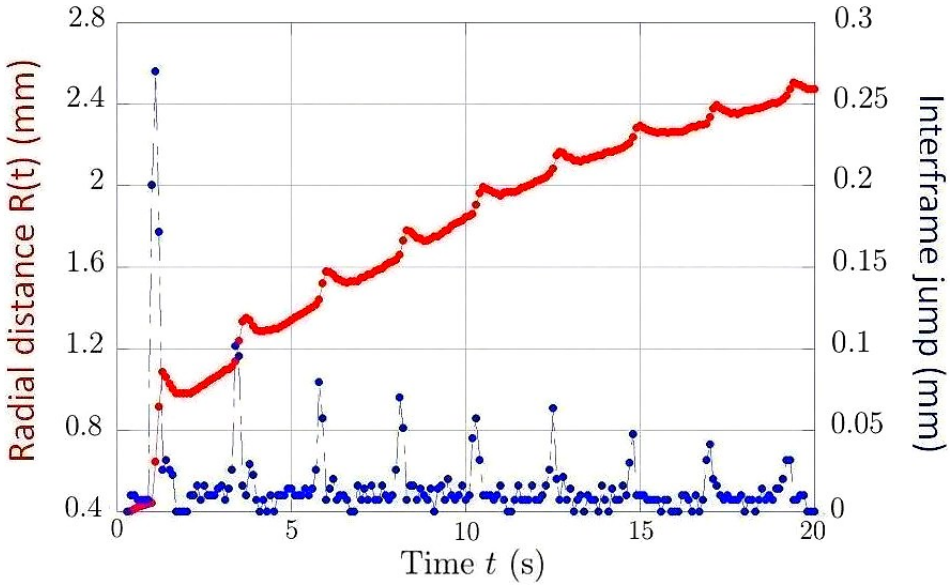

Figure 3.42: Pulsatile flow. (*Red curve*) Jerky time evolution of the radial distance R of a tracer particle to the hot bead. (*Blue curve*) 'Jumps' in the position of the tracer particle between frames n and $n+1$ used for estimating its speed (values $\times 10\,\mu$m/s). Hot bead fully immersed at Z $= -1$ mm underwater. Heating power: $\mathcal{P} \approx 97$ mW. Pulse period: $\mathcal{T}_{\text{pulse}} \approx 2.25$ s. Data from a record at 10 fps.

It is not the first time that oscillatory regimes are reported in systems where Marangoni convection is at play, leading to both experimental [54] and theoretical [55] investigations. Note the striking resemblance between our practical situation and the experimental setup

depicted in Fig. 2 of ref. [56], the only clear difference being that there a surfactant droplet is immersed instead of a hot bead, meaning that in this case spontaneous oscillations arise from solutocapillary rather than thermocapillary convection. As a matter of fact, it may be that the flower–like azimuthal instability we are interested in is related to hydrothermal waves (see for instance [57, 58]), a hypothesis suggested by the existence of star–shaped standing waves as the one shown in Fig. 4–(c) of [55].

To finish, I would like to mention Shtern and Hussain's theoretical analysis of the azimuthal instability [59]. They defend the thesis of an inertial origin of the instability, basing their study on the exact solution of the 'Navier–Stokes–Fourier' problem derived earlier by Bratukhin and Maurin [60]. Surprisingly, they predict that the quadrupole is the first unstable mode (onset at a critical Reynolds $\mathrm{Re}_c = 115$), not the dipole. However, recent observations [2] revealed that the flower–like azimuthal instability studied in the present work exists including at very small scales ($5\,\mu$m magnetic spheres were trapped in a two–beam optical levitator), which seems to rule out the scenario proposed in [59].

In the next chapter, we will address theoretically the problem of the thermocapillary convection induced by a point heat source localised at the water/air interface, solving the incompressible Stokes equation within the half–space filled with water. An exact solution will also be derived in the nonlinear temperature–advected regime and the theoretical groundwork on which to build a model of the instability will be laid down.

Chapter 4

The route towards a theory of the instability

In this chapter, we lay the theoretical groundwork on which to build a description of the azimuthal instability observed in the hot bead experiment. In sec. 4.1, we provide the physical framework of our study by presenting the governing equations of the system accompanied by a set of boundary conditions. In sec. 4.2, an axisymmetric solution is worked out analytically in the presence of thermal advection. This particular solution is viewed as the ground state meant to model the base flow observed under slight heating conditions. A generalised form of the Lamb's solution [61], derived from a non−standard solving of the Stokes equation within a half−space, is provided in sec. 4.3. Finally, in order to grasp the azimuthal instability, the ground state derived in sec. 4.2 shall be perturbed by non−axisymmetric states picked from this 'hemispherical' Lamb's solution (sec. 4.4).

4.1 Problem formulation

We study the thermocapillary flow induced by a pointlike heat source at the water/air interface. The excess temperature arising in the vicinity of the hot spot creates surface stresses that drive the fluid motion, a phenomenon called the Marangoni effect. Let water fill a cylindrical vessel of radius R and height h such that the upward oriented axis (unit vector $\mathbf{e}_z$) coincides with its revolution axis. In the following, we assume a perfectly flat interface located at $z = 0$ (see Appendix I for a justification of this hypothesis).

The Navier – Stokes equation, which governs the evolution of the velocity $\mathbf{V}$ of a flow subjected to an internal pressure gradient $\boldsymbol{\nabla}\mathrm{P}$, writes (Appendix I)

$$\rho\left(\partial_t \mathbf{V} + \mathbf{V}.\boldsymbol{\nabla}\mathbf{V}\right) = \eta\boldsymbol{\nabla}^{\mathbf{2}}\mathbf{V} - \boldsymbol{\nabla}\mathrm{P}\,, \tag{4.1}$$

where η and ρ are the fluid dynamic viscosity and mass density, respectively. Temperature variations are assumed slight enough for these quantities to be temperature – independent. At room temperature $\mathrm{T}_{room} \approx 20°\mathrm{C}$ and under atmospheric pressure $\mathrm{P}_{atm} \approx 1\mathrm{bar}$ (STP : Standard Temperature and Pressure conditions), $\eta \sim 10^{-3}\,\mathrm{Pa.s}$ and $\rho \sim 10^{3}\,\mathrm{kg.m^{-3}}$.

Let a be some characteristic length scale of the system and U denote the typical flow velocity scale. Defining the following quantities

$$\mathbf{r} \doteq \frac{\mathbf{R}}{a}\,,\quad \mathbf{v} \doteq \frac{\mathbf{V}}{U}\,,\quad \mathrm{p} \doteq \frac{\mathrm{P}}{(\eta U/a)}\,,\quad \tilde{t} \doteq \frac{t}{(a/U)}\,, \tag{4.2}$$

enables one to rewrite Eq. (4.1) in dimensionless form

$$\mathrm{Re}\left(\partial_{\tilde{t}}\mathbf{v} + \mathbf{v}.\boldsymbol{\nabla}\mathbf{v}\right) = \boldsymbol{\nabla}^{\mathbf{2}}\mathbf{v} - \boldsymbol{\nabla}\mathrm{p}\,, \tag{4.3}$$

where $\boldsymbol{\nabla}\bullet \doteq \frac{\mathrm{d}}{\mathrm{d}\mathbf{r}}\bullet$. The dimensionless parameter $\mathrm{Re}\,(a, U)$ is called the Reynolds number. The latter can be interpreted as the ratio between the magnitudes of the inertial $\rho\mathbf{V}.\boldsymbol{\nabla}\mathbf{V}$ and the viscous $\eta\boldsymbol{\nabla}^{\mathbf{2}}\mathbf{V}$ terms or, equivalently, as the ratio between the characteristic times $\tau_{\mathrm{diff}} = a^2/\nu$ ($\nu \doteq \eta/\rho$: kinematic viscosity) and $\tau_{\mathrm{conv}} = a/U$ associated with momentum diffusion and convection over the length a. The Reynolds number is therefore given by

$$\mathrm{Re} = \frac{Ua}{\nu}\,. \tag{4.4}$$

In what follows, we focus our attention on stationary flow regimes so that we drop the partial time derivative in Eq. (4.3). Inertial effects are further disregarded ($\mathrm{Re} \ll 1$) since we consider relatively small length and velocity scales (in the experiments, we have

$a \sim 100\,\mu$m and $U \sim 100\,\mu$m/s yielding Re $\sim 10^{-2}$). Consequently, the Navier – Stokes equation (4.3) reduces to the much simpler Stokes equation

$$\boldsymbol{\nabla^2 \mathbf{v}} = \boldsymbol{\nabla} \mathrm{p}\,. \tag{4.5}$$

We assume an incompressible fluid. The continuity equation expressing the volume conservation of a flow subjected to pressure reads

$$\boldsymbol{\nabla .}\, \mathbf{v} = 0\,. \tag{4.6}$$

Eqs (4.5) – (4.6) form the purely hydrodynamic part of the problem addressed here. These equations are supplemented by the advection – diffusion heat equation

$$\rho c_p \left(\partial_t \Theta + \mathbf{V}.\boldsymbol{\nabla}\Theta\right) = \kappa \nabla^2 \Theta + Q\,\delta(\mathbf{R})\,, \tag{4.7}$$

with Q the total heating power radiated by the pointlike heat source[1,2]. c_p and κ stand for the specific heat capacity and thermal conductivity of the liquid, respectively. Both are assumed constant despite a non – uniform temperature distribution. Along with the mass density ρ, they define the thermal diffusivity as $D \doteq \kappa/(\rho c_p)$. For water under STP conditions, $c_p \approx 4.2 \times 10^3\,\mathrm{J.\,kg^{-1}.\,K^{-1}}$ and $\kappa \approx 0.6\,\mathrm{W.\,m^{-1}.\,K^{-1}}$ so that $D \sim 10^{-7}\,\mathrm{m^2.\,s^{-1}}$.

Using again definitions (4.2) together with a 'temperature field' $\vartheta \doteq \Theta/\Delta T$ yields the following dimensionless form of Eq. (4.7)

$$\mathrm{Pe}\left(\partial_{\tilde{t}}\,\mathbf{v} + \mathbf{v}.\boldsymbol{\nabla}\vartheta\right) = \nabla^2\vartheta + q\,\delta(\mathbf{r})\,, \qquad q = \frac{Q}{\kappa \Delta T a}\,, \tag{4.8}$$

with the Péclet number Pe defined as

$$\mathrm{Pe} = \frac{Ua}{D}\,. \tag{4.9}$$

Note the strong similarity between Eqs (4.3) and (4.8) : the Péclet number Pe plays for heat transport a role analogous to the Reynolds number Re for momentum transport, the thermal diffusivity D appearing as the counterpart of the kinematic viscosity ν.

[1] We assume a 'perfect source' in the sense that 100% of the energy it absorbs is supposed to heat the liquid. This explains why Q is here below indifferently called the 'injected power' or the 'heating power'.

[2] In fact, assuming a pointlike heat source amounts to making the hypothesis that its spatial extent a is much smaller than the radius R of the container, $a \ll R$. In the viewing area such that $a \ll |\mathbf{R}| \ll R$, the source can be approximated as a point whose power density is expressed as $Q_v(\mathbf{R}) = Q\delta(\mathbf{R})$ introducing naturally the Dirac delta distribution $\delta(\mathbf{R})$, while the size of the vessel then becomes irrelevant.

Once again, attention is paid to steady flow regimes and thus Eq. (4.8) restricts to

$$\mathrm{Pe}\,\mathbf{v}.\boldsymbol{\nabla}\vartheta = \nabla^2\vartheta + q\,\delta(\mathbf{r})\,, \tag{4.10}$$

where the velocity field $\mathbf{v}$ derived beforehand from Eqs (4.5) – (4.6) appears as an input. Eq. (4.10) invites us to view the Péclet number Pe measuring the intensity of thermal advection as a control parameter that can be tuned by varying the amount of injected power Q. Thermal advection prevails in the asymptotic regime $\mathrm{Pe} \gg 1$. Conversely, in the diffusive limit we have $\mathrm{Pe} \ll 1$ and one is then left with a set of purely linear equations.

As usual, boundary conditions specific to our framework 'close' the differential system. The boundary condition at the very heart of this study is the Marangoni condition

$$\eta\left(\boldsymbol{\nabla}_{\parallel}\mathrm{V}_z + \partial_z\mathbf{V}_{\parallel}\right)\big|_{z=0} = \boldsymbol{\nabla}_{\parallel}\,\gamma\,, \tag{4.11}$$

where the projection of a vector $\mathbf{a}$ onto the horizontal (xy) – plane of the interface $(z=0)$ is defined as $\mathbf{a}_{\parallel} \doteq (\mathbb{1} - \mathbf{e}_z\mathbf{e}_z)\,.\,\mathbf{a}$. This relation stating that surface tension inhomogeneities induce shear stresses at the interface that put the fluid into motion is the mathematical expression of the Marangoni effect. A key ingredient of our study is the linearised equation of state satisfied by the temperature – dependent surface tension $\gamma(\Theta)$ for slight deviations from its equilibrium value $\gamma_0 = \gamma(\Theta_0)$

$$\gamma(\Theta) = \gamma_0 - \gamma_{\mathrm{T}}\,(\Theta - \Theta_0)\ . \tag{4.12}$$

As the constant $\gamma_{\mathrm{T}} \doteq |\mathrm{d}\gamma/\mathrm{d}\Theta|$ is in the order of $\gamma_{\mathrm{T}} \sim 10^{-4}\,\mathrm{N.\,m^{-1}.\,K^{-1}}$ [40], this equation is valid over a wide temperature range. The surface tension decreasing with increasing temperature, liquid is pulled from the hot to the cold regions of the interface at a typical speed $U \sim \gamma_{\mathrm{T}}\Delta T/\eta$. In the geometry under consideration, a centrifugal thermocapillary flow extends from the hot bead in central position to the edges of the cylindrical container.

On top of that, we assume a zero mass flux across the interface

$$\mathrm{V}_z\big|_{z=0} = 0\,. \tag{4.13}$$

The thermal conductivity of water being far larger than that of air (under STP conditions $\kappa_{air} \approx 0.0234\,\mathrm{W.\,m^{-1}.\,K^{-1}}$, $\kappa_{water} \approx 26\,\kappa_{air}$) amounts to neglecting any heat flux through the interface

$$\partial_z\Theta\big|_{z=0} = 0\,. \tag{4.14}$$

Obviously, such assumptions no longer hold in the presence of evaporation (Appendix I).

In sum, we aim at solving the $(\mathbf{v},\vartheta)-$coupled system of partial differential equations

$$\boldsymbol{\nabla^2}\mathbf{v} = \boldsymbol{\nabla}\mathrm{p}\,, \tag{4.15a}$$

$$\boldsymbol{\nabla}.\,\mathbf{v} = 0\,, \tag{4.15b}$$

$$\mathrm{Pe}\,\mathbf{v}.\boldsymbol{\nabla}\vartheta = \nabla^2\vartheta + q\,\delta(\mathbf{r})\,, \tag{4.15c}$$

with the additional requirements that far away from the heat source : (1) the temperature returns to its equilibrium value entailing the suppression of all Marangoni stresses and hence a zero thermocapillary velocity; (2) the overall flow velocity falls to zero and (3) the pressure field tends to a constant value

$$\vartheta, \mathbf{v}, \mathrm{p} \underset{|\mathbf{r}|\to+\infty}{\longrightarrow} \vartheta_0, \mathbf{0}, \mathrm{p}_0\,. \tag{4.16}$$

The latter equations are supplemented by the boundary conditions

$$\frac{1}{r}\Big[r\,\partial_r \mathrm{v}_\theta - \mathrm{v}_\theta - \partial_c \mathrm{v}_r\Big]\Big|_{c_I=0} = -\,\partial_r\vartheta\,|_{c_I=0}\,, \tag{4.17a}$$

$$\Big[\partial_\varphi \mathrm{v}_\theta - \partial_c \mathrm{v}_\varphi\Big]\Big|_{c_I=0} = -\,\partial_\varphi\vartheta\,|_{c_I=0}\,, \tag{4.17b}$$

$$\mathrm{v}_\theta|_{c_I=0} = 0\,, \tag{4.17c}$$

$$\partial_c\vartheta|_{c_I=0} = 0\,, \tag{4.17d}$$

in spherical polar coordinates (r,θ,φ) including in general the azimuthal (φ) dependence. Introducing the parameters $c \doteq \cos\theta$ and $s \doteq \sin\theta = \sqrt{1-c^2}$ instead of simply working with the polar angle θ greatly simplifies the calculations. For convenience, we consider that water fills the upper half–space $z \geqslant 0$ wherein $c \in [0,1]$, the position $c_I = 0$ $(\theta_I = \pi/2)$ corresponding to the interfacial plane (normal unit vector $\mathbf{n} \equiv \mathbf{e}_\theta$). For later purposes, the equations are here written in dimensionless form with special emphasis on the '$r-$ and $\varphi-$Marangoni' boundary conditions (4.17a) – (4.17b).

4.2 The base flow state

As an initial step, our goal is to derive the axisymmetric solution to the advection–diffusion problem in the far–field limit, *i.e.* for a pointlike heat source. This solution is considered as the base flow state whose stability in response to azimuthal perturbations shall be probed (sec. 4.4). For comparison's sake, we first derive the temperature field in the purely diffusive regime $\mathrm{Pe} = 0$ prior to addressing the nonlinear regime of finite Péclet numbers $\mathrm{Pe} \neq 0$ for which heat is also transported through advection.

4.2.1 Linear regime $\mathrm{Pe} = 0$

Temperature field

In the diffusive regime $\mathrm{Pe} = 0$, the differential system (4.15a) – (4.15c) becomes linear as the temperature field is then fully decoupled from the flow. In this case, the temperature turns out to be a harmonic function, namely a function obeying the Laplace's equation

$$\nabla^2 \vartheta = 0\,. \tag{4.18}$$

This equation is readily solved in spherical polar coordinates (r, θ, φ) using the method of separation of variables. Since the corresponding derivation can be found in any textbook of mathematical physics, let me simply recall the general solution

$$f(r,\theta,\varphi) = \sum_{l=0}^{+\infty} \sum_{m=-l}^{+l} \left[A_{lm} r^l + \frac{B_{lm}}{r^{l+1}} \right] \left\{ C_{lm} P_l^m(\cos\theta) + D_{lm} Q_l^m(\cos\theta) \right\} \mathrm{e}^{im\varphi}\,, \tag{4.19}$$

where the $\{P_l^m(\cos\theta)\}$ and the $\{Q_l^m(\cos\theta)\}$ are the associated Legendre polynomials of the first and the second kind, respectively. We will discuss in sec. 4.3 how and why this general solution shall be modified in our study. Let us precise right now that the $\{Q_l^m\}$ functions are irrelevant in most physics problems because of their diverging behaviour. The terms $\sim r^l$ in the radial part of expression (4.19), in addition to diverging at infinity, are associated with the solution to the Laplace's equation inside a sphere (see refs [64, 65]) and are thus discarded from the current analysis which assumes a pointlike heat source.

In our case, expression (4.19) yields the following far – field axisymmetric temperature in the diffusive regime ($P_0^0 = 1$)

$$\Theta(|\mathbf{R}|) = \Theta_0 + \Delta T \frac{a}{\sqrt{\mathrm{R}^2 + \mathrm{Z}^2}}\,, \qquad \mathbf{R} = \mathrm{R}\mathbf{e}_r + \mathrm{Z}\mathbf{e}_z\,, \tag{4.20}$$

which fulfills the condition $\Theta \to \Theta_0$ far from the heat source ($|\mathbf{R}| \to +\infty$). For latter purposes, it is useful to define $a\Delta T \doteq Q/(2\pi\kappa)$. Even though no intrinsic length scale is considered in the model, this relation offers a convenient way of linking the injected power Q to the temperature elevation ΔT on the surface of the heat source. Evaluated at the interface $\mathrm{Z} = 0$ and rewritten in dimensionless form, expression (4.20) becomes

$$\boxed{\vartheta^{(0)}(r) = \frac{\psi^{(0)}(0)}{r}\,,} \tag{4.21}$$

where $\psi^{(0)}(0)$ represents the interfacial temperature amplitude in the diffusive regime $\mathrm{Pe} = 0$ flagged with the superscript '$^{(0)}$'.

Velocity field

Let us now derive the velocity field $\mathbf{v}^{(0)}$. Although there is no coupling between the temperature and the velocity in the purely diffusive regime $\mathrm{Pe} = 0$, in the sense that the advective nonlinearity is then ruled out, both fields are related through the Marangoni boundary conditions (4.17a) – (4.17b) at the interface where the temperature field shapes the velocity. It is proper to seek velocity components that are $\sim 1/r$, since this choice complies with the radial Marangoni boundary condition (4.17a) which then balances terms that are all $\sim 1/r^2$ on both sides of the equation

$$\underbrace{\frac{1}{r}\left[r\,\partial_r\left(\tfrac{1}{r}\bullet\right) - \left(\tfrac{1}{r}\bullet\right) - \partial_c\left(\tfrac{1}{r}\bullet\right)\right]\Big|_{c_I=0}}_{\sim 1/r^2} = \underbrace{-\,\partial_r\vartheta\,|_{c_I=0}}_{\sim 1/r^2}\,,$$

where the temperature field is the one given by (4.21). Note that the azimuthal Marangoni boundary condition (4.17b) yields $\mathrm{v}_\varphi = 0$ as a direct consequence of axisymmetry.

Solving the Stokes equation (4.15a) to work out the velocity field $\mathbf{v}^{(0)}$ requires deriving first the pressure field. The divergence of the Stokes equation reveals that the pressure field is a harmonic function[3] (as the temperature in this regime) and thus satisfies

$$\nabla^2\mathrm{p} = 0\,. \tag{4.22}$$

We have just seen why it is appropriate to look for velocity components scaling as $1/r$, in keeping with the r – Marangoni boundary condition. In the same spirit, balancing the powers of $1/r$ on both sides of the Stokes equation

$$\underbrace{\boldsymbol{\nabla^2}\mathbf{v}}_{\sim(1/r^2)\times(1/r)=\,1/r^3} = \underbrace{\boldsymbol{\nabla}\mathrm{p}}_{\sim(1/r)\times ???=\,1/r^3}\,,$$

calls for a pressure field $\mathrm{p} \sim 1/r^2$. The general solution (4.19) to the Laplace's equation elucidated in the case $l = 1$ then yields the pressure field

$$\mathrm{p}_{(10)}(r,c) = \frac{\pi_{(10)}}{r^2}\,P_1^0(c) = \frac{\pi_{(10)}}{r^2}\,c\,, \tag{4.23}$$

where the subscript '(10)' means $l = 1$ and $m = 0$ (axisymmetric state). The notation $\pi_{(10)}$ for the integration constant anticipates on the general derivation to come in sec. 4.3.

[3] This property is actually a direct consequence of fluid incompressibility. Indeed, we have $\boldsymbol{\nabla}.\boldsymbol{\nabla^2}\mathbf{v} = \nabla^2\left(\boldsymbol{\nabla}.\mathbf{v}\right) = 0$ only because $\boldsymbol{\nabla}.\mathbf{v} = 0$.

Projecting next the vector Stokes equation (4.15a) onto the axes of the spherical basis, we are left with the following differential system for $(lm) = (10)$

$$\left[s^2 v'_{r,(10)}\right]' = -2p_{(10)}\,, \tag{4.24a}$$

$$\left[s^2 v'_{\theta,(10)}\right]' - \frac{1}{s^2}\, v_{\theta,(10)} = 2s v'_{r,(10)} - s p'_{(10)}\,, \tag{4.24b}$$

$$\left[s^2 v'_{\varphi,(10)}\right]' - \frac{1}{s^2}\, v_{\varphi,(10)} = 0\,, \tag{4.24c}$$

where the primed quantities are derivatives with respect to c. These are equations for the polar part $\{v_{j,(10)}(c)\}_{j\in\{r,\theta,\varphi\}}$ of the velocity components since the radial part, already set in our representation of the fields, here acts as a global prefactor which is ultimately ruled out. Eq. (4.24a) corresponds to the projection of the vector Stokes equation (4.15a) onto the radial direction, while Eqs (4.24b) – (4.24c) are the polar ($\theta-$angular) and azimuthal ($\varphi-$angular) Stokes equations, respectively. Due to axisymmetry, the latter equation is completely uncoupled from the first two equations, so that the function $v_{\varphi,(10)}(c)$ can be derived in a fully independent way.

With expression (4.23) for the pressure field, the differential equation we need to solve in order to derive the radial velocity component $v_{r,(10)}$ writes

$$\left[s^2 v'_{r,(10)}\right]' = -2\pi_{(10)} c\,. \tag{4.25}$$

Integrating this equation once with respect to c and dividing all terms by s^2 ($c \neq 1$) yields

$$v'_{r,(10)}(c) = -\pi_{(10)} \frac{c^2}{1-c^2} + \frac{K_{r,(10)}}{1-c^2}\,, \tag{4.26}$$

with $K_{r,(10)} \in \mathbb{R}$ a second integration constant. Making use of the standard antiderivative $\int 1/(1-c^2)\,\mathrm{d}c = (1/2)\ln[(1+c)/(1-c)] + cst$, we soon arrive to the expression

$$v_{r,(10)}(c) = \pi_{(10)} c + \frac{\bar{K}_{r,(10)}}{2} \ln\left(\frac{1+c}{1-c}\right) + \widetilde{K}_{r,(10)}\,. \tag{4.27}$$

But then regularising this form in $c_s = 1$ necessarily imposes that $\bar{K}_{r,(10)} = 0$. In fact, $(1/2)\ln[(1+c)/(1-c)] = Q_0^0(c)$ is the $(lm) = (00)$ associated Legendre polynomial of the second kind that has to be removed from the physical solution because of its logarithmic singularity at the branch point $c_s = 1$. Finally, the radial velocity $v_{r,(10)}$ is given by

$$v_{r,(10)}(c) = \pi_{(10)} c + \rho_{(-10)}\,, \tag{4.28}$$

where the constant $\widetilde{K}_{r,(10)}$ is renamed $\rho_{(-10)}$ to comply with forthcoming notations.

We next turn to Eq. (4.24b) for the polar velocity component $v_{\theta,(10)}$. We have now everything that is needed to elucidate the right–hand side of this equation and get

$$(1-c^2)\,v''_{\theta,(10)}(c) - 2c\,v'_{\theta,(10)}(c) - \frac{1}{1-c^2}\,v_{\theta,(10)}(c) = \pi_{(10)}s\,. \tag{4.29}$$

By virtue of the linearity of the Stokes equation, the function $v_{\theta,(10)}$ can be viewed as the superposition of the homogeneous solution $v^{\mathcal{H}}_{\theta,(10)}$ and a particular solution $v^{P}_{\theta,(10)}$ of the whole equation (4.29), $v_{\theta,(10)}(c) = v^{\mathcal{H}}_{\theta,(10)}(c) + v^{P}_{\theta,(10)}(c)$. To lighten the notation, the subscript '(10)' is dropped for a while.

One can readily check that the homogeneous solution of Eq. (4.29) is of the form

$$v^{\mathcal{H}}_{\theta}(c) = \frac{1}{\sqrt{1-c^2}}\left[\sigma^{\star}c + \sigma^{\star\star}\right]. \tag{4.30}$$

This last form evidently diverges in $c_s = 1$ and hence must be regularised in that point. Regularisation is here straightforward and leads to the necessary condition $\sigma^{\star\star} = -\sigma^{\star}$ and consequently to

$$v^{\mathcal{H}}_{\theta}(c) = -K^{\mathcal{H}}_{\theta}\sqrt{\frac{1-c}{1+c}}\,. \tag{4.31}$$

As usual, the particular solution v^{P}_{θ} is searched in the form of the right–hand side $v^{P}_{\theta}(c) = K^{P}_{\theta}s$. Differentiating this form twice with respect to c and inserting the results in Eq. (4.29) yields by identification $K^{P}_{\theta} = -\pi_{(10)}/2$, so that we end up with

$$v^{P}_{\theta}(c) = -\frac{\pi_{(10)}}{2}\,s\,, \tag{4.32}$$

and thereby

$$v_{\theta,(10)}(c) = -\frac{\pi_{(10)}}{2}\sqrt{1-c^2} - \rho_{(-10)}\sqrt{\frac{1-c}{1+c}}\,, \tag{4.33}$$

where the above integration constant $K^{\mathcal{H}}_{\theta}$ has been renamed $\rho_{(-10)}$ in order to match with the general expressions that we will derive in sec. 4.3.

To finish, one remarks that Eq. (4.24c) for the azimuthal velocity component $v_{\varphi,(10)}$ exhibits exactly the same structure as the homogeneous equation for the polar velocity component $v_{\theta,(10)}$, so that we immediately conclude

$$v_{\varphi,(10)}(c) = \sigma_{(00)}\sqrt{\frac{1-c}{1+c}}\,. \tag{4.34}$$

Before going further, a wise precaution is to check that the velocity components we have derived satisfy the incompressibility condition

$$s^2 v'_{\theta} - c v_{\theta} = s v_r\,. \tag{4.35}$$

It then only remains to apply the interfacial boundary conditions, so as to relate the integration constants $\left\{\pi_{(10)}, \rho_{(-10)}, \sigma_{(00)}\right\}$ to one another and express each of them in terms of the sole temperature amplitude $\psi^{(0)}(0)$, a natural approach since this quantity controls the intensity of the thermally – driven flow.

From the zero mass flux boundary condition across the interface (4.17c) one gets $\rho_{(-10)} = -\pi_{(10)}/2$, while the radial Marangoni condition (4.17a) yields $\rho_{(-10)} = \psi^{(0)}(0)/2$ and the azimuthal Marangoni condition (4.17b), which leads us to $\sigma_{(00)} = 0$, confirms afterhand that $\mathrm{v}_{\varphi,(10)} = 0$ as expected from axisymmetry. Bringing all results together, we are ultimately left with the velocity vector

$$\boxed{\mathbf{v}^{(0)}_{(10)}(r,c) = \frac{\psi^{(0)}(0)}{2r} \begin{pmatrix} 1-2c \\ c\sqrt{\dfrac{1-c}{1+c}} \\ 0 \end{pmatrix}_{(\mathbf{e}_r, \mathbf{e}_\theta, \mathbf{e}_\varphi)}} , \tag{4.36}$$

that goes together with the pressure field

$$\boxed{\mathrm{p}^{(0)}_{(10)}(r,c) = -\frac{\psi^{(0)}(0)}{r^2}\, c\,.} \tag{4.37}$$

4.2.2 Nonlinear regime $\mathrm{Pe} \neq 0$

We now address the far – field axisymmetric state $(lm) = (10)$ in the nonlinear regime of finite Péclet numbers $\mathrm{Pe} \neq 0$. The analysis gets more involved in this case due to thermal advection coupling the temperature to the flow velocity through the additional contribution '$\mathrm{Pe}\,\mathbf{v}.\boldsymbol{\nabla}\vartheta$' in the heat equation.

Most importantly, we note that it is still adequate to seek long – range temperature and velocity fields scaling as $1/r$. Indeed, the structure of the advective coupling term is such that equal powers of $1/r$ are then ensured on both sides of the heat equation

$$\mathrm{Pe} \underbrace{\mathbf{v}}_{\sim (1/r)} . \underbrace{\boldsymbol{\nabla}\vartheta}_{\sim (1/r^2)} = \underbrace{\nabla^2\vartheta}_{\sim 1/r^3} . \qquad \underbrace{\qquad}_{= 1/r^3}$$

Besides, since the velocity field $\mathbf{v}_{(10)}$ is governed in the nonlinear regime by exactly the same couple of equations (4.15a) – (4.15b) as in the linear regime, its spatial dependence remains unchanged. Yet, one shall not forget the subtlety that the Marangoni stresses, expressed by the interfacial boundary conditions (4.17a) – (4.17b), relate the temperature

to the velocity in a way that impels us to distinguish between the interfacial temperature amplitude $\psi(0)$ in the nonlinear regime $\mathrm{Pe} \neq 0$, and its counterpart in the linear regime $\mathrm{Pe} = 0$ denoted $\psi^{(0)}(0)$, with the superscript '$^{(0)}$' to dispel any confusion. It ensues from this observation that the velocity field $\mathbf{v}_{(10)}$ plays the role of an input needed to derive the nonlinear temperature field $\vartheta_{(10)}$.

In steady–state conditions, the energy balance equation reads

$$\boldsymbol{\nabla}\mathbf{.}\ \mathbf{J} = \mathcal{Q}\,\delta(\mathbf{R})\,, \qquad \mathcal{Q} \doteq \frac{Q}{\rho c_p}\,, \tag{4.38}$$

where we recall that Q is the total heating power released by the pointlike heat source. The heat current $\mathbf{J}$ can be expressed as the sum of two terms[4]

$$\mathbf{J} = \mathbf{J}_{\mathrm{adv}} + \mathbf{J}_{\mathrm{diff}} = \mathbf{V}\Theta - D\boldsymbol{\nabla}\Theta\,, \tag{4.39}$$

the contributions of thermal advection and diffusion, respectively. Before proceeding any further, let us write Eq. (4.38) in dimensionless form

$$\boldsymbol{\nabla}\mathbf{.}\ \mathbf{j} = q\,\delta(\mathbf{r})\,, \tag{4.40}$$

with a dimensionless 'heat current' $\mathbf{j} = \mathrm{Pe}\,\mathbf{v}\vartheta - \boldsymbol{\nabla}\vartheta$ and the 'heating power' $q \doteq Q/(\kappa \Delta T a)$.

Temperature field

Let us first consider the continuity equation satisfied by the heat current, *i.e.* $\boldsymbol{\nabla}\mathbf{.}\ \mathbf{j} = 0$. This equation writes in spherical coordinates

$$\frac{1}{r^2}\,\partial_r\left(r^2 \mathrm{j}_r\right) - \frac{1}{r}\,\partial_c\left(s\mathrm{j}_\theta\right) + \frac{1}{rs}\,\partial_\varphi\,\mathrm{j}_\varphi = 0\,. \tag{4.41}$$

However, in the far–field limit for which $\mathbf{v}_{(10)}, \vartheta_{(10)} \sim 1/r$, the heat current $\mathbf{j}_{(10)} \sim 1/r^2$ and the first term of (4.41) thus vanishes. What is more, we focus on the axisymmetric state $m = 0$ which, by definition, does not depend on the azimuthal angle φ. As a result, Eq. (4.41) simply reduces to

$$\partial_c\left(s\mathrm{j}_{\theta,\,(10)}\right) = 0\,. \tag{4.42}$$

With both the velocity vector (4.36) taken as an input to upcoming calculations and a temperature field scaling here again as $1/r$, the ensuing differential equation for the polar part of the temperature field $\psi_{(10)}(c)$ is

$$\left[\left(1-c^2\right)\psi'_{(10)}(c) + \overline{\mathrm{Pe}}\,c\,(1-c\,)\,\psi_{(10)}(c)\right]' = 0\,, \qquad \overline{\mathrm{Pe}} \doteq \frac{\mathrm{Pe}}{2}\,\psi_{(10)}(0)\,. \tag{4.43}$$

[4] The reason why the expression of the advective current $\mathbf{J}_{\mathrm{adv}}$ is as simple as $\mathbf{V}\Theta$ is due to flow incompressibility. Indeed, we have the identity $\boldsymbol{\nabla}\mathbf{.}\,(\mathbf{V}\Theta) = \mathbf{V}\mathbf{.}\boldsymbol{\nabla}\Theta + \Theta\,(\boldsymbol{\nabla}\mathbf{.}\mathbf{V}) = \mathbf{V}\mathbf{.}\boldsymbol{\nabla}\Theta$ since $\boldsymbol{\nabla}\mathbf{.}\mathbf{V} = 0$.

This last equation integrated once with respect to c yields

$$\psi'_{(10)}(c) + \overline{\mathrm{Pe}}\,\frac{c}{1+c}\,\psi_{(10)}(c) = \frac{\mathrm{K}}{1-c^2}\ , \tag{4.44}$$

with $\mathrm{K} \in \mathbb{R}$ an integration constant which shall be set to zero so as to eliminate the singularity in $c_s = 1$. We are then left with a separable differential equation. Once the latter properly rewritten and integrated, we end up with the following non–trivial form of the temperature field

$$\boxed{\vartheta_{(10)}(r,c) = \frac{\psi_{(10)}(0)}{r}\,(1+c\,)^{\mathrm{Pe}}\,\mathrm{e}^{-\mathrm{Pe}\,c}\ , \qquad c \in [0,1]\,,} \tag{4.45}$$

where, for the sake of clarity, the 'modified' Péclet number $\overline{\mathrm{Pe}}$ will be simply denoted Pe from now on. Also bear in mind that $\psi_{(10)}(0)$ represents the temperature magnitude at the interface in the presence of thermal advection.

Though in a very specific case $(lm) = (10)$, we have derived an analytical solution of the advection–diffusion heat equation. Interestingly, an exact solution of the 'Navier–Stokes–Fourier' problem has been derived more than half a century ago by Bratukhin and Maurin in [60] (see also [59]). We checked that the more general expression these authors got gives back the form (4.45) in the low Reynolds regime, as expected (see Appendix J).

Energy balance

The last step of the present derivation consists in determining the interfacial temperature amplitude $\psi_{(10)}(0)$. This can be done by integrating the energy balance equation (4.40) over a half–sphere $(\mathcal{S})$ of radius $r_{\mathcal{S}}$ centred on the origin O in the upper half–space $c \in [0,1]$. We are then left with the surface integral [5]

$$\iint_{(\mathcal{S})} \mathbf{j}\,.\,\mathbf{d}\boldsymbol{\mathcal{S}} = 2\pi r_{\mathcal{S}}^2 \int_0^1 \mathrm{j}_r(r_{\mathcal{S}},c)\,\mathrm{d}c = \frac{Q}{\kappa \Delta T a}\ , \tag{4.46}$$

where the infinitesimal vector surface element $\mathbf{d}\boldsymbol{\mathcal{S}}$ of the half–sphere $(\mathcal{S})$, given by $\mathbf{d}\boldsymbol{\mathcal{S}} = r_{\mathcal{S}}^2 \sin\theta d\theta d\varphi\,\mathbf{e}_r$, rewrites with respect to $c \doteq \cos\theta$ as $\mathbf{d}\boldsymbol{\mathcal{S}} = -\,r_{\mathcal{S}}^2\,dc\,d\varphi\,\mathbf{e}_r$.

[5] Actually, the initial volume integral is transformed into a flux integral over the closed surface $(\Sigma) \doteq \{(\mathcal{S}) \cup (\mathcal{D})\}$ by applying the Green–Ostrogradski theorem. Yet the integral over $\mathcal{D}$, defined as the disk corresponding to the intersection of the half–sphere $(\mathcal{S})$ with the interfacial plane (Π), does not contribute here as neither heat nor mass fluxes pass through the interface (this is a reasonable assumption insofar as the air being a gas has negligible thermal conductivity and viscosity compared with water).

Here below, both cases of finite and vanishing Péclet numbers are compared relating the parameters in the nonlinear regime to those defined in the diffusive limit $\mathrm{Pe} \ll 1$. The latter parameters, taken as reference quantities, bear the superscript '$^{(0)}$'.

- Diffusive limit $\mathrm{Pe} \ll 1$:

  This limit amounts to discarding the advection term in the heat equation (4.15c). We have shown that the temperature field writes in this case $\vartheta^{(0)}(r) = \psi^{(0)}(0)/r$, so that the diffusive heat current is $\mathbf{j^{(0)}}(r) = -\boldsymbol{\nabla}\vartheta^{(0)} = \psi^{(0)}(0)/r^2\,\mathbf{e}_r$. This expression put in the integrand of (4.46) provides the reference temperature amplitude

  $$\underline{\underline{\psi^{(0)}(0) = \frac{Q}{2\pi\kappa\Delta T a}}}\ . \tag{4.47}$$

  Let $U^{(0)}$ denote the typical Marangoni velocity in this diffusion – dominated regime. It is then convenient to define a reference 'Péclet number' as $\mathrm{Pe} \doteq aU^{(0)}/D$. Let us remind the reader that the temperature rise ΔT on the surface of the heat source has been yet specified through the relation $a\Delta T = Q/(2\pi\kappa)$. According to (4.47), this amounts to fixing $\psi^{(0)}(0) = 1$. Finally considering that $U^{(0)} = \gamma_{\mathrm{T}}\Delta T/\eta$ yields a reference 'Péclet number'

  $$\underline{\underline{\mathrm{Pe}^{(0)} = \frac{\rho c_p|\gamma_{\mathrm{T}}|Q}{2\pi\eta\kappa^2}}}\ . \tag{4.48}$$

  Unsurprisingly, both the temperature and the velocity are $\propto Q$ in the linear regime : the stronger the heating of the bead, the higher the flow velocity (Fig. 4.1).

- Nonlinear regime $\mathrm{Pe} \neq 1$:

  The nonlinear regime corresponds to the physical situation wherein both diffusive and advective heat transport occur, namely the regime of finite Péclet values. With the above velocity components (4.36) and the temperature field (4.45), one is left with a total heat current of the form

  $$\mathbf{j}_{(10)}(r,c) = \frac{\psi(0)}{r^2}\left[1 + \mathrm{Pe}\,(1-2c)\right](1+c)^{\mathrm{Pe}}\,\mathrm{e}^{-\mathrm{Pe}\,c}\,\mathbf{e}_r\ , \tag{4.49}$$

  where we remind that the notation Pe stands in fact for $\overline{\mathrm{Pe}} \doteq (\mathrm{Pe}/2)\,\psi_{(10)}(0)$. In the nonlinear regime, the Marangoni velocity U can be thus expressed in function of the heating power Q — or, equivalently, the Péclet number $\mathrm{Pe} \doteq aU/D$ be expressed in terms of $\mathrm{Pe}^{(0)} \propto Q$ — through the implicit relation

  $$\boxed{\mathrm{Pe}^{(0)} = \mathrm{Pe}\int_0^1 \left[1 + \mathrm{Pe}\,(1-2c)\right](1+c)^{\mathrm{Pe}}\,\mathrm{e}^{-\mathrm{Pe}\,c}\,\mathrm{d}c\ ,} \tag{4.50}$$

  according to Eq. (4.46).

The latter relation is tackled in the following situations :

☞ Weakly nonlinear regime : for $\mathrm{Pe} \ll 1$, one can expand the integrand as follows

$$\mathrm{Pe}^{(0)} = \mathrm{Pe} \int_0^1 \left\{ 1 + \mathrm{Pe}\left[1 - 3c + \ln(1+c) \right] + \dots \right\} \mathrm{d}c = \mathrm{Pe} - \delta\, \mathrm{Pe}^2 + \dots \,, \qquad (4.51)$$

with $\delta = (3/2) - 2\ln 2 \approx 0.11$. Inverting this last relation yields

$$\mathrm{Pe} = \mathrm{Pe}^{(0)} \left[1 + \delta\, \mathrm{Pe}^{(0)} + \dots \right] , \qquad (4.52)$$

showing that the velocity in the weakly nonlinear regime is slightly larger ($\delta > 0$) than in the purely linear regime.

☞ Strongly nonlinear regime : there is no other way than to invert the integral (4.50) numerically. For comparison, the Marangoni velocity is also plotted in this case on Fig. 4.1. The graph shows that heat is essentially dissipated by advection as the Péclet number increases. Dissipation proves much more efficient than in the linear regime, since it is here advection – enhanced. This explains why the temperature increase now becomes a sublinear function of the injected power Q. Given that all parameter sets are proportional to Q, they are proportional to one another, which mathematically translates into the identity $U/U^{(0)} = \mathrm{Pe}/\mathrm{Pe}^{(0)} = \psi(0)/\psi^{(0)}(0)$, so that one obtains in the end [6]

$$\vartheta_{(10)}(r,c) = \frac{\psi^{(0)}(0)}{r} \frac{(1+c)^{\mathrm{Pe}}\, \mathrm{e}^{-\mathrm{Pe}\, c}}{\displaystyle\int_0^1 \left[1 + \mathrm{Pe}\,(1-2c) \right] (1+c)^{\mathrm{Pe}}\, \mathrm{e}^{-\mathrm{Pe}\, c}\, \mathrm{d}c} \,, \qquad \psi^{(0)}(0) = \frac{Q}{2\pi\kappa\Delta T a} \,. \qquad (4.53)$$

[6] It can be demonstrated that the above integral is equal to

$$\int_0^1 \left[1 + \mathrm{Pe}\,(1-2c) \right] (1+c)^{\mathrm{Pe}}\, \mathrm{e}^{-\mathrm{Pe}\, c}\, \mathrm{d}c = \mathrm{e}^{\mathrm{Pe}}\, (\mathrm{Pe} - 1)\, \zeta(\mathrm{Pe}) + 2^{\,2+\mathrm{Pe}}\, \mathrm{e}^{-\mathrm{Pe}} - 2 \,,$$

with the quantity $\zeta(\mathrm{Pe})$ given by

$$\zeta(\mathrm{Pe}) = \mathrm{E}_{-\mathrm{Pe}}\,(\mathrm{Pe}) - 2^{\,1+\mathrm{Pe}}\, \mathrm{E}_{-\mathrm{Pe}}\,(2\mathrm{Pe}) \,,$$

where $\mathrm{E}_n(x)$ is the 'generalised' exponential integral function defined as

$$\mathrm{E}_n(x) \doteq \int_1^{+\infty} \frac{\mathrm{e}^{-\lambda x}}{\lambda^n}\, \mathrm{d}\lambda \,, \quad (x,n) \in \mathbb{R}^2 \,.$$

It is equally interesting to see how strongly the temperature and the velocity can influence each other through advective coupling $\mathbf{V}.\boldsymbol{\nabla}\Theta$. In this respect, Fig. 4.2 clearly reveals to what point isotherms can deform with increasing Péclet number : from concentric circles in the linear regime ($\mathrm{Pe} = 0$), the isotherms strongly deform at sufficiently high Péclet number ($\mathrm{Pe} = 5$), finally taking a bilobate shape and getting closer and closer to the interface.

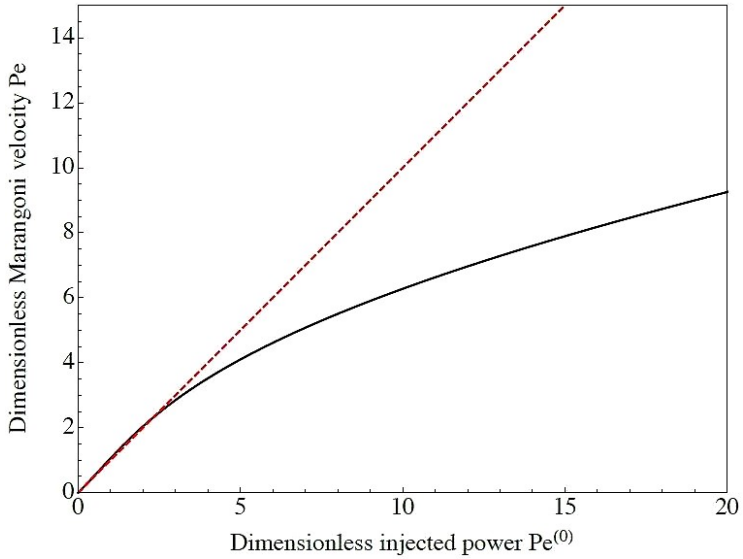

Figure 4.1: Evolution of the Marangoni velocity with increasing heating. (*Solid curve*) Nonlinear regime including the effects of thermal advection. (*Dashed line*) Diffusive limit $\mathrm{Pe} \ll 1$. Since the Péclet number Pe is proportional to the Marangoni velocity and $\mathrm{Pe}^{(0)}$ is proportional to the injected power Q, we can as well plot in dimensionless units $\mathrm{Pe} = f(\mathrm{Pe}^{(0)})$ as we do here.

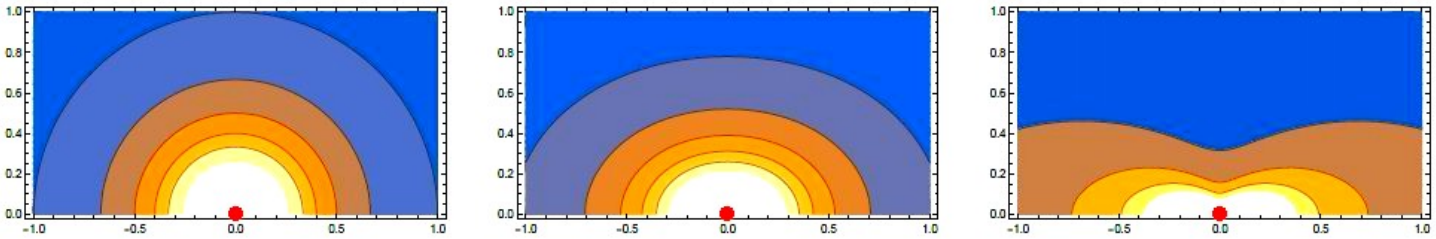

Figure 4.2: Distortion of bulk isotherms with increasing heating. (*From left to right*) $\mathrm{Pe} = 0$, 1 and 5. Hot bead depicted by a red ball (not to scale).

4.3 The hemispherical Lamb's solution

The far–field axisymmetric solution $(lm) = (10)$ derived above in the nonlinear regime is meant to model the base flow observed experimentally at low heating powers. In order to capture the azimuthal instability of this primary flow arising for a sufficiently strong heating of the bead, one should perturb the ground state by non–axisymmetric states whose role is to break the initial rotational symmetry into an annulus of vortex pairs periodically distributed all around the source. These perturbative fields are to be selected among generic states of the 'hemispherical' Lamb's solution that we derive now.

4.3.1 Generic forms of the fields

Our aim is to solve the 'Stokes problem', namely the differential equations (4.15a)–(4.15b), within the upper half–space $c \in [0,1]$. As customary, we seek solutions with separated variables. Extending the former rationale to arbitrary powers of $1/r$, we set temperature and velocity fields sharing in common generic terms $\sim 1/r^l$ while the latter are $\sim 1/r^{l+1}$ for the pressure field. Besides that, the 2π–periodic azimuthal part of the solutions compels us to introduce a multipolar expansion with generic terms $\sim \mathrm{e}^{im\varphi}$. This explains why we take the fields in the ansatz forms

$$\mathrm{p}\,(r,c,\varphi) = \sum_{l,m} \mathrm{p}_{\,(lm)} = \sum_{l,m} \frac{1}{r^{l+1}}\, p_{\,(lm)}(c)\, \mathrm{e}^{im\varphi}\,, \tag{4.54a}$$

$$\mathrm{v}_j\,(r,c,\varphi) = \sum_{l,m} \mathrm{v}_{j,\,(lm)} = \sum_{l,m} \frac{1}{r^{l}}\, v_{j,\,(lm)}(c)\, \mathrm{e}^{im\varphi}\,, \quad j \in \{r,\theta,\varphi\}\,, \tag{4.54b}$$

$$\vartheta\,(r,c,\varphi) = \sum_{l,m} \vartheta_{\,(lm)} = \sum_{l,m} \frac{1}{r^{l}}\, \psi_{\,(lm)}(c)\, \mathrm{e}^{im\varphi}\,. \tag{4.54c}$$

Note that the c–dependent part of the pressure and the velocity fields is written in italics, unlike the associated total fields denoted by straight letters. Here the parameter l labels the consecutive powers of $1/r$ while m is the azimuthal wavenumber.

4.3.2 Equations for the functions $\{p_{\,(lm)}(c)\}$ and $\{v_{j,\,(lm)}(c)\}_{j\in\{r,\theta,\varphi\}}$

The radial and azimuthal dependences of the fields being fixed in the forms (4.54a)–(4.54c), it therefore remains to derive the polar functions $\{p_{\,(lm)}(c)\}$ and $\{v_{j,\,(lm)}(c)\}_{j\in\{r,\theta,\varphi\}}$. Let us start with the elucidation of the incompressibility condition (4.15b). The divergence of the velocity field writes in spherical coordinates (using $\partial_\theta \bullet = -s\partial_c \bullet$)

$$\boldsymbol{\nabla}\boldsymbol{.}\,\mathbf{v} = \frac{1}{r^2}\,\partial_r\left(r^2 \mathrm{v}_r\right) - \frac{1}{r}\,\partial_c\left(s\mathrm{v}_\theta\right) + \frac{1}{rs}\,\partial_\varphi \mathrm{v}_\varphi\,. \tag{4.55}$$

One obtains after little algebra the differential equation for the functions $\{v_{\theta,(lm)}(c)\}$

$$s^2 v'_\theta - c\, v_\theta = -(l-2)\, s v_r + im v_\varphi \ . \tag{4.56}$$

Next comes the explicitation of the Stokes equation (4.15a) yielding the hereafter set of coupled differential equations for the velocity components $\{v_{j,(lm)}(c)\}_{j\in\{r,\theta,\varphi\}}$

$$\left[s^2 v'_r\right]' + \left\{(l-1)(l-2) - \frac{m^2}{s^2}\right\} v_r = -(l+1)\, p \ , \tag{4.57a}$$

$$\left[s^2 v'_\theta\right]' + \left\{l\,(l-1) - \frac{1+m^2}{s^2}\right\} v_\theta = 2 s v'_r + 2im\,\frac{c}{s^2}\, v_\varphi - s p' \, , \tag{4.57b}$$

$$\left[s^2 v'_\varphi\right]' + \left\{l\,(l-1) - \frac{1+m^2}{s^2}\right\} v_\varphi = -2\,\frac{im}{s}\, v_r - 2im\,\frac{c}{s^2}\, v_\theta + \frac{im}{s}\, p \ . \tag{4.57c}$$

Remarkably, the symmetry of these equations is such that both angular functions $v_\theta(c)$ and $v_\varphi(c)$ display the same prefactor $(1+m^2)/s^2$, whereas for the radial function $v_r(c)$ we only have m^2/s^2. The structure of these equations further reveals that the states $(lm) = \{(1m),(2m)\}$ play a special role[7]. Indeed, one notices that the angular equations become simpler as $l = 1$, the same holding for the radial equation when $l = 1$ or $l = 2$. Technical details on how to obtain these equations are provided in Appendix K.

The differential system still has to be 'closed'. As seen previously, this requirement is fulfilled by taking the divergence of the Stokes equation (4.15a), which leads to the Laplace's equation (4.22) for the pressure field. Elucidating it in spherical coordinates yields the canonical form of the associated Legendre differential equation ([66], 8.1.1)

$$\left(1-c^2\right)\frac{\mathrm{d}^2 p_{(lm)}}{\mathrm{d}c^2} - 2c\,\frac{\mathrm{d}p_{(lm)}}{\mathrm{d}c} + \left[l(l+1) - \frac{m^2}{1-c^2}\right] p_{(lm)} = 0\,. \tag{4.58}$$

In summary, the system of coupled differential equations whose solving provides the expressions of the generic functions $\{p_{(lm)}(c)\}$ and $\{v_{j,(lm)}(c)\}_{j\in\{r,\theta,\varphi\}}$ reads

$$\left[s^2 p'\right]' + \left(l\,(l+1) - \frac{m^2}{s^2}\right) p = 0\,, \tag{4.59a}$$

$$s^2 v'_\theta - c\, v_\theta = -(l-2)\, s v_r + im v_\varphi\,, \tag{4.59b}$$

$$\left[s^2 v'_r\right]' + \left\{(l-1)(l-2) - \frac{m^2}{s^2}\right\} v_r = -(l+1)\, p\,, \tag{4.59c}$$

$$\left[s^2 v'_\theta\right]' + \left\{l\,(l-1) - \frac{1+m^2}{s^2}\right\} v_\theta = 2 s v'_r + 2im\,\frac{c}{s^2}\, v_\varphi - s p'\,, \tag{4.59d}$$

$$\left[s^2 v'_\varphi\right]' + \left\{l\,(l-1) - \frac{1+m^2}{s^2}\right\} v_\varphi = -2\,\frac{im}{s}\, v_r - 2im\,\frac{c}{s^2}\, v_\theta + \frac{im}{s}\, p\,. \tag{4.59e}$$

[7] The case $l = 0$ is tantamount to considering a uniform velocity field preexisting the introduction of the heat source, which is not our physical framework.

The solving strategy of this system for both the axisymmetric $(lm) = (l0)$ and the non–axisymmetric $(lm)_{m\neq 0}$ states is detailed in Appendix L. Keep in mind that Eq. (4.59a) is the cornerstone of the Stokes problem that makes its solving quite straightforward.

4.3.3 Derivation of the hemispherical Lamb's solution

As just seen, the pressure field obeys the associated Legendre differential equation (4.58). Still, the forthcoming analysis is not standard as we will explain it now.

In most situations commonly encountered in physics (*e.g.* in quantum mechanics), one is interested in solutions that are regular over the whole space $c \in [-1, 1]$. The solution of Eq. (4.58) is then $p_{(lm)}(c) \propto P_l^m(c)$, where the $\{P_l^m(c)\}$ are the associated Legendre polynomials of degree l and order m defined for $m \geqslant 0$ as

$$P_l^m(c) = \left(1 - c^2\right)^{m/2} \frac{\mathrm{d}^m}{\mathrm{d}c^m} P_l(c) \ , \tag{4.60}$$

with $\{P_l(c)\}$ the Legendre polynomials of degree l. For negative orders, the associated Legendre polynomials $\left\{P_l^{-m}(c)\right\}$ can be inferred from the $\{P_l^m(c)\}$ thanks to the relation $P_l^{-m}(c) = (-1)^m \dfrac{(l-m)!}{(l+m)!} P_l^m(c)$. From (4.60), it ensues that $P_l^m(c) = 0$ if $|m| > l$.

In the present case, however, regular solutions are required only in the upper half–space $c \in [0, 1]$. As shown in Appendix M, the solution of Eq. (4.58) is then $p_{(lm)}(c) \propto \mathcal{P}_l^m(c)$ with the associated Legendre function $\mathcal{P}_l^m(c)$ here defined as ([66], 8.1.2)

$$\boxed{\mathcal{P}_l^m(c) = \left(\frac{1-c}{1+c}\right)^{|m|/2} {}_2F_1\left(-l,\, l+1,\, 1+|m|\,;\, \frac{1-c}{2}\right) , \qquad c \in [0, 1] \,,} \tag{4.61}$$

where the special function ${}_2F_1\left(\alpha, \beta, \gamma\,; z\right)$ is known as the Gauss hypergeometric function (short presentation in Appendix M). As can be noticed, working in a half–space results in the use of a rather unconventional definition of the Legendre functions. As a matter of fact, the azimuthal wavenumber m is no longer limited to $(2l+1)$ integer values in the range $[\![-l, l]\!]$ but fully unconstrained. A consequence of this is that the 'hemispherical Lamb's solution' includes singular terms absent from its more classical version : for $|m| \leqslant l$, one recovers (up to a normalising constant) the 'usual' associated Legendre polynomials $\{P_l^m(c)\}$ while the $\{\mathcal{P}_l^m(c)\}$ defined in (4.61) do not vanish for $|m| > l$, by contrast with more standard studies. A few essential properties of the associated Legendre functions $\{\mathcal{P}_l^m(c)\}$ are summarised in Appendix M and several examples are listed in Appendix N.

Pressure field

From the foregoing discussion one concludes that the $c-$dependent part of the pressure field $p_{(lm)}(c)$ satisfying the associated Legendre differential equation (4.58) is given by

$$p_{\,(lm)}(c) = \frac{2\,(2l-1)}{l+1}\,\pi_{(lm)}\,\mathcal{P}_l^{\,m}(c)\,, \tag{4.62}$$

with $\pi_{(lm)}$ an integration constant to be specified later applying the boundary conditions. The prefactor $2\,(2l-1)\,/\,(l+1)$ is introduced for convenience only, as will be clear below.

The introduction of an operatorial formalism is of great relevance to the simplification of analytical calculations. We define what we call the Legendre differential operator as

$$\underline{\underline{\hat{\mathcal{L}}_m \bullet \doteq \left(1-c^2\right)\frac{\mathrm{d}^2}{\mathrm{d}c^2}\bullet - 2c\,\frac{\mathrm{d}}{\mathrm{d}c}\bullet - \frac{m^2}{1-c^2}\bullet}}\;. \tag{4.63}$$

The lower index 'm' stresses the fact that $\hat{\mathcal{L}}$ depends on the azimuthal wavenumber m but not on the parameter l. This definition is used to redraft (4.58) as the following eigenvalue equation associated with the operator $\hat{\mathcal{L}}$

$$\boxed{\hat{\mathcal{L}}_m\,\mathcal{P}_l^{\,m} = -l\,(l+1)\,\mathcal{P}_l^{\,m}\,.} \tag{4.64}$$

Hence we see that the associated Legendre functions $\{\mathcal{P}_l^{\,m}(c)\}$ are the eigenfunctions of the operator $\hat{\mathcal{L}}$ with eigenvalues equal to $\epsilon_l = -l\,(l+1)$.

The next step is to derive the velocity components. As the corresponding calculations are of no interest for the physics but purely technical, the interested reader is referred to Appendix O for a detailed derivation. Let us go straight to the general form of the Lamb's solution in the upper half$-$space $c \in [0,1]$:

- Pressure :

$$\mathrm{p}\,(r,c,\varphi) = \sum_{l=1}^{+\infty}\sum_{m=-\infty}^{+\infty}\frac{1}{r^{l+1}}\frac{2\,(2l-1)}{l+1}\,\pi_{(lm)}\,\mathcal{Y}_l^{\,m}(c,\varphi)\;. \tag{4.65}$$

- Radial velocity :

$$\mathrm{v}_r\,(r,c,\varphi) = \sum_{l=1}^{+\infty}\sum_{m=-\infty}^{+\infty}\frac{1}{r^l}\left[\pi_{(lm)}\,\mathcal{Y}_l^{\,m}(c,\varphi) + \rho_{(l-2,\,m)}\,\mathcal{Y}_{l-2}^{\,m}(c,\varphi)\right]\;. \tag{4.66}$$

- Polar velocity :

$$\begin{aligned}
&\mathrm{v}_\theta\,(r,c,\varphi) = \frac{\psi_{(10)}(0)}{2r}\,c\sqrt{\frac{1-c}{1+c}} \\
&+\sum_{\substack{m=-\infty\\(m\neq 0)}}^{+\infty}\frac{1}{rs}\left[\frac{1}{6}\,(m+2)\,\pi_{(1m)}\,\mathcal{Y}_2^m(c,\varphi)+(1+m)\,\rho_{(-1m)}\,\mathcal{Y}_1^m(c,\varphi)+\sigma_{(0m)}\,\mathcal{Y}_0^m(c,\varphi)\right] \\
&\qquad+\sum_{l=2}^{+\infty}\sum_{m=-\infty}^{+\infty}\frac{1}{r^l}\left[\frac{l-2}{l\,(l+1)}\,\pi_{(lm)}\,s\,\frac{\partial\mathcal{Y}_l^m(c,\varphi)}{\partial c}\;+\;\frac{\rho_{(l-2,\,m)}}{l-1}\,s\,\frac{\partial\mathcal{Y}_{l-2}^m(c,\varphi)}{\partial c}\right. \\
&\qquad\qquad\left.+\frac{im\sigma_{(l-1,\,m)}}{s}\,\mathcal{Y}_{l-1}^m(c,\varphi)\right]. \qquad (4.67)
\end{aligned}$$

- Azimuthal velocity :

$$\begin{aligned}
&\mathrm{v}_\varphi\,(r,c,\varphi) = \\
&-\sum_{\substack{m=-\infty\\(m\neq 0)}}^{+\infty}\frac{1}{r}\,\frac{is}{m}\left[\frac{1}{6}\,(m+2)\,\pi_{(1m)}\frac{\partial\mathcal{Y}_2^m(c,\varphi)}{\partial c}+(1+m)\,\rho_{(-1m)}\frac{\partial\mathcal{Y}_1^m(c,\varphi)}{\partial c}+\sigma_{(0m)}\frac{\partial\mathcal{Y}_0^m(c,\varphi)}{\partial c}\right. \\
&\qquad\left.-\,\pi_{(1m)}\mathcal{Y}_1^m(c)-\rho_{(-1m)}\mathcal{Y}_0^m(c)\right] \\
&\qquad+\sum_{l=2}^{+\infty}\sum_{m=-\infty}^{+\infty}\frac{1}{r^l}\left\{-im\left[\frac{l-2}{l\,(l+1)}\,\pi_{(lm)}\,\frac{\mathcal{Y}_l^m(c,\varphi)}{s}+\frac{\rho_{(l-2,\,m)}}{l-1}\,\frac{\mathcal{Y}_{l-2}^m(c,\varphi)}{s}\right]\right. \\
&\qquad\qquad\left.-\left(\frac{is}{m}\right)im\sigma_{(l-1,\,m)}\,\frac{\partial\mathcal{Y}_{l-1}^m(c,\varphi)}{\partial c}\right\}. \qquad (4.68)
\end{aligned}$$

We have introduced generalised spherical harmonics defined as $\mathcal{Y}_l^m(c,\varphi)\doteq\mathcal{P}_l^m(c)\,\mathrm{e}^{im\varphi}$. We remind that the explicit forms of the associated Legendre functions are provided in Appendix N, if needed. Also note that the generic integration constant $\sigma_{(l-1,\,m)}$ has been redefined making a prefactor im appear explicitly (the latter originates in fact from $\partial_\varphi\mathcal{Y}_l^m$), so as to obtain a form more in line with the usual writing of the Lamb's solution.

Both angular velocity components are split into several parts : first the $(lm)=(10)$ part of the solution which required a separate analysis, followed by the generic states $(lm)=(1m)_{m\neq 0}$ and ultimately the whole remaining part for $l\geqslant 2,\forall m$. The $(10)-$term of the polar velocity is given under the simplified form we end up with once all boundary conditions are applied. Besides, one remembers that axisymmetry imposes $\sigma_{(00)}=0$ which explains why no $(10)-$term appears in the expression of the azimuthal velocity.

4.3.4 Comparison with precursor works

The above derivation evidences that the 'hemispherical' solution to the Stokes equation contains the classical Lamb's solution [61], plus supplementary terms only regular in the half−space $c \in [0,1]$. Actually, some of these additional terms have been already discussed in previous works and we now verify that our results are consistent with these studies.

The far−field axisymmetric solution $(lm) = (10)$

To our knowledge, the far−field axisymmetric solution $(lm) = (10)$ was first derived by Bratukhin and Maurin in their work [60] (see also [3]−[59]), more than half a century ago. Our own analysis yields the velocity components

$$v_{r,\,(10)}(c) = \rho_{(-10)}\,(1-2c)\ , \tag{4.69a}$$

$$v_{\theta,\,(10)}(c) = \rho_{(-10)}\,\frac{cs}{1+c}\ , \tag{4.69b}$$

which turn out to be exactly the same expressions as those of Eq. (4.1) in ref. [3].

The dipolar solution $(lm) = (21)$

Another salient state is the dipolar solution $(lm) = (21)$ whose velocity components write

$$v_{r,\,(21)}(c) = \pi_{(21)}\mathcal{P}_2^1(c) + \rho_{(01)}\mathcal{P}_0^1(c) = \frac{1}{s}\left[\rho_{(01)} + \left(\frac{\pi_{(21)}}{2} - \rho_{(01)}\right)c - \frac{\pi_{(21)}}{2}\,c^3\right]\ , \tag{4.70a}$$

$$v_{\theta,\,(21)}(c) = \rho_{(01)}\,s\mathcal{P}'^1_0(c) + \frac{i\sigma_{(11)}}{s}\,\mathcal{P}_1^1(c) = \frac{i\sigma_{(11)}}{2} - \frac{\rho_{(01)}}{1+c}\ , \tag{4.70b}$$

$$v_{\varphi,\,(21)}(c) = -\frac{i\rho_{(01)}}{s}\,\mathcal{P}_0^1(c) + \sigma_{(11)}\,s\mathcal{P}'^1_1(c) = -i\left[\frac{\rho_{(01)}}{1+c} - \frac{i\sigma_{(11)}}{2}\,c\right]\ , \tag{4.70c}$$

the latter being deliberately given in these unusual forms to allow for direct comparison with the expressions found in [3] (adapted to our notations)

$$v_{r,\,(21)}(c) = t_3\,\frac{1}{s}\left(1-c^3\right) - t_4\,cs = \frac{1}{s}\left[t_3 - t_4\,c + (t_4 - t_3)\,c^3\right]\ , \tag{4.71a}$$

$$v_{\theta,\,(21)}(c) = t_5 - \frac{t_3}{1+c}\ , \tag{4.71b}$$

$$v_{\varphi,\,(21)}(c) = -i\left[\frac{t_3}{1+c} - t_5\,c\right]\ . \tag{4.71c}$$

As we can see, there exists a perfect matching between both sets of expressions (4.70) and (4.71) if one makes the following identification between coefficients

$$t_3 = \rho_{(01)}\,, \tag{4.72a}$$

$$t_4 = -\frac{\pi_{(21)}}{2} + \rho_{(01)}\,, \tag{4.72b}$$

$$t_5 = \frac{i\sigma_{(11)}}{2}\,. \tag{4.72c}$$

4.3.5 Representation of the flow modes

In this part, we focus our attention on the axisymmetric flow state $(lm) = (10)$ and on the non – axisymmetric flow state $(lm) = (21)$. In order to specify the 'hemispherical' Lamb's solution in our physical framework, we first apply the no – flux interfacial boundary condition (4.17c) followed by the couple of Marangoni conditions (4.17a) – (4.17b) which introduce the quantities $\left\{\psi_{(lm)}(0)\right\}$, namely the temperature magnitudes at the interface. Since the latter surely play a key role in the scenario of the instability, relating the integration constants $\left\{\pi_{(lm)}, \rho_{(l-2,m)}, \sigma_{(l-1,m)}\right\}$ to the $\left\{\psi_{(lm)}(0)\right\}$ is essential. In a second step, each flow state is plotted in the horizontal plane (xOy) of the interface as well as in the cross – sectional plane (xOz) prior to superimposing both states (10) and (21).

Application of the interfacial boundary conditions

Axisymmetric flow state $(lm) = (10)$

Let us start with the generic expression of the velocity vector $\mathbf{v}_{(10)}(r,c)$

$$\mathbf{v}_{(10)}(r,c) = \frac{1}{r}\begin{pmatrix} \pi_{(10)}\, c + \rho_{(-10)} \\ -\dfrac{\pi_{(10)}}{2}\, s - \rho_{(-10)}\sqrt{\dfrac{1-c}{1+c}} \\ \sigma_{(00)}\sqrt{\dfrac{1-c}{1+c}} \end{pmatrix}_{(\mathbf{e}_r, \mathbf{e}_\theta, \mathbf{e}_\varphi)}\,. \tag{4.73}$$

The no – flux interfacial boundary condition (4.17c) immediately yields the relation among constants $\pi_{(10)} = -2\rho_{(-10)}$. The '$r$ – Marangoni' boundary condition (4.17a) then states that $\pi_{(10)} = -\psi_{(10)}(0)$, while the '$\varphi$ – Marangoni' condition (4.17b) leads to $\sigma_{(00)} = 0$ in compliance with axisymmetry. So we have $\left\{\pi_{(10)}, \rho_{(-10)}, \sigma_{(00)}\right\} = \left\{-\psi_{(10)}(0), \psi_{(10)}(0)/2, 0\right\}$

and the velocity components (4.73) then simplify to

$$\mathbf{v}_{(10)}(r,c) = \frac{\psi_{(10)}(0)}{2r} \begin{pmatrix} 1-2c \\ c\sqrt{\dfrac{1-c}{1+c}} \\ 0 \end{pmatrix}_{(\mathbf{e}_r,\mathbf{e}_\theta,\mathbf{e}_\varphi)} \quad . \tag{4.74}$$

Non – axisymmetric flow state $(lm) = (21)$

The generic expression of the velocity vector $\mathbf{v}_{(21)}(r,c,\varphi)$ writes

$$\mathbf{v}_{(21)}(r,c,\varphi) = \frac{\mathrm{e}^{i\varphi}}{r^2} \begin{pmatrix} \dfrac{\pi_{(21)}}{2}\, cs + \rho_{(01)}\sqrt{\dfrac{1-c}{1+c}} \\ -\dfrac{\rho_{(01)}}{1+c} + \dfrac{i\sigma_{(11)}}{2} \\ -\dfrac{i\rho_{(01)}}{1+c} - \dfrac{\sigma_{(11)}}{2}\, c \end{pmatrix}_{(\mathbf{e}_r,\mathbf{e}_\theta,\mathbf{e}_\varphi)} \quad . \tag{4.75}$$

In this case, the no – flux condition (4.17c) yields $\sigma_{(11)} = -2i\rho_{(01)}$. The '$r$ – Marangoni' condition (4.17a) gives next $\pi_{(21)}/2 - \rho_{(01)} = -2\psi_{(21)}(0)$, supplemented by $\rho_{(01)} = \psi_{(21)}(0)/2$ from the 'φ – Marangoni' condition (4.17b), so that we end up with $\{\pi_{(21)}, \rho_{(01)}, \sigma_{(11)}\} = \{-3\psi_{(21)}(0), \psi_{(21)}(0)/2, -i\psi_{(21)}(0)\}$ and the velocity components (4.75) hence reduce to

$$\mathbf{v}_{(21)}(r,c,\varphi) = \frac{\psi_{(21)}(0)}{2r^2} \begin{pmatrix} -\left(3c^2+3c-1\right)\sqrt{\dfrac{1-c}{1+c}}\cos\varphi \\ \dfrac{c}{1+c}\cos\varphi \\ -\dfrac{c^2+c-1}{1+c}\sin\varphi \end{pmatrix}_{(\mathbf{e}_r,\mathbf{e}_\theta,\mathbf{e}_\varphi)} \quad , \tag{4.76}$$

where only the real part of the velocity vector has been kept (keeping instead the imaginary part simply amounts to rotating the fields by an angle $+\pi/2$).

Plotting the flow states

Here are plotted in the interfacial plane (xOy) as well as in the vertical cut plane (xOz) the streamlines corresponding to the flow modes (10) and (21). Separate plots are first displayed, followed by plots of the superposed state $\{(10)+(21)\}$. Each time, a density

plot of the velocity norm is also shown so as to provide an insight into the variation of the flow intensity along these planes. The plots are realised with Wolfram Mathematica's functions 'StreamPlot' and 'DensityPlot' which, as a preliminary step, require converting all velocity components into cartesian coordinates (see Appendix P for details).

Axisymmetric flow state $(lm) = (10)$

Unsurprisingly, this mode is axisymmetric with a surface flow consisting of diverging streamlines and a bulk flow consisting of what is seemingly a pair of counter–rotating vortices (Fig. 4.3). However, since an unbounded medium is considered theoretically, these vortices close at infinity. By virtue of axisymmetry, the 'flow slices' have the same morphology in any cut plane around the vertical axis (Oz). Therefore, the overall flow structure is that of a torus whose revolution axis is centred on the source located at the origin (not sketched on the plots). The flow axisymmetry is also reflected in the interfacial velocity norm whose map exhibits concentric circles of declining intensity. An ascending column of accelerated liquid, similar to the one observed experimentally, is evidenced by the map of the velocity norm displaying a plume–like shape beneath the source.

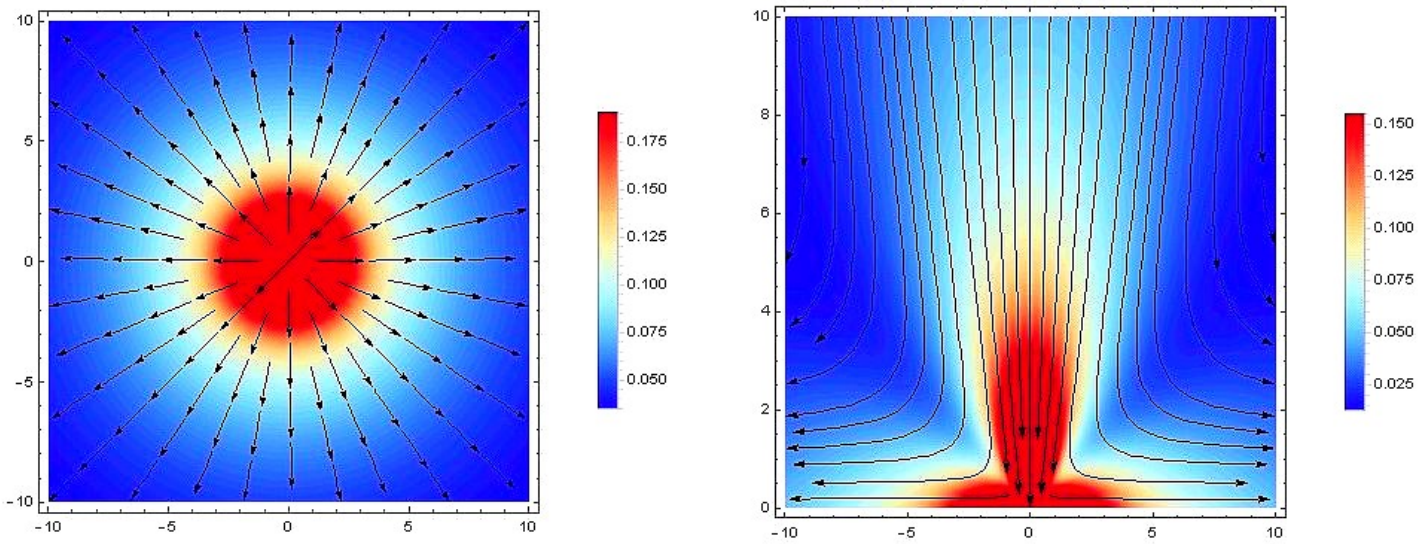

Figure 4.3: Maps of the streamlines (arrows) and the velocity norm (density plot) associated with the flow state (10) **in the interfacial plane** (xOy) **(*left figure*) and the vertical cut plane** (xOz) **(*right figure*).** The abscissa is $-10 \leqslant x \leqslant 10$ and the ordinate $-10 \leqslant y \leqslant 10$. For convenience, we choose positive values of z in the range $0 \leqslant z \leqslant 10$ (water fills the upper half–space). Values on the colour scales are dimensionless.

Non – axisymmetric flow state $(lm) = (21)$

Here the axisymmetry of the flow is clearly broken, with a preferential direction along the mirror symmetry axis of the interfacial dipole (Fig. 4.4). Remarkably, on the bulk view, a 'third vortex' seems to emerge in the middle of the original torus (compare with Fig. 4.3). On top of that, streamlines located to the left of the point source are now oriented rightward. Such a flow reversal may be caused by various sources of asymmetry (sec. 2.6). Curiously, whereas this flow mode (21) is evidently non – axisymmetric, the distribution map of its velocity norm keeps an axisymmetric structure.

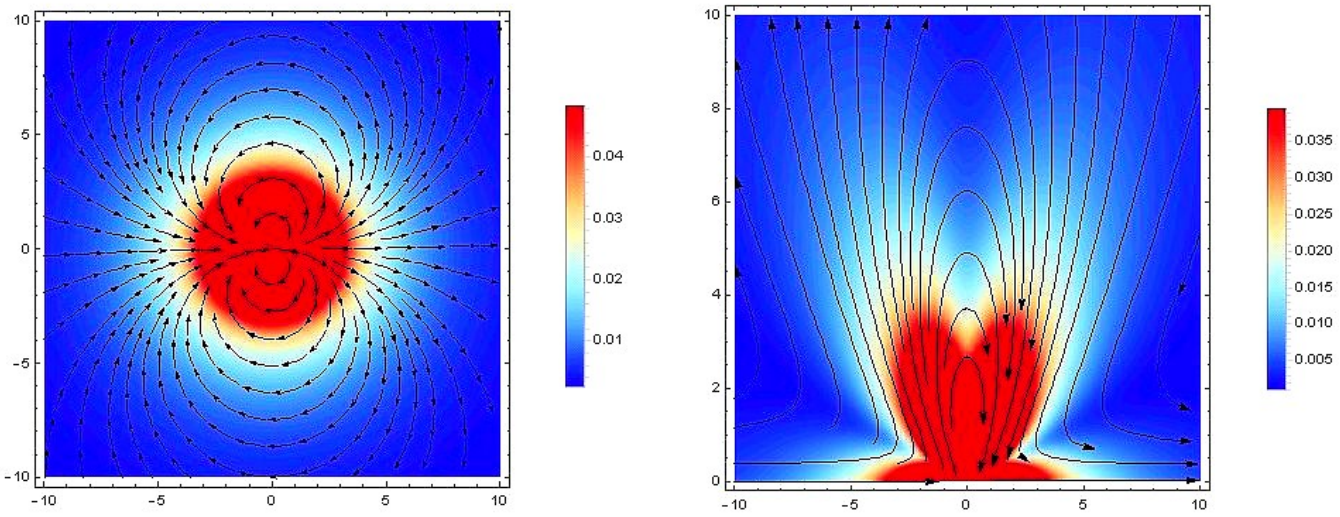

Figure 4.4: Maps of the streamlines (arrows) and the velocity norm (density plot) associated with the flow state (21) **in the interfacial plane** (xOy) **(*left figure*) and the vertical cut plane** (xOz) **(*right figure*).** Same comments as above.

Superposed state $\{(10) + (21)\}$

Fig. 4.5 shows the superposed flow state $\{(10) + (21)\}$. The flow is dipolar close to the source and tends to an axisymmetric shape (Fig. 4.3) at infinity. Contrary to the 'pure dipole' of Fig. 4.4, the streamlines enveloping the present dipole seem 'brushed back' with a 'polarisation tail' pointing towards the region $x \to -\infty$. This asymmetry also appears in the distribution of the velocity norm whose density plot exhibits a potato – shaped central region of high velocity 'squashed' in its rear part, and a localised area of minimum velocity in the back of the dipole. When plotting the total state $\{(10) + (21)\}$, the same weight has been arbitrarily given to both the axisymmetric (10) and the dipolar (21) contributions (Appendix P). By changing the amplitude of either component, one can exacerbate either the axisymmetric or the dipolar flow without modifying the general aspect of the maps.

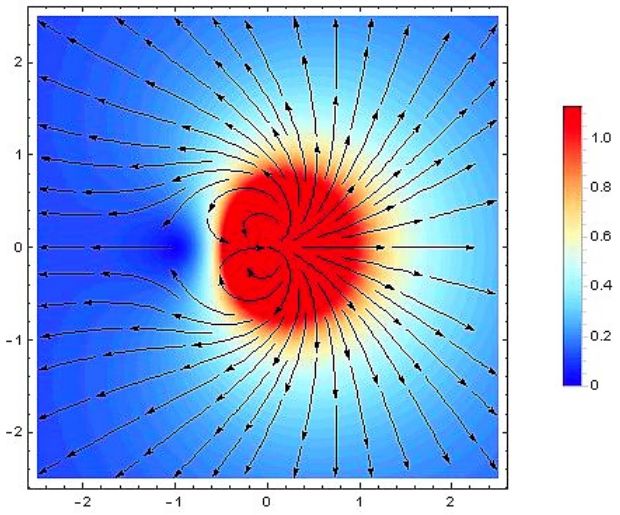

Figure 4.5: Maps of the streamlines (arrows) and the velocity norm (density plot) of the superposed flow state $\{(10)+(21)\}$ in the interfacial plane (xOy). Here the abscissa is $-2.5 \leqslant x \leqslant 2.5$ and the ordinate $-2.5 \leqslant y \leqslant 2.5$. Dimensionless colour scale.

4.4 First steps towards grasping the instability

In this section, we make a short presentation geared to preparing the ground for the capture of the instability. Now that the exact solution to the $(\mathbf{V},\Theta)-$coupled problem in the far−field axisymmetric regime $(lm)=(10)$ has been derived, we should perform its stability analysis. More precisely, the point is to probe the stability of the base flow $(lm)=(10)$ in response to azimuthal perturbations.

The main difficulty lies here in finding a correct approach to perform the stability analysis of the advection−diffusion heat equation :

- Let us introduce time−dependent amplitudes in the ansatz forms (4.54) of the fields. Considering then the complete, unsteady, advection−diffusion equation yields the following balance of powers of $1/r$

$$\mathrm{Pe}\,(\underbrace{\partial_t\mathbf{v}}_{\sim 1/r^{l}}+\underbrace{\underbrace{\mathbf{v}}_{\sim 1/r^{l}}\cdot\underbrace{\boldsymbol{\nabla}\vartheta}_{\sim 1/r^{l+1}}}_{=1/r^{2l+1}})=\underbrace{\nabla^2\vartheta}_{\sim 1/r^{l+2}}\ .$$

  For this time−dependent equation to admit a solution, all the terms on its left as well as on its right side must share in common the same radial dependence, which imposes the constraint $l=2l+1=l+2$. However, it is easy to be convinced that

there exists no value of l satisfying both equalities simultaneously. We ought to conclude that trying to solve 'order – by – order' the unsteady advection – diffusion equation is doomed to failure. Instead, one shall insert in the above equation the full series (4.54) defining the fields, next couple modes until a perfect matching of the radial powers is obtained, and finally solve the ensuing equation if possible. In the first instance, however, we waive such a stability analysis.

- Turning back to the steady advection – diffusion heat equation, we are left with

$$\mathrm{Pe}\underbrace{\underbrace{\mathbf{v}}_{\sim 1/r^l}\cdot\underbrace{\boldsymbol{\nabla}\vartheta}_{\sim 1/r^{l+1}}}_{=1/r^{2l+1}} = \underbrace{\nabla^2\vartheta}_{\sim 1/r^{l+2}}\,.$$

Here the 'matching condition' which writes $2l+1=l+2$ is fulfilled only for $l=1$. One thus sets perturbative fields scaling as $1/r$. Examining the linear stability of far – field perturbations is what Shtern *et al.* did in [59]. If the perturbation of the base flow state $(\widehat{\mathbf{v}},\widehat{\vartheta})$ (expressions (4.36) and (4.45)) by generic non – axisymmetric states $(1m)_{m\neq 0}$ does not trigger the instability, one should then try to destabilise it with higher – order non – axisymmetric states $(2m)_{m\neq 0}$, $(3m)_{m\neq 0}$ and so on. This approach is not forbidden by the above equation. Indeed, considering a velocity field $\mathbf{v}\sim 1/r^l$ and a temperature field $\vartheta\sim 1/r^{\widetilde{l}}$ leads to the condition $l+\widetilde{l}+1=\widetilde{l}+2$ which holds $\forall\,\widetilde{l}$ provided that $l=1$.

4.5 Discussion

In this chapter, we essentially derived the solution to the incompressible Stokes equation within a half – space. We saw how the classical Lamb's solution shall be generalised in this approach : restricting the solving to a half – space yields the relaxation of the constraint $m\in[\![-l,l]\!]$ and thus the substitution of the associated Legendre polynomials $\{P_l^m(c)\}$ by associated Legendre functions $\{\mathcal{P}_l^m(c)\}$ defined also for $|m|>l$. The on – axis singularity in $c_s=1$ is tackled by a regularisation process consisting in an adequate factorisation of c – dependent polynomials.

Moreover, we derived the far – field axisymmetric $(lm)=(10)$ solution to the nonlinear $(\mathbf{V},\Theta)$ – coupled advective problem. The latter models the axisymmetric flow observed experimentally under slight heating conditions. A future work on our route towards a theory of the instability would be to study the response of this ground state to azimuthal perturbations. Still, the present case is complicated by the special way powers of $1/r$

are related through the advection – diffusion heat equation, entailing a strategy different from a standard linear stability analysis based on studying the sign of a time/spatial – dependent growth rate. Intriguingly, the stability analysis carried out by Shtern and Hussain in [59] does not predict the onset of a dipolar flow state ($m = 1$). According to their work, the quadrupolar flow ($m = 2$) is the first unstable mode rather than the dipole. Anyhow, deriving the 'hemispherical' Lamb's solution was a preliminary step that provided us with non – axisymmetric flow states to serve as perturbative fields.

The fundamental flow states (10) and (21) plotted in sec. 4.3.5, though unveiling in a promising way the existence of multipolar modes in the 'hemispherical' Lamb's solution, still differ from the flow patterns observed experimentally. This is actually not surprising since the current theoretical model is far from grasping the whole intricacy of the real system, *e.g.* it does not take into account the (almost) unavoidable presence of surface – active impurities adsorbed on the water/air interface, nor does it address the generation of counterflows due to liquid confinement in our small experimental cell ...

To finish, it should also be stressed that the no – flux and the Marangoni boundary conditions are insufficient for expressing all integration constants $\left\{\pi_{(lm)}, \rho_{(l-2,m)}, \sigma_{(l-1,m)}\right\}$ in terms of the interfacial temperature amplitudes $\left\{\psi_{(lm)}(0)\right\}$. For instance, they do not yield any information regarding the constants $\pi_{(11)}$ or $\pi_{(22)}$. To fix this issue, one should add a near – field boundary condition in the model, presumably the no – slip condition on the surface of the hot bead which is then considered a spherical particle of finite radius a.

Conclusion

In this thesis, we studied the flow that a point source generates at the water/air interface. Given the rotationally invariant geometry of the system, one naturally expects a purely radial flow. Such a flow exists, but is only the 'ground state'. As soon as perturbations become sufficiently strong, the axisymmetry of the base flow is broken giving place to pairs of counter – rotating vortices periodically distributed all around the source.

This azimuthal instability can be observed using various setups that are all based on axisymmetrically – fed surface flows. We reviewed in the literature systems that harness the Marangoni effect, either chemical or thermal. The most common process uses some surface active material injected at a point of the interface or under it : a centrifugal flow is created this way through the chemical Marangoni effect [4, 5, 6, 7, 48, 67, 68, 69, 70]. An alternative option to induce a divergent flow at the water surface consists in heating the interface locally so as to generate a thermally driven Marangoni flow [71] – [74].

As pointed out several times in this work, a key ingredient is here the state of the water/air interface under practical conditions. One cannot explain the hydrodynamic responses observed in the experiments without taking into account surfactant molecules adsorbed on the real interface. The surfactant elastic layer resists the centrifugal flow, which results in remarkable consequences : at low forcing, very weak flows develop on the interface and the latter may be even completely blocked; yet the interface unfreezes under strong enough forcing conditions, which gives rise to multipolar flow patterns, the most basic one being a dipole formed by a pair of counter – rotating vortices.

Similar hydrodynamic multipoles have already been reported by a few authors on the occasion of various experiments [4] – [7], and even accidentally sometimes [49]. However, to date, there exists no sound theory of this instability in the literature. The phenomenon

investigated here is *a priori* very intricate as it involves the surfactant concentration Γ and the temperature Θ fields that are both coupled to the flow velocity $\mathbf{V}$ [75]–[79].

In this thesis, we contributed to the understanding of this general problem through addressing specific points. We designed two original experiments while, on the theoretical level, we focused on the ideal case of a thermocapillary flow devoid of surfactants.

Our water jet experiment (chapter 2) is certainly the most simple realisation of a divergent flow one may imagine. Its implementation is quite easy, this experiment being also 'minimalist' in the sense that it only couples the surfactant concentration Γ to the flow velocity $\mathbf{V}$. Despite its great simplicity, it seems we have been the first to use such a tool for probing the elastic response of the surfactant–laden interface. We have learnt many things from this experiment, especially the following points:

- At low jet speed V_{inj}, the interface is blocked and the flow, which is confined to the bulk, takes the form of a torus centred on the axis of the source. We have seen that the morphology of the base flow as well as its dimensions are well captured by the recent theory of Bickel *et al.* and the numerical simulations performed by J-C. Loudet [45]. The fact that the flow features are explained by the presence of a surfactant layer at the interface is now well established.

- Above a threshold injection speed $V_{\text{inj}}^{\star}$, the axisymmetric base flow is destabilised and the flow becomes dipolar. The interface unlocks along the median axis of the dipole vortex pair, which is a region of high velocity. We characterised the dipolar flow measuring the maximum velocity $V_{\max}$ along the interface. We have shown that $V_{\max}$ plays the role of an 'order parameter' which quantifies the magnitude of the dipole. Surprisingly, the value of $V_{\max}$ seems to depend solely upon the injection speed V_{inj}, and not on the distance H separating the injector from the surface. This result is very counterintuitive, to such an extent that we do not know how to interpret the unlocking of the interface. It will be of utmost importance to see whether the upcoming theory of the instability grasps this point.

The originality of our hot bead experiment (chapter 3) lies in the way we implement it, with a laser–heated carbon microbead stuck onto the end of an optic fibre. From a qualitative point of view, the heating power $\mathcal{P}$ plays a role analogous to the injection speed V_{inj} in the jet experiment, and strong similarities exist between the flow structures observed at varying $\mathcal{P}$ or V_{inj}. A thermocapillary convection torus appears under low heating conditions and is replaced by multivortex flow patterns at higher heating levels.

Still, we did not observe a complete blockage of the interface : the surface flow velocity is not zero but decreases as $1/r^2$ at low temperatures. Besides, the thermocapillary flow we observed at high powers was often quadrupolar. According to our observations, the 'torus – to – multipole' transition occurs at some finite $\mathcal{P}$ but the system's behaviour is strongly hysteretic and the flows may vary a lot from one experiment to another, to such an extent that we are not able to construct a graph of $V_{\max}$ in function of $\mathcal{P}$ that would be the thermal counterpart of what we plotted in the jet experiment.

The hot bead setup is rather easy to operate but offers a poor level of reproducibility. It must be noted that thermal excitation couples the fields $\mathbf{V}$, Θ and Γ, leading to a higher level of complexity compared with the jet configuration. We probed the coupling between $\mathbf{V}$ and Γ through the elastic response to laser shutdown of the surfactant – laden interface, and also the 'hydrothermal' coupling ($\mathbf{V}$, Θ) by the simultaneous observation of both the surface flow and the temperature maps. We checked that the streamlines align with the isotherms at high power $\mathcal{P}$, which is the behaviour predicted by the theory when heat is essentially transported through advection, *i.e.* at large thermal Péclet numbers.

The advective coupling between $\mathbf{V}$ and Θ is the nonlinear framework we focused on in the theoretical part of the thesis (chapter 4). We derived an exact solution to this problem in the case of a pristine interface ($\Gamma = 0$). We have shown that a point heat source sitting across the water/air interface can trigger different flow modes. The purely radial flow appears as the 'fundamental mode' independent of the azimuth φ. On the contrary, the structures of the 'excited modes' explicitly depend on φ. We insisted on the particular mode (21) whose flow pattern recalls the vortex dipoles observed experimentally.

The reader has understood that explaining this instability is a difficult matter and that we are far from a complete theory of this phenomenon. The theory shall reproduce the flow structures observed in the experiments as elementary solutions of the governing equations and provide a detailed analysis of their stability. Numerical simulations may be a powerful tool in parallel with the theory but are also very difficult to achieve. Major efforts are needed to go further and the road promises to be long and winding, but it is worth taking on the challenge given the 'universality' of this instability. To be convinced of this, one just has to glance at the examples gathered in Fig. 4.6. One notes that this instability appears over a broad spectrum of length scales and in a wealth of practical situations, from the optical manipulation of heat absorbing microparticles [2] to the stunning vortical structures generated by a bubbly column in a champagne glass [50, 51].

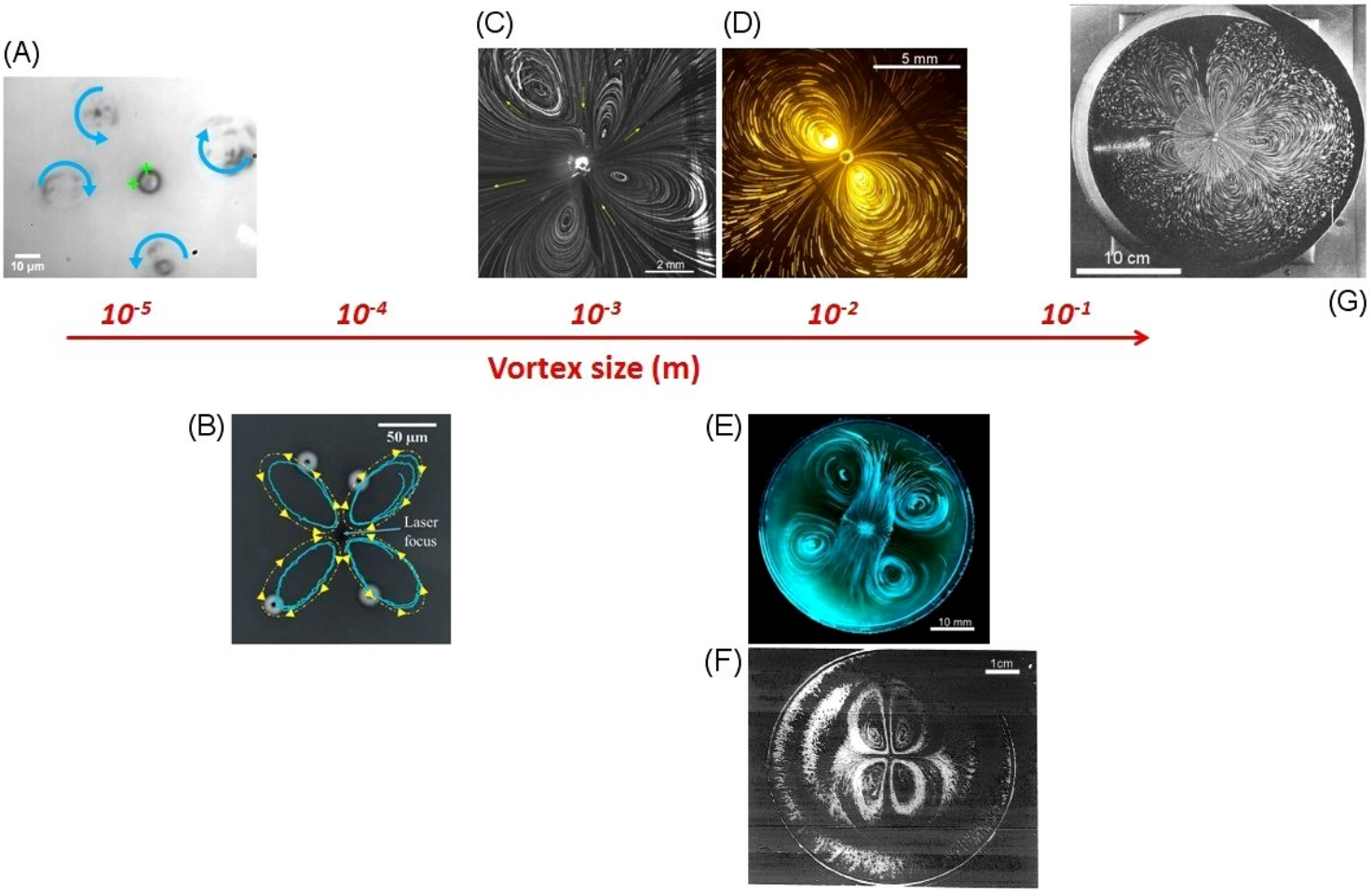

Figure 4.6: A universal instability. The azimuthal instability studied in this work is observed in a wealth of practical situations, with a typical vortex size that can range over at least four decades. (A) Laser−induced quadrupole around an optically trapped microsphere at the water/air interface [2]. (B) Quadrupolar flow pattern developing on the surface of a laser−illuminated solution of photoswitchable surfactants [80]. (C) Example of a quadrupolar surface flow arising in our laser−heated carbon bead experiment. (D) A dipole observed in our submerged jet experiment. (E) A quadrupolar pattern of 2D convective cells forming on the surface of champagne poured into a flute [50, 51]. (F) Quadrupole created by a thin air jet perpendicularly impinging the surface of a horizontal soap film [49]. (G) Marangoni−driven octupolar flow on a surfactant−enriched water bath [4].

According to our observations, controlling both the nature and amount of surfactants adsorbed at the water/air interface is the prime area for improvement. Unfortunately, we cannot do much better with our setups, primarily due to contaminants inevitably present in the ambient air. The production of 'zero surfaces', namely surfaces pure from molecules of foreign substances, is a delicate affair. One attempt in this direction is to work with silicone oil instead of water [5, 57], the latter being less prone to contamination owing to its lower surface tension. As for us, inspired by the 'blowing' experiment of Couder *et al.* ([49], § 4), we propose an alternative to our water jet setup that consists in hitting the interface perpendicularly with a jet of an inert gas, *e.g.* argon, in a neutral atmosphere. One major asset of this approach is to dispense us from using pipes and syringes that are important sources of contamination. In future experiments, it will also be worth grafting the Milli – Q water purification system directly onto the setup, to avoid contaminating the interface during the transport of the sample from one room to the other. We hope to attain this way purity levels comparable to those set in Langmuir – Blodgett throughs, where the amount of surfactant material adsorbed at the interface is finely controlled.

To conclude, the take – home message of this thesis is that even traces of a surfactant can alter surface tension driven flows at the water/air interface and set the elasticity conditions for the onset of the instability. In that respect, this work is complementary to the wealth of experimental and theoretical studies recently performed in a geometry similar to that of our water jet experiment [6, 67, 68]. Besides, this thesis contributes to a better understanding of how a free hot microsphere confined to a liquid surface can morph into an active particle able to self – propel at large speeds, through harnessing the vortex pairs intrinsic to the azimuthal instability it has induced. Our hot bead experiment might also serve as a 'toy model' to better apprehend the swimming of microorganisms. Finally, despite their apparent simplicity both systems explored in this work still harbour a plethora of amazing phenomena.

Appendices

Appendix A

Complementary information on the setups

A.1 Dimensions of the different parts of the setups

Either a small or a large cell is used (Fig. A.1). The wider cell serves us to study whether the instability is due to flow confinement (sec. 2.5.1). The cells and the glass lid are made of optical glass. The tank has an inner diameter $\varnothing_{\mathrm{t}}^{\mathrm{in}}$ 69.5 mm and a height $h_{\mathrm{t}} = 42$ mm. Its cover is pierced for passing the pumping pipe therethrough. The injection tube has an inner diameter $\varnothing_{\mathrm{inj}}^{\mathrm{in}}$ 0.55 mm* (outer diameter $\varnothing_{\mathrm{inj}}^{\mathrm{out}}$ 0.8 mm). An outlying tube of same diameter is flush with the bottom of the cell to drain liquid while disturbing the bulk flow as little as possible. The hydraulic circuit consists of a 1.3 mm thick silicon tygon tubing. In the 'head – to – tail syringes' setup, a pair of 2 mL capacity syringes (purchased from Chance) with an inner diameter $\varnothing_{\mathrm{s}}^{\mathrm{in}}$ 8.9 mm is used.

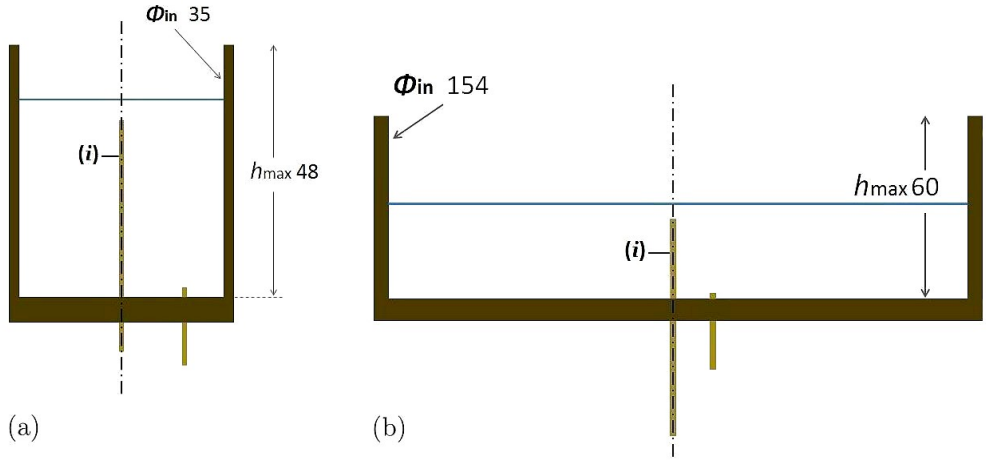

Figure A.1: Dimensions of the small (a) and large (b) cells (not to scale). Diameters and heights expressed in mm. The injection nozzle (i) has an inner diameter $\varnothing_{\mathrm{inj}}^{\mathrm{in}}$ 0.55 mm.

**Nota bene* : The inner diameter of the injection nozzle is more precisely $546 \pm 10\,\mu$m. This incertitude is obtained by a circular fit of the nozzle on microscopy images (Fig. 2.36).

A.2 Typical values of the control parameters

A broad range of gap values is explored in the 'gravity flow' setup, from slightly positive $H \sim 0.1\,$mm up to $H \approx 1\,$cm. Experiments at small $H \approx 0.25\,$mm, moderate $H \approx 1\,$mm and big $H \approx 2.5\,$mm gaps are conducted in the 'head – to – tail syringes' configuration. The 'gravity flow' setup supplies injection rates Q_{inj} in the order of a few mm^3/s (detailed calculation of Q_{inj} provided in Appendix B), that is injection speeds V_{inj} of a few cm/s. A bit more intense jet flows are generated with the syringe pump : here Q_{inj} ranges from $1.67\,$mm^3/s up to $33.33\,$mm^3/s, corresponding to V_{inj} in the interval $0.7 - 14\,$cm/s.

A.3 Special precautions

Special care has to be taken with the 'head – to – tail syringes' setup. The latter main drawback is the difficulty to remove air bubbles that nucleate within the syringe bodies and the flexible pipes. Bubbles must be wiped out clearing the pipes thoroughly so as to inhibit parasitic pressure differences that would cause the plungers to move irregularly. Moreover, stick – slip issues appear at low injection rates. Another limitation while working with the syringe pump is the short experiment time, not exceeding the few minutes needed for the translating part of the apparatus to reach the mechanical stop.

Appendix B

The injection rate Q_{inj} in the 'gravity flow' configuration

B.1 General presentation

In the 'gravity flow' configuration, the calculation of the injection rate Q_{inj} is a problem of filling/emptying a container. Because of the close – loop functioning of our hydraulic circuit, any variation of the liquid level in the cell results from the combined effects of injection and pumping : when injection is stronger (resp. weaker) than pumping, the level of liquid in the cell increases (resp. decreases) with time. The quantity $Q_{\text{gap}} = S\,(\mathrm{d}H/\mathrm{dt})$ (S : cross – sectional area of the cell) takes both evolutions into account, being positive or negative according to whether the gap H increases with time $\mathrm{d}H/\mathrm{dt} > 0$ (resp. decreases with time $\mathrm{d}H/\mathrm{dt} < 0$). The value of Q_{gap} is set fixing the height difference Δ between the liquid levels in the cell and in the reservoir.

Let Q_{inj} be the injection rate we want to calculate and Q_{pump} the pumping rate. Injection (resp. pumping) is a gain (resp. a loss) of liquid for the system. The outcome $\Delta Q = +Q_{\text{inj}} - Q_{\text{pump}}$ between what the system gains and what it looses corresponds precisely to Q_{gap} , so that we end up with the relation

$$Q_{\text{inj}} - Q_{\text{pump}} \equiv Q_{\text{gap}} = S\,\frac{\mathrm{d}H}{\mathrm{dt}}\ . \tag{B.1}$$

If H increases with time then $\mathrm{d}H/\mathrm{dt} > 0$ leading to $Q_{\text{inj}} > Q_{\text{pump}}$ as expected. If H decreases with time, this means $\mathrm{d}H/\mathrm{dt} < 0$ and corresponds to the case $Q_{\text{pump}} > Q_{\text{inj}}$.

Let us treat an example to get a better idea of how Q_{inj} is computed. The calculation is divided into two main stages :

- Calculation of Q_{gap}

  The calculation of Q_{gap} is based on the time tracking of the gap. The graph $H(t)$ reveals that the gap evolves linearly with time. Fig. B.1 shows an example of the regular decrease of the gap for an experiment lasting nearly fifty minutes. A linear fit yields the negative slope value $\mathrm{d}H/\mathrm{dt} \approx -0.13\,\mathrm{mm/min}$. With a cross-sectional area S of our cylindrical cell $S = \pi R^2 \approx 962\,\mathrm{mm}^2$, we obtain $Q_{\text{gap}} \approx -2.02\,\mathrm{mm}^3/\mathrm{s}$.

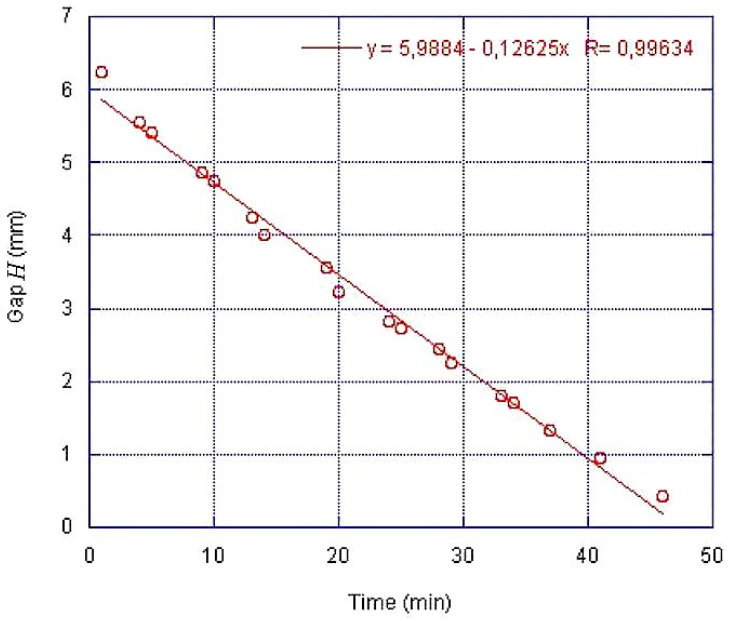

Figure B.1: Time evolution of the gap H.

  Remark: Most of the time, we make the approximation $\mathrm{d}H/\mathrm{dt} \cong \Delta H/\Delta t_{\text{exp}} = (H_f - H_i)/\Delta t_{\text{exp}}$ with H_i and H_f the initial and final values of the gap, and Δt_{exp} the experiment time. Although this a rough approach compared with meticulously tracking the gap over a long time, it captures the right order of magnitude of Q_{gap}.

- Calculation of Q_{pump}

  The calculation of the pumping rate Q_{pump} is based on the counting of the average number of droplets Nd the peristaltic pump discharges in the tank per unit time. In fact, the numbers fixed on the pump control box (denoted PR for 'Pumping Rate') are related but not identical to the true pumping rates Q_{pump}. A complementary experiment is hence needed in order to determine Nd for a whole set of 'pumping rates' PR. A linear relationship is evidenced between these two quantities (Fig. B.2). A linear fit yields the slope value $\Delta\mathrm{Nd}/\Delta(\mathrm{PR}) \approx 0.1$, meaning that on average one droplet more falls in the tank each time the pumping rate is increased by ten units.

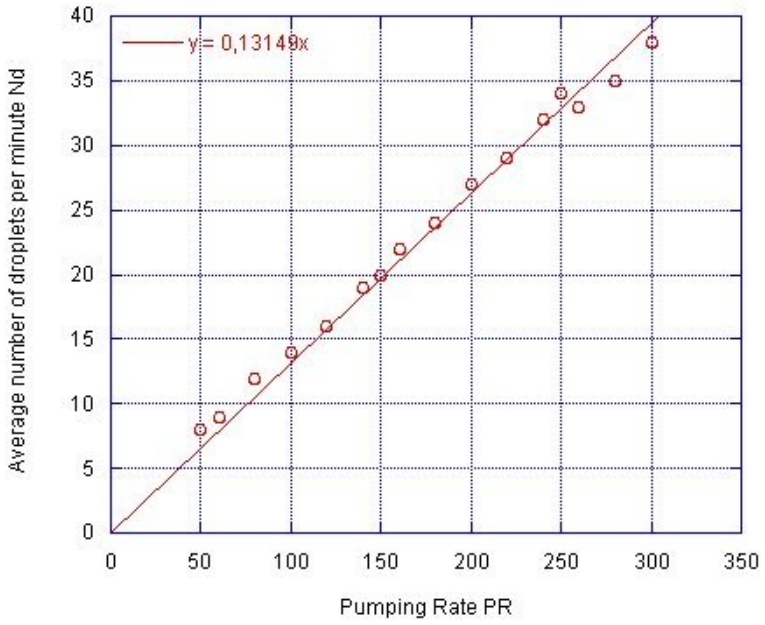

Figure B.2: Average number of droplets Nd **released in the tank every minute in function of the pumping rate PR.**

The pumping rate is PR = 150 in the experiment considered here. One reads on Fig. B.2 the value Nd = 20 for PR = 150. We still have to express this volume rate in mm^3/s. This is possible thanks to a preliminary experiment in which a container is used to collect a known number N of droplets. This amount of N droplets is weighed to deduce the mass m_d of a single droplet. We find $m_\mathrm{d} \approx 29.7\,\mathrm{mg}$. It is then straightforward to determine the total mass of Nd = 20 droplets. With the density of water $\rho_\mathrm{water} = 10^3\,\mathrm{kg}/\mathrm{m}^3$, one obtains $Q_\mathrm{pump} \approx 9.90\,\mathrm{mm}^3/\mathrm{s}$.

Eq. (B.1) yields $Q_\mathrm{inj} \approx 9.90 - 2.02 \approx 7.9\,\mathrm{mm}^3/\mathrm{s}$. The injection speed is $V_\mathrm{inj} = Q_\mathrm{inj}/s$ (s: cross−section of the injector, $s = \pi r_\mathrm{inj}^2 \approx 0.238\,\mathrm{mm}^2$). One finds $V_\mathrm{inj} \approx 3.3\,\mathrm{cm}/\mathrm{s}$, a value typical of the injection speeds attainable in the 'gravity flow' setup.

B.2 Increasing/decreasing gap experiments

In our configuration, pumping balances injection almost exactly, so that a slow variation of the gap $|\mathrm{d}H/\mathrm{dt}| \sim 0.1\,\mathrm{mm}/\mathrm{min}$ is imposed yielding $|Q_\mathrm{gap}| \approx 1.6\,\mathrm{mm}^3/\mathrm{s}$. Pumping rates Q_pump set in the increasing gap experiments are in the range $(9.9 - 11.9)\,\mathrm{mm}^3/\mathrm{s}$ and $(14.4 - 16.8)\,\mathrm{mm}^3/\mathrm{s}$ in the decreasing gap experiments. We get an injection speed $V_\mathrm{inj} \approx 5.25\,\mathrm{cm}/\mathrm{s}$ (resp. $V_\mathrm{inj} \approx 5.88\,\mathrm{cm}/\mathrm{s}$) in the increasing (resp. decreasing) gap experiments.

Appendix C

Technical information on flow visualisation

The exposure time (ET), *i.e.* the time over which the camera sensors are lit, is another parameter that must be tuned. The latter is fixed according to $\mathrm{FPS} \leqslant \mathrm{FPS}_{\max} = 1/\,\mathrm{ET}$, $\mathrm{FPS}_{\max}$ being the maximum attainable frame rate (for example, if $\mathrm{ET} = 0.04\,\mathrm{s}$, it is impossible for the camera to run at a frame rate faster than $1/0.04 = 25$ images/s). The ORCA-flash camera offers exposure times from $20\,\mu\mathrm{s}$ up to $10\,\mathrm{s}$, while the exposure times of the C5985 camera are in the range $1/10\,\mathrm{s} - 300\,\mathrm{s}$. To ensure sufficiently bright images one can either increase the exposure time, but this restricts even more the maximum frame rate, or simply increase the gain (magnitude of light amplification). Scale bars are obtained from calibration (table C.1). The X and Y calibrations differ on the side views but are identical on the top views. In fact, the cell is astigmatic because of its curved sidewall having unequal curvatures in two perpendicular planes about the optical axis. This default of rotational symmetry results in two distinct foci. The tracer particles are thus imaged as lozenges rather than bright spots, especially those located far from the optical axis. A correction lens (CL) is placed between the sample and the side camera to fix this issue (Fig. 2.4). This improves the quality of the pictures but a slight length distorsion between the X and Y directions remains, which explains the above discrepancy.

	TC : C5985/SC : ORCAflash-2.8	TC : ORCAflash-2.8/SC : C5985
Top views	$37.81\,\mu$m/pix (par $= 1$)	$52.08\,\mu$m/pix (par $= 1$)
Side views	$33.04\,\mu$m/pixX (par ≈ 1.142)	$31.90\,\mu$m/pix (average)

Figure C.1: Calibrations of the cameras. TC : top camera/SC : side camera. 'par' : 'pixel aspect ratio'. par ≈ 1.142 corresponds to X−pixels (pixX) and Y−pixels (pixY) such that pixY/pixX ≈ 1.142. 'average' indicates that the corresponding scale is obtained by averaging both X and Y calibrations.

Appendix D

Complementary information on dye injection

We first detail the way dye injection experiments are realised. Then we comment on the correlation between the 'coloured cloud' and the underpinning hydrodynamic structure.

D.1 Practical details

Dye injection slotting the end of a pipette into the drainage tube at the bottom of the tank causes an overpressure that strongly disturbs the multipolar flows. To bypass this issue, we design a minicup with a hole drilled into its bottom to fit it to the drainage tube. Fluorescein is injected in the cup which channels most of the colouring until it gets aspired by the drainage tube and flows out in the cell (Fig. D.1).

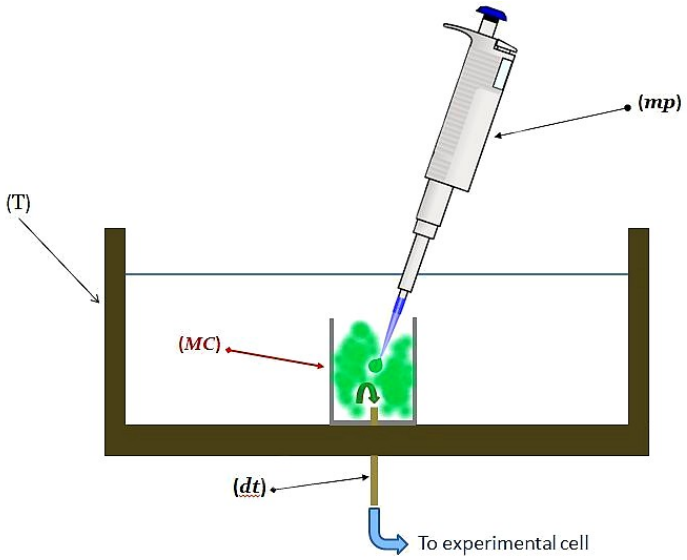

Figure D.1: The minicup. (mp) : micropipette ; (MC) : minicup ; (dt) : drainage tube ; (T) : tank.

Two observation modes are implemented (Fig. D.2) : a volume lighting (fig. a) and laser tomography (fig. b).

- *Volume lighting* — The cloud is uniformly illuminated by blue laser light supplied by a Coherent Innova 300 argon ion laser source ($\lambda_{\mathrm{Ar}} = 488\,\mathrm{nm}$, 60 mW) and guided by a multimode fibre. Speckle noise, which gives the emitted light a granular aspect, is suppressed shaking the fibre with a vibrator at a sufficiently high frequency. Fluorescein shines bright green under ultraviolet lighting. The main absorption and emission peaks appear in water at $\lambda_{\mathrm{abs}} = 494\,\mathrm{nm}$ and $\lambda_{\mathrm{em}} = 521\,\mathrm{nm}$, respectively.

  Projections of the coloured cloud volume are captured by the cameras. Either the top camera (TC) or the side camera (SC) can be replaced by a digital reflex camera (model Nikon D300, settings : ISO 1000, high sensitivity for photography in dark environments; shutter speed 1/15 s with aperture iris diaphragm at $f/5.6$; camera lens $f85\,\mathrm{mm}$ + close − up lens, namely a convergent lens used for macro photography) to take high − resolution colour photographs of the cloud (scales : $11.45\,\mu$m/pix, with par = 1, for the top views and $8.83\,\mu$m/pixX, with par ≈ 1.082, for the side views).

- *Laser tomography* — Another way of looking at the coloured cloud is through a top − down scanning of its structure. This technique called tomography yields additional information as slices of the cloud are now obtained instead of projections.

  The volume lighting is turned into a horizontal laser sheet vertically displaced by a motor connected to a low frequency signal generator (Agilent's 33210A model, 10 MHz function/arbitrary waveform generator). A $\nu = 140\,\mathrm{mHz}$ square − wave signal is selected. This way, it takes $T_{\mathrm{sweep}} = (1/2) \times (1/\nu) \approx 3.57\,\mathrm{s}$ to sweep the coloured structure from top to bottom. In steady state, the coloured structure extends over depths not exceeding twice the gap, that is a few mms, whereas the laser sheet travels a distance $\Delta h = 11\,\mathrm{mm}$ thus sweeping the whole coloured cloud. The success of such a laser sweeping experiment relies on one's ability to ensure uniform illumination as well as very regular motion of the laser sheet. One also needs to make sure that the sweeping velocity U_{sweep} is neither too fast nor too slow. If U_{sweep} were to be too fast, one would obtain a poor spatial resolution of the coloured structure with a 3D reconstruction based on an insufficient number of frames. Conversely, if U_{sweep} were to be too slow, the risk would be that some significant change in the shape of the coloured cloud occurs before sweeping is completed.

  Finally, a 3D reconstruction is achieved using the plugin 'Volume Viewer' from ImageJ (the structure associated with a dipolar surface flow is presented in sec. 2.3.2).

ImageJ creates a stack in which an 'altitude' is assigned to each frame, so that two successive slices are separated by a distance δz defined as the ratio of the travelling distance $\Delta h = 11\,\text{mm}$ of the laser sheet over the sweeping time $T_{\text{sweep}} = 3.57\,\text{s}$ to the total number of recorded frames $N_{\text{frames}} = \text{FPS} \times T_{\text{sweep}} = 45.4 \times 3.57 \approx 162$. One finds $\delta z = \Delta h / N_{\text{frames}} \approx 67.90\,\mu\text{m}$. The reconstructed volume is thus a cluster of $\delta x\,\delta y\,\delta z = (52.08 \times 52.08 \times 67.90)\,\mu\text{m}^3$ voxels (3D pixels).

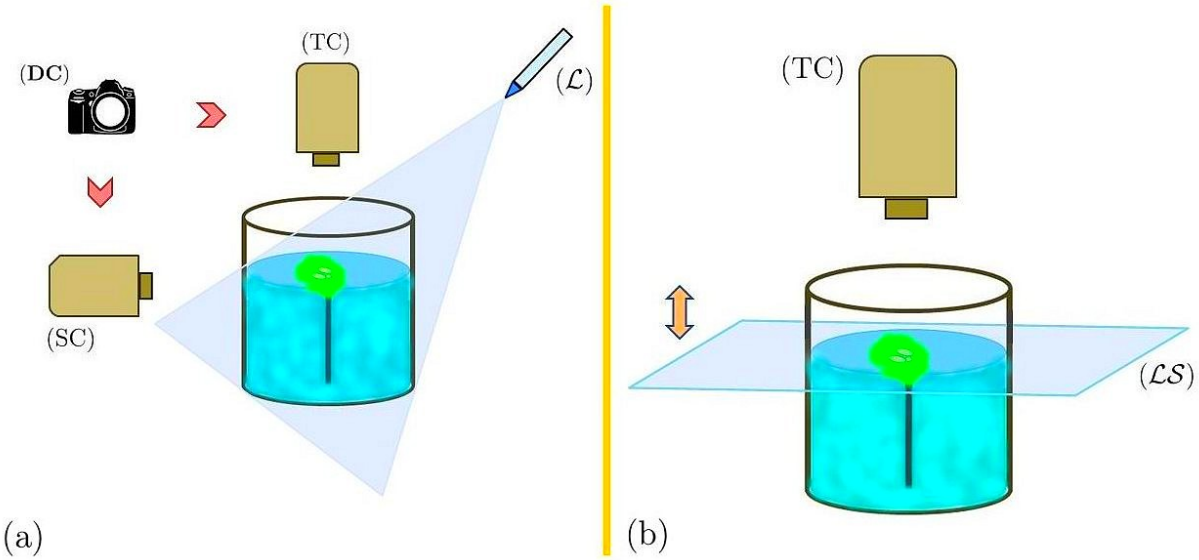

Figure D.2: Dye injection experiments. (a) Projection views obtained via a volume lighting of the coloured cloud. (b) Laser tomography to cut up the coloured structure into slices. ($\mathcal{L}$) and ($\mathcal{LS}$): blue laser light source and laser sheet, respectively. (TC) and (SC) are the top and the side cameras. (DC) is a digital camera used to capture high−resolution colour photographs of the cloud.

D.2 Comments on transport mechanisms

In the dye injection experiments, the coloured cloud undergoes (1) advection, (2) thermal agitation which causes molecular diffusion and (3) gravity responsible for sedimentation. In an ideal experiment, the cloud subject to the sole action of (1) traces the flow structure faithfully. Still, (2) and (3) cannot be ruled out in actual experiments, which introduces some discrepancy between the coloured cloud and the hydrodynamic structure it covers.

On the one hand, sedimentation makes the cloud collapse. This effect is delayed using a 'light' fluorescein solution. For instance, with a concentration $\mathcal{C}_{\text{Fluo}} = 4 \times 10^{-4}\,\text{mol/L}$ the sedimentation−limited time is $\tau_{\text{sed}} \sim 1\,\text{min}$. Let τ_{feed} be the typical feeding time over

which dye is supplied to the bath. Writing that $s\,V_{\rm inj}\,\tau_{\rm feed} = \mathcal{V}_{\rm color}$ ($s = \pi r_{\rm inj}^2 \approx 0.238\,{\rm mm}^2$, area of the injection nozzle ; $V_{\rm inj} \sim 1\,{\rm cm.s}^{-1}$, typical injection speed and $\mathcal{V}_{\rm color} \approx 200\,\mu{\rm L}$, injected volume of dye), one finds $\tau_{\rm feed} \sim \tau_{\rm sed} \sim 1\,{\rm min}$. The cloud is thus fully visible over a convenient time $\Delta t \sim 1\,{\rm min}$, a crucial point for a correct analysis of its morphology.

On the other hand, diffusion makes the cloud blurry. Let L be the typical distance separating two structural elements we shall differentiate in order to figure out the cloud shape properly. Our observations yield $L = 1\,{\rm mm}$. If the colouring diffuses over a length comparable to L during the time $\tau_{\rm sed}$, it becomes impossible to get an accurate picture of the cloud structure. Let l be the distance a dye molecule submitted to diffusion travels over $\tau_{\rm sed}$. Its diffusion constant D is estimated through the Stokes – Einstein formula (taking $a \sim 1\,{\rm nm}$ as the size of a dye molecule). One finds $D \approx 2.2 \times 10^{-10}\,{\rm m}^2/{\rm s}$. The mean square displacement obeying the law $l^2 = 6D\tau_{\rm sed}$, one ends up with a distance $l \approx 0.3\,{\rm mm} < L$ over the time $\tau_{\rm sed} \sim 1\,{\rm min}$, meaning that diffusion only slightly affects the coloured cloud whose structure remains interpretable over the observation time. Therefore, we expect the coloured cloud and the underpinning hydrodynamic structure to be strongly correlated, provided that the gap H is kept constant for the flow to be in a (quasi-)stationary state.

Appendix E

Complementary information on shadowgraphy

In this appendix, we first present shadowgraphy principles adapted to our own situation and give the experimental protocol to characterise the 'hydraulic bump' generated by the water jet. We next derive useful relations to calculate the bulge dimensions and conclude with a concrete example on how to apply them.

E.1 General presentation

The water jet induces a deformation of the interface above the injection point. Owing to the cylindrical geometry of the jet, assuming a bump−like axisymmetric deformation of the interface is pretty natural. A collimated light beam uniformly illuminates the surface over an area of approximately 1 cm in width centred on the injector's axis. Fig. E.1 depicts the way a collimated light beam reflects off a bump−like deformation. The direction of reflection of each incident ray of light depends essentially upon the local curvature of the deformed surface in a region close to the point of incidence. This explains the variations of the light intensity collected on a screen placed above the surface, with alternating brighter and darker areas compared with the uniform distribution of the reflected light observed for undeflected rays in the presence of a perfectly planar interface.

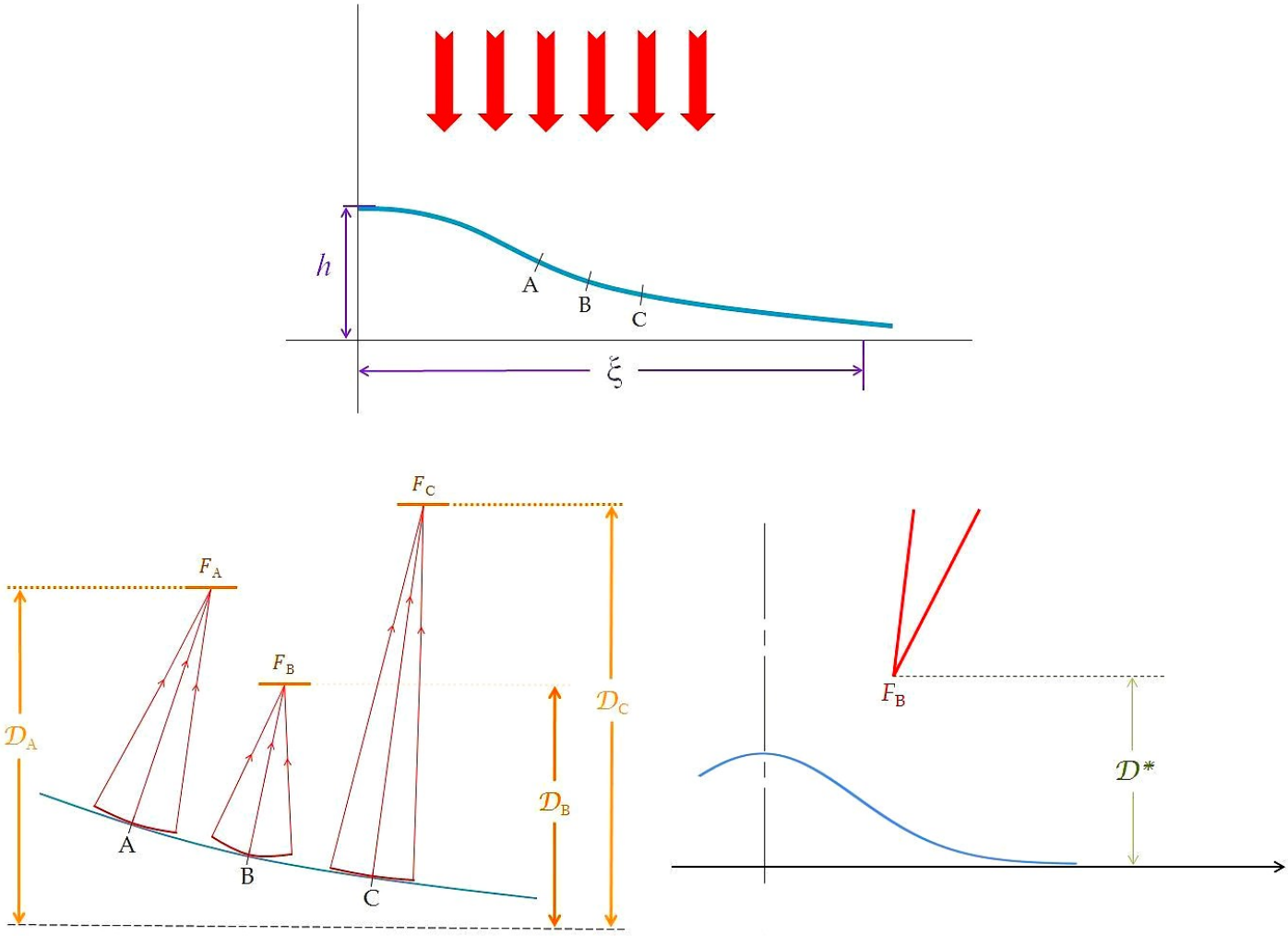

Figure E.1: Collimated light beam reflecting on a hydraulic bump of height h and extent ξ (*top figure*). (*Bottom left figure*) Profile of the bump approximated by a series of parabolic mirrors of local curvature radii R_i focusing light at a distance $R_i/2$ above the interface. Three points of incidence A, B, C taken along the bump such that $1/R_{\rm B} > 1/R_{\rm A} > 1/R_{\rm C}$. So the focal point $F_{\rm B}$ of the parabolic mirror centred on point B is the closest to the interface and $F_{\rm C}$ is the furthest. The minimum distance $\mathcal{D}_{\rm B}$ for which the focusing of the reflected rays is the strongest sets the critical distance $\mathcal{D}^\star$. (*Bottom right figure*) Cross−section of the caustic, namely the locus of all the focal points $\{F_i\}$ defined as the intersections of the multiple rays reflecting on the parabolic mirrors. Two branches merge into a cusp (singularity) located in $F_{\rm B}$.

The vision of a hydraulic bump is corroborated by the quasi – circular caustic imaged on the shadowgrams ('shadowgraphy stains') of the deformed surface (Fig. E.2).

- State (1) corresponds to a planar surface. The shadowgram is thus uniformly bright.
- The intermediate state (2) is observed for a slightly deformed interface. The water jet is too weak to strongly perturb the surface and/or the gap H is too big. Yet this minor deformation of the interface results in a lowered light intensity in the central part of the shadowgram. At this stage of the evolution this darker region does not have a sharp edge but is quite blurry.
- As soon as the surface deformation becomes sufficiently important, the shadowgram switches to state (3). A caustic appears in the centre of the shadowgram as a ring of intense brightness circumscribing a light extinction area.
- In the case of still larger deformations (not shown on Fig. E.2), the annular caustic expands until the dark disk covers the entire shadowgram.

Note that the incident laser beam, viewed as a cylinder of light impacting the surface with an angle of incidence θ, leaves on the interface a light spot whose outer shape is elliptic.

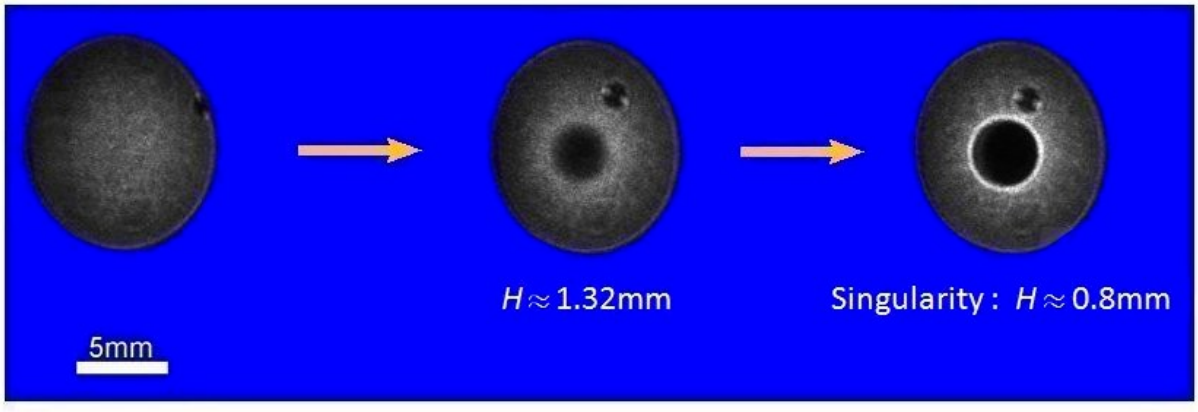

Figure E.2: Evolution of the shadowgram with a growing bump – like deformation of the interface. A poorly lit central area forms at a gap $H \approx 1.32\,\text{mm}$ as a result of the reflected light rays being angled outwards (Fig. E.1). A brilliant annular caustic appears at a gap $H \approx 0.8\,\text{mm}$. The parasitic cast shadow visible next to the centre is probably due to some impurity.

E.2 Experimental protocol

One displaces the screen (OS) in the reflected beam and seeks the critical distance $\mathcal{D}^\star$ at which the caustic first appears on it. However, if the observation plane intercepts the beam well before or after the reflected rays intersect, the shadowgrams are blurry and thus harm a correct measurement of the deformation. Setting $D^\star = 40\,\mathrm{cm}$ turns out to be suited for capturing small deformations. In this regard, the minimum detectable height $h_{\min}$ of the hydraulic bump is limited by the little space available in our laboratory. The greatest critical distances $\mathcal{D}^\star$ that can be accessed do not exceed a few metres. Introducing the latter order of magnitude in the formulas (E.1) below yields $h_{\min} \sim 0.1\,\mu\mathrm{m}$. $\mathcal{D}^\star$ shall be substantially reduced to measure sharper deformations, in which case the screen is placed on top of the cell at $D^\star \approx 2.5\,\mathrm{cm}$ above the free surface (Fig. E.3).

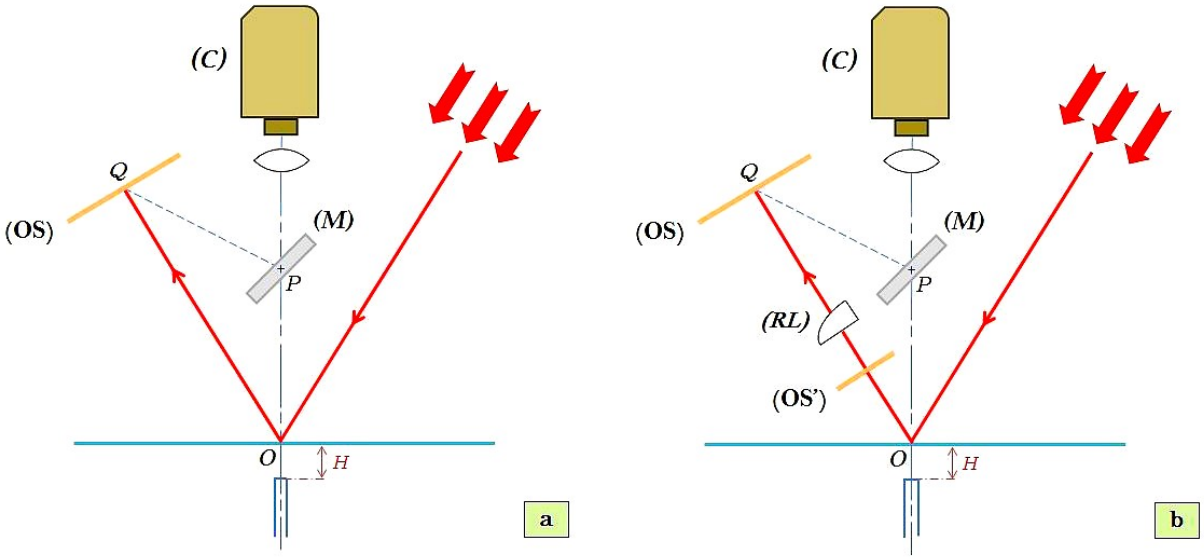

Figure E.3: Setups for measuring either small (a) or large (b) surface deformations. The top camera (C) focuses on the surface (point O). A flat mirror (M) is interposed on the optical path between the camera and the interface so that the camera sees the screen (OS). The distances PQ and PO must be equal to get a focused image on the screen. In configuration (a), the distance OQ between the surface and the recording plane is $D^\star = 40\,\mathrm{cm}$. In (b), the screen is brought closer to the interface while preserving a focused image: a relay lens (RL) forms on (OS) a sharp image of the shadowgram captured on an auxiliary screen (OS') placed at $D^\star \approx 2.5\,\mathrm{cm}$ from the interface. Note that both setups are suited for direct flow visualisation thanks to the swivelable mirror (M).

We start our experiments at a big gap H which is progressively decreased. As long as $OQ \ll D^\star$ the surface deformation is barely discernable. The gap getting smaller and smaller, a caustic first appears on the shadowgram when $OQ = D^\star$. Finally, the

typical height h and extent ξ of the hydraulic bump are inferred from the dimensions of its shadowgram and the experimental value of $D^\star$ using the formulas

$$h = \frac{1}{4\alpha\lambda^2\gamma}\,\frac{x^{\star\,2}}{\mathcal{D}^\star\cos\theta}\;, \tag{E.1a}$$

$$\xi = \frac{x^\star}{\lambda\gamma}\;, \tag{E.1b}$$

where $\alpha \approx 0.446$ and $\lambda = \sqrt{\beta}\left(1+\mathrm{e}^{-\beta}/\alpha\right) \approx 1.836$ ($\beta \approx 1.230$) are prefactors derived from the curvature function f'' of a gaussian deformation. γ is the ratio of the widths of the final and the inital shadowgrams (Fig. E.2). $x^\star$ denotes the abscissa of the caustic on the recording plane. Details on the derivation of formulas (E.1) are given below.

E.3 Derivation of the bump height h and extent ξ

Here we derive a simplified version of expressions (E.1) providing the geometric features of the 'hydraulic bump', its height h and extent ξ, in function of the critical distance $\mathcal{D}^\star$ and the shadowgram properties.

Let f be the function representing the deformation profile in the vertical cut plane $(y0z)$. The deformation state is calculated using the light slit method (Fig. E.4). Though in practice the laser beam exhibits a circular cross–section, all the information about the deformation is preserved with this method. By virtue of axisymmetry, the totality of the shadowgram can be inferred from the light slit reflection imaged on the screen. Fig. E.5 sketches top and side views of the surface deformation.

All three unit vectors $\hat{\mathbf{u}}_i$, $\hat{\mathbf{u}}_r$ and $\hat{\mathbf{u}}_n$ (Figs E.4 and E.5) belong to the plane that is perpendicular to the deformed surface at point $P(0,a,f(a))$. By definition, $\hat{\mathbf{u}}_r$ and $\hat{\mathbf{u}}_i$ are mirror images of each other with respect to the axis the vector $\hat{\mathbf{u}}_n$ is directed along. Assuming a gentle slope of the deformation profile, *i.e.* $|f'(a)| \ll 1 \;\; \forall\, a \in [-A,+A]$, the reflected ray coming out from point P satisfies the system

$$\left\{\begin{array}{lcl} y + 2f'(a)\,z & = & a\,, \\ x\cos\theta + z\sin\theta & = & 0\,, \end{array}\right. \tag{E.2}$$

derived from the condition $\boldsymbol{PM} \wedge \hat{\mathbf{u}}_r = \mathbf{0}$, M being a generic point of the reflected ray.

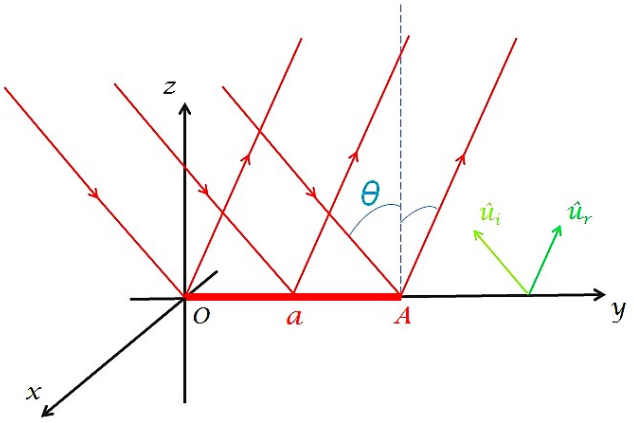

Figure E.4: Calculating the interface deformation with the light slit method. A laser sheet, depicted by a set of parallel incident rays (angle of incidence θ), illuminates a segment of length $2A$ located on the liquid surface along the axis (Oy). The reflected beam is imaged on a screen (not sketched) and the deformation state deduced from the light slit reflection. $\hat{\mathbf{u}}_i$ and $\hat{\mathbf{u}}_r$ are two unit vectors aligned with the directions of incidence and reflection, respectively. For simplicity, since the deformation is axisymmetric relative to the vertical axis (Oz), only a half−segment is represented.

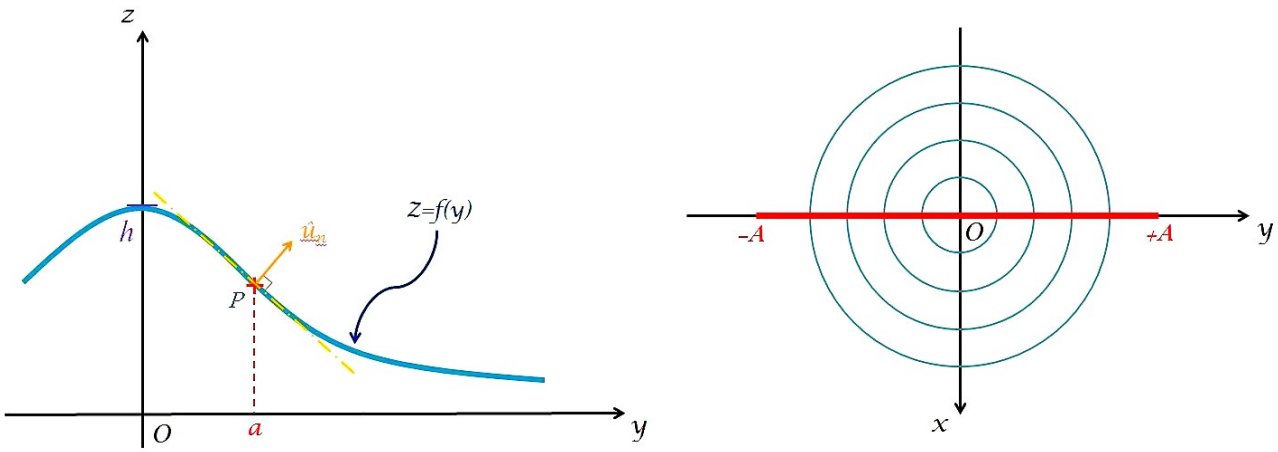

Figure E.5: Geometry of the deformation profile. (*Left figure*) Side view of the axisymmetric bump−like deformation of the interface. $\hat{\mathbf{u}}_n$ is the unit vector normal to the deformation profile $z = f(y)$ at point $P(0, a, f(a))$. (*Right figure*) Top view of the hydraulic bump. Each circle corresponds to a set of points located at a given altitude z.

The next stage is to determine the caustic, *i.e.* the envelope drawn by the intersection points of all reflected rays. Deriving $y + 2f'(a)\,z - a = 0$ with respect to a yields

$$\left\{ \begin{array}{rcl} y & = & a - \dfrac{f'(a)}{f''(a)} \ , \\ z & = & \dfrac{1}{2f''(a)} \ . \end{array} \right. \tag{E.3}$$

We consider a gaussian shape $f(a) = h \exp(-a^2/\xi^2)$ of the interface deformation which, by the way, is most probably a realistic assumption. With the reduced variables $t = a/\xi$ and $(\overline{y}(t), \overline{z}(t)) = (y(t)/\xi\,,\ (4h/\xi) \times z(t)/\xi\,)$, one obtains the parametric equations

$$\left\{ \begin{array}{rcl} \overline{y}(t) & = & -\dfrac{2t^3}{1-2t^2}\ , \\ \overline{z}(t) & = & -\dfrac{1}{1-2t^2}\,\mathrm{e}^{t^2}\ . \end{array} \right. \tag{E.4}$$

On Fig. E.6, we see two branches merging into a cusp S (singularity) whose coordinates are S $(\overline{y}^\star \approx 1.836 \equiv \lambda, \overline{z}^\star \approx 2.242 \equiv 1/\alpha)$ so that

$$\xi = \frac{y^\star}{\lambda}\ , \tag{E.5a}$$

$$h = \frac{1}{4\alpha\lambda^2}\,\frac{y^{\star\,2}}{\mathcal{D}^\star}\ . \tag{E.5b}$$

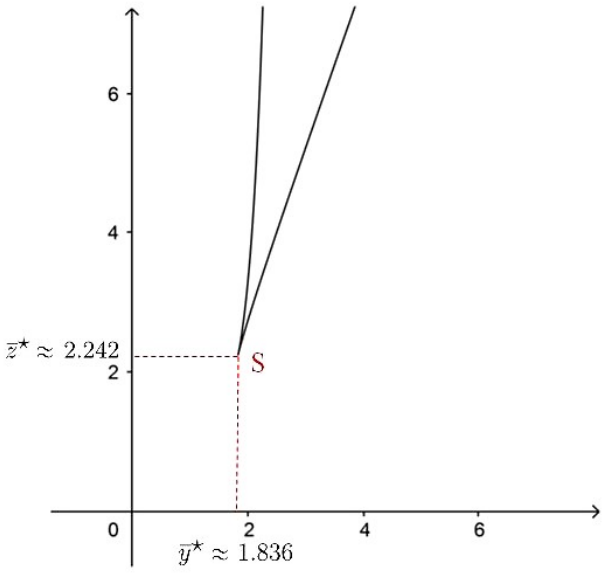

Figure E.6: Cross – sectional plot of the caustic $(\overline{y}(t), \overline{z}(t))$ in the cut plane (yOz).

The latter expressions are not exactly the same as Eqs (E.1) (apart from the fact that $x^\star$ is arbitrarily renamed $y^\star$). Actually, Eqs (E.1) are more general being valid whatever the angle of incidence θ (not only in the particular plane $(y0z)$ for which $\theta = 0$) and taking into account correction effects due to the parabolic curvature of the meniscus at larger distances from the source, through the introduction of the scale factor γ (Fig. E.7).

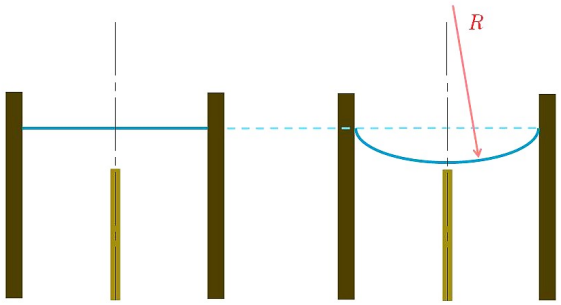

Figure E.7: Correction effects due to the curved meniscus. As the gap decreases, the meniscus gets hollower. Its concave shape is approximated by a parabolic mirror (radius of curvature R) that makes the reflected rays converge, resulting in extra light in the peripheral region of the shadowgrams.

E.4 Application of the formulas

We present a concrete application of formulas (E.1). We consider an experiment achieved at an injection speed $V_{\text{inj}} \approx 3.3\,\text{cm/s}$. The gap is decreased over $\Delta t \approx 1\text{h}$, from $H \approx 7.7\,\text{mm}$ down to $H \approx 0.5\,\text{mm}$. Fig. E.8 gives the dimensions of shadowgrams captured in such conditions. The scale factor γ, *i.e.* the ratio of the sizes of shadowgrams A and B, has to be estimated. We have $\gamma_{\text{H}} = (2b)_{\text{B}}/(2b)_{\text{A}} = 3.71/8.32 \approx 0.446$ along the horizontal axis and $\gamma_{\text{V}} = (2a)_{\text{B}}/(2a)_{\text{A}} \approx 0.510$ along the vertical direction. We keep the mean value $\gamma \approx 0.478$. We also need $x^\star$, the radius of the ring–shaped caustic at the very moment the latter appears on the screen. On shadowgram B, we measure $x^\star = \left[(2c)_{\text{B}} + (2d)_{\text{B}}\right]/4 \approx 1.08\,\text{mm}$. With $\alpha = 0.446$, $\lambda = 1.836$ and $D^\star = 40\,\text{cm}$ ($\cos\theta \approx 1$), formulas (E.1) finally yield a bump extent $\xi \approx 1.23\,\text{mm}$ and a height $h \approx 1.01\,\mu\text{m}$, that is an aspect ratio $\xi/h \approx 1218$! More estimates of the bulge dimensions are gathered on Fig. 2.32.

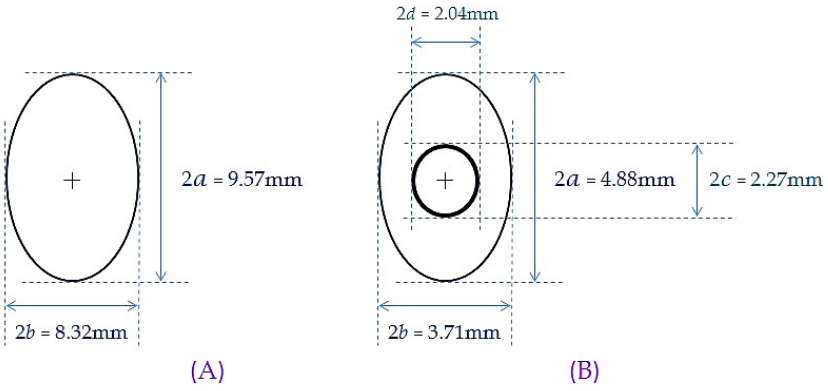

Figure E.8: Dimensions of typical shadowgrams. The gap is $H \approx 1.6\,\text{mm}$ when the 'critical shadowgram' B is captured ($\mathcal{D}^\star = 40\,\text{cm}$).

Appendix F

Portfolio of PIV maps

This appendix is a comprehensive collection of PIV maps for many different values of the control parameters. Double entry tables are provided, each square containing a map for a given couple (H, V_{inj}). On Figs F.1 – F.4 are displayed maps of the surface velocity magnitude $|\vec{v}_s|$, its components $v_{\parallel}$ and $v_{\perp}$ along the symmetry axis of the dipole as well as a direction perpendicular to it, and also the vorticity field ω. Velocity and vorticity maps are normalised by quantities denoted v_M and ω_M, the 'maximum' velocity and vorticity computed from the 1‰ numerical points of highest intensity. The length of all velocity vectors is set to unity so as to better distinguish the dipolar flow pattern.

A natural question concerns the evolution of the flow properties as the water jet is intensified and/or the gap is varied. Unsurprisingly, for a given gap, both the surface velocity and the vorticity increase with increasing injection speed. Moreover, the velocity declines at large gaps $H \approx 2.5\,\text{mm}$ probably due to flow confinement.

Also observe how the multicoloured area on the $|\vec{v}_s|$ – maps extends forward as the injection speed increases. As the gap grows, this high velocity area broadens and takes a crescent shape (clearly visible for $V_{\text{inj}} = 7\,\text{cm/s}$ and $H = 2.5\,\text{mm}$), while the red (positive) and blue (negative) regions of the vorticity fields get more and more oblong. Here again we attribute these facts to flow confinement.

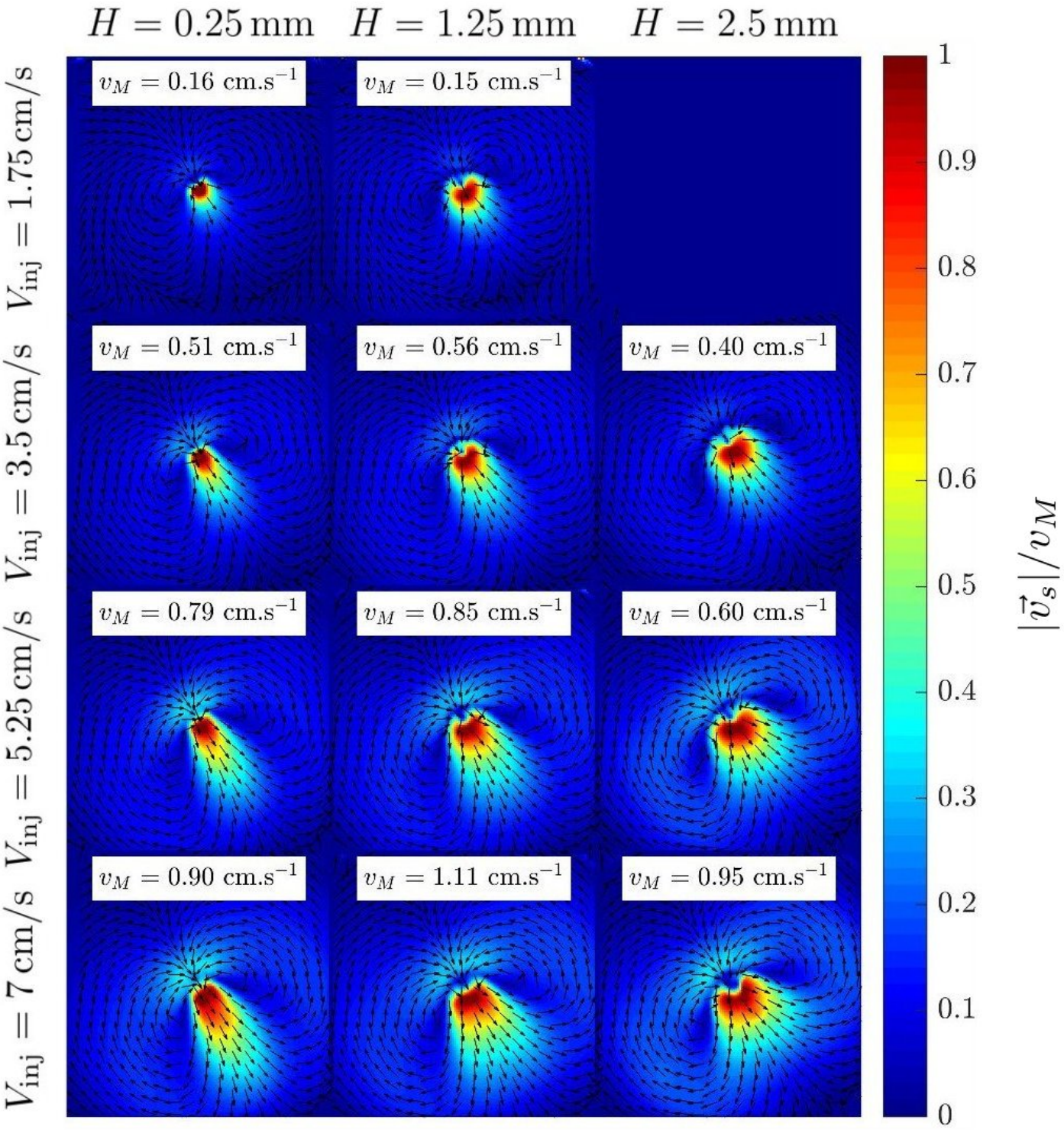

Figure F.1: Collection of PIV maps showing the normalised magnitude of the surface velocity $|\vec{v}_s|/v_M$ for different couples (H, V_{inj}) of the control parameters.

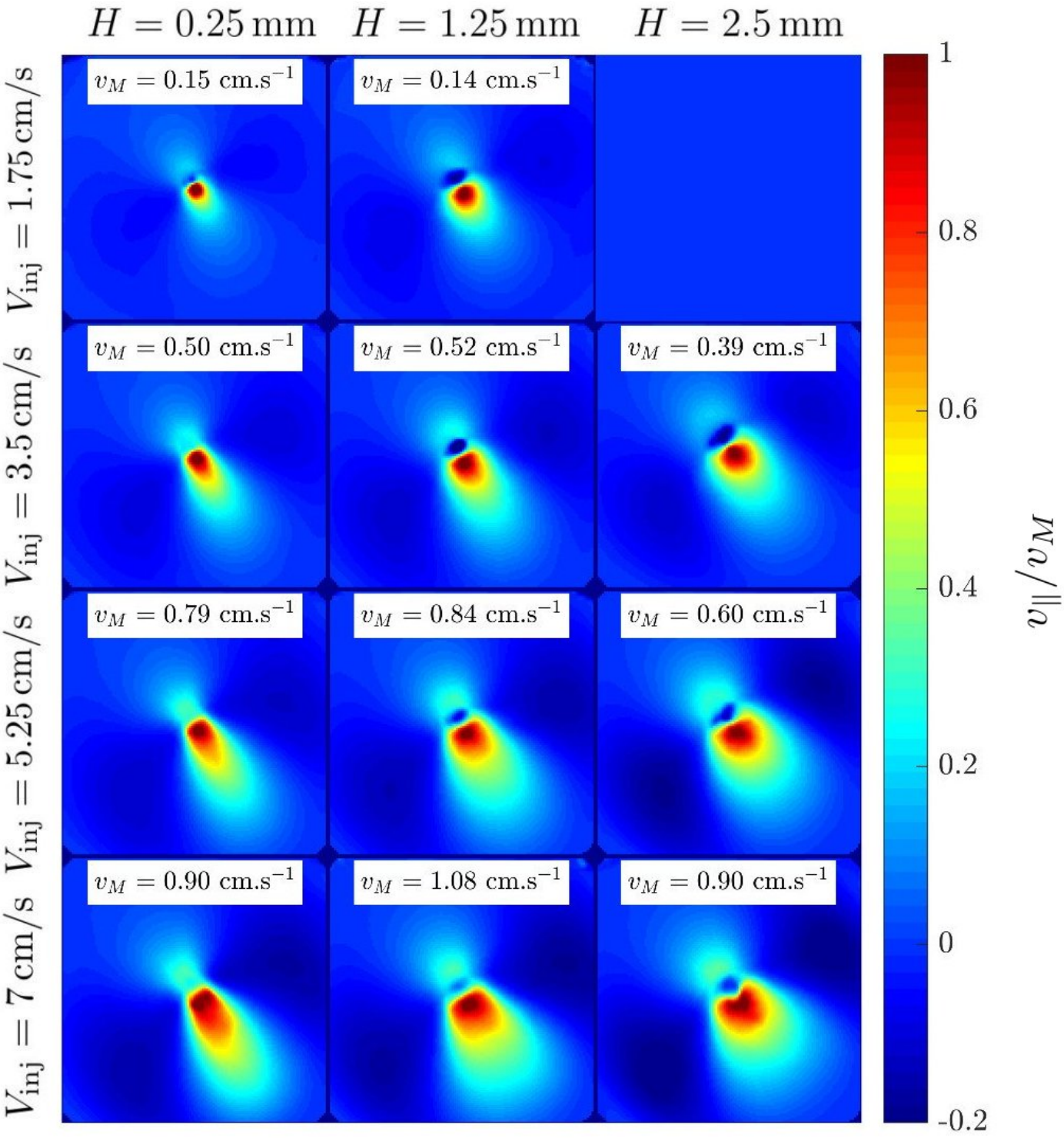

Figure F.2: Collection of PIV maps showing the normalised velocity $v_{\parallel}/v_M$ along the dipole symmetry axis, for different couples (H, V_{inj}).

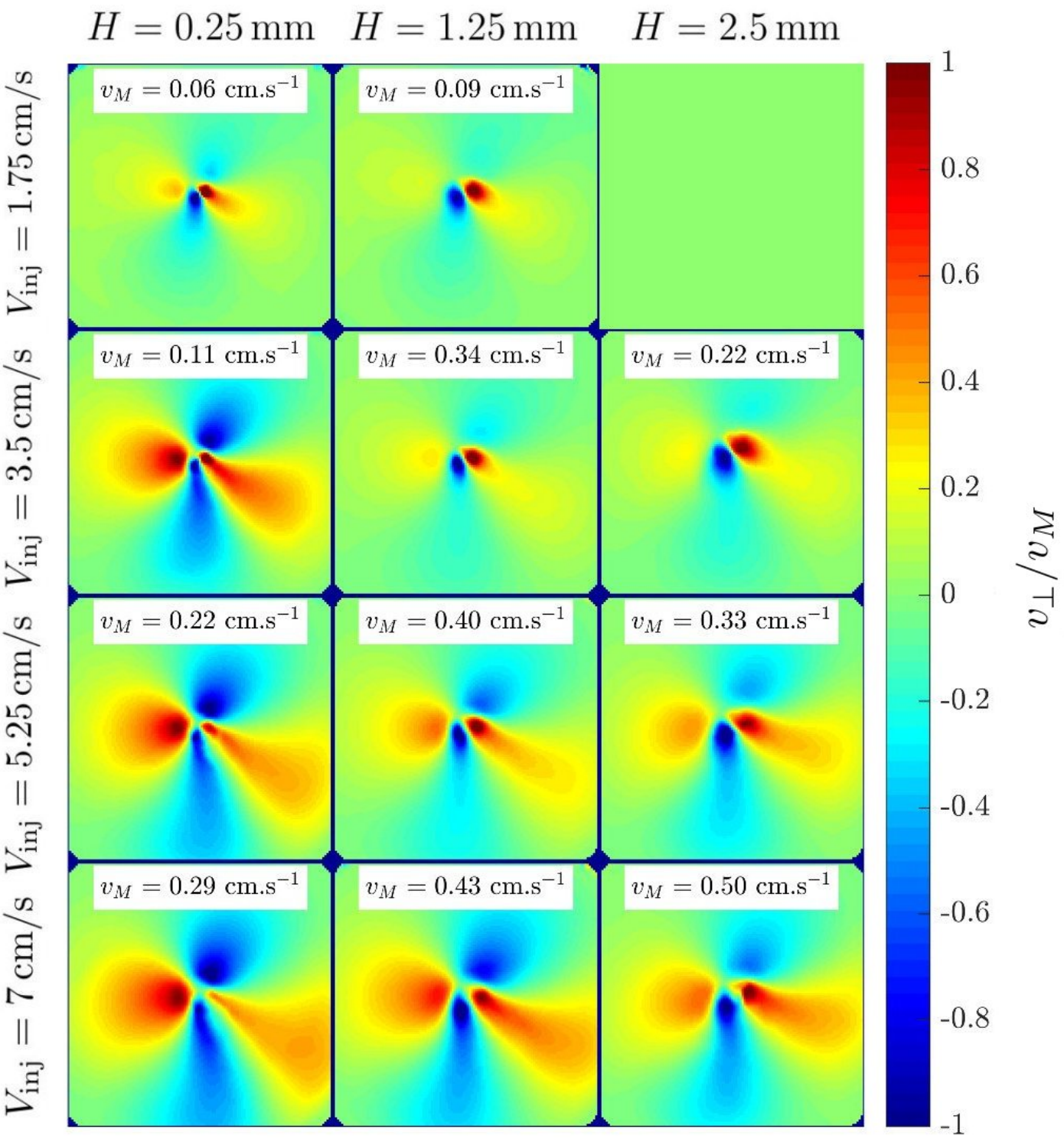

Figure F.3: Collection of PIV maps showing the normalised velocity $v_\perp/v_M$ along the direction perpendicular to the dipole symmetry axis, for different couples (H, V_{inj}).

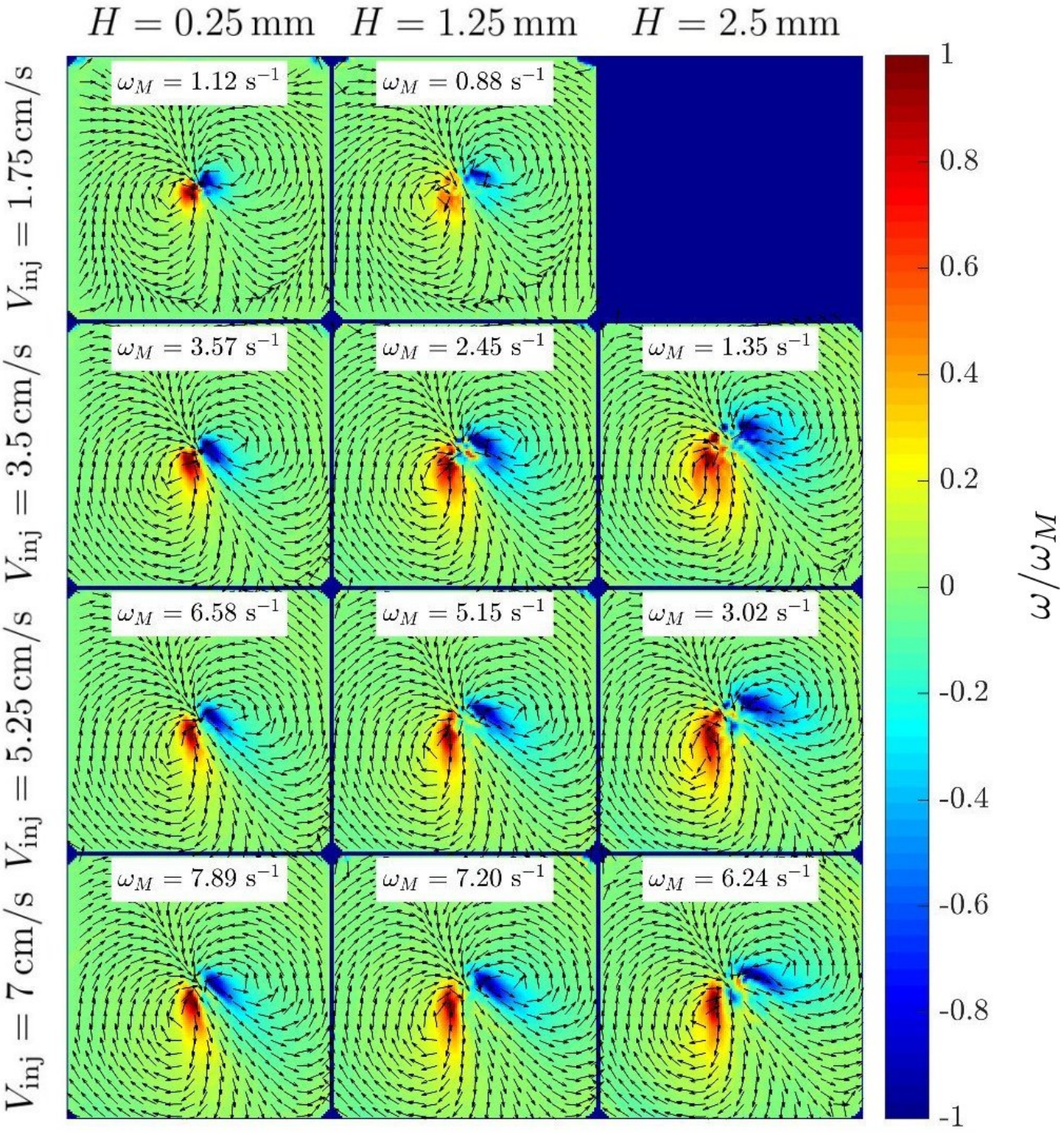

Figure F.4: Collection of PIV maps showing the normalised vorticity ω/ω_M for various couples (H, V_{inj}). The velocity vector field is the one displayed in Fig. F.1.

Appendix G

Technical information on the cameras

This appendix is devoted to a technical presentation of the cameras used to record the flows in the hot bead experiments.

Two EO – 1312M cameras (Edmund Optics) capture either horizontal (HV) or side (SV) views of the flows. The EO – 1312M is a 1.3 megapixel (full resolution 1280×1024 pixels), 8 bit, B/W CCD camera offering exposure times in the range $0.053 - 57.245$ ms and frame rates in the interval $6.10 - 17.45$ fps. Spatial calibration experiments yield, for the bottom and the side camera, the X and Y scales reported in table G.1.

	Bottom Camera	Side Camera
X scale (μm/pixX)	7.10	7.94
Y scale (μm/pixY)	Idem	9.43
Pixel Aspect Ratio (par)	1	$9.43/7.94 \approx 1.188$

Figure G.1: Spatial calibrations of the bottom and the side EO cameras.

The bottom EO camera is replaced when necessary by a pco.pixelfly camera from PCO, the latter being a 1.4 megapixel (full resolution 1392×1040 pixels) 14 bit CCD camera with available exposure times in the range $1\,\mu\text{s} - 1$ min and frame rates in the interval $7.3 - 13.5$ fps. The bottom camera is further equipped with a microscope objective from Edmund Optics, so that the calibration is now a function of the zoom (table G.2). Extension tubes are also added to the objectives of the cameras where relevant. The flows are usually recorded at a rate of 10 frames per second.

Zoom	Scale (μm/pix)
0.75	8.22
1	6.19
1.5	4.21
2	3.20
2.5	2.53
3	2.11

Figure G.2: Zoom – dependent scales of the bottom camera.

The side camera is mounted on a xyz translation stage to enable focus correction each time the laser sheet is displaced. Another xyz stage is utilised for the centring of the cuvette on the bottom camera axis. The position of both cameras, as well as that of the experimental cell is read on dial test indicators (Mitutoyo's model 2046F) with a 0.01 mm accuracy. Red – orange filters prevent the camera sensors from being damaged by direct exposure to intense laser light while allowing fluorescent light to pass.

Image acquisition is done with 'uEye Cockpit', a software from the IDS Software Suite adapted for the EO cameras, and with 'Camware', a control application for the PCO camera systems. Just like in the water jet experiment, time – lapse photography yields average frames whereon the distribution of the streamlines unveils the flow patterns.

Appendix H

The bead collage setup

Sticking a microbead onto the end of an optic fibre is a delicate affair that requires a setup specially designed for this purpose (Fig. H.1). The first step is to use a fibre optic stripper (*e.g.* the model NN203 from the No−Nik series of Clauss strippers) to strip the fibre to the cladding ($\varnothing_{\text{cladding}} = 125\,\mu\text{m}$). Next, the extremity of the fibre should be cleanly cut off by the diamond blade of a fibre optic cleaver such as Fujikura's CT−05 model. We take care to clean well the edges of the fibre paying particular attention to its cross−section. In practice, impurities deposited on the fibre are efficiently removed after a few hours soaking in Hellmanex. Hellmanex is a liquid alkaline concentrate, produced by Hellma, to be diluted in water to a few percent before use as a detergent.

Then comes sticking. The fibre is placed under a microscope (Olympus model IMT−2, magnification 20×). We spread on one side of a microscope slide a tiny amount of a glassy carbon spherical powder (particle size between 200 and 400 μm) purchased from Alfa Aesar, while a droplet of photocrosslinkable glue (NOA 65, a UV−curing adhesive from Norland) is deposited on the other side. With the manual xyz translation stage the fibre is mounted on and the xy translational control knobs of the microscope, the tip of the fibre is positioned right above the glue droplet prior to being soaked with it. Shortly after, the fibre is placed vertically to an isolated carbon bead. A fine pre−alignment of the fibre axis with the carbon bead is crucial to ensure coaxial sticking. The fibre is then lowered until a capillary bridge of glue forms between the surface of the microsphere and the extremity of the fibre. At this precise moment, the curing of the adhesive is conducted by a $\Delta t \approx 1\,\text{min}$ exposure to UV light from a Thorlabs CS2010 high power UV curing LED system (surface power density delivered at $\lambda = 365\,\text{nm}$ and with a continuous mode tuned at 85% : $\mathcal{P}_d = 167\,\text{mW/cm}^2$). The good completion of these steps is monitored by means of a CCD camera (Hamamatsu model C2400 XC−77) equipped with an extension tube

topped by a Zeiss Luminar lens (focal length $f63$) suited for photomacrography (working distance $d \approx 76\,\mathrm{mm}$). Finally, the strength of the bonding is checked by shooting at the bead with a 5 bar air pressure gun. Fig. H.2 is a photograph of a glassy carbon microbead successfully stuck onto the end of the optic fibre.

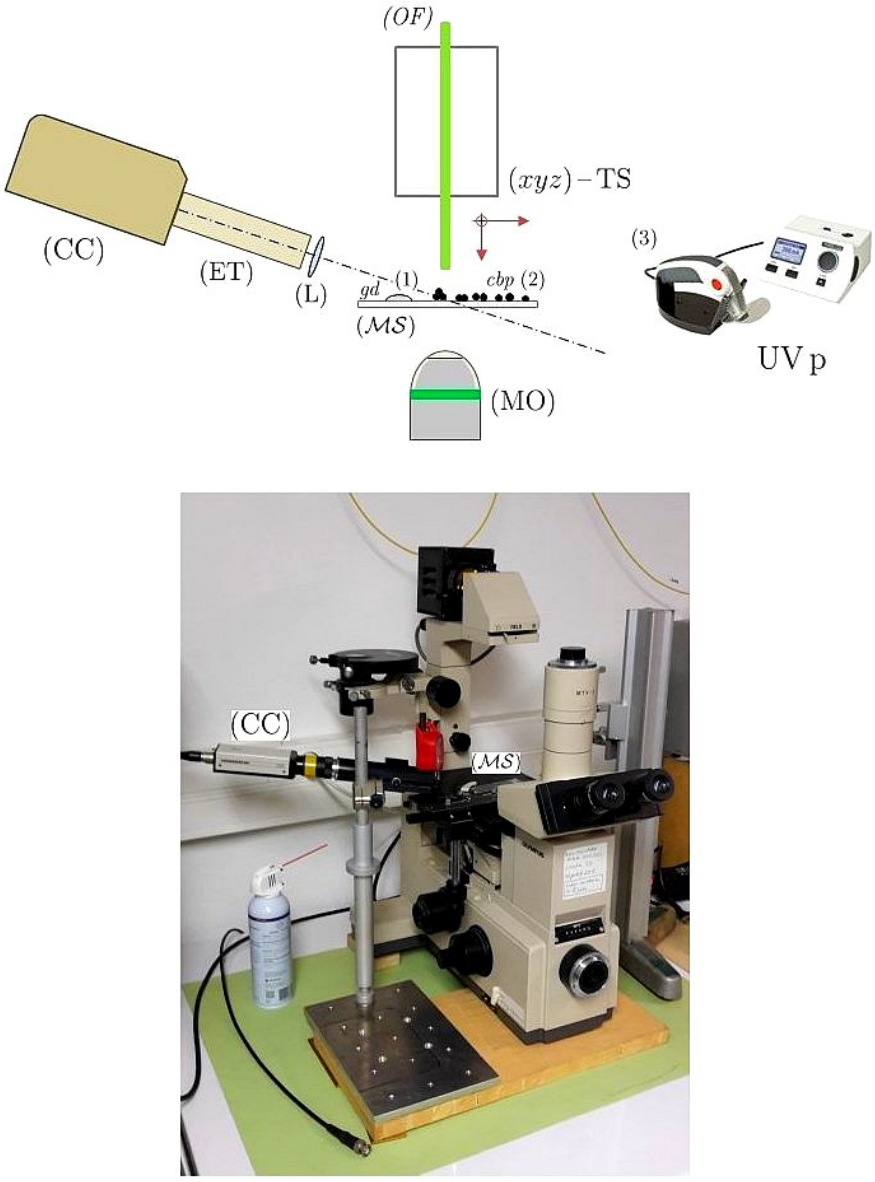

Figure H.1: The bead collage setup. (*Top figure*) Schematic of the device (not to scale). ($\mathcal{MS}$) microscope slide; *(OF)* optic fibre; $(xyz)-$TS, xyz translation stage; (MO) microscope objective; $\{(\mathrm{CC})+(\mathrm{ET})+(\mathrm{L})\}$, control camera + extension tube + lens. Step (1): soak the tip of the optic fibre in the glue droplet *gd*. Step (2): find an isolated sphere in the carbon bead powder *cbp* and stick it onto the fibre. Pay attention to the bead alignment with the fibre axis. Step (3): cure the adhesive with the 'UV pistol' (*image taken from Thorlabs official website).* (*Bottom figure*) Photograph of the setup under actual operating conditions. Same abbreviations.

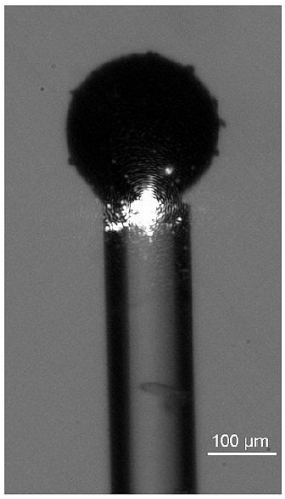

Figure H.2: A carbon microbead stuck onto the end of an optic fibre. The patch of light is probably stray light diffused through the adhesive. *Image from A. Mombereau's internship report.*

Appendix I

Three simplifying assumptions

In this appendix we discuss the validity of three assumptions made to simplify our study : (1) the interface is flat, (2) thermogravity is negligible and (3) evaporation is negligible.

I.1 The flat interface hypothesis

Assuming a flat interface can be justified thanks to an estimation of the capillary number Ca which quantifies the effect of viscous drag forces relative to surface tension forces acting on a fluid interface. This number is defined as the dimensionless ratio

$$\mathrm{Ca} \doteq \frac{\eta U}{\gamma}\,, \tag{I.1}$$

with η the dynamic viscosity of water, γ its surface tension and U the flow velocity scale. At room temperature $\mathrm{T}_{room} \approx 20°\mathrm{C}$ and under atmospheric pressure $\mathrm{P}_{atm} \approx 1\mathrm{bar}$, the dynamic viscosity of pure water is $\eta \sim 10^{-3}\,\mathrm{Pa.s}$. Its surface tension is $\gamma \approx 72.8\,\mathrm{mN.\,m^{-1}}$. As for the typical flow velocity, our experiments provide $U \sim 100\,\mu\mathrm{m/s}$. The capillary number involved in the present study is therefore in the order of $\mathrm{Ca} \sim 10^{-6} \ll 1$, meaning that the flow is largely dominated by capillary forces that tend to minimise the interfacial area keeping it as plane as possible (contrary to viscous forces that would deform the interface). The simplifying assumption of a flat interface is thus a good approximation.

I.2 Neglecting thermogravity

The reason why thermogravity (buoyancy force $\rho\mathbf{g}$) is neglected here becomes clear while comparing the orders of magnitude of two dimensionless parameters, the Rayleigh Ra and the Marangoni Ma numbers. The Rayleigh number Ra, comparing the 'intensity' of

thermogravity to dissipation (thermal diffusion + viscosity), is given by

$$\mathrm{Ra} \doteq \frac{\rho g \alpha \Delta T h^3}{\eta D} \ , \qquad \alpha \doteq -\frac{1}{\rho_0} \left.\frac{\partial \rho}{\partial \Theta}\right|_{\Theta = \Theta_0} . \tag{I.2}$$

The buoyancy force stems from the fluid mass density dependence on the temperature. A linear relation is assumed : $\rho(\Theta) = \rho_0 \left[1 - \alpha \left(\Theta - \Theta_0\right)\right]$, where α is the coefficient of thermal expansion (thermodynamic stability imposes in general a positive constant α for pure liquids). Such a simple law only holds for slight deviations from the equilibrium mass density $\rho_0 = \rho(\Theta_0)$. Under STP conditions, $\alpha \approx 1.5 \times 10^{-4}\,\mathrm{K}^{-1}$ for pure water. Taking a temperature gap $\Delta T \sim 10\,\mathrm{K}$ between the hot bead and the quiescent flow at infinity, a thermal diffusivity $D \sim 10^{-7}\,\mathrm{m}^2.\,\mathrm{s}^{-1}$ and a cuvette height $h = 3\,\mathrm{mm}$, one finds $\mathrm{Ra} \sim 10^3$.

The Marangoni number Ma comparing thermocapillarity to dissipation is defined as

$$\mathrm{Ma} \doteq \frac{\gamma_\mathrm{T} \Delta T R}{\eta D} \ , \quad \gamma_\mathrm{T} \doteq \left|\frac{\mathrm{d}\gamma}{\mathrm{d}\Theta}\right| . \tag{I.3}$$

With $\gamma_\mathrm{T} \sim 10^{-4}\,\mathrm{N.\,m^{-1}.\,K^{-1}}$ and a cuvette radius $R \sim 1\,\mathrm{cm}$ one gets $\mathrm{Ma} \sim 10^5$, two orders of magnitude greater than Ra, which justifies ruling out thermogravitary effects.

I.3 Neglecting evaporation

In our experiments with a hot bead of radius $a \sim 100\,\mu\mathrm{m}$, there appears no clear sign of evaporation effects able to influence the flow structure. Our hot particle is actually too big for evaporation to have a substantial impact on the thermocapillary flow. Indeed, as discussed by A. Girot in his master's thesis [62], the evaporation speed scales as $1/a$ and is therefore expected to outweigh any other physical mechanism at very small scales.

In this regard, optical trapping experiments of tiny particles ($a \approx 5\,\mu\mathrm{m}$) carried out by A. Girot during his internship revealed a stunning effect : tracer particles located close enough to the trapped sphere would be like attracted by it and get stuck to its surface at the precise moment the laser is switched on. This phenomenon is presumably attributable to evaporation which is especially intense in the vicinity of the heat source : as long as the air above the surface is not saturated with water vapour, local mass losses due to evaporation shall be continuously balanced by an influx of water, which explains the centripetal motion of tracer particles observed as the laser is switched on, *i.e.* when evaporation is active (and, conversely, why particles are 'repelled' by the hot sphere when the laser is switched off). A more detailed discussion of this phenomenon can be found in [2]. Useful approaches to theoretical models of evaporation are reviewed in [63].

Appendix J

Consistency with Bratukhin's solution

In this appendix, we check that the nonlinear temperature field (4.45) we obtained in the far–field axisymmetric regime $(lm) = (10)$ is consistent, in the low Reynolds limit $\mathrm{Re} \ll 1$, with the solution derived by Bratukhin and Maurin [60].

Let us start with Shtern's writing [59] of Bratukhin's analytical solution to the steady–state 'Navier–Stokes–Fourier' problem (the general framework wherein inertia is also considered in addition to thermal advection)

$$\vartheta = \vartheta_0 \left[\frac{\lambda}{\gamma} (1+c)^{\mu} - \frac{\mu}{\gamma} (1+c)^{\lambda} \right]^{-2\mathrm{Pr}} , \tag{J.1}$$

with Pr the Prandtl number defined as $\mathrm{Pr} \doteq \nu/D = \mathrm{Pe}/\mathrm{Re}$ and

$$\gamma \doteq (1+2\mathrm{Re})^{1/2} , \tag{J.2a}$$
$$\lambda = (1+\gamma)/2 , \tag{J.2b}$$
$$\mu = (1-\gamma)/2 . \tag{J.2c}$$

Note that we use $c \doteq \cos\theta$ instead of Shtern's notation x. In the low Reynolds limit $\mathrm{Re} \ll 1$ we have the first–order approximations

$$\gamma \underset{\mathrm{Re}\ll 1}{\sim} 1 + \mathrm{Re} , \tag{J.3a}$$
$$\lambda \sim 1 + \frac{\mathrm{Re}}{2} , \tag{J.3b}$$
$$\mu \sim -\frac{\mathrm{Re}}{2} , \tag{J.3c}$$

approximations which, once introduced in (J.1), yield

$$\frac{1}{\gamma}\left[\lambda\,(1+c)^{\mu}-\mu\,(1+c)^{\lambda}\right] \underset{\mathrm{Re}\ll 1}{\sim} (1-\mathrm{Re})\left\{\left(1+\tfrac{\mathrm{Re}}{2}\right)\left[1-\tfrac{\mathrm{Re}}{2}\ln(1+c)\right]+\tfrac{\mathrm{Re}}{2}\,(1+c)\left[1+\tfrac{\mathrm{Re}}{2}\ln(1+c)\right]\right\} = 1+\tfrac{\mathrm{Re}}{2}\left[c-\ln(1+c)\right]+\mathcal{O}(\mathrm{Re}^2)\,. \quad \text{(J.4)}$$

Finally, noting that at finite Péclet number Pe working in the viscous regime $\mathrm{Re}\ll 1$ amounts to taking the asymptotic limit $\mathrm{Pr}\to+\infty$, we write

$$\frac{\vartheta}{\vartheta_0} \underset{\mathrm{Re}\ll 1}{\longrightarrow} \left\{1+\tfrac{\mathrm{Re}}{2}\left[c-\ln(1+c)\right]\right\}^{-2\,(\mathrm{Pe}/\mathrm{Re})} = \mathrm{e}^{-2\,\frac{\mathrm{Pe}}{\mathrm{Re}}\ln\left\{1+\frac{\mathrm{Re}}{2}[c-\ln(1+c)]\right\}} \underset{\mathrm{Re}\ll 1}{\sim} \mathrm{e}^{-\mathrm{Pe}\,[c-\ln(1+c)]} = (1+c)^{\mathrm{Pe}}\,\mathrm{e}^{-\mathrm{Pe}\,c}\,, \quad \text{(J.5)}$$

which is exactly the same polar dependence as that of expression (4.45).

Appendix K

Derivation of the radial and the angular Stokes equations

This appendix provides a detailed derivation of the Stokes equations (4.57a) – (4.57c). What we do basically is elucidating the projections of the vector Stokes equation (4.15a) onto the directions of the spherical basis vectors $(\mathbf{e}_r, \mathbf{e}_\theta, \mathbf{e}_\varphi)$.

Let us first recall the expression of the nabla operator in spherical coordinates

$$\boldsymbol{\nabla}\bullet = \begin{pmatrix} \partial_r \bullet \\ -\dfrac{s}{r}\,\partial_c \bullet \\ \dfrac{1}{rs}\,\partial_\varphi \bullet \end{pmatrix}_{(\mathbf{e}_r, \mathbf{e}_\theta, \mathbf{e}_\varphi)} , \tag{K.1}$$

With a pressure field $\mathrm{p}_{(lm)}(r, c, \varphi)$ in the form of (4.54a) one finds

$$\boldsymbol{\nabla}\mathrm{p}_{(lm)} = -\frac{\mathrm{e}^{im\varphi}}{r^{l+2}} \begin{pmatrix} (l+1)\,p \\ sp' \\ -\dfrac{im}{s}\,p \end{pmatrix}_{(\mathbf{e}_r, \mathbf{e}_\theta, \mathbf{e}_\varphi)} , \tag{K.2}$$

where the prime $'$ denotes differentiation with respect to c.

We further need the vector laplacian of the velocity field whose components write in spherical coordinates

$$\boldsymbol{\nabla^2 v}\,\big|_r \doteq \boldsymbol{\nabla^2 v}\,.\,\mathbf{e}_r = \Delta \mathrm{v}_r - \frac{2}{r^2}\,\mathrm{v}_r + \frac{2}{r^2}\,\partial_c(s\mathrm{v}_\theta) - \frac{2}{r^2 s}\,\partial_\varphi \mathrm{v}_\varphi\ , \tag{K.3a}$$

$$\boldsymbol{\nabla^2 v}\,\big|_\theta \doteq \boldsymbol{\nabla^2 v}\,.\,\mathbf{e}_\theta = \Delta \mathrm{v}_\theta - \frac{1}{r^2 s^2}\,\mathrm{v}_\theta - \frac{2s}{r^2}\,\partial_c \mathrm{v}_r - \frac{2c}{r^2 s^2}\,\partial_\varphi \mathrm{v}_\varphi\ , \tag{K.3b}$$

$$\boldsymbol{\nabla^2 v}\,\big|_\varphi \doteq \boldsymbol{\nabla^2 v}\,.\,\mathbf{e}_\varphi = \Delta \mathrm{v}_\varphi - \frac{1}{r^2 s^2}\,\mathrm{v}_\varphi + \frac{2}{r^2 s}\,\partial_\varphi \mathrm{v}_r + \frac{2c}{r^2 s^2}\,\partial_\varphi \mathrm{v}_\theta\ , \tag{K.3c}$$

with $\Delta \mathrm{v}_j$ the $j-$component ($j \in \{r, \theta, \varphi\}$) of the scalar laplacian given by

$$\Delta \mathrm{v}_j = \frac{1}{r}\,\partial_r^2\,(r\mathrm{v}_j) + \frac{1}{r^2}\,\partial_c\left[s^2 \partial_c \mathrm{v}_j\right] + \frac{1}{r^2 s^2}\,\partial_\varphi^2 \mathrm{v}_j\ . \tag{K.4}$$

Inserting in (K.3a)$-$(K.3c) velocity components in the form of (4.54b), one is left with

$$\boldsymbol{\nabla^2 v}_{(lm)}\,\big|_r = \frac{\mathrm{e}^{im\varphi}}{r^{l+2}}\left\{\left[s^2 v_r'\right]' + \left((l-1)(l-2) - \frac{m^2}{s^2}\right) v_r\right\}, \tag{K.5a}$$

$$\boldsymbol{\nabla^2 v}_{(lm)}\,\big|_\theta = \frac{\mathrm{e}^{im\varphi}}{r^{l+2}}\left\{\left[s^2 v_\theta'\right]' + \left(l\,(l-1) - \frac{1+m^2}{s^2}\right) v_\theta - 2s v_r' - 2im\,\frac{c}{s^2}\,v_\varphi\right\}, \tag{K.5b}$$

$$\boldsymbol{\nabla^2 v}_{(lm)}\,\big|_\varphi = \frac{\mathrm{e}^{im\varphi}}{r^{l+2}}\left\{\left[s^2 v_\varphi'\right]' + \left(l\,(l-1) - \frac{1+m^2}{s^2}\right) v_\varphi + 2\,\frac{im}{s}\,v_r + 2im\,\frac{c}{s^2}\,v_\theta\right\}. \tag{K.5c}$$

Note that the incompressibility condition (4.56) is used to get the above form (K.5a).

Finally, projecting the Stokes equation onto the axes $\boldsymbol{\nabla^2 v}\,\big|_j - \boldsymbol{\nabla}\mathrm{p}\,\big|_j = 0$ yields

$$\left[s^2 v_r'\right]' + \left\{(l-1)(l-2) - \frac{m^2}{s^2}\right\} v_r = -\,(l+1)\,p\ , \tag{K.6a}$$

$$\left[s^2 v_\theta'\right]' + \left\{l\,(l-1) - \frac{1+m^2}{s^2}\right\} v_\theta = 2s v_r' + 2im\,\frac{c}{s^2}\,v_\varphi - s p'\ , \tag{K.6b}$$

$$\left[s^2 v_\varphi'\right]' + \left\{l\,(l-1) - \frac{1+m^2}{s^2}\right\} v_\varphi = -2\,\frac{im}{s}\,v_r - 2im\,\frac{c}{s^2}\,v_\theta + \frac{im}{s}\,p\ . \tag{K.6c}$$

Appendix L

Strategy for solving the Stokes problem

The aim of this appendix is to prepare the ground for analytical calculations by providing 'solving recipes' of the Stokes problem (4.59a) – (4.59e). As will become clear, solving this differential system is easier in axisymmetric ($m = 0$) than in non – axisymmetric ($m \neq 0$) cases, resulting in slightly different solving strategies.

L.1 Solving strategy for axisymmetric states $(lm) = (l0)$

In the case of axisymmetric states $(lm) = (l0)$, the system (4.59a) – (4.59e) simplifies to

$$\left[s^2 p_0'\right]' + l\,(l+1)\,p_0 = 0\,, \tag{L.1a}$$

$$s^2 v_{\theta,0}' - c\,v_{\theta,0} = -(l-2)\,s v_{r,0}\,, \tag{L.1b}$$

$$\left[s^2 v_{r,0}'\right]' + (l-1)(l-2)\,v_{r,0} = -\,(l+1)\,p_0\,, \tag{L.1c}$$

$$\left[s^2 v_{\theta,0}'\right]' + \left\{l\,(l-1) - \frac{1}{s^2}\right\} v_{\theta,0} = 2 s v_{r,0}' - s p_0'\,, \tag{L.1d}$$

$$\left[s^2 v_{\varphi,0}'\right]' + \left\{l\,(l-1) - \frac{1}{s^2}\right\} v_{\varphi,0} = 0\,. \tag{L.1e}$$

Two differential equations are here uncoupled from the others, those for the functions $\{p_{(l0)}(c)\}$ and $\{v_{\varphi,(l0)}(c)\}$, so that the latter can be derived in a fully independent way. On top of that, the right – hand side of both the incompressibility (L.1b) and the polar Stokes equation (L.1d) no longer depend on v_φ as a direct consequence of axisymmetry. The 'solving recipe' of this system is hence quite straightforward: for a given value of l,

1. First, solve the differential equation (L.1a) to work out $p_{(l0)}(c)$.

2. Insert the obtained expression of $p_{(l0)}(c)$ in the right – hand side of the radial Stokes equation (L.1c) and solve it to get $v_{r,(l0)}(c)$.

3. Compute $p'_{(l0)}(c)$ and $v'_{r,\,(l0)}(c)$. Next, substitute their expressions into the right–hand side of the polar Stokes equation (L.1d) and solve it to derive $v_{\theta,\,(l0)}(c)$ (you can equally solve the incompressibility equation (L.1b)).

4. To finish, solve separately the azimuthal Stokes equation (L.1e) to determine $v_{\varphi,\,(l0)}(c)$.

L.2 Solving strategy for non–axisymmetric states $(lm)_{m\neq 0}$

Solving the Stokes problem (4.59a)–(4.59e) in non–axisymmetric cases $(lm)_{m\neq 0}$ is a bit more tricky. The difficulty essentially lies in the fact that we are compelled to derive an auxiliary equation for the $\{v_{\theta,\,(lm)}(c)\}_{m\neq 0}$ family of functions.

Eq. (4.59a), which is now the only one to be completely uncoupled, plays the role of a 'starter' and should thus be solved in the first place. We then repeat the above solving process up to the moment we need to derive a new differential equation satisfied by $v_{\theta,\,(lm)}(c)$. Indeed, the polar Stokes equation (4.59d) cannot be solved as long as the still unknown functions $\{v_{\varphi,\,(lm)}(c)\}_{m\neq 0}$ are not eliminated from its right–hand side. This is readily achieved multiplying the incompressibility condition (4.59b) by $2c/s^2$ prior to substituting the corresponding expression of the quantity $2im\,(c/s^2)\,v_\varphi$ in (4.59d). Finally, we end up with

$$s^2 v''_\theta - 4c\,v'_\theta + \left(l\,(l-1) - \frac{1+m^2-2c^2}{s^2}\right) v_\theta = 2s v'_r + 2\,(l-2)\,\frac{c}{s}\,v_r - s p'\,. \qquad \text{(L.2)}$$

The rest of the solving is completed in the same spirit as previously. In sum, the solving process presented here enables one to derive the functions $\{p_{\,(lm)}(c)\}_{m\neq 0}$, followed by the velocity components $\{v_{r,\,(lm)}(c)\}_{m\neq 0}$, $\{v_{\theta,\,(lm)}(c)\}_{m\neq 0}$ and $\{v_{\varphi,\,(lm)}(c)\}_{m\neq 0}$ in that order.

Appendix **M**

From the Gauss hypergeometric function to associated Legendre functions

This appendix inspired by chapter 15 of ref. [66] is devoted to a brief presentation of the Gauss hypergeometric function that stresses out its relation to the associated Legendre functions (4.61). The presentation ends with some useful properties.

M.1 The Gauss hypergeometric function as a series

The Gauss hypergeometric function ${}_2F_1(\alpha,\,\beta,\,\gamma\,;z)$ is a special function defined by the hypergeometric series

$$ {}_2F_1(\alpha,\,\beta,\,\gamma\,;z) \doteq \sum_{k=0}^{+\infty} \frac{(\alpha)_k\,(\beta)_k}{(\gamma)_k}\,\frac{z^k}{k!}\,, \quad |z|<1\,, \tag{M.1} $$

with $(.)_k$ the Pochhammer symbol defined by

$$ (q)_k \doteq \begin{cases} 1 & \text{for } k=0\,, \\ q\,(q+1)\,...\,(q+k-1) & \text{for } k>0\,, \end{cases} \tag{M.2} $$

so that ${}_2F_1(\alpha,\,\beta,\,\gamma\,;z)$ writes explicitly

$$ {}_2F_1(\alpha,\,\beta,\,\gamma\,;z) = 1+\frac{\alpha\beta}{\gamma}\frac{z}{1!}+\frac{\alpha\,(\alpha+1)\,\beta\,(\beta+1)}{\gamma\,(\gamma+1)}\frac{z^2}{2!}+\ldots \tag{M.3} $$

Remarkably, the Gauss hypergeometric function can also be expressed in terms of the Euler's Gamma function as follows

$$ {}_2F_1(\alpha,\,\beta,\,\gamma\,;z) = \frac{\Gamma(\gamma)}{\Gamma(\alpha)\Gamma(\beta)}\sum_{k=0}^{+\infty}\frac{\Gamma(\alpha+k)\Gamma(\beta+k)}{\Gamma(\gamma+k)}\,\frac{z^k}{k!}\,. \tag{M.4} $$

Below are provided a few important properties satisfied by ${}_2F_1\,(\alpha,\,\beta,\,\gamma\,;z)$:

- One key trait of ${}_2F_1\,(\alpha,\,\beta,\,\gamma\,;z)$ is that the above series (M.1) stops if either α or β is a negative integer, in which case it simply reduces to a $z-$dependent polynomial of degree l. This is actually our case since $\alpha = -l$ ($\beta = l+1$) and the associated Legendre functions (4.61) then explicitly write for $m \geqslant 0$ and $c \in [0,1]$

$$\mathcal{P}_l^m(c) = \left(\frac{1-c}{1+c}\right)^{m/2} \sum_{k=0}^{l} (-1)^k \binom{l}{k} \frac{(l+1)_k}{(1+m)_k} \left(\frac{1-c}{2}\right)^k . \tag{M.5}$$

- For $\gamma = 1+m$ ($m \in \mathbb{N}$), the second fundamental solution of Eq. (4.58), namely the associated Legendre functions of the second kind $\{Q_l^m(c)\}$, exhibit logarithmic singularities of the form $\ln\left[(1-c)\,/\,(1+c)\right]$ and are thus discarded in our study.

- Bailey's theorem offers a simple way of calculating Gauss hypergeometric functions of the form ${}_2F_1(\alpha,\,1-\alpha\,,\gamma\,;1/2)$ using the relation

$${}_2F_1\left(\alpha,\,1-\alpha\,,\gamma\,;\frac{1}{2}\right) = \frac{\Gamma\left(\dfrac{\gamma}{2}\right)\Gamma\left(\dfrac{\gamma+1}{2}\right)}{\Gamma\left(\dfrac{\gamma+\alpha}{2}\right)\Gamma\left(\dfrac{\gamma-\alpha+1}{2}\right)} \quad . \tag{M.6}$$

  Here $\{\alpha,\gamma\} = \{-l,\,1+m\}$ and $z = 1/2$ corresponds to the interface position $c_I = 0$.

M.2 Euler's hypergeometric differential equation

It is also possible to define the Gauss hypergeometric function ${}_2F_1\,(\alpha,\,\beta,\,\gamma\,;z)$ on the basis of the equation it obeys, known as Euler's hypergeometric differential equation

$$z\,(1-z)\,\frac{\mathrm{d}^2F}{\mathrm{d}z^2} + \Big[\gamma - (\alpha+\beta+1)\,z\,\Big]\frac{\mathrm{d}F}{\mathrm{d}z} - \alpha\beta F = 0\ . \tag{M.7}$$

Let us demonstrate that the Gauss hypergeometric function we have to consider, in the upper half−space $c \in [0,1]$ and for $m \geqslant 0$, is indeed the one for which $\alpha = -l$, $\beta = l+1$, $\gamma = 1+m$ and $z_+ = (1-c)/2$. Our starting point is the associated Legendre differential equation (4.58) satisfied by the $\{\mathcal{P}_l^m(c)\}$. Since we require the $\{\mathcal{P}_l^m(c)\}$ to be regular in the upper half−space $c \in [0,1]$, we naturally look for them in the form ($m \geqslant 0$)

$$\mathcal{P}_+(c) = \left(\frac{1-c}{1+c}\right)^{m/2} \Phi_+(c)\,, \tag{M.8}$$

where $\Phi_+(c)$ is an unknown function to be identified.

One differentiates (M.8) twice and substitutes the expressions of $\mathcal{P}'_+(c)$ and $\mathcal{P}''_+(c)$ into the Legendre equation (4.58). Ultimately, one is left with[1]

$$\left(1-c^2\right)\Phi''_+(c) - 2\,(c+m)\,\Phi'_+(c) + l\,(l+1)\,\Phi_+(c) = 0\,. \tag{M.10}$$

The last stage consists in changing the variable from c to z_+ defined as $z_+ \doteq (1-c)\,/\,2$. Rewriting Eq. (M.10) with respect to z_+ yields nothing but Eq. (M.7) with $\alpha = -l$, $\beta = l+1$, $\gamma = 1+m$ so that $\Phi_+(c) \equiv F\,(-l,\,l+1,\,1+m\,;(1-c)\,/\,2)$ and finally

$$\mathcal{P}_+(c) = \left(\frac{1-c}{1+c}\right)^{m/2} {}_2F_1\left(-l,\,l+1,\,1+m\,;\frac{1-c}{2}\right)\,. \tag{M.11}$$

M.3 Properties of the associated Legendre functions

Here are reported some properties of the associated Legendre functions $\{\mathcal{P}_l^m(c)\}$:

- The $\{\mathcal{P}_l^m(c)\}$ are the eigenfunctions of the Legendre differential operator $\hat{\mathcal{L}}$ with eigenvalues equal to $\epsilon_l = -l\,(l+1)$, *i.e.*

$$\hat{\mathcal{L}}\mathcal{P}_l^m \doteq \left\{\left(1-c^2\right)\frac{\mathrm{d}^2}{\mathrm{d}c^2} - 2c\,\frac{\mathrm{d}}{\mathrm{d}c} - \frac{m^2}{1-c^2}\right\}\mathcal{P}_l^m(c) = -l\,(l+1)\,\mathcal{P}_l^m\,. \tag{M.12}$$

  Note also that

$$\hat{\mathcal{L}}\left[c\mathcal{P}_l^m\right] = 2\left(1-c^2\right)\frac{\mathrm{d}\mathcal{P}_l^m}{\mathrm{d}c} - \left(l^2+l+2\right)c\,\mathcal{P}_l^m\,. \tag{M.13}$$

- As readily checked on the eigenvalue equation (M.12), $\mathcal{P}^m_{-(l+1)}(c) = \mathcal{P}_l^m(c)$.

- Recurrence relations ($c \geqslant 0$ and $m \geqslant 0$):

$$\left(1-c^2\right)\frac{\mathrm{d}\mathcal{P}_l^m}{\mathrm{d}c} = (l-m)\,\mathcal{P}^m_{l-1} - lc\,\mathcal{P}_l^m\,, \tag{M.14a}$$

$$\left(1-c^2\right)\frac{\mathrm{d}\mathcal{P}_l^m}{\mathrm{d}c} = (l+1)\,c\,\mathcal{P}_l^m - (l+m+1)\,\mathcal{P}^m_{l+1}\,, \tag{M.14b}$$

$$(l+m)\,\mathcal{P}_l^m = (2l-1)\,c\,\mathcal{P}^m_{l-1} - (l-m-1)\,\mathcal{P}^m_{l-2}\,. \tag{M.14c}$$

[1] The very same rationale is easily adaptable to the lower half−space $c \in [-1,0]$ and $m \geqslant 0$ setting this time the regular form $\mathcal{P}_-(c) = [\,(1+c)\,/\,(1-c)\,]^{m/2}\,\Phi_-(c)$, where '$c$' is replaced by '$-c$' according to the up−down symmetry of the system. Next introducing the change of variable $z_- \doteq (1+c)\,/\,2$ leads again to equation (M.7) with exactly the same values of the parameters. Finally, as Eq. (4.58) is invariant when 'm' is transformed into '$-m$', the solution for negative values of m is simply $\mathcal{P}_l^{-m}(c) = \mathcal{P}_l^m(c)$, so that bringing everything together yields in the end

$$\mathcal{P}_l^m(c) = \left(\frac{1-|c|}{1+|c|}\right)^{|m|/2} {}_2F_1\left(-l,\,l+1,\,1+|m|\,;\frac{1-|c|}{2}\right)\,, \tag{M.9}$$

as the general solution of the Legendre equation (4.58), $\forall m \in \mathbb{Z}$ and c either in $[0,1]$ or $[-1,0]$.

Appendix N

Associated Legendre functions of interest

Here are tabulated the explicit forms of the $\{\mathcal{P}_l^m(c)\}$ appearing in the derivation of the generalised Lamb's solution, as well as their first derivatives $\{\mathcal{P}'_l{}^m(c)\}$.

	$\mathcal{P}_l^m(c)$	$\mathcal{P}'_l{}^m(c)$
$l=0$	$\left(\frac{1-c}{1+c}\right)^{\frac{m}{2}}$	$-m\,\frac{(1-c)^{\frac{m}{2}-1}}{(1+c)^{\frac{m}{2}+1}}$
$l=1$	$\frac{c+m}{1+m}\left(\frac{1-c}{1+c}\right)^{\frac{m}{2}}$	$-\frac{(c^2+mc+m^2-1)}{1+m}\,\frac{(1-c)^{\frac{m}{2}-1}}{(1+c)^{\frac{m}{2}+1}}$
$l=2$	$\frac{3c^2+3mc+m^2-1}{(1+m)(2+m)}\left(\frac{1-c}{1+c}\right)^{\frac{m}{2}}$	$-\frac{\left[6c^3+6mc^2+3(m^2-2)c+m(m^2-4)\right]}{(1+m)(2+m)}\,\frac{(1-c)^{\frac{m}{2}-1}}{(1+c)^{\frac{m}{2}+1}}$

Figure N.1: Associated Legendre functions $\{\mathcal{P}_l^m(c)\}_{l\in\{0,1,2\}}$ and their first derivatives.

Appendix O

Derivation of the velocity components

In this appendix we present in great detail the derivation of the velocity components $\{v_{j,(lm)}(c)\}_{j\in\{r,\theta,\varphi\}}$. By virtue of the linearity of the Stokes problem, the latter are of the form $v = v^{\mathcal{H}} + v^{P}$, *i.e.* the superposition of the homogeneous solution $v^{\mathcal{H}}$ and of a particular solution v^{P} of the complete equation to be solved.

Radial velocity

As a first step, we prepare the ground for the application of the operatorial formalism rewriting the radial Stokes equation (4.59c) in the following way

$$\hat{\mathcal{L}} v_r + (l-1)(l-2)\, v_r = -(l+1)\, p \ . \tag{O.1}$$

One recognises on the left–hand side the Legendre differential equation of degree $l-2$, which means that the homogeneous solution is $v_r^{\mathcal{H}}(c) \propto \mathcal{P}_{l-2}^{m}(c)$. Besides, as in the right–hand side of (O.1) only appears $p_{(lm)}(c) \propto \mathcal{P}_l^m(c)$, a particular solution v_r^P is searched under the form $v_r^P(c) = K_r\, \mathcal{P}_l^m(c)$, with K_r a constant to work out. Making use of the eigenvalue equation (4.64), one finally comes to the result

$$v_{r,(lm)}(c) = \pi_{(lm)}\, \mathcal{P}_l^m(c) + \rho_{(l-2,m)}\, \mathcal{P}_{l-2}^m(c) \ , \tag{O.2}$$

with $\rho_{(l-2,m)}$ another integration constant to be determined.

Polar velocity

To render calculations easier, it is convenient to define the auxiliary velocity field $\widetilde{v}_\theta \doteq s v_\theta$. Inserting $\widetilde{v}_\theta$ in the polar equation (L.2) yields the differential equation

$$\hat{\mathcal{L}}\, \widetilde{v}_\theta + l\,(l-1)\, \widetilde{v}_\theta = 2s^2 v_r' + 2\,(l-2)\, c\, v_r - s^2 p' \, . \tag{O.3}$$

For the very same reason as before, the homogeneous solution is $v_\theta^{\mathcal{H}}(c) \propto \mathcal{P}_{l-1}^m(c)/s$ which diverges on the $z-$axis ($c_s = 1$) for axisymmetric states ($m = 0$). The latter are thus to be handled separately in the upcoming analysis.

We now turn to the inhomogeneous equation. By virtue of the linearity of Eq. (O.3), the particular solution $\widetilde{v}_\theta^P$ can be written as the sum of two terms $\widetilde{v}_\theta^{P1}$ and $\widetilde{v}_\theta^{P2}$ with

$$\widetilde{v}_\theta^{P1} = K_1\, s^2 \frac{\mathrm{d}\mathcal{P}_l^m}{\mathrm{d}c}\ , \tag{O.4a}$$

$$\widetilde{v}_\theta^{P2} = K_2\, s^2 \frac{\mathrm{d}\mathcal{P}_{l-2}^m}{\mathrm{d}c}\ , \tag{O.4b}$$

the constants $K_1 \propto \pi_{(lm)}$ and $K_2 \propto \rho_{(l-2,\,m)}$ having yet to be determined.

The guiding idea is to transform all derivatives into linear combinations of associated Legendre functions, in order to apply Eq. (4.64) repeatedly. This can be achieved using the recurrence relation (M.14a) or (M.14b). This way, derivatives are eliminated and we ultimately get rid of the terms $\propto c$ using the formula (M.14c).

Inserting successively the above forms (O.4a) – (O.4b) in the left – hand side (LHS) of Eq. (O.3), one finds $\mathrm{LHS} = \mathrm{LHS}_1 + \mathrm{LHS}_2$ where

$$\mathrm{LHS}_1 = 2\,l\,(l+m+1)\,K_1\,\mathcal{P}_{l+1}^m\ , \tag{O.5a}$$

$$\mathrm{LHS}_2 = 2\,(l-1)\,(l-m-2)\,K_2\,\mathcal{P}_{l-3}^m\ . \tag{O.5b}$$

Using then the solutions (4.62) for the pressure field and (O.2) for the radial velocity, one rewrites the right – hand side (RHS) of Eq. (O.3) as $\mathrm{RHS} = \mathrm{RHS}_1 + \mathrm{RHS}_2$ with

$$\mathrm{RHS}_1 = 2\,\frac{l-2}{l+1}\,(l+m+1)\,\pi_{(lm)}\,\mathcal{P}_{l+1}^m\ , \tag{O.6a}$$

$$\mathrm{RHS}_2 = 2\,(l-m-2)\,\rho_{(l-2,\,m)}\,\mathcal{P}_{l-3}^m\ . \tag{O.6b}$$

Comparing (O.5a) and (O.6a) on the one hand, (O.5b) and (O.6b) on the other hand, finally yields the constants

$$K_1 = \frac{l-2}{l\,(l+1)}\,\pi_{(lm)}\,, \tag{O.7a}$$

$$K_2 = \frac{1}{l-1}\,\rho_{(l-2,\,m)}\,, \tag{O.7b}$$

the expression of K_2 being obviously valid only if $l \neq 1$.

Coming back to the original field $v_\theta = \widetilde{v}_\theta / s$, we draw the partial conclusion that

$$v_{\theta,\,(lm)}(c) = s \left[\frac{l-2}{l\,(l+1)}\,\pi_{(lm)}\,\frac{\mathrm{d}\mathcal{P}_l^m}{\mathrm{d}c} + \frac{\rho_{(l-2,\,m)}}{l-1}\,\frac{\mathrm{d}\mathcal{P}_{l-2}^m}{\mathrm{d}c} \right] + \frac{1}{s}\,\sigma_{(l-1,\,m)}\,\mathcal{P}_{l-1}^m(c)\,, \quad \forall l \geqslant 2\,. \tag{O.8}$$

In fact, another form of solution (O.8) valid including for $l = 1$ can be derived in a fairly simple way starting from expressions (O.6a)–(O.6b). The latter suggest seeking a particular solution of the form $\widetilde{v}_\theta^P = \widetilde{v}_\theta^{P1} + \widetilde{v}_\theta^{P2} = \overline{K_1}\,\mathcal{P}_{l+1}^m + \overline{K_2}\,\mathcal{P}_{l-3}^m$. As previously, this decomposition is inserted in the left–hand side of Eq. (O.3) and, after some algebra, one gets from the identification $\mathrm{LHS}_{1,\,2} \equiv \mathrm{RHS}_{1,\,2}$

$$\overline{K_1} = -\frac{(l-2)\,(l+m+1)}{(l+1)\,(2l+1)}\,\pi_{(lm)}\,, \tag{O.9a}$$

$$\overline{K_2} = \frac{l-m-2}{2l-3}\,\rho_{(l-2,\,m)}\,. \tag{O.9b}$$

And so we are this time left with the following alternative representation of the solution to Eq. (O.3), valid even for $l = 1$,

$$v_{\theta,\,(lm)}(c) = \frac{1}{s}\left[-\frac{(l-2)\,(l+m+1)}{(l+1)\,(2l+1)}\,\pi_{(lm)}\,\mathcal{P}_{l+1}^m(c) + \frac{l-m-2}{2l-3}\,\rho_{(l-2,\,m)}\,\mathcal{P}_{l-3}^m(c) + \sigma_{(l-1,\,m)}\,\mathcal{P}_{l-1}^m(c) \right], \quad \forall l \geqslant 1\,. \tag{O.10}$$

For later purposes, let us examine in greater detail the particular case $l = 1$. From expression (O.10), one readily obtains

$$v_{\theta,\,(1m)}(c) = \frac{1}{s}\left[\frac{1}{6}\,(m+2)\,\pi_{(1m)}\,\mathcal{P}_2^m(c) + (1+m)\,\rho_{(-1m)}\,\mathcal{P}_1^m(c) + \sigma_{(0m)}\,\mathcal{P}_0^m(c) \right], \tag{O.11}$$

where we have used $\mathcal{P}_{-2}^m = \mathcal{P}_1^m$ (Appendix M). The explicit form reads (Appendix N)

$$v_{\theta,\,(1m)}(c) = \frac{1}{s}\left[\frac{\pi_{(1m)}}{6\,(1+m)}\left(3c^2 + 3mc + m^2 - 1\right) + \rho_{(-1m)}\,(c+m) + \sigma_{(0m)} \right] \left(\frac{1-c}{1+c} \right)^{\frac{m}{2}}. \tag{O.12}$$

This last expression is regular $\forall\, c \in [0,1]$ save in the axisymmetric case $m = 0$ for which it diverges in $c_s = 1$ and needs thus to be regularised. Evaluating (O.12) in $m = 0$ yields

$$v_{\theta,\,(10)}(c) = \frac{1}{s}\left[\frac{\pi_{(10)}}{6}\left(3c^2 - 1\right) + \rho_{(-10)}c + \sigma_{(00)} \right], \tag{O.13}$$

expression that we factorise in the following manner

$$v_{\theta,\,(10)}(c) = \frac{\pi_{(10)}}{2s}\left[c^2 + \frac{2\rho_{(-10)}}{\pi_{(10)}}\,c + \left(\frac{2\sigma_{(00)}}{\pi_{(10)}} - \frac{1}{3} \right) \right]. \tag{O.14}$$

For this last form to be regular everywhere, $c = 1$ must be a root of the quadratic polynomial enclosed by the square brackets, *i.e.*

$$[\dots] = (c-1)\left[c + \left(\frac{2\rho_{(-10)}}{\pi_{(10)}} + 1\right)\right] . \tag{O.15}$$

This regularisation process fixes the constant $\sigma_{(00)}$ to $\sigma_{(00)} = -\left[(1/3)\,\pi_{(10)} + \rho_{(-10)}\right]$, so that we end up with the well–behaved function

$$v_{\theta,\,(10)}(c) = -\frac{\pi_{(10)}}{2}\sqrt{1-c^2} - \rho_{(-10)}\sqrt{\frac{1-c}{1+c}} \ , \tag{O.16}$$

which is exactly the one (4.33) already derived in the separate treatment of sec. 4.2.1.

Azimuthal velocity

The modes $\left\{v_{\varphi,\,(lm)}(c)\right\}$ are easily inferred from the incompressibility condition (4.56)

$$v_\varphi = -\frac{is}{m}\left[\frac{\mathrm{d}\widetilde{v}_\theta}{\mathrm{d}c} + (l-2)\,v_r\right] . \tag{O.17}$$

Of course, this expression holds solely for $m \neq 0$. As a result, we will have to treat once again the axisymmetric states separately.

Starting from $\widetilde{v}_\theta \doteq s v_\theta$ with expression (O.8) for v_θ (only valid for $l \geqslant 2$), the trick to make calculations straightforward is using twice on the expression of $\widetilde{v}_\theta'$ — once for ${\mathcal{P}'}_l^m$ and once more for ${\mathcal{P}'}_{l-2}^m$ — the relation $\left[s^2 {\mathcal{P}'}_l^m(c)\right]' = \left\{m^2/\,s^2 - l\,(l+1)\right\}\mathcal{P}_l^m(c)$ which is simply a redraft of the Legendre equation (4.58). In doing so, one obtains

$$v_{\varphi,\,(lm)}(c) = -\frac{im}{s}\left[\frac{l-2}{l\,(l+1)}\,\pi_{(lm)}\,\mathcal{P}_l^m(c) + \frac{\rho_{(l-2,\,m)}}{l-1}\,\mathcal{P}_{l-2}^m(c)\right] - \frac{is}{m}\,\sigma_{(l-1,\,m)}\,\frac{\mathrm{d}\mathcal{P}_{l-1}^m}{\mathrm{d}c} \ , \quad \forall l \geqslant 2 \, . \tag{O.18}$$

It is worth stressing the fact that where derivatives of Legendre functions appear in the expression (O.8) of v_θ, here they do not, and vice versa.

It is clear that once again the case $l = 1$ has to be handled separately. The form (O.2) and the expression (O.11) inserted in (O.17) yield ($\mathcal{P}_{-1}^m = \mathcal{P}_0^m$, Appendix M)

$$v_{\varphi,\,(1m)}(c) = -\frac{is}{m}\left[\frac{1}{6}\,(m+2)\,\pi_{(1m)}\frac{\mathrm{d}\mathcal{P}_2^m}{\mathrm{d}c} + (1+m)\,\rho_{(-1m)}\frac{\mathrm{d}\mathcal{P}_1^m}{\mathrm{d}c} + \sigma_{(0m)}\frac{\mathrm{d}\mathcal{P}_0^m}{\mathrm{d}c} \right.$$
$$\left. - \pi_{(1m)}\mathcal{P}_1^m(c) - \rho_{(-1m)}\mathcal{P}_0^m(c)\right] , \quad m \neq 0 \, . \tag{O.19}$$

To finish, we recall that a direct calculation yields the form (4.34) of $v_{\varphi,\,(10)}$.

Appendix P

Expressions of the $(lm) = \{(10), (21)\}$ velocity fields in cartesian coordinates

The velocity fields associated with the flow states $(lm) = \{(10), (21)\}$ are converted into cartesian coordinates in the interfacial plane (xOy) and in the vertical cut plane (xOz).

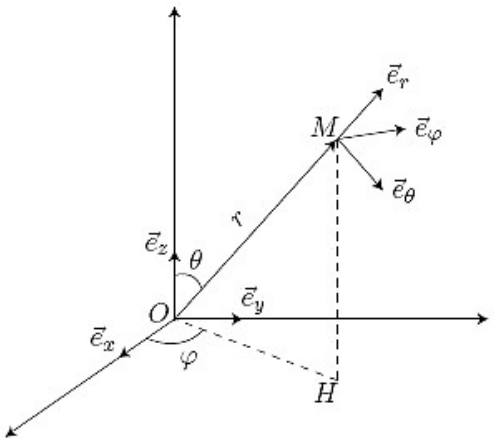

Figure P.1: Spherical coordinates.

According to the way angles are defined in Fig. P.1, the cartesian coordinates (x, y, z) can be expressed in terms of the spherical coordinates (r, θ, φ) as follows

$$x = r \sin\theta \cos\varphi = rs \cos\varphi \,, \tag{P.1a}$$

$$y = r \sin\theta \sin\varphi = rs \sin\varphi \,, \tag{P.1b}$$

$$z = r \cos\theta = rc \,. \tag{P.1c}$$

- The interfacial plane (xOy) is characterised by $\theta_I = \pi/2$, *i.e.* $c_I = 0$ ($\forall\, r \in [0, +\infty[$ and $\varphi \in [0, 2\pi]$) such that

$$x = r\cos\varphi\,, \tag{P.2a}$$
$$y = r\sin\varphi\,, \tag{P.2b}$$
$$z = 0\,, \tag{P.2c}$$

with $r^2 = x^2 + y^2$ and the after relations among spherical and cartesian basis vectors

$$\mathbf{e}_r(\theta = \pi/2) = \cos\varphi\,\mathbf{e}_x + \sin\varphi\,\mathbf{e}_y = \frac{x}{r}\,\mathbf{e}_x + \frac{y}{r}\,\mathbf{e}_y\ , \tag{P.3a}$$
$$\mathbf{e}_\varphi(\theta = \pi/2) = -\sin\varphi\,\mathbf{e}_x + \cos\varphi\,\mathbf{e}_y = -\frac{y}{r}\,\mathbf{e}_x + \frac{x}{r}\,\mathbf{e}_y\ , \tag{P.3b}$$

and $\mathbf{e}_\theta(\pi/2) \equiv \mathbf{n}$ is the unit vector normal to the plane (xOy).

- The vertical cut plane (xOz) is characterised by $\varphi = 0$ ($\forall\, r \in [0, +\infty[$ and $c \in [0, 1]$). This time we have

$$x = rs\,, \tag{P.4a}$$
$$y = 0\,, \tag{P.4b}$$
$$z = rc\,, \tag{P.4c}$$

where $r^2 = x^2 + z^2$ and

$$\mathbf{e}_r(\varphi = 0) = \sin\theta\,\mathbf{e}_x + \cos\theta\,\mathbf{e}_z = \frac{x}{r}\,\mathbf{e}_x + \frac{z}{r}\,\mathbf{e}_z\ , \tag{P.5a}$$
$$\mathbf{e}_\theta(\varphi = 0) = \cos\theta\,\mathbf{e}_x - \sin\theta\,\mathbf{e}_z = \frac{z}{r}\,\mathbf{e}_x - \frac{x}{r}\,\mathbf{e}_z\ , \tag{P.5b}$$

with now the unit vector $\mathbf{e}_\varphi(0)$ normal to the plane (xOz).

P.1 Axisymmetric state $(lm) = (10)$

Once boundary conditions (4.17a) – (4.17c) applied, one is left with

$$\mathbf{v}_{(10)}(r, c) = \frac{\psi_{(10)}(0)}{2r} \begin{pmatrix} 1 - 2c \\ c\sqrt{\dfrac{1-c}{1+c}} \\ 0 \end{pmatrix}_{(\mathbf{e}_r, \mathbf{e}_\theta, \mathbf{e}_\varphi)}\ . \tag{P.6}$$

Using then the above relations, one readily obtains the 2D vector fields

$$\mathbf{v}_{(10)}(x,y) = \frac{\psi_{(10)}(0)}{2} \begin{pmatrix} \dfrac{x}{x^2+y^2} \\ \dfrac{y}{x^2+y^2} \end{pmatrix}_{(\mathbf{e}_x,\,\mathbf{e}_y)} , \tag{P.7a}$$

$$\mathbf{v}_{(10)}(x,z) = \frac{\psi_{(10)}(0)}{2} \begin{pmatrix} \dfrac{x\left[x^2 - z\left(x^2+z^2\right)^{1/2}\right]}{\left(x^2+z^2\right)^{3/2}\left[z+\left(x^2+z^2\right)^{1/2}\right]} \\ -\dfrac{z^2}{\left(x^2+z^2\right)^{3/2}} \end{pmatrix}_{(\mathbf{e}_x,\,\mathbf{e}_z)} . \tag{P.7b}$$

The interfacial temperature amplitude $\psi_{(10)}(0)$ is set to 1 in the plots of sec. 4.3.5.

P.2 Non – axisymmetric state $(lm) = (21)$

Here the application of the boundary conditions (4.17a) – (4.17c) leads us to

$$\mathbf{v}_{(21)}(r,c,\varphi) = \frac{\psi_{(21)}(0)}{2r^2} \begin{pmatrix} -\left(3c^2+3c-1\right)\sqrt{\dfrac{1-c}{1+c}}\cos\varphi \\ \dfrac{c}{1+c}\cos\varphi \\ -\dfrac{c^2+c-1}{1+c}\sin\varphi \end{pmatrix}_{(\mathbf{e}_r,\,\mathbf{e}_\theta,\,\mathbf{e}_\varphi)} , \tag{P.8}$$

taking the real part of the original velocity vector. This time, one is left with the after 2D vector fields

$$\mathbf{v}_{(21)}(x,y) = \frac{\psi_{(21)}(0)}{2} \begin{pmatrix} \dfrac{x^2-y^2}{\left(x^2+y^2\right)^2} \\ \dfrac{2xy}{\left(x^2+y^2\right)^2} \end{pmatrix}_{(\mathbf{e}_x,\,\mathbf{e}_y)} , \tag{P.9a}$$

$$\mathbf{v}_{(21)}(x,z) = \frac{\psi_{(21)}(0)}{2} \begin{pmatrix} \dfrac{x^2\left(1-\dfrac{3z}{\left(x^2+z^2\right)^{1/2}}-\dfrac{3z^2}{x^2+z^2}\right)+z^2}{\left(x^2+z^2\right)^{3/2}\left[z+\left(x^2+z^2\right)^{1/2}\right]} \\ -\dfrac{3xz^2}{\left(x^2+z^2\right)^{5/2}} \end{pmatrix}_{(\mathbf{e}_x,\,\mathbf{e}_z)} . \tag{P.9b}$$

The temperature constant $\psi_{(21)}(0)$ is also arbitrarily set to 1 in the plots of sec. 4.3.5.

P.3 Superposed state $\{(10) + (21)\}$

The total vector field that corresponds to the superposition of flow states $\{(10) + (21)\}$ is simply defined as $\mathbf{v}_{\text{tot}} \doteq \mathbf{v}_{(10)} + \mathbf{v}_{(21)}$ so that we obtain after little algebra

$$\mathbf{v}_{\text{tot}}(x,y) = \begin{pmatrix} \dfrac{x^2\,(x+1) + y^2\,(x-1)}{2\,(x^2+y^2)^2} \\ \\ \dfrac{y\left[x\,(x+2) + y^2\right]}{2\,(x^2+y^2)^2} \end{pmatrix}, \tag{P.10a}$$

$$\mathbf{v}_{\text{tot}}(x,z) = \begin{pmatrix} \dfrac{x\left(x + x^2 - \dfrac{3xz}{(x^2+z^2)^{1/2}} - \dfrac{3xz^2}{x^2+z^2} - z\left(x^2+z^2\right)^{1/2}\right) + z^2}{2\,(x^2+z^2)^{3/2}\left[z + (x^2+z^2)^{1/2}\right]} \\ \\ \dfrac{3xz^4}{4\,(x^2+z^2)^4} \end{pmatrix}, \tag{P.10b}$$

making the arbitrary choice $\psi_{(10)}(0) = \psi_{(21)}(0) = 1$. Since there is no physical reason to assign the same weight to both the axisymmetric (10) and the dipolar (21) components, we encourage the interested reader to change the relative contribution of these flow states by fixing unequal temperature magnitudes, *e.g.* $\psi_{(10)}(0) = 1$ and $\psi_{(21)}(0) = 3$.

Bibliography

[1] A. Ashkin. Acceleration and Trapping of Particles by Radiation Pressure. *Phys. Rev. Lett.* **24,** 156–159 (1970).

[2] A. Girot, N. Danné, A. Würger, T. Bickel, F. Ren, J-C. Loudet, and B. Pouligny. Motion of Optically Heated Spheres at the Water–Air Interface. *Langmuir* **32,** 2687–2697 (2016).

[3] A. Würger. Thermally driven Marangoni surfers. *J. Fluid Mech.* **752,** 589–601 (2014).

[4] A. F. Pshenichnikov and S. S. Yatsenko. Convective Diffusion from a Concentrated Source of a Surfactant. *Proceedings of Perm State University. Fluids Dynamics.* **Issue 5. No. 316 [in Russian],** p. 175 (1974).

[5] A. I. Mizev and A. I. Trofimenko. Effect of an Insoluble Surfactant Film on the Stability of the Concentration–Driven Marangoni Flow. *Fluid Dynamics* **49 (1),** 26–36 (2014).

[6] M. Roché, Z. Li, I. M. Griffiths, S. Le Roux, I. Cantat, A. Saint-Jalmes, and H. A. Stone. Marangoni Flow of Soluble Amphiphiles. *Phys. Rev. Lett.* **112,** 208302 (2014).

[7] S. Le Roux, M. Roché, I. Cantat, and A. Saint-Jalmes. Soluble surfactant spreading: How the amphiphilicity sets the Marangoni hydrodynamics. *Phys. Rev. E* **93,** 013107 (2016).

[8] H. Kim, K. Muller, O. Shardt, S. Afkhami, and H. A. Stone. Solutal Marangoni flows of miscible liquids drive transport without surface contamination. *Nature Phys.* **13,** 1105–1111 (2017).

[9] Y. Uematsu, D. J. Bonthuis, and R. R. Netz. Impurity effects at hydrophobic surfaces. *Curr. Opin. Electrochem.* **13,** 166–173 (2019).

[10] V. Levich. Physicochemical Hydrodynamics. *Prentice Hall* (1962).

[11] S. Takagi and Y. Matsumoto. Surfactant Effects on Bubble Motion and Bubbly Flows. *Annu. Rev. Fluid Mech.* **43,** 615–636 (2011).

[12] R. D. Deegan, O. Bakajin, T. F. Dupont, G. Huber, S. R. Nagel, and T. A. Witten. Capillary flow as the cause of ring stains from dried liquid drops. *Nature* **389,** 827–829 (1997).

[13] H. Hu and R. G. Larson. Marangoni Effect Reverses Coffee−Ring Depositions. *J. Phys. Chem. B* **110,** 7090−7094 (2006).

[14] H. Kim, F. Boulogne, E. Um, I. Jacobi, E. Button, and H. A. Stone. Controlled Uniform Coating from the Interplay of Marangoni Flows and Surface−Adsorbed Macromolecules. *Phys. Rev. Lett.* **116,** 124501 (2016).

[15] J. C. Berg and A. Acrivos. The effect of surface−active agents on convection cells induced by surface tension. *Chem. Eng. Sci.* **20 (8),** 737−745 (1965).

[16] F. J. Peaudecerf, J. R. Landel, R. E. Goldstein, and P. Luzzatto-Fegiz. Traces of surfactants can severely limit the drag reduction of superhydrophobic surfaces. *PNAS* **114 (28),** 7254−7259 (2017).

[17] O. Manor, I. U. Vakarelski, X. Tang, S. J. O'Shea, G. W. Stevens, F. Grieser, R. R. Dagastine, and D. Y. C. Chan. Hydrodynamic Boundary Conditions and Dynamic Forces between Bubbles and Surfaces. *Phys. Rev. Lett.* **101,** 024501 (2008).

[18] A. Maali, R. Boisgard, H. Chraibi, Z. Zhang, H. Kellay, and A. Würger. Viscoelastic Drag Forces and Crossover from No−Slip to Slip Boundary Conditions for Flow near Air−Water Interfaces. *Phys. Rev. Lett.* **118,** 084501 (2017).

[19] B. Néel and E. Villermaux. The spontaneous puncture of thick liquid films. *J. Fluid Mech.* **838,** 192−221 (2018).

[20] W. A. Ducker. Contact Angle and Stability of Interfacial Nanobubbles. *Langmuir* **25 (16),** 8907−8910 (2009).

[21] S. Das, J. H. Snoeijer, and D. Lohse. Effect of impurities in description of surface nanobubbles. *Phys. Rev. E* **82,** 056310 (2010).

[22] Y. Uematsu, D. J. Bonthuis, and R. R. Netz. Charged Surface−Active Impurities at Nanomolar Concentration Induce Jones−Ray Effect. *J. Phys. Chem. Lett.* **9,** 189−193 (2018).

[23] Effet Marangoni aux interfaces fluides. *Thèse de doctorat de Sébastien Le Roux sous la direction de Arnaud Saint−Jalmes et la codirection de Isabelle Cantat, Université Rennes 1* (2015).

[24] P. G. de Gennes, F. Brochard−Wyart, and D. Quéré. Gouttes, bulles, perles et ondes. *Belin* (2002).

[25] H-J. Butt, K. Graf, and M. Kappl. Physics and Chemistry of Interfaces. *Wiley−VCH* (2006).

[26] J. Rowlinson and B. Widom. Molecular theory of capillarity. *Oxford University Press* (1982).

[27] J.W. Gibbs. On the Equilibrium of Heterogeneous Substances. *Transactions of the Connecticut Academy of Arts and Sciences* (1878).

[28] G. L. Van der Mensbrugghe. Sur la tension superficielle des liquides considérée au point de vue de certains mouvements observés à leur surface. *M. Hayez, imprimeur de l'Académie Royale de Belgique* (1869).

[29] C. Marangoni. Sull'espansione delle goccie d'un liquido galleggianti sulla superfice di altro liquido. *Pavia tipografia dei Fratelli Fusi* (1865).

[30] C. Tomlinson. On the Motions of Camphor on the Surface of Water. *Proceedings of the Royal Society of London* (1862).

[31] J. Thomson. On certain curious Motions observable at the Surfaces of Wine and other Alcoholic Liquors. *The London, Edinburgh and Dublin Philosophical Magazine and Journal of Science* **10,** 330 – 333 (1855).

[32] L. E. Scriven and C. V. Sternling. The Marangoni Effects. *Nature* **187,** 186 – 188 (1960).

[33] J-B. Fournier and A-M. Cazabat. Tears of Wine. *Europhys. Lett.* **20 (6),** 517 – 522 (1992).

[34] J. D. Berry, M. J. Neeson, R. R. Dagastine, D. Y. C. Chan, and R. F. Tabor. Measurement of surface and interfacial tension using pendant drop tensiometry. *Journal of Colloid and Interface Science* **454,** 226 – 237 (2015).

[35] A. J. Prosser and E. I. Franses. Adsorption and surface tension of ionic surfactants at the air – water interface: review and evaluation of equilibrium models. *Colloids and Surfaces A: Physicochem. Eng. Aspects* **178,** 1 – 40 (2001).

[36] E. J. Stamhuis. Basics and principles of particle image velocimetry (PIV) for mapping biogenic and biologically relevant flows. *Aquatic Ecology* **40 (4),** 463 – 479 (2006).

[37] H. Abdulmouti. Particle imaging velocimetry (PIV) technique: principles and applications, review. *Yanbu Journal of Engineering and Science* **6,** 35 – 65 (2013).

[38] M. Raffel, C. E. Willert, and J. Kompenhans. Particle image velocimetry: a practical guide. *Springer Science & Business Media* (2007).

[39] W. Thielicke and E. J. Stamhuis. PIVlab: Towards User – fiendly, Affordable and Accurate Digital Particle Image Velocimetry in MATLAB. *Journal of Open Research Software* **2 (1)** (2014).

[40] R. V. Birikh, V. A. Briskman, M. G. Velarde, and J-C. Legros. Liquid Interfacial Systems. *CRC Press* (2003).

[41] A. Pockels. On the Relative Contamination of the Water – Surface by Equal Quantities of Different Substances. *Nature* **46,** 418 – 419 (1892).

[42] G. J. Elfring, L. G. Leal, and T. M. Squires. Surface viscosity and Marangoni stresses at surfactant laden interfaces. *J. Fluid Mech.* **792,** 712 – 739 (2016).

[43] R. Palaparthi, D. T. Papageorgiou, and C. Maldarelli. Theory and experiments on the stagnant cap regime in the motion of spherical surfactant – laden bubbles. *J. Fluid Mech.* **559,** 1 – 44 (2006).

[44] C. Ybert and J-M. di Meglio. Ascending air bubbles in protein solutions. *Eur. Phys. J. B* **4,** 313 – 319 (1998).

[45] T. Bickel, J-C. Loudet, G. Koleski, and B. Pouligny. Hydrodynamic response of a surfactant−laden interface to a radial flow. *Phys. Rev. Fluids* **4,** 124002 (2019).

[46] H. Hu and R. G. Larson. Analysis of the Effects of Marangoni Stresses on the Microflow in an Evaporating Sessile Droplet. *Langmuir* **21,** 3972−3980 (2005).

[47] P. A. Kralchevsky, K. D. Danov, and N. D. Denkov. Chemical Physics of Colloid Systems and Interfaces in Handbook of Surface and Colloid Chemistry. *CRC Press* (2015).

[48] M. Arangalage, X. Li, F. Lequeux, and L. Talini. Dual Marangoni effects and detection of traces of surfactants. *Soft Matter* **14,** 3378−3386 (2018).

[49] Y. Couder, J-M. Chomaz, and M. Rabaud. On the hydrodynamics of soap films. *Physica D* **37,** 384−405 (1989).

[50] G. Liger-Belair, C. Cilindre, F. Beaumont, P. Jeandet, and G. Polidori. Evidence for ascending bubble driven flow patterns in champagne glasses, and their impact on gaseous CO_2 and ethanol release under standard tasting conditions (review). *Bubble Science, Engineering and Technology* **4 (1),** 35−48 (*W. S. Maney and Son Ltd*, 2012).

[51] F. Beaumont, G. Liger−Belair, and G. Polidori. Unveiling self−organized two−dimensional (2D) convective cells in champagne glasses. *Journal of Food Engineering* **188,** 58−65 (2016).

[52] G. Gaussorgues. Infrared Thermography. *Chapman & Hall* (1994).

[53] Microscopie à l'angle de Brewster: transitions de phases et défauts d'orientation dans des films monomoléculaires. *Thèse de doctorat de Sylvie Hénon sous la direction de Jacques Meunier, Université Paris 6* (1993).

[54] Y. Kamotani, S. Ostrach, and J. Masud. Oscillatory thermocapillary flows in open cylindrical containers induced by CO_2 laser heating. *International Journal of Heat and Mass Transfer* **42,** 555−564 (1999).

[55] Yu. K. Bratukhin, S. O. Makarov and A. I. Mizev. Oscillating thermocapillary convection regimes driven by a point heat source. *Fluid Dynamics* **35 (2),** 232−241 (2000).

[56] N. M. Kovalchuk. Spontaneous oscillations due to solutal Marangoni instability: air/water interface. *Cent. Eur. J. Chem.* **10 (5),** 1423−1441 (2012).

[57] A. B. Ezersky, A. Garcimartín, J. Burguete, H. L. Mancini, and C. Pérez-García. Hydrothermal waves in Marangoni convection in a cylindrical container. *Phys. Rev. E* **47 (2),** 1126−1131 (1993).

[58] Ondes non−linéaires à une et deux dimensions dans une mince couche de fluide. *Thèse de doctorat de Nicolas Garnier sous la direction de Arnaud Chiffaudel, Université Paris 7* (2000).

[59] V. Shtern and F. Hussain. Azimuthal instability of divergent flows. *J. Fluid Mech.* **256,** 535−560 (1993).

[60] Y. K. Bratukhin and L. N. Maurin. Thermocapillary convection in a fluid filling a half−space. *J. Appl. Math. Mech.* **31,** 577−580 (1967).

[61] H. Lamb. Hydrodynamics. *Dover* (1945).

[62] A. Girot. Flotteurs Marangoni auto−propulsés dans un piège optique. Master's thesis (2015).

[63] A-M. Cazabat and G. Guéna. Evaporation of macroscopic sessile droplets. *Soft Matter* **6,** 2591−2612 (2010).

[64] M. Schmitt and H. Stark. Marangoni flow at droplet interfaces: Three−dimensional solution and applications. *Phys. Fluids* **28,** 012106 (2016).

[65] O. Pak and E. Lauga. Generalized squirming motion of a sphere. *J. Eng. Math.* **88 (1),** 1−28 (2014).

[66] M. Abramowitz and I. A. Stegun. Handbook of Mathematical Functions with Formulas, Graphs, and Mathematical Tables. *Applied Mathematics Series **55.** United States Department of Commerce, National Bureau of Standards. Dover* (1972).

[67] M. M. Bandi, V. S. Akella, D. K. Singh, R. S. Singh, and S. Mandre. Hydrodynamic Signatures of Stationary Marangoni−Driven Surfactant Transport. *Physical Review Letters* **119,** 264501 (2017).

[68] S. Mandre. Axisymmetric spreading of a surfactant driven by self−imposed Marangoni stress under simplified transport. *J. Fluid Mech.* **832,** 777−792 (2017).

[69] F. Wodlei, J. Sebilleau, J. Magnaudet, and V. Pimienta. Marangoni−driven flower−like patterning of an evaporating drop spreading on a liquid substrate. *Nature Communications* **9,** 820−831 (2018).

[70] L. Keiser, H. Bense, P. Colinet, J. Bico, and E. Reyssat. Marangoni Bursting: Evaporation−Induced Emulsification of Binary Mixtures on a Liquid Layer. *Physical Review Letters* **118,** 074504 (2017).

[71] H. C. Kuhlmann and U. Schoisswohl. Flow instabilities in thermocapillary−buoyant liquid pools. *J. Fluid Mech.* **644,** 509−535 (2010).

[72] A. K. Sen and S. H. Davis. Steady thermocapillary flows in two−dimensional slots. *J. Fluid Mech.* **121,** 163−186 (1982).

[73] S. H. Davis. Thermocapillary Instabilities. *Ann. Rev. Fluid Mech.* **19,** 403−435 (1987).

[74] Convection thermocapillaire et thermogravitaire dans un fluide chauffé localement sur sa surface libre. *Thèse de doctorat de Éric Favre sous la direction de Yves Fautrelle, réalisée à l'Institut National Polytechnique de Grenoble* (1997).

[75] A. Shmyrov, A. Mizev, V. Demin, M. Petukhov, and D. Bratsun. On the extent of surface stagnation produced jointly by insoluble surfactant and thermocapillary flow. *Advances in Colloids and Interface Science* **255,** 10−17 (2017).

[76] A. Mizev. Influence of an adsorption layer on the structure and stability of surface tension driven flows. *Physics of Fluids* **17,** 122107 (2005).

[77] A. Thess, D. Spirn, and B. Jüttner. A two−dimensional model for slow convection at infinite Marangoni number. *J. Fluid Mech.* **331,** 283−312 (1997).

[78] B. Carpenter and G. M. Homsy. The effect of surface contamination on thermocapillary flow in a two−dimensional slot. Part 2. Partially contaminated interfaces. *J. Fluid Mech.* **155,** 429−439 (1985).

[79] G. M. Homsy and E. Meiburg. The effect of surface contamination on thermocapillary flow in a two−dimensional slot. *J. Fluid Mech.* **139,** 443−459 (1984).

[80] S. N. Varanakkottu, S. D. George, T. Baier, S. Hardt, M. Ewald, and M. Biesalski. Particle Manipulation Based on Optically Controlled Free Surface Hydrodynamics. *Angew. Chem. Int. Ed.* **52,** 7291−7295 (2013).